Comparative planetary circulation regimes in simple general circulation models

Yixiong Wang

St Cross College

University of Oxford

A thesis submitted for the degree of

Doctor of Philosophy

Trinity 2014

Acknowledgements

First of all, I would like to thank my supervisor — Professor Peter Read, for offering me this great opportunity to pursuit a DPhil project on planetary atmospheric circulation dynamics in AOPP, and providing inspiring and insightful guidance as well as continuous encouragement throughout my DPhil research. A lot has been learnt from him during my years as his student. His enthusiasm about the physical essence of geophysical fluid systems, and his in-depth knowledge regarding quite a broad range of different research topics are really impressive. It is no doubt a marvelous and enjoyable experience being his student.

My thanks also goes to many students and researchers in AOPP. I would like to thank Dr. Joao Mendonca for his help in setting up the two-band radiative transfer scheme. I would also like to thank Dr. Roland Young for kindly helping me using the "octopi" computer cluster, and all members in the AOPP GFD group for lots of helpful discussions. I am particularly indebt to Dr. Hartmut Borth of University of Hamburg for his help on technical details of coupling between dynamical core and radiative scheme, and Professor Klaus Fraedrich, Dr. Edilbert Kirk and Dr. Salvatore Pascale for various useful conversations and discussions during and after my visit to Hamburg in 2011.

I am sincerely grateful to my parents for supporting me both mentally and materially during my DPhil studies. And I would like to thank my wife Si Chen for her love, support and company.

Abstract

This thesis presents the studies of terrestrial planetary atmospheric circulation regimes using simplified GCMs with different levels of complexity. Two different versions of the simplified GCM PUMA (Portable University Model for the Atmosphere) are used — PUMA-S with Newtonian cooling scheme and PUMA-G with a semi-grey two-band radiative transfer scheme and dry convective adjustment. A series of controlled experiments are conducted by varying planetary rotation rate and imposed equator-to-pole temperature difference using PUMAS-S, and by varying rotation rate, planetary obliquity, and the ratio of optical depth in long-wave (thermal radiation) band to that in short-wave (stellar radiation) band using PUMA-G. These defining parameters are further combined with each other into dimensionless forms to establish parameter spaces, in which the occurences of different circulation regimes are mapped and classified. For the PUMA-S experiments, very coherent trends when varying planetary rotation rate (thermal Rossby number) is found. It is demonstrated that the GRW mechanism is mainly responsible for the equatorial super-rotation observed in our experiments. Regular baroclinic waves are obtained at intermediate values of thermal Rossby number and depend strongly on the strength of radiative and frictional damping. Global atmospheric energetics in terms of Lorenz energy cycle and meridional heat transport efficiency also exhibits strong dependence on planetary rotation rate from our PUMA-S experiments. Theories of geostrophic turbulence (especially the recently introduced zonostrophic turbulence) and jet formation are examined using the PUMA-S experiments. For the PUMA-G experiments, Similar trends are observed with respect to varying planetary rotation rates, while new regimes like strongly subrotating (in the retrograde direction) atmospheres are found when varying obliquity in PUMA-G. Tidally-locked planets are also studied by modifying the incoming stellar irradiation in PUMA-G. It is found that atmospheric optical depth in the long-wave band plays an important role in setting the heat transport efficiency from day-side to night-side.

Contents

List of Figures

Chapter 1

Introduction

1.1 The Problem and general approach

The study of atmospheric general circulation, which dates back to the 18th century with the pathbreaking work by Hadley (1735), has been greatly enriched by explorations (both observational and theoretical) of other planets since the last century. Within our solar system, substantial atmospheres were discovered on a series of planetary bodies: Venus, Mars, the gas/ice giants (Jupiter, Saturn, Uranus and Neptune), and Titan—the largest moon of Saturn (see Table 1.1). Our knowledge of the dynamics, radiative properties, and chemical compositions of these planets as well as the atmospheres wrapping around them have grown to a reasonably satisfactory extent, by means of ground-based, orbital and in-situ observations. Beyond the kingdom of the Sun, more than 800 extrasolar planets (a.k.a. exoplanets) have been detected using various astronomical observation techniques, and many of them are believed to hold atmospheres around (see the review of Seager & Deming (2010)). The differences of climate and circulation regimes amongst these planetary atmospheres are strikingly significant. Even our two nearest neighbours pose an impressive contrast: a hot and high pressure (nearly 90 times of the Earth!) inferno on Venus in contrast

Planet	g ($\times g_E$)	Albedo (%)	Surface temperature (K)	Surface pressure (bar)	Atmospheric composition
Venus	0.905	75	737	92	$96.5\%CO_2, 3.5\%N_2$ $0.015\%SO_2, 0.002\%H_2O$
Earth	1.000	30.6	288	1	$78\%N_2, 21\%O_2,$ $0.038\%CO_2, < 1\%H_2O$
Mars	0.379	25.0	184 night, 242 day	0.004-0.009	$95.3\%CO_2, 2.7\%N_2,$ $0.021\%H_2O$
Jupiter	2.530	34.3	165	$\gg 1000$	$89.8\%H_2, 10.2\%He,$ $0.3\%CH_4, 0.026\%NH_3$
Saturn	1.065	34.2	134	$\gg 1000$	$96.3\%H_2, 3.25\%He,$ $0.45\%CH_4, 0.0125\%NH_3$
Uranus	0.905	30.0	76	$\gg 1000$	$82.5\%H_2, 19.0\%He,$ $1.5\%CH_4$
Neptune	1.14	29.0	72	$\gg 1000$	$80.0\%H_2, 19.0\%He,$ $1.5\%CH_4$
Titan	0.14	22.0	93.7	1.47	$98.4\%N_2, 1.4\%CH_4,$ $0.1\%H_2$

Table 1.1: Basic properties of the planetary atmospheres within the Solar System

to a cold and extremely low pressure (1% of the Earth!) desert–world on Mars.

From a physicist's viewpoint, all of these planetary atmospheres can be abstracted as rotating, stratified fluids moving under mechanical/electromagnetic(.etc) forcings from the host star and the underlying planet. It is thus natural to ask the question as to what characteristic factors most fundamentally determine the various circulation patterns that we observe in those exotic worlds, and also our own.

The meaning of giving a complete answer to this question is not just to satisfy our sheer intellectual curiosity. The understanding of the dominating factors and mechanisms of the general circulation is a prerequisite to our understanding of the climate variability of the Earth both in the past and in the future. Besides, light could be shed on the potential habitability questions of exoplanets by studying the parameter dependence of the general circulation regime.

The general methodology employed by most theoreticians for this sort of problem

is to establish a model atmosphere which is usually built upon various reasonable idealisations, and then gain insights by studying the behaviours of this model atmosphere. In most cases, simple models incorporating dynamic constraints and key physical processes are used rather than the highly complex and "realistic" models with great details, which seek to simulate the climate and atmospheric circulation in great quantitative detail. This is of course partly due to the convenience of handling a simpler model, but more importantly, because it tells us more about fundamental physical processes and causal relationships, which are usually not explicitly expressed or straightforward to extract in the results of complex models. By conducting sequences of controlled experiments and sensitivity tests on these simple models (either numerical or laboratory), dominating factors for the formation and maintenance of circulation regimes can be highlighted and distinguished from those of secondary importance.

Laboratory analogues of the planetary atmosphere usually take the form of viscous stratified fluids confined in a rotating annulus (or tank) heated from the boundaries. This configuration, although devoid of spherical geometry and radiative processes, captures the essential physics of the atmospheric circulation, that is, a fluid in rotation under the forcing of differential stellar heating. Since the pioneering work of Hide (1953) and Fultz et al. (1959), much knowledge of the atmospheric general circulation as well as other aspects of atmospheric dynamics has been gained by studying these flow patterns (see Hide & Mason (1975), Lorenz (1967)). Flow behaviours under various conditions have been thoroughly measured and classified, and their dependence on non-dimensional parameters can be shown by mapping the flow patterns within a parameter space (the resulting map is known as a *regime diagram*). Nowadays this method is still continually providing considerable enlightenment (both for scientific research and for education) in the study of geophysical fluid dynamical systems (e.g. see Read et al. (1998), Read (2001), Wordsworth et al. (2008), Illari et al. (2009)).

Another approach is to make use of simplified numerical models of planetary atmospheres to investigate the behaviour of the circulation. There has been a series of work taking the parameter approach to study the circulation since 1970s (Hunt (1979), Williams & Holloway (1982), Williams (1988a), Williams (1988b), Del Genio & Suozzo (1987), Jenkins (1996)), with the motivations ranging from paleoclimate simulation to GCM parameter optimisation. Depending on the purpose of studies, the parameters to tune within a simple GCM include planetary rotation rate, planetary radius, gravity, obliquity etc. Thus similar (although more complicated perhaps) regime diagrams are expected to be produced by such numerical experiments. And some of the previous studies have yielded preliminary regime diagrams (Geisler et al. (1983)). However, a systematic investigation and exploration of the parameter space has not yet been made. And this is one of the major motivations of the present project.

In this project, we will use the simplified GCM—PUMA (Portable University Model of Atmospheres) developed by the Meteorological Institute, University of Hamburg, as well as its modified version with two-band radiative-transfer, to conduct controlled experiments and sensitivity tests on factors like planetary rotation rate, obliquity and so on. Corresponding non–dimensional parameters are suitably defined to construct a dimensionless parameter space in which circulation regimes are mapped.

1.2 Diversity of observed terrestrial planetary circulation regimes

Most planets (either Solar System or extra-solar ones) that we have detected are either terrestrial or gaseous/icy. The latter ones differ significantly from the former ones mostly because of their lack of a well-defined solid planetary surface. Besides,

most of these giants (with Uranus as an exception for example) are still emitting considerable amount of radiation from their deep interiors (this radiation comes from the heat released by the gravitational accretion during the planetary formation, see Dowling (1995)), making the giant planets' circulations partly driven by internal heat sources. Given such fundamental differences, we will mainly focus on the circulation regimes of terrestrial planets (planets with shallow atmospheres, solid surface, and no internal heat sources) in this project.

In principle, the study of the general circulation of a prototypical planetary atmosphere is a coupled dynamics-radiation problem (see Fig. 1.1). The concept of the so-called 'atmospheric heat engine' is frequently used to illustrate this idea (see Barry et al. (2002), Peixoto J.P. (1992)). Differential heating drives the meridional motion of the atmosphere, and this horizontal advection prevents the atmosphere from reaching a state of local radiative equilibrium, thus maintaining the net heating (cooling) at the equator (the poles). Hadley (1735) first realised this point (that the circulation is driven by differential heating) and proposed an axisymmetric meridionally circulating atmosphere to account for the prevailing trade winds over tropical regions. Subsequent observations then revealed that this heat-driven overturning circulation (now known as 'Hadley Cell') gives way to baroclinic waves and eddies in the extra-tropical regions.

1.2.1 Earth and Mars

The zonal and temporal mean of Earth's general circulation structure, as shown in Fig. 1.2, is characterised by three circulation cells and one jet stream in each hemisphere, with meridional surface temperature difference of around 50K. Atmospheric temperature decreases with height in the troposphere and increases with height in stratosphere, due to the existence of the ozone layer in upper stratosphere.

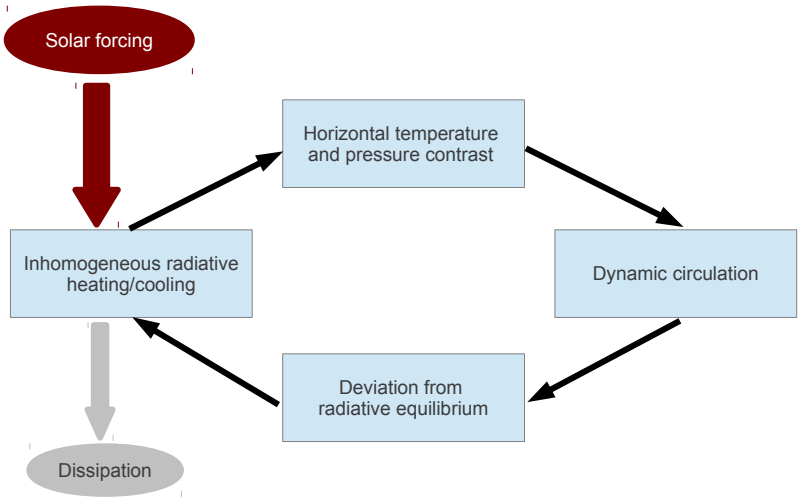

Figure 1.1: Schematic of the nature of atmospheric general circulation.

As our neighbour and one of the most thoroughly observed planets within our Solar System, Mars shares a lot of atmospheric circulation features in common with the Earth. Both the Hadley cells and the baroclinic zones are found on this red desert planet. And its similar rotation rate to the Earth determines many of these similarities in their circulation regimes.

As we can see from Figs. 1.2 and 1.3, the Martian annual mean circulation looks quite like that of the Earth, with two thermally-direct Hadley cells lying roughly anti-symmetrically along the equator, as well as two indirect cells at higher latititudes where baroclinic eddy activities are predominant and geostrophic balance stands. Baroclinic jet streams can also be found on Mars although at a higher latitudes than those on the Earth. The temperature field is featured by an equatorial warm core graduately cooling towards the poles within the troposphere, with more complicated latitudinal variations in the middle and upper atmosphere. It should be pointed out that seasonal variation of the Martian circulation is significantly greater than that of the Earth. For most times of the year, especially during those solstice seasons, the circulation is dominated by a cross-equator global Hadley cell which transports heat and mass from one hemisphere to the other. And the surface wind pattern at those times has eastward wind at the winter hemisphere and westward wind at the

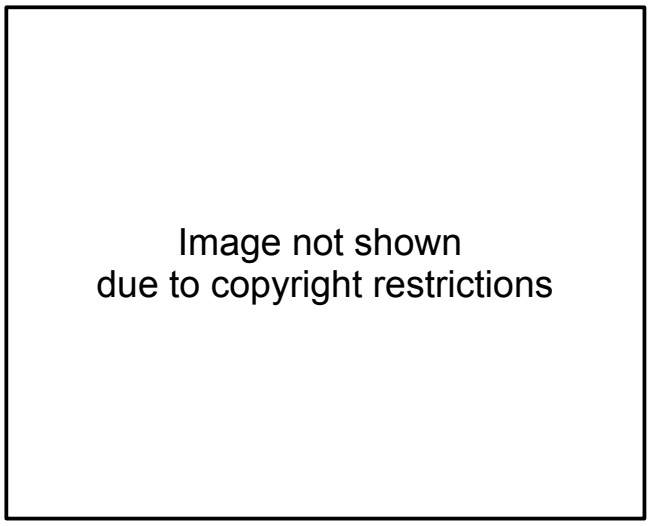

Figure 1.2: Earth's annual and zonal mean climatology, (a) temperature, (b) zonal wind, (c) meridional mass streamfunction. From Kallberg et al. (2004) based on ECMWF datasets.

summer hemisphere, just like the wind distribution of Earth's middle atmosphere. There is a short time around the solstice when the summer pole temperature is even larger than the equator. This greater extent of seasonal variation is mostly because of the small thermal inertia of the Martian climate system (thin atmosphere and lack of ocean) as well as its larger orbital eccentricity. Moreover, the baroclinic waves on Mars tend to behave more regularly and coherently than their chaotic counterparts in Earth's atmosphere (as observed by the Viking lander, see Barnes (1981)), a phenomenon possibly rooted in the smaller planetary radius (implying larger thermal Rossby number) of Mars. In spite of these differences, the circulation patterns of Mars and the Earth are in most respects similar to each other, sharing a series of features of rapidly rotating planets in common.

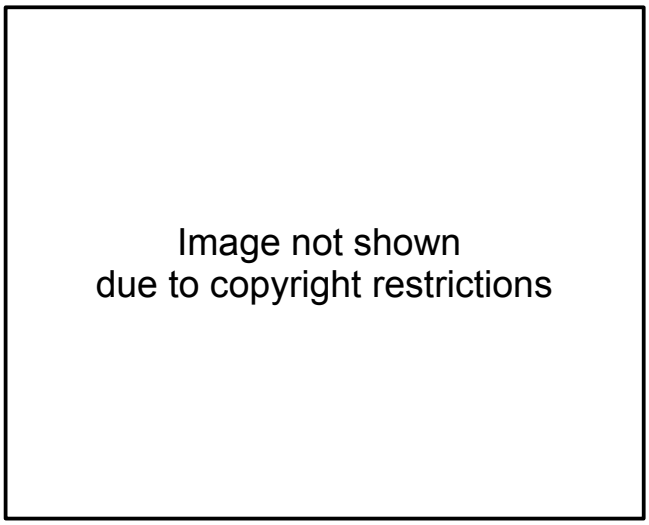

Figure 1.3: Annual and zonal mean martian climatology from GCM results, (a) temperature, (b) zonal wind, (c) meridional mass streamfunction. From Read & Lewis (2004a)

1.2.2 Venus and Titan

Venus and Titan are slowly rotating planets with very different circulation regimes to those of the Earth and Mars. GCM simulations(see Fig. 1.4) show that the zonal–mean circulation of Venus is dominated by two hemispheric Hadley cells ranging from the equator to very high latitudes. This, together with the very large radiative time scale on these two planets, leads to a much smaller latitudinal temperature difference compared with the Earth and Mars. It can thus be implied that the atmospheres of Venus and Titan are largely barotropic rather than baroclinic.

The most remarkable feature of the zonal wind field is the globally prograde upper level wind. This is different from the situation on Mars and the Earth where prograde wind is only observed in extratropical regions while the equatorial atmosphere is dominated by deep eastward winds. This excess of angular momentum, compared

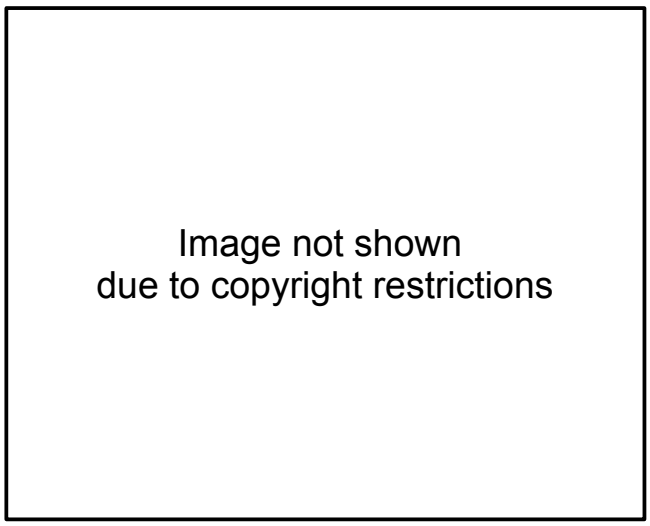

Figure 1.4: Venus climatology from GCM results, (a) temperature, (b) zonal wind, (c) meridional mass streamfunction. From Lee et al. (2005)

with the angular momentum air would have in co–rotation with the underlying solid body, is known as the 'super–rotation' (Read (1986b)). This is a unique characteristic of the slowly rotating planets.

The very fast wind speed on Venus and Titan compared with the underlying solid planets indicates that geostrophic balance is no longer valid. In fact, cyclostrophic balance (the balance between centrifugal force and the pressure gradient force) is believed to be the dominant meridional force balance of the large scale dynamics on Venus and Titan.

1.2.3 Terrestrial exoplanets

Exoplanets (a.k.a extrasolar planets) refer to planets beyond the Solar System. Since the first discovery in the 1990s (Wolszczan & Frail (1992), Mayor & Queloz (1995)), more than 1000 exoplanets[1] have been detected via various observational techniques (radial-velocity approach, transiting light-curve approach, gravitational lense approach etc., see review by Seager & Lissauer (2010)). Preliminary observational

[1]According to the Extrasolar Planets Encyclopaedia (`http://exoplanet.eu`), 1055 exoplanets have been discovered until 30 December 2013.

constraints obtained using current technology have revealed a great variety of orbital/planetary parameters among these exoplanets. The exotic conditions of these planets in terms of planetary mass, stellar irradiation and planetary composition have led to a series of new terminology like "Hot Jupiter" , "Hot Neptune" , "Super Earth" and so on.

One of the central and ultimate questions brought up by the discovery of more and more exoplanets is the potential habitability of these planets (especially the terrestrial ones with solid surface) for terrestrial life. Most of the terrestrial planets detected so far are essentially "Super Earths" , since they are easier to be discovered based on current observational techniques. Nevertheless, there is a growing number of lower-mass Earth-like planets being discovered recently following NASA's successful Kepler mission. Direct measurement of planetary radius and mass is available using transit observations and Doppler velocity data. Additional information on the planetary rotation rate can be inferred if the planet is in a tidally-locked state, in which case the planet's rotation period is equal to its revolutionary period. In order to estimate the atmospheric circulation/climate conditions of such exoplanets based on these limited observational data, systematic investigations of their circulation regimes' dependence on planetary parameter like rotation rate, obliquity angle, atmospheric opacity and so on must be conducted.

1.3 Laboratory experiments and the regime diagram

Rotating annulus experiments provide an intuitive laboratory approach to study various geophysical fluid problems including the planetary atmospheric circulation. The idea of conducting systematic controlled experiments and building up regime diagrams is essentially inspired by similar methodologies originally used in the context

of such laboratory experiments. The fluid in a rotating annulus is confined by two coaxial cylinders, and the whole system rotates around the vertical axis of symmetry with constant angular velocity. If the outer cylinder is heated and the inner cylinder is cooled, this configuration roughly mimics the atmospheric circulation of terrestrial planets forced by differential heating at relatively low obliquity.

At least two parameters (the rotation rate and the imposed temperature difference between the inner and the outer cylinders) can be modified to conduct controlled experiments. But directly using the value of rotation rate or temperature difference to construct the parameter space in which circulation regimes are categorised might shed little light on our quantitative understanding of the behaviour of planetary atmospheres, since it could not get rid of the influence of the specific experimental configuration which is obviously far different from planetary atmospheres in terms of characteristic length/time scales, working fluid density, etc. In order to avoid the influence of particular experimental configurations and obtain generalisable results, non-dimensional parameters are adopted using the dynamical similarity theory. Previous experiments (e.g. Hide & Mason (1975)) have revealed that the most relevant parameters of the rotating annulus experiments are the Taylor number ($\mathcal{T}_a$) and the thermal Rossby number ($\mathcal{R}o$):

$$\begin{aligned} \mathcal{T}_a &= \frac{4\Omega^2 L^5}{\nu^2 D} \\ \mathcal{R}_o &= \frac{g\alpha\Delta T D}{\Omega^2 L^2} \end{aligned} \tag{1.1}$$

where L is the channel width, D the depth, Ω the rotation rate, ΔT the imposed temperature difference, ν the kinematic viscosity coefficient of the fluid and α the volumetric thermal expansion coefficient.

Using thermal Rossby number and Taylor number to construct a 2-D parameter space, we can map the occurence of the type of flow observed in the experiments. The map obtained shows the parametric dependence of the flow regime, and is known as

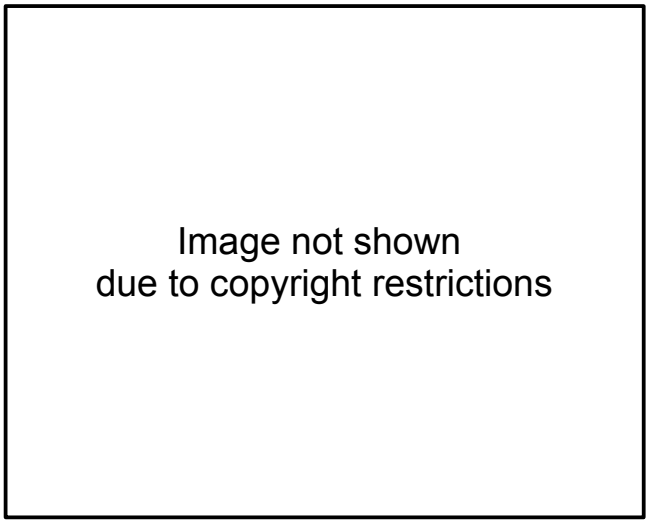

Figure 1.5: Regime diagram from Hide & Mason (1975). Note that for historical reasons, thermal Rossby number is written as Θ rather than $\mathcal{R}o$. 45° slope lines from the top left to the bottom right are experiments with same horizontal temperature difference. Numbers at individual points represent the observed wavenumbers.

the regime diagram (see Fig. 1.5). At least three distinct regimes can be found in such a regime diagram obtained using rotating annulus experiments: axisymmetric steady flow; steady or vacillating regular waves; irregular or turbulent waves.

1.4 Parametric approach using GCMs

The history of using numerical models to study atmospheric behaviour is roughly as long as the laboratory rotating annulus experiments. However, a majority of the previous efforts on numerical studies were focussed on the developing capabilities of numerical weather prediction on synoptic time scales, or highly comprehensive Earth-based GCMs to study the climate variability. Sensitivity tests and controlled experiments on planetary parameters, on the other hand, have not been given much systematic attention within the numerical modelling community (previous studies taking parametric approach using numerical models tend to use relatively complex models, e.g. GCMs with radiation and moisture schemes that are designed specifically for Earth's atmosphere, see Williams (1988a), Williams (1988b), Barry et al. (2002)).

One of the early fruitful attempts is that done by Geisler et al. (1983) focussing on the dependence of circulation regimes on planetary rotation rate. A simplified GCM using Newtonian cooling and a linear surface drag scheme was adopted to construct a regime diagram, as shown in Fig. 1.6. Four different flow patterns were identified: a steady wave dominated by a single zonal wavenumber and constant amplitude (denoted by black solid dots with the dominant wavenumber labelled at its right side); a vacillating wave flow with one or two dominant zonal wavenumbers (denoted by black solid triangles with dominating wavenumbers labelled at its right side); irregular waves (denoted by black solid dots with no wavenumber labelled). Similar to the laboratory regime diagram, runs with constant temperature differences are located along a diagnonal straight line. Point A is the terrestrial point with $\Delta T = 60K, \Omega = 7 \times 10^{-5}\mathrm{s}^{-1}$. Most of the runs done by Geisler et al. (1983) were with rotation rate smaller than that of the Earth and temperature difference smaller than $60K$. A systematic investigation including higher rotation rate and larger temperature differences is therefore needed to explore regimes with these parameter configurations.

The most comprehensive study on the sensitivity of Earth-like planetary atmospheres to planetary parameters so far is probably that done by Williams in the late 1980s (Williams (1988a),Williams (1988b)). The effect of changing rotation rate, obliquity and so on are studied using both dry atmosphere GCM and moist atmosphere GCM. Various circulation patterns observed in these experiments are summarised qualitatively, and are further supported by other studies (e.g. Navarra & Boccaletti (2002), Del Genio & Suozzo (1987)). Surprisingly, however, no regime diagram was derived from these studies, making it less than straightforward to generalise and apply the corresponding results to real planetary atmospheres.

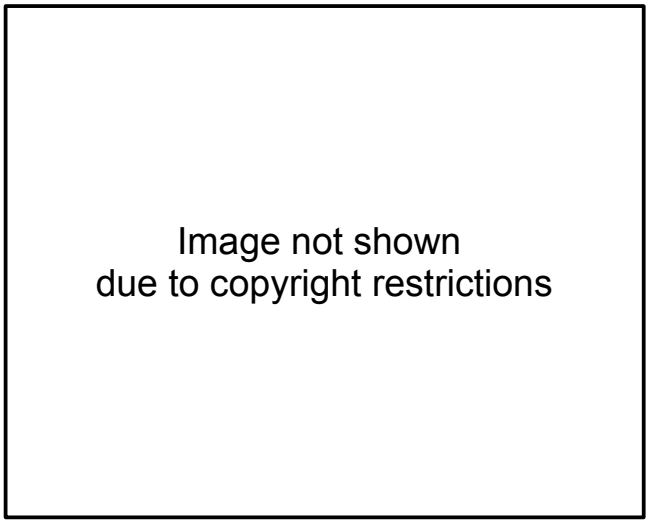

Figure 1.6: Regime diagram from Geisler et al. (1983). The thick black curve represents the boundary between axisymmetric regime (white circles) and non-axisymmetric regimes (black circles and triangles). Black circles with numbers represent runs in which steady waves with constant amplitude were found with one dominating wavenumber indicated by the associated number near the points. The black triangles represent runs of vacillating waves with one or two dominant wavenumbers as indicated by the associated numbers. Other solid points represent runs with irregular waves.

1.5 Scientific questions and model choice

As indicated in the previous sections, a systematic investigation of the parametric dependence of atmospheric general circulation on the defining planetary parameters is needed, for providing insights into both theoretical understandings of atmospheric circulation and potential habitability issues with regard to terrestrial exoplanets. By conducting experiments that covers a relatively broad range of parameter space with respect to a carefully chosen set of dimensionless parameters, this project not only reveals the diversity of circulation regimes that can be obtained by simply varying a few external parameters, but also provides key insights into a series of scientific questions that are important to our understanding of the fundamental mechanisms of atmospheric general circulation.

Planetary atmospheres have long been viewed as heat engines which convert ther-

mal energy into mechanical energy (see discussions in e.g. Peixoto J.P. (1992)). For the instance of Earth's atmosphere, the ultimate energy source that drives the atmospheric heat engine is the solar radiation. The atmosphere is heated either directly by solar radiation, or indirectly by ground infrared emission and latent heat release via the hydrological cycle. The absorbed thermal energy is then transformed into potential energy, a tiny fraction of which is further transformed into kinetic energy. A more detailed and meteorologically more meaningful picture can be obtained by calculating the Lorenz energy cycle, which decomposes the available potential energy and kinetic energy into zonal mean and eddy components. With a series of different circulation regimes discovered in this project, it is a natural question to ask as to how their Lorenz energy cycles look like.

Another important aspect of the atmospheric energetics is the heat transport efficiency, especially in the meridional direction, by dynamical processes. For baroclinic planetary atmospheres like that of the Earth, heat redistribution depends heavily on the transport property of turbulent eddies, which is still not well understood. Using the experiments conducted in this project, the dependence of dynamic heat transport efficiency on planetary parameters like rotation rate is studied, which will shed lights on the approach to parameterise the eddy heat transport.

Planetary atmospheric circulation at the global scale has very large Reynolds number, which indicates that the flow is highly turbulent with fine structures of eddies and waves. A thorough understanding of the planetary atmospheric circulation can not avoid the study of the so-called "macroturbuluence" . 2-D turbulence theories, especially the geostrophic turbulence theory, have long been studied as a possible paradigm of atmospheric macroturbulence. This basically states that for baroclinic atmospheres on rotating planets, kinetic energy (KE) is transferred from smaller scales to larger scales via an *inverse cascade* process, whose signature in a log-log KE spectrum is an inertial range with a $-5/3$ slope. Recent studies by Schneider &

Walker (2006) found that the scale separation predicted by the geostrophic turbulence theory is not valid for experiments they conducted over a range of parameters using a simplified GCM, which questions the applicability of the geostrophic turbulence theory to real planetary atmospheres.

Moreover, studies by Galperin and coworkers (see e.g. Galperin & Sukoriansky (2010), Galperin et al. (2006), Sukoriansky et al. (2002)) in the past decade discovered a special form of geostrophic turbulence, known as "zonostrophic turbulence" , which shows highly anisotropic structures in terms of KE spectra and is closely related to rapidly rotating fluids with multiple zonal jets. According to their studies, flows of zonostrophic turbulence regime tend to reserve the inertial range (which associates with the $-5/3$ slope) in the eddy component of the KE spectra, and scale separation was found in their numerical experiments. In addition, a friction-dominated regime where inverse energy cascade and scale separation are largely suppressed was also found by Galperin and coworkers, which can be related to the experiments reported in the studies of Schneider & Walker (2006). As Galperin and coworkers only used 2-D barotropic models in their studies, it is highly necessary to investigate the KE spectra, the cross-scale spectral energy/enstrophy fluxes, and the scale separation and associated inertial ranges in the context of GCMs in our project. Insights into the applicability of zonostrophic and geostrophic turbulence to planetary atmospheres can be obtained by carefully diagnosing our experiment results across a range of defining parameters.

As advocated by Held (2005), when facing highly complex systems like planetary atmospheres, investigations such as we proposed to conduct is best done using a hierarchy of models with varying levels of complexity. One of the advantages is that by adding complexity of physical processes step by step, the corresponding impact of the physical processes on the general circulation can be highlighted by comparing results from different models.

PUMA is used as a baseline model in this project because it has simple but generic physics schemes and the code is easy to be modified to include additional levels of complexity. For this project, two different versions of the PUMA model are adopted — PUMA-S and PUMA-G. PUMA-S (the original PUMA model as developed by the Meteorological Institute, University of Hamburg) uses a Newtonian relaxation scheme to represent the diabatic heating/cooling effects, whereas PUMA-G is a version that we coded to replace this Newtonian relaxation scheme with a two-band semi-grey radiative transfer scheme and dry convective adjustment. Since the characteristic timescale of radiative heating/cooling appears explicitly in the Newtonian relaxation scheme, PUMA-S is very convenient to use when this radiative timescale needs to be modified, as shown in the study of steady baroclinic waves in Chapter 3. On the other hand, by introducing a more physical scheme of radiative transfer (compared with Newtonian relaxation), PUMA-G enables us to study the effect of varying planetary obliquity and atmospheric optical properties without specifying an *ad hoc* radiative timescale. Another advantage of PUMA-G is that, by changing the distrubtion of incoming stellar radiation at top of the atmosphere in PUMA-G appropriately, it enables the modelling of tidally-locked planets (as shown in Chapter 8), which is known as an important type of exoplanet that we have been found so far.

1.6 Highlight of new findings and thesis outline

The primary new findings of this thesis include the following:

- A systematic exploration of parameter spaces is conducted revealing a rich variety of circulation regimes, which covers a wider range of parameters than previous studies (see e.g.Geisler et al. (1983)).

- Zonostrophic turbulence regime is discovered using PUMA-S when surface friction is weak. This is the first time that zonostrophic turbulence is found in a

3D baroclinic model.[2]

- The energy/enstrophy transfer between different spatial scales in zonostrophic turbulence is studied explicitly using spectral fluxes defined by Boer & Shepherd (1983). This diagnosis has been used to study Earth's atmosphere extensively (see e.g.Burgess et al. (2013)) but has not been applied to flows in zonostrophic turbulence regime. In addition to the power-law signature in kinetic energy spectra, insights obtained from such spectral flux diagnostics provide further evidence that flows observed in our weak-friction experiments are indeed zonostrophic turbulence.

- A generic two-band radiative-convective model is built in PUMA-G, which differs from other two-band models (e.g. model by Heng (2011)) in that our model makes no preassumptions on vertical/meridional distribution of radiative absorbers in the atmosphere.

- A new approach to analytically solve the two-band radiative-transfer problem is presented, which differs from the existing treatment by Guillot (2010) in that our approach starts from the two-stream radiative transfer equations widely used in meteorological literatures, whereas the approach in Guillot (2010) starts from the various moments of the radiation field which is a formulation usually used in astrophysics literatures.

This thesis is organised as the following: Chapter 2 describes the model numerics and physics of the simplifed GCM PUMA-S that we use. Chapter 3 presents the classification and phenomenology of the global circulation regimes observed in PUMA-S, with detailed discussions on super-rotation and regular baroclinic waves. Chapter 4 discusses the heat transfer efficiency and its dependence on planetary rotation rate

[2]Previous numerical studies on zonostrophic turbulence tend to use 2D barotropic models with artificial source of energy pumping at a specific wavenumber (see e.g. Galperin et al. (2006)).

based on the PUMA-S experiments. Chapter 5 investigates the multiple-jet regime and the applicability of idealised geostrophic/zonostrophic turbulence theories to simulated planetary atmospheres in PUMA-S. Chapter 6 describes the model physics of the semi-grey radiative-convective scheme and the resultant PUMA-G. Chapter 7 then presents the regimes found using PUMA-G by varying rotation rate, planetary obliquity and the strength of greenhouse effect. A study on the tidally-locked terrestrial planetary atmospheric circulation focussing on the heat redistribution efficiency is presented in Chapter 8. Chapter 9 summarises the major conclusions and discusses the directions of future work.

Chapter 2

PUMA-S model

PUMA is a simplified GCM developed by the Meteorological Institute, University of Hamburg. It consists of a pseudo-spectral dynamical core based on the Simple Global Circulation Model (SGCM) described by Hoskins & Simmons (1975), plus several highly simplified physical processes. The original version of PUMA (PUMA-S hereafter) has a Newtonian cooling scheme is used to represent the radiative heating and cooling, and surface friction is assumed to have the form of linear Rayleigh friction. The hydrological cycle, cloud and aerosol physics, as well as biological effects are not taken into account in this simplified model.

2.1 Spherical harmonics expansion

PUMA-S uses a finite difference method in the vertical direction and a spectral transformation method based on spherical harmonics expansion in the horizontal direction to discretise the governing equations of the atmosphere. For any horizontal variable $F(\lambda, \phi)$ on a spherical surface we can use spherical harmonic function as expansion

basis to obtain the representation of F as:

$$F(\lambda, \phi) = \sum_{m=-\infty}^{\infty} \sum_{n=|m|}^{\infty} f_n^m Y_n^m(\lambda, \phi), \tag{2.1}$$

where $Y_n^m(\lambda, \phi) = e^{im\lambda} P_n^m(\sin\phi)$ is the spherical harmonic function at latitude ϕ and longitude λ, n the total wavenumber, m the zonal wavenumber, $P_n^m(\sin\phi)$ the normalised associated Legendre polynomial in $\sin\phi$, and f_n^m is the spectral amplitude coefficient of F. For numerical computation, the expansion has to be truncated at certain wavenumbers for m and n. PUMA-S adopts a triangular truncation which truncates m and n at the same wavenumber N:

$$F(\lambda, \phi) = \sum_{n=0}^{N_T} \sum_{m=-n}^{n} f_n^m Y_n^m(\lambda, \phi), \tag{2.2}$$

where the truncation wavenumber N_T can be set to $N_T = 21, 31, 42, 85, 127, 170, ...$, corresponding to horizontal resolution of T21, T31,..., T170.

2.2 Dynamical core

The dynamical core of the model is based on the primitive equations describing the conservation of momentum, mass and energy. They can be written in a dimensionless form as the following:

Vorticity equation

$$\frac{\partial(\zeta + f)}{\partial t} = \frac{1}{(1-\mu^2)} \frac{\partial F_v}{\partial \lambda} - \frac{\partial F_u}{\partial \mu} + P_\zeta \tag{2.3}$$

Divergence equation

$$\frac{\partial D}{\partial t} = \frac{1}{(1-\mu^2)} \frac{\partial F_u}{\partial \lambda} + \frac{\partial F_v}{\partial \mu} - \nabla^2 \left(\frac{U^2 + V^2}{2(1-\mu^2)} + \Phi + T_0 \ln p_s \right) + P_D \tag{2.4}$$

Hydrostatic equilibrium

$$\frac{\partial \Phi}{\partial \ln \sigma} = -T \tag{2.5}$$

Continuity equation

$$\frac{\partial \ln p_s}{\partial t} = -\int_0^1 A \mathrm{d}\sigma \tag{2.6}$$

First law of thermodynamics

$$\frac{\partial T'}{\partial t} = -\frac{1}{(1-\mu^2)}\frac{\partial (UT')}{\partial \lambda} - \frac{\partial (VT')}{\partial \mu} + DT' - \dot{\sigma}\frac{\partial T}{\partial \sigma} + \kappa \frac{T}{p}\omega + \frac{J}{c_p} + P_T, \tag{2.7}$$

where

$$F_u = V(\zeta + f) - \dot{\sigma}\frac{\partial U}{\partial \sigma} - T'\frac{\partial \ln p_s}{\partial \mu} \tag{2.8}$$

$$F_v = -U(\zeta + f) - \dot{\sigma}\frac{\partial V}{\partial \sigma} - T'(1-\mu^2)\frac{\partial \ln p_s}{\partial \mu} \tag{2.9}$$

$$A = D + \overrightarrow{V} \cdot \nabla \ln p_s \tag{2.10}$$

$$U = u\cos\phi, V = v\cos\phi \tag{2.11}$$

and the physical meaning of the variables are:

T	temperature
T_0	reference temperature
$T' = T - T_0$	temperature deviation
ζ	relative vorticity
D	Divergence
p_s	surface pressure
p	pressure
Φ	geopotential
t	time
λ, ϕ	longitude, latitude
μ	$\sin\phi$
σ	p/p_s Sigma coordinate in vertical direction
$\dot{\sigma} = d\sigma/dt$	vertical velocity in σ coordinate system
$\omega = dp/dt$	vertical velocity in pressure coordinate system
u, v	zonal and meridional velocity component
$\overrightarrow{V}$	(u, v)
$f = 2\Omega \sin\phi$	Coriolis parameter
J	diabatic heating rate
c_p	specific heat capacity of dry air at constant pressure
κ	R/c_p where R is the specific gas constant

Variables within these equations are nondimensionalised by scaling. Vorticity and divergence are scaled by Ω, pressure p and p_s by the Earth's mean surface pressure $1011hPa$, temperature T and T_0 by $a^2\Omega^2/R$ (here a is the radius of the Earth), geopotential Φ by $a^2\Omega^2/g$, and time t by Ω^{-1}. The initial state is set to a motionless atmosphere with constant temperature in the horizontal dimension, whose vertical profile is determined by the restoration temperature field. A white-noise perturbation is applied to the surface pressure field at the beginning of the model calculation.

Time stepping is implemented using a semi-implicit scheme which calculates the non-linear part of the equations with an explicit time differencing scheme and calculates the linear part of the equations with an implicit time differencing scheme.

2.3 Parameterisation of physical processes

2.3.1 Friction

Dissipation terms in the vorticity and divergence equations are parameterised as Rayleigh friction:

$$P_\zeta = \frac{\zeta}{\tau_F(\sigma)} + H_\zeta \tag{2.12}$$

$$P_D = \frac{D}{\tau_F(\sigma)} + H_D, \tag{2.13}$$

where $\tau_F(\sigma)$ is the characteristic timescale of momentum dissipation, H_ζ and H_D are the hyperdiffusion terms (defined in subsection 2.3.3). In our experiments, $\tau_F(\sigma)$ is set to about 1 Earth day in the lowest layers (where $\sigma > 0.8$, as 0.8 is roughly the level corresponding to the top of planetary boundary layer) and ∞ in the free atmosphere (where $\sigma \leq 0.8$).

2.3.2 Diabatic Heating

Diabatic heating and cooling of the atmosphere is parameterised by a simple linear Newtonian relaxation formulation:

$$\frac{J}{c_p} + P_T = \frac{T_R - T}{\tau_R(\sigma)} + H_T, \tag{2.14}$$

where τ_R is the characteristic timescale for the temperature field to relax towards the prescribed restoration temperature field, and H_T is a hyperdiffusion term. The

restoration temperature field is prescribed as a function of latitude and height:

$$T_R(\phi, \sigma) = T_{Rz}(\sigma) + f(\sigma) T_{Rl}(\phi), \tag{2.15}$$

in which

$$T_{Rz}(\sigma) = (T_{Rz})_{tp} + \sqrt{\left[\frac{L}{2}(z_{tp} - z(\sigma))\right]^2 + S^2} + \frac{L}{2}\Big(z_{tp} - z(\sigma)\Big), \tag{2.16}$$

where $(T_{Rz})_{tp} = (T_{Rz})_{grd} - L z_{tp}$ is the restoration temperature at the tropopause, L the vertical lapse rate, z_{tp} the global constant height of the tropopause, $(T_{Rh})_{grd}$ the restoration temperature at the ground. The constant S acts as a smoothing term at the tropopause. In the vertical direction, the restoration temperature field essentially consists of a troposphere with constant (moist) adiabatic lapse rate and an isothermal stratosphere. If S is set to zero, then there will be an abrupt discontinuous change of temperature at the transition between troposphere and stratosphere. In our experiments, $L = 0.0065$ K/m, $z_{tp} = 12000$ m and $S = 2$ K. The vertical restoration temperature profile is shown in Fig. 2.1 with surface temperature of 288 K.

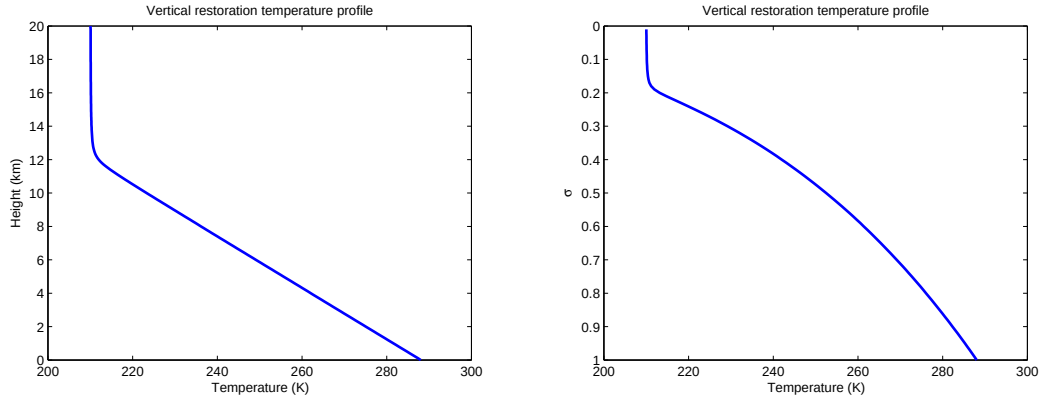

Figure 2.1: Vertical profile of the restoration temperature as a function of height (left) and σ-coordinate (right), with ground temperature of 288 K.

The meridional variation of the restoration temperature field is formulated by

$$T_R(\phi) = (\Delta T_R)_{NS}\frac{\sin\phi}{2} - (\Delta T_R)_{EP}\Big(\sin^2\phi - \frac{1}{3}\Big), \tag{2.17}$$

where $(\Delta T_R)_{EP}$ is the prescribed constant restoration temperature difference between the equator and the poles, $(\Delta T_R)_{NS}$ is the variable part of the meridional temperature gradients which can be made to change with time to simulate an annual cycle.

The meridional variation is modulated in altitude by the function $f(\sigma)$ so that the variation vanishes at the isothermal tropopause, that is assumed to be:

$$f(\sigma) = \begin{cases} \sin\left(\frac{\pi}{2}\left(\frac{\sigma-\sigma_{tp}}{1-\sigma_{tp}}\right)\right) & \text{if } \sigma \geq \sigma_{tp} \end{cases} \tag{2.18}$$

Th

ference

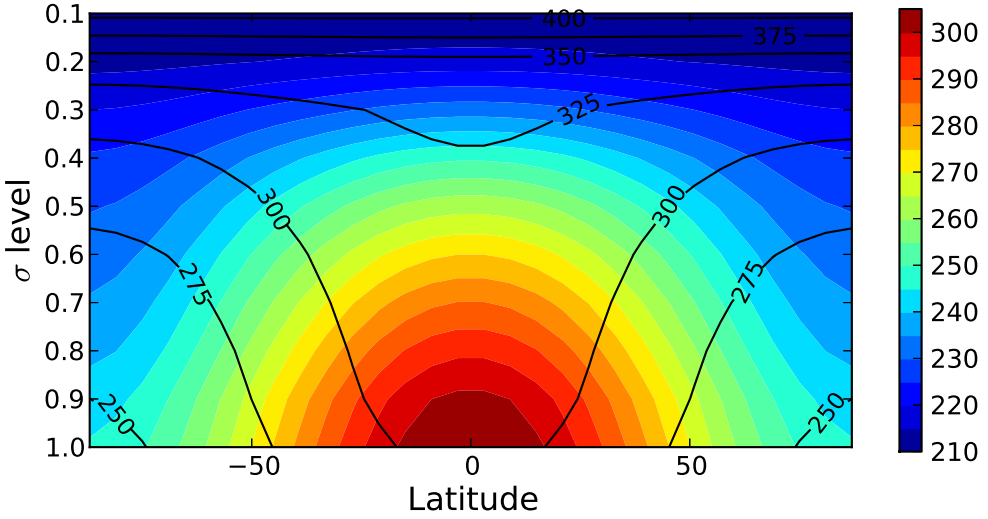

Figure 2.2: Restoration temperature (colour) and potential temperature (contour) field with equator-to-pole temperature difference of 60 K.

2.3.3 Hyperdiffusion

Hyperdiffusion terms H_ζ, H_D and H_T are needed (cf. Eqs. (2.12), (2.13) and (2.14)) in order to represent the effect of subgrid horizontal mixing and energy dissipation. For an arbitrary model variable Q (Q might be ζ, D or T), we have the hyperdiffusion in the following form:

$$H = -(-1)^h K \nabla^{2h} Q(\lambda, \mu, t) \tag{2.19}$$

or, in spectral form,

$$H = -(-1)^h K \nabla^{2h} \sum_\gamma Q_\gamma(t) Y_\gamma(\lambda, \mu), \tag{2.20}$$

in which $\gamma = (n, m)$ designates the spectral modes (where $n = 1, 2, 3, ...$ denotes the total wave number and $m = 0, \pm1, \pm2, \pm3, ...$ denotes the zonal wave number, retaining only $|m| \leq n$ to represent a triangular form of truncation), and Y_γ are the spherical harmonics.

Using the condition that the spectral modes with $n = N_T$ are damped with a prescribed time scale τ_H, we have

$$H_\gamma = -\frac{1}{\tau_H} Q_\gamma(t) Y_\gamma(\lambda, \mu) \quad \text{if } n = N_T, \tag{2.21}$$

so that

$$K = \frac{1}{\tau_H} \Big(\frac{a^2}{N_T(N_T+1)} \Big)^h, \tag{2.22}$$

where N_T is the truncation limit of the total wave number (e.g. T21 corresponds to $N_T = 21$).

Thus,

$$H_\gamma = -\frac{1}{\tau_H} \Big(\frac{n(n+1)}{N_T(N_T+1)} \Big)^h Q_\gamma(t) Y_\gamma(\lambda, \mu). \tag{2.23}$$

For this study, a standard value of h is of 4 was used, and the diffusion time scale

was usually set to $\tau_H = 1/4$ Earth day.

2.3.4 Vertical descretisation

PUMA-S uses a finite difference method to discretise in the vertical direction in terms of σ-coordinate $\sigma = p/p_s$. We typically use 10 equally spaced vertical levels in our experiments ($\sigma = 0.05, 0.15, 0.25, ..., 0.95$). Half-levels (interfaces) are defined in between full levels and at $\sigma = 0.0$ and $\sigma = 1.0$. Prognostic variables ζ, D, and T are defined at full levels while $\dot{\sigma}$ is defined at half-levels. Vertical velocity is set to zero ($\dot{\sigma} = 0$) at the upper($\sigma = 0.0$) and lower($\sigma = 1.0$) boundaries.

Chapter 3

Circulation regimes in an atmosphere modelled by PUMA-S

This chapter presents part of the studies based on the diagnostic results of the controlled experiments with PUMA-S. Section 3.1 describes the experiment setup and definitions of the dimensionless parameters of the regime diagram. This is followed by a brief overview and classification of the major circulation regimes observed in our experiments in Section 3.2. Sections 3.3.1 and 3.3.2 then discuss the trends observed in the zonal mean and eddy/wave diagnostics. The super-rotation regime and regular baroclinic waves regime are discussed in detail in Sections 3.4-3.5. The irregular baroclinic waves regime is not discussed in detail, since it is essentially an Earth-like circulation regime which has been more thoroughly understood compared with other regimes. Studies on the multiple-jet regime are presented in Chapter 5.

3.1 Experiment design and regime diagram

PUMA-S is used in this chapter to study the behaviour of a prototype planetary atmosphere (albeit the atmospheric composition, gravitational acceleration and planetary radius are still set to terrestrial values). The model is set up with no topographical

effect (e.g. normal drag, gravity waves excited by terrain, thermal contrast between continents and oceans...). Seasonal and diurnal cycles are switched off and a fixed annual mean thermal forcing is applied through Newtonian relaxation.

Controlled experiments are conducted by varying rotation speed Ω and the equator-to-pole temperature difference ΔT_h. We tested three values of ΔT_h =60 K, 10 K, and 5 K. For each value of ΔT_h, eight values of Ω ($\Omega^* = \Omega/\Omega_E = 8, 4, 2, 1, 1/2, 1/4, 1/8, 1/16$, where Ω_E is the rotation rate of the Earth) were investigated. This leads to the experiments shown in Fig. 3.2. Horizontal resolution was set to T42 for slowly rotating experiments ($\Omega^* \leq 1$), T127 for faster rotating experiments with $\Omega^* = 2, 4$, and T170 for experiments with $\Omega^* = 8$. For all the experiments, there were 10 vertical levels ($\sigma = 0.1, 0.2, 0.3, ..., 1.0$). Frictional timescale τ_f was set to 0.6 Earth day at $\sigma = 1.0$ and 1.6 Earth days at $\sigma = 0.9$ with zero value at all other levels above, producing an Ekman-like planetary boundary layer. The radiative timescale τ_t was set to 30 Earth days in the free atmosphere and decreases to 2.5 Earth days at $\sigma = 1.0$. The initial condition in each case was an isothermal atmosphere at rest. Each experiment was run for 10 model years (360 day per model year) to ensure that a statistically steady state was reached and all of the following diagnostics were based on the 10th model year data unless otherwise stated.

The circulation regime shown in Fig. 3.2 is constructed by the thermal Rossby number $\mathcal{R}o$ and the frictional Taylor number $\mathcal{T}a_f$, defined as the following (see Read (2011), Mitchell & Vallis (2010)):

$$\begin{aligned} \mathcal{R}o &= \frac{R\Delta\theta_h}{\Omega^2 a^2} \\ \mathcal{T}a_f &= 4\Omega^2\tau_{ft}^2 \end{aligned} \tag{3.1}$$

where $\Delta\theta_h$ is the equator-to-pole potential temperature difference, a the planetary radius, R the gas constant and τ_{ft} the characteristic spin-down time of the total atmosphere (rather than just the boundary layer whose spin-down time is explicitly

set by the profile of τ_f as stated above).

3.1.1 Spin-down timescale

The relationship between τ_{ft} and τ_f can be derived by considering the spin-down of an atmosphere with pressure scale height H and a Rayleigh-friction boundary layer of thickness d (vertical range of boundary layer is defined as model levels with finite frictional timescales). For simplicity, the free atmosphere is assumed to be geostrophic and the boundary layer frictional timescale τ_f is assumed to be constant over height. Following the conventions of Ekman layer analysis, let us start from the diagnostic equation of momentum within this Rayleigh boundary layer:

$$-\frac{1}{\rho}\frac{\partial p}{\partial x} + fv - \frac{u}{\tau_f} = 0, \tag{3.2a}$$

$$-\frac{1}{\rho}\frac{\partial p}{\partial y} - fu - \frac{v}{\tau_f} = 0. \tag{3.2b}$$

Assuming that the free atmosphere is in geostrophic balance, and that the pressure gradient doesn't change very much from the boundary layer to the free atmosphere, then we have:

$$-\frac{1}{\rho}\frac{\partial p}{\partial x} = -fv_g, \quad -\frac{\partial p}{\partial y} = fu_g, \tag{3.3}$$

where (u_g, v_g) is the geostrophic wind.

Thus Eqs. (3.2a) and (3.2b) can be rewritten as:

$$f(v - v_g) - \frac{u}{\tau} = 0, \tag{3.4a}$$

$$f(u - u_g) + \frac{v}{\tau} = 0. \tag{3.4b}$$

This linear equation set can be easily solved:

$$u = \frac{f\tau_f}{f^2\tau_f^2 + 1}(f\tau_f u_g - v_g), \tag{3.5a}$$

$$v = \frac{f\tau_f}{f^2\tau_f^2 + 1}(f\tau_f v_g + u_g). \tag{3.5b}$$

By vertically integrating the continuity equation within the boundary layer, we can obtain

$$w_T = -\int_0^d (\frac{\partial u}{\partial x} + \frac{\partial v}{\partial y})\mathrm{d}z - w|_{z=0}, \tag{3.6}$$

where w_T and $w|_{z=0}$ are the vertical velocity at the top of the boundary layer and the ground level respectively. Further assuming that $w|_{z=0} = 0$, and substituting Eqs (3.5a) and (3.5b) into Eq. (3.6), we can get:

$$\begin{aligned} w_T &= -\int_0^d \frac{f\tau_f}{f^2\tau_f^2 + 1}(-\frac{\partial v_g}{\partial x} + \frac{\partial u_g}{\partial y})\mathrm{d}z \\ &= \int_0^d \frac{f\tau_f}{f^2\tau_f^2 + 1}\zeta_g \mathrm{d}z, \end{aligned} \tag{3.7}$$

where ζ_g is the geostrophic vorticity. (Note that geostrophic divergence is zero.)

If we assume that τ_f is constant within the boundary layer ($\partial\tau/\partial z = 0$), then we have

$$w_T = \frac{f\tau_f}{f^2\tau_f^2 + 1} d\zeta_g. \tag{3.8}$$

For the geostrophic free atmosphere above this boundary layer, the Q-G vorticity equation is essentially

$$\frac{D\zeta_g}{Dt} = f\frac{\partial w}{\partial z}. \tag{3.9}$$

Assuming that the scale height of the free atmosphere is H and the vertical velocity

at the top of the free atmosphere is zero, then

$$\begin{aligned}\frac{D\zeta_g}{Dt} &= f\frac{w(H)-w(d)}{H} \\ &= -\frac{f^2\tau_f}{f^2\tau_f^2+1}\frac{d}{H}\zeta_g.\end{aligned} \tag{3.10}$$

This indicates that the free atmosphere spins down with a characteristic timescale of

$$\begin{aligned}\tau_{ft} &= \frac{f^2\tau_f^2+1}{f^2\tau_f}\frac{H}{d} \\ &= \left(\tau_f+\frac{1}{f^2\tau_f}\right)\frac{H}{d}.\end{aligned} \tag{3.11}$$

For our experiments shown in Fig. 3.2, $f \sim 10^{-4}\mathrm{s}^{-1}$ and $\tau_f \sim 10^6\mathrm{s}$, therefore the second term in the bracket is very small compared to the first term, and we have

$$\tau_{ft} \sim \tau_f\frac{H}{d}. \tag{3.12}$$

3.1.2 Spin-down experiments

Spin-down experiments were performed using PUMA-S to test the validity of Eq. (3.12). The initial condition of the model atmosphere was set to a state with relative vorticity $\zeta = 1.05f$, where f is the planetary vorticity. Diabatic heating/cooling processes in terms of Newtonian relaxation is switched off, with only the mechanical damping (Rayleigh friction) at work. This leads to an exponential decay of the total kinetic energy of the atmosphere:

$$E_k(t) = E_{k0}\mathrm{e}^{-t/\tau_{ft}}. \tag{3.13}$$

which can be rewritten in logarithmic form as

$$\ln E_k(t) = -\frac{1}{\tau_{ft}}t + \ln E_{k0}. \tag{3.14}$$

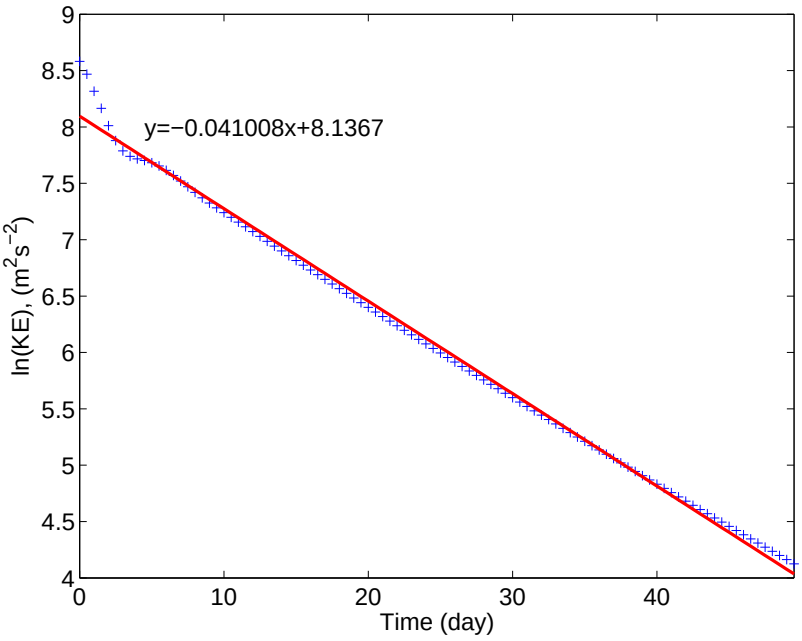

Figure 3.1: Globally-averaged logarithmic kinetic energy of the atmosphere with respect to time of the first 50 days of the spin-down experiment. $\tau_f = 2.0$ days and the boundary layer is set to be $0.9 < \sigma < 1.0$. Data was sampled at a frequency of twice per day.

Therefore by plotting the logarithmic kinetic energy with respect to time, we can perform a linear regression to estimate the slope $-\frac{1}{\tau_{ft}}$ of Eq. (3.14). Fig. 3.1 shows the results obtained from an experiment with $\tau_f = 1.0$ day and $H/d \sim 10$ (boundary layer assumed to be the region of $0.9 < \sigma < 1.0$). Linear regression using least square approach indicates $-\frac{1}{\tau_{ft}} \sim 0.041$. This corresponds to $\tau_{ft} \sim 24$ days, which is not too different from the value of 20 days predicted by Eq. (3.12). Thus the relationship derived above, although based on various crude approximations including assuming the free atmosphere as homogeneous shallow-water layer, is reasonably accurate for estimating the global spin-down timescale based on the frictional timescale within the planetary boundary layer.

Our experiments are configured with values of H and d such that $H/d \sim 5$, leading

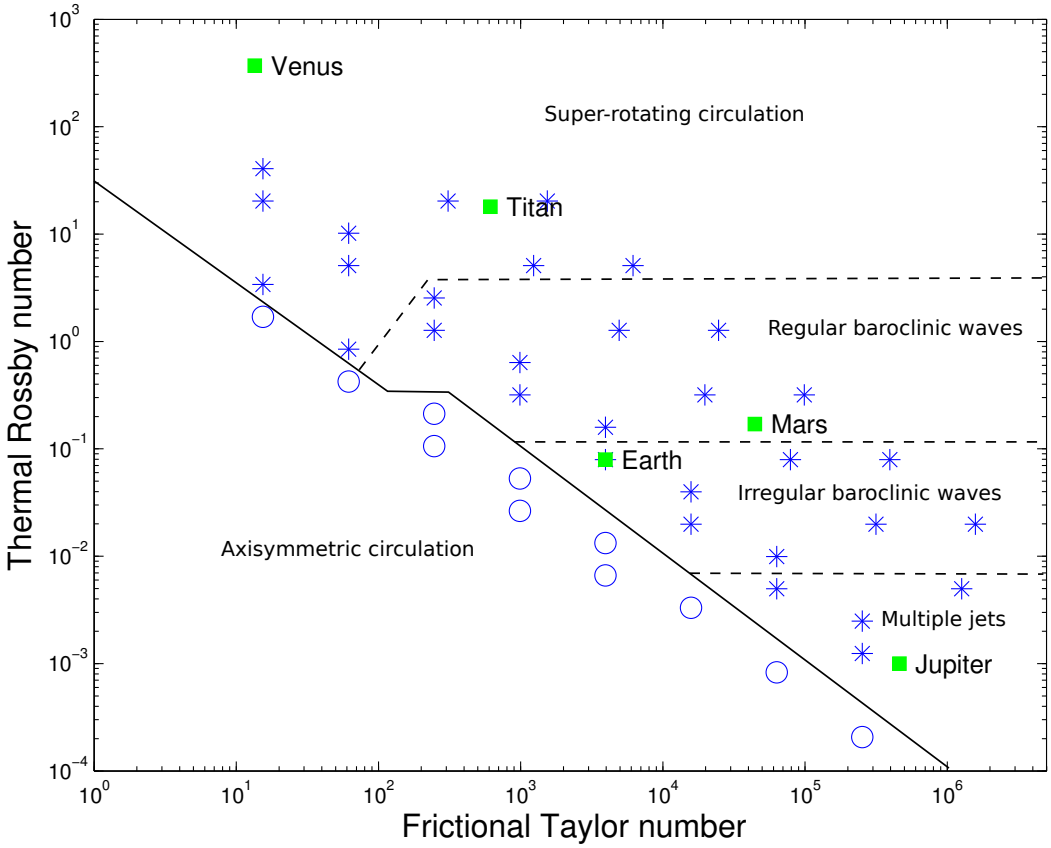

Figure 3.2: Regime diagram showing the various circulation regimes with respect to characteristic dimensionless parameters. Stars refer to experiments in which wavy flows are discovered, whereas circles are experiments in which axisymmetric flows are found. Some Solar System planets are labeled as squares. The solid line delineates the boundary between axisymmetric circulations and circulations with wavy/turbulent flows. The dashed lines are the boundaries between different circulation regimes within the wavy/turbulent region.

to the frictional Taylor number of

$$\mathcal{T}a_f = 4\Omega^2\tau_{ft}^2 \sim 100\Omega^2\tau_f^2, \tag{3.15}$$

where τ_f is approximately 1 Earth day given the profile of τ_f as stated above.

3.2 Classification of circulation regimes

The regime diagram shown in Fig. 3.2 is obtained by mapping the occurrences of the observed circulation regimes within a parameter space spanned by thermal Rossby number $\mathcal{R}o$ and frictional Taylor number $\mathcal{T}a_f$. Five different types of global circulation can be found in this regime diagram.

Axisymmetric flow. In our experiments, axisymmetric flows are found in the lower left region of the regime diagram, with sufficiently small equator-to-pole temperature contrast or strong enough frictional damping. Axisymmetric circulations are characterised by smooth laminar flows encircling the axis of planetary rotation, with no wave/eddy disturbances.

Cyclostrophic, super-rotating flow. Due to the weakness of the Coriolis force on these slow rotators, the major force balance accounting for the large-scale atmospheric motion is between pressure gradient force and the centrifugal force, which is known as cyclostrophic balance (see Holton (1992)). Another unique feature of this kind of circulation is that there is typically a very strong prograde wind over the equatorial regions, in contrast to the retrograde wind in Earth's tropical atmosphere, a phenomenon known as equatorial super-rotation (Read (1986b)). Fig. 3.3 shows a cross-section of the zonal mean zonal wind averaged over the last 360 model days in the experiment with a rotation rate of $\Omega_E/16$, which shows substantial eastward (prograde) wind in the upper atmosphere over the equator. The extratropical jet streams, which are usually located in mid-latitude or subtropics in Earth's atmosphere, are pushed further polewards due to the expanded Hadley cells under weak rotational constraints.

Regular baroclinic flow. For planets with an intermediate thermal Rossby number (larger than Earth's, but smaller than those of Venus and Titan), the planetary baroclinic waves tend to be very regular and coherent in structure. Fig. 3.4 shows a polar view snapshot of the geopotential height field in the experiment with rotation

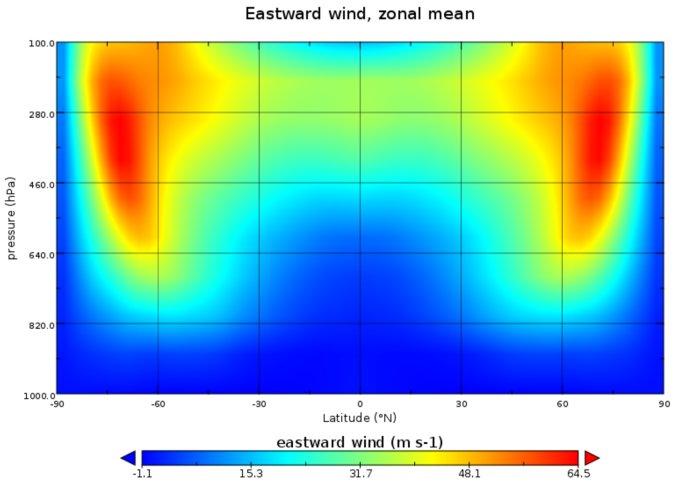

Figure 3.3: Zonal mean zonal wind for experiment with rotation rate of $1/16\Omega_E$. Positive value refers to prograde direction.

rate of $\Omega_E/2$. This experiment has roughly the same thermal Rossby number as that of Mars, and a regular baroclinic wave with the dominant wavenumber-4 mode is found at 500mb level [1].

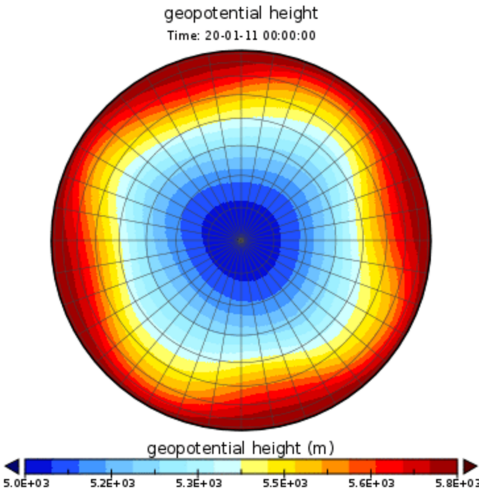

Figure 3.4: Snapshot of the geopotential height field at 500mb level for experiment with rotation rate of $1/2\Omega_E$, viewed from above the north pole.

Irregular baroclinic flow. This is the circulation regime that resembles the Earth's atmospheric circulation more closely than other regimes reported here, characterised

[1] Regular baroclinic waves with dominant wavenumber other than 4 are also found in experiments by changing radiative and frictional timescales, see Section 3.5

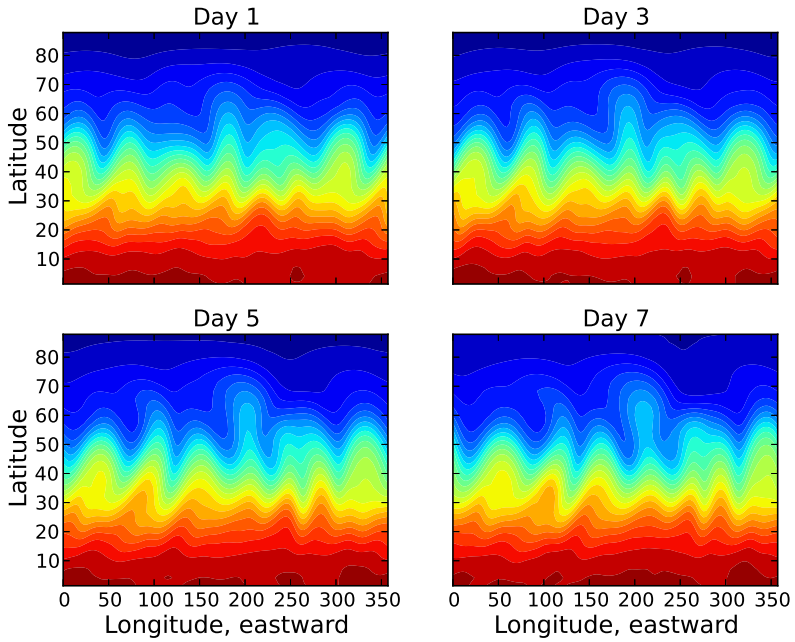

Figure 3.5: Latitude-longitude snapshots of the streamfunction at 500mb level in the Northern Hemisphere for the experiment with rotation rate of $1\Omega_E$, showing the evolution of the flow over one week (day 3241, 3243, 3245, and 3247 in the 10-year run).

by irregular baroclinic waves with mixed wavenumbers. Fig. 3.5 shows the evolution of the flow field in the Northern Hemisphere over 7 Earth days for the experiment with rotation rate of $1\Omega_E$. It can be seen that the shape of the wavy structure changes irregularly with time in terms of both phase and amplitude.

Multiple zonal jet flow. For planets with much smaller thermal Rossby number ($\mathcal{R}_o < 10^{-2}$), the development of geostrophic turbulence leads to the formation and maintenance of multiple eddy-driven jets in the presence of a strong β-effect and weak friction. Characterised by multiple eddy-driven jets over the extratropical regions, flows in this region of parameter space develop strongly zonal structures at planetary scale, as shown in Fig. 3.6, in contrast to the global wavy structures of other non-axisymmetric regimes. Gas giant planets in the Solar System (Jupiter, Saturn, Uranus and Neptune) all exhibit strongly zonal multiple jets (Showman et al. (2010)) as reflected in their banded appearances. Fig. 3.7 shows the zonal mean zonal wind

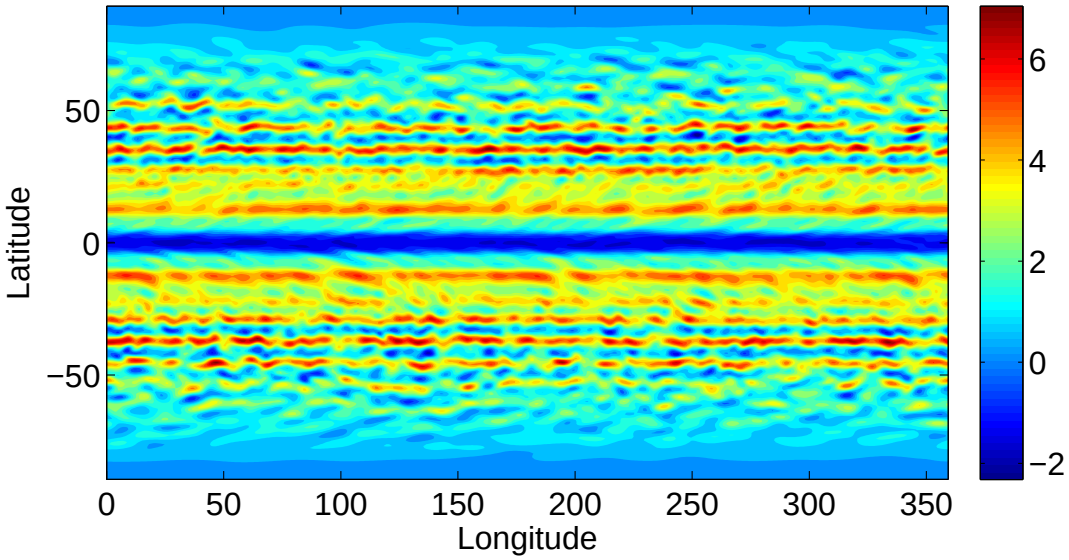

Figure 3.6: Snapshot of the zonal wind u at 100mb of the experiment $\Omega^* = 8$. Unit: ms^{-1}.

cross-section of the experiment with $\Omega^* = 8$, which has about the same $\mathcal{R}_o$ as Jupiter (as can be appreciated from Fig. 3.2). Recent studies suggest that such banded zonal jets can be found in the Earth's oceans as well (for example, as found in the eddy-resolving ocean model simulations of the North Pacific Ocean, see Galperin et al. (2004)).

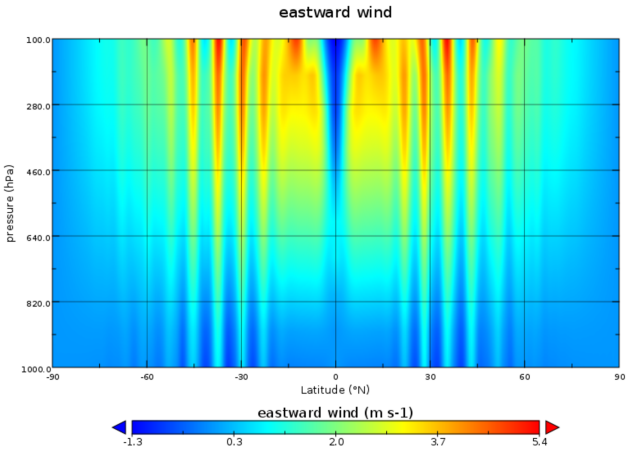

Figure 3.7: Zonal mean zonal wind of experiment with rotation rate of $8\Omega_E$.

The diversity of circulation regimes shown in this regime diagram prompted a

series of fundamental questions regarding the general circulation of planetary atmospheres: What determines the preferred eddy scales in a planetary atmosphere? How does the planetary rotation rate affect the meridional heat transport? What causes and maintains the equatorial superrotation when rotation rate is low? What determines the selection of wavenumbers in steady baroclinic waves? Why do eddies organise themselves into jets and what insights can be obtained on the jet formation mechanism from modern theories of geostrophic turbulence? With these questions in mind we will investigate the structures and trends of the circulation regimes in the following sections.

3.3 Phenomenology

3.3.1 Zonal mean diagnostics

Since the incoming solar radiation which serves as the ultimate energy source of the atmospheric circulation generally varies most in the meridional direction, the large-scale motion of the atmosphere has greater variations in the meridional direction than in the zonal direction, especially when averaging over a long time period (more than one year, for example). Thus analysis of the zonal average of the meteorological variables takes a significant role in the study of atmospheric general circulation. The zonal mean zonal wind (u) contours for the runs with different Ω and $\Delta T_h = 60$ K are shown in Fig. 3.8-3.9 with the meridional mass streamfunction superimposed using colour shades.

The fast rotating experiments ($\Omega^* > 1$) are characterised by multiple extratropical jet streams. The generation and maintenance of these jets through upscale energy cascade which is characteristic of geostrophic turbulence will be discussed in Chapter 5. At this stage we focus on the change of global structures—the increase of the number of jets with Ω. Under the f-plane approximation, the inverse energy cascade

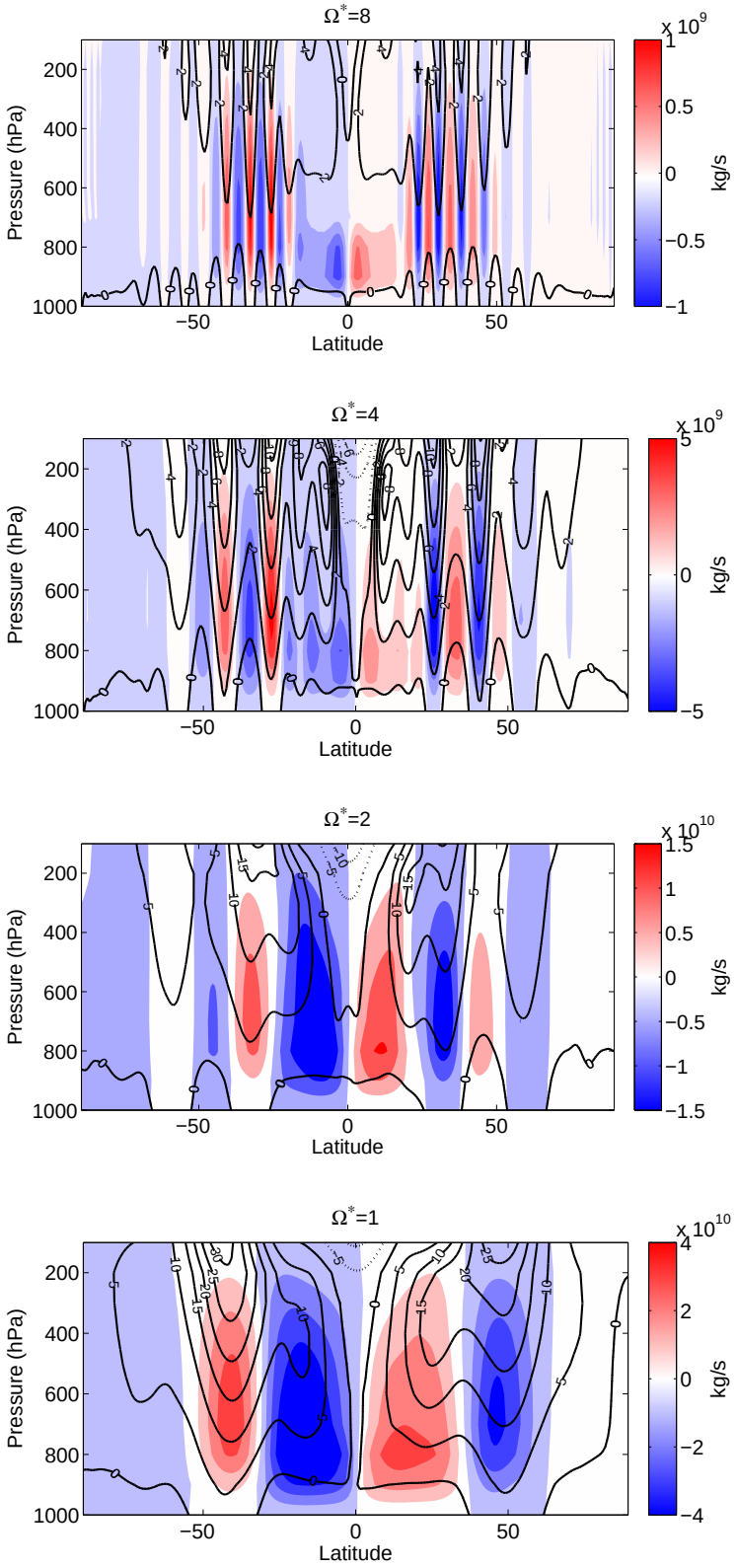

Figure 3.8: Zonal mean zonal wind and meridional streamfunction of $\Omega^* = 8, 4, 2, 1$.

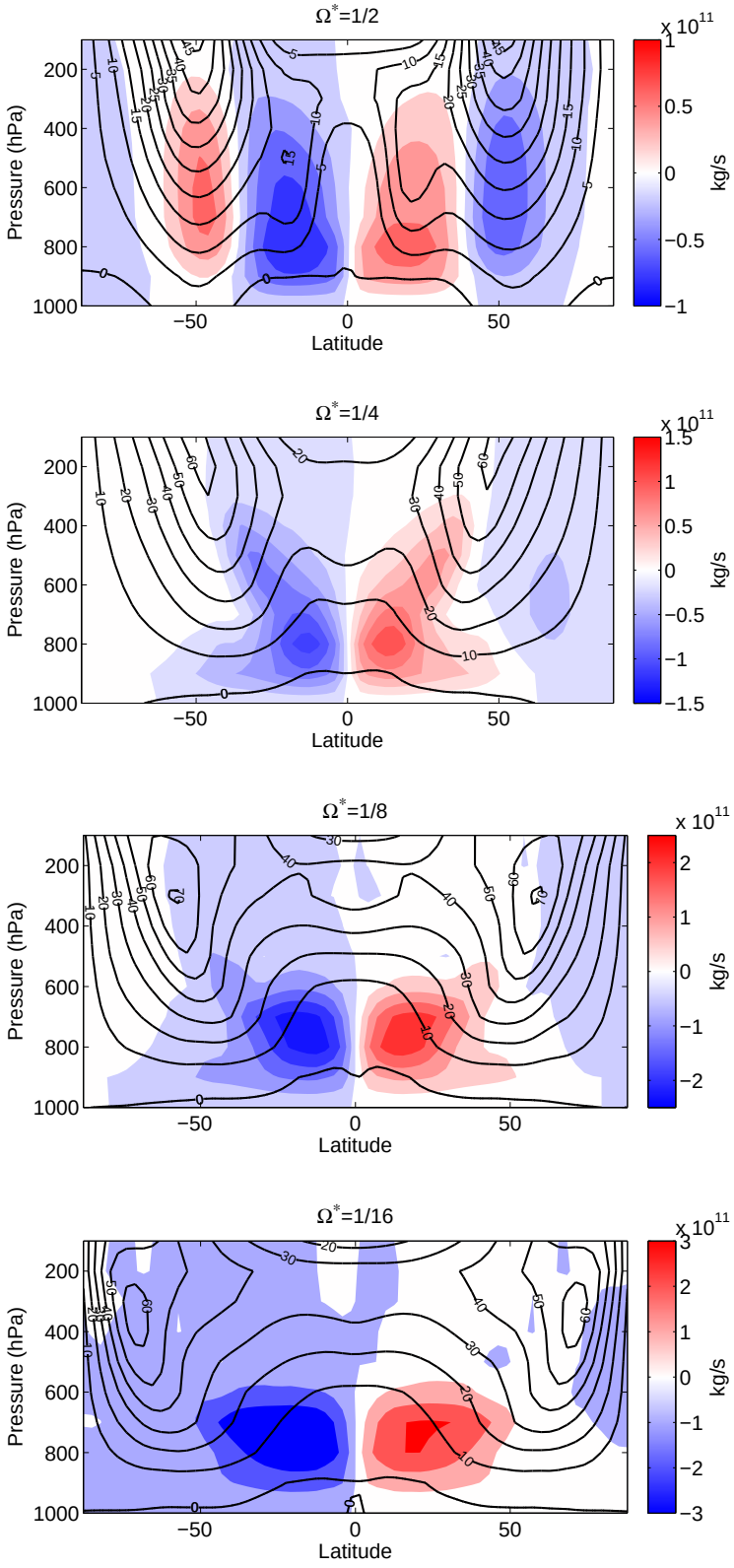

Figure 3.9: Same as Fig. 3.8, but for $\Omega^* = 1/2, 1/4, 1/8, 1/16$.

will lead to large isotropic vortices rather than alternating zonal jets and bands. Rhines (1975) first proposed a theory for 2-D turbulence on β-plane which explains the elongation of the structure of large scale eddies along the zonal direction caused by the latitudinal variation of Coriolis parameter f. According to Rhines (1975), the characteristic latitudinal range of such anisotropy can be estimated by the Rhines scale:

$$L_R = \pi \left(\frac{U}{\beta} \right)^{1/2}, \tag{3.16}$$

in which U is the characteristic wind speed. Applying the thermal wind relationship to estimate U (e.g. Read (2011)) leads to[2]:

$$L_R \simeq \pi \left(\frac{R \Delta \theta_h}{4\Omega^2} \right)^{1/2}. \tag{3.17}$$

The number of jets expected on a planet then can be estimated by

$$N_J = \frac{a}{L_R}. \tag{3.18}$$

Table 3.1 shows the number of jets on a planet surface predicted by Eq. (3.18). For experiments with very slow rotation rates ($\Omega^* < 1/4$), N_J is smaller than 1. This means the picture of an eddy-driven jet through an inverse energy cascade in the framework of geostrophic turbulence is no longer valid as the Rhines scale L_R exceeds the size of the planetary domain. The jets observed in these slowly rotating experiments are primarily due to the quasi-conservation of angular momentum of the upper branch of the extended thermally direct Hadley cell. At $\Omega^* = 1$, the predicted number of jets is 2.26, which approximately corresponds to the regime of two prograde

[2]The original argument in Rhines (1975) uses U_{rms}, which is the root mean square velocity. The estimation here using thermal wind relationship essentially gives a zonal mean $[U]$. Calculations indicate that the difference between U_{rms} and $[U]$ estimated using thermal wind relationship is not significant for runs not in zonostrophic turbulence regime. Flows in zonostrophic turbulence regime tend to have $U_{\text{rms}} \ll [U]$ For more discussions on zonotrophic turbulence, see Chapter 5.

Ω^*	1/16	1/8	1/4	1/2	1	2	4	8
N_J	0.14	0.28	0.57	1.13	2.26	4.53	9.03	18.08

Table 3.1: Number of jets predicted by Eq.(3.18) for experiments with $\Delta\theta_h = 60$K.

jet per hemisphere. For experiments with fast rotation rates ($\Omega^* > 1$), Eq. (3.18) predicts up to 18 jets for $\Omega^* = 8$. This is consistent with the zonal wind cross-section plot shown in Fig. 3.8 where at least 8 jets can be located in each hemisphere.

As we can see from Figs. 3.8-3.9, the subtropical jet stream moves to higher latitude as the rotation rate decreases, which is consistent with the prediction from the quasi-inviscid axisymmetric Hadley cell theory (see Held & Hou (1980)). The intensity of the jet stream grows stronger as the rotation rate decreases until $\Omega^* = 1/8$. For the $\Omega^* = 1/16$ run, the extratropical jet (~ 60 m s^{-1}) is actually weaker than that in the $\Omega^* = 1/8$ run (~ 70 m s^{-1}). In principle, there are two competing factors determining the intensity of the extratropical jet stream as the rotation rate decreases. The jet stream reaches higher latitude, thus gaining more angular momentum than in the lower latitude. On the other hand, the reduction in rotation rate actually decreases the angular momentum of the whole planet, thus reducing the angular momentum obtained by the poleward moving jet stream. For the runs from $\Omega^* = 1$ to $\Omega^* = 1/8$, the first factor dominates and the jet intensity gets stronger for smaller rotation rate. But for the $\Omega^* = 1/16$ run, the latter factor dominates and the angular momentum of the background planetary rotation reduces a significant enough amount to offset the angular momentum gain caused by the poleward motion of the jet stream (similar results were found by Navarra & Boccaletti (2002)).

This poleward movement of the subtropical jet stream is a clear indication of the expansion of Hadley cell in each hemisphere as the rotation rate decreases, which can be evaluated by the zonal mean merdional mass streamfunction, defined in the

pressure coordinate system as (see Peixoto J.P. (1992)):

$$\Psi = \frac{2\pi a}{g} \cos\phi \int_0^P dp'[\overline{v}],$$

where a is the planetary radius, $[\overline{v}]$ the zonal and temporal mean meridional velocity, ϕ the latitude and P the surface atmospheric pressure.

As we can see, there are basically three cells in each hemisphere for the terrestrial rotation rate ($\Omega^* = 1$). The positive values of Ψ represent clockwise flow and the negative values represent counter-clockwise flow, while the magnitude reflects the strength of the overturning. Thus the poleward edge of the overturning Hadley circulation can be estimated by the latitude of the boundary between the tropical cell and the adjacent mid-latitude cell. In this case ($\Omega^* = 1$), the expansion of the Hadley cell in each hemisphere is roughly 30° which is consistent with the observational value for the Earth. As the rotation rate decreases, the overturning Hadley cell expands and gets intensified, just as predicted in the previously cited Held & Hou (1980) model. In fact, at the lowest rotation rate $\Omega^* = 1/16$, only one strong hemispherically dominating Hadley cell is found in each hemisphere while the other two cells at mid- and high-latitudes disappear. Within the Hadley cell, baroclinicity (i.e. horizontal temperature difference in the meridional direction) is considerably weaker compared to that in the extratropical baroclinic eddy zones. This feature is reflected in the zonal mean temperature cross-sections in Figs.3.10-3.11.

3.3.2 Non-axisymmetric features — eddies/waves

For rapidly rotating planets like the Earth and Mars, the maintenance of the general circulation and the transport of heat and momentum depend significantly on the interactions between transient eddies and the mean flow. In the absence of eddies, the atmosphere of the mid- and high-latitudes would reach a state of radiative equi-

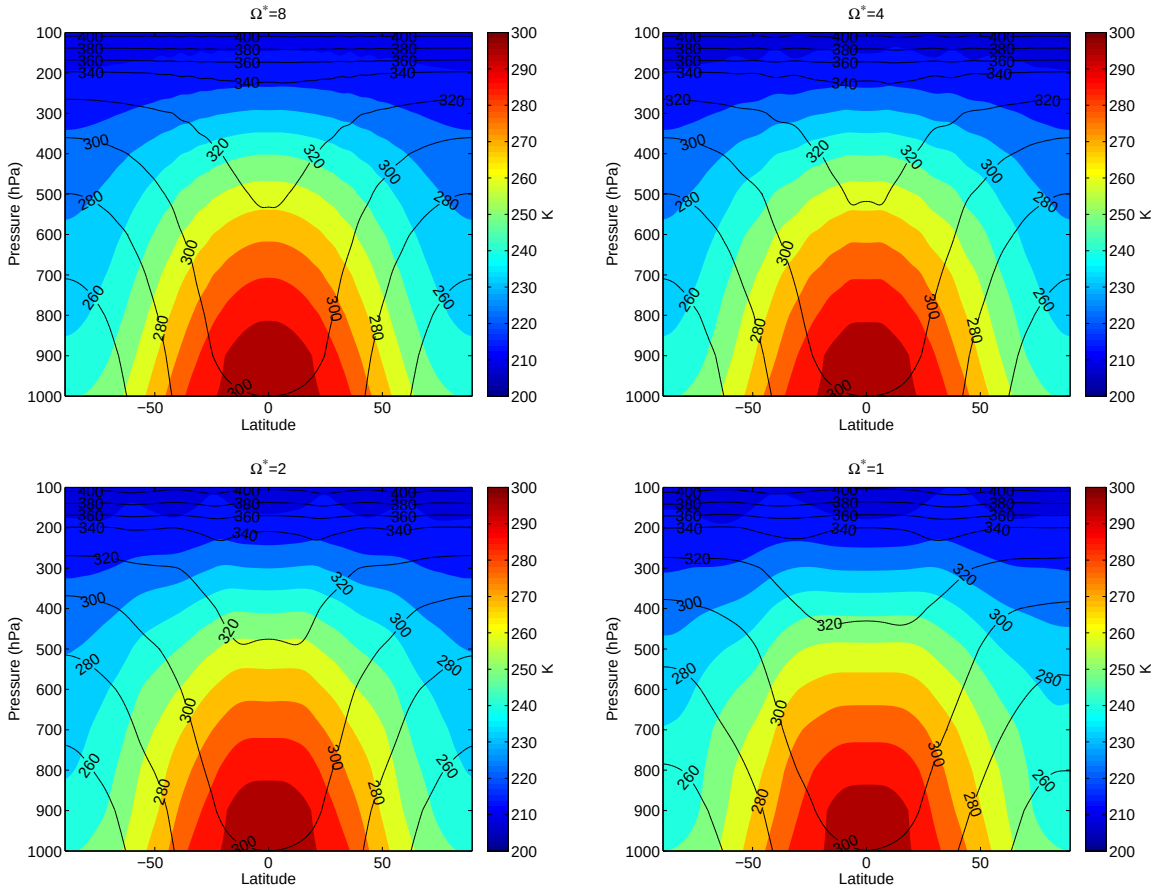

Figure 3.10: Zonal and temporal mean temperature of $\Omega^* = 8, 4, 2, 1$.

librium, which is characterised by larger meridional temperature contrasts than we observe here. Thermal winds induced by such strong temperature gradients would then lead to wind shears in the vertical direction which are baroclinically unstable. The baroclinic eddy transport of heat considerably reduces the equator-to-pole temperature difference from that predicted by radiative equilibrium. In this section, we will investigate the general trends of eddy activity with planetary rotation rate.

Figs. 3.12-3.13 show the zonal wavenumber amplitude spectra of geopotential height at 500mb level from experiments with various rotation rates. As the rotation rate decreases, the eddies become more and more confined to smaller wavenumbers, which is consistent with the trend of the energy-containing scales, the Rossby deformation radius and the Rhines scale. At high rotation rates (e.g. $\Omega^* = 4$ and

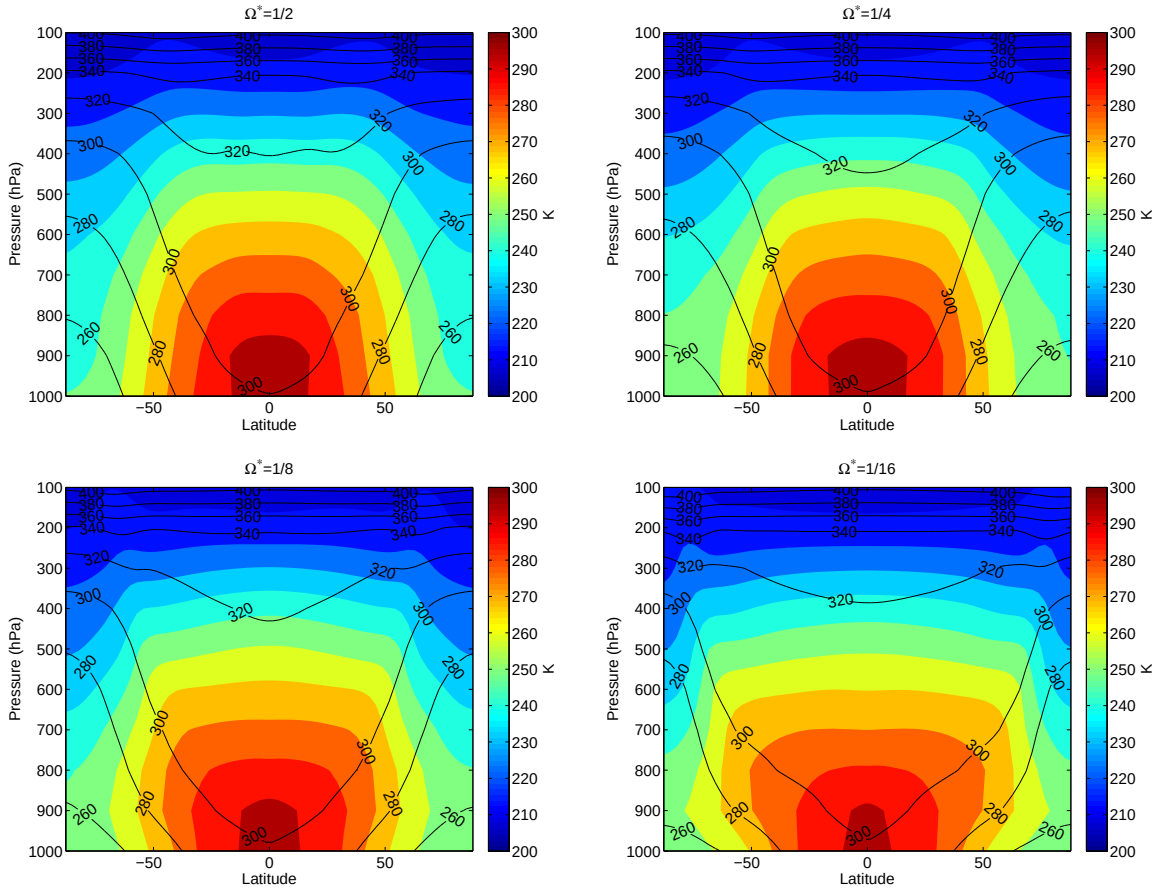

Figure 3.11: Same as Fig. 3.10, but for $\Omega^* = 1/2, 1/4, 1/8, 1/16$.

8), noticeable parallel banded structures can be seen in the extratropical latitudes, indicating the existence of multiple baroclinic zones, as would be expected if the characteristic eddy length scale is significantly smaller than the planetary domain. The Fourier amplitude is smaller for high rotation rate spectra as a result of the decreased eddy length scale, which leads to smaller intensity of perturbations. The maximum amplitude is reached around $\Omega^* = 1/2 \sim 1/4$, which combined with the fact that baroclinic conversion rate peaks around $\Omega^* = 1/2$ and kinetic energy conversion (CK) between zonal flow and eddies changes direction at $\Omega^* = 1/2 \sim 1/4$, corroborates that baroclinic wave developments are suppressed with slow planetary rotations, and the wave activity at $\Omega^* = 1/8 \sim 1/16$ has a significant contribution from barotropic instability. The maximum strength of eddy activities is found at

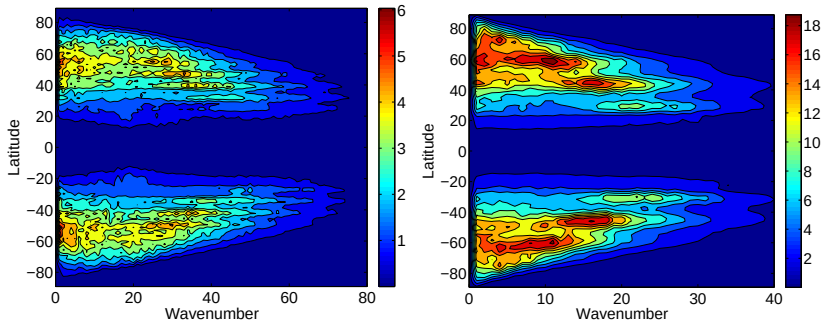

(a) $\Omega = 8$

(b) $\Omega = 4$

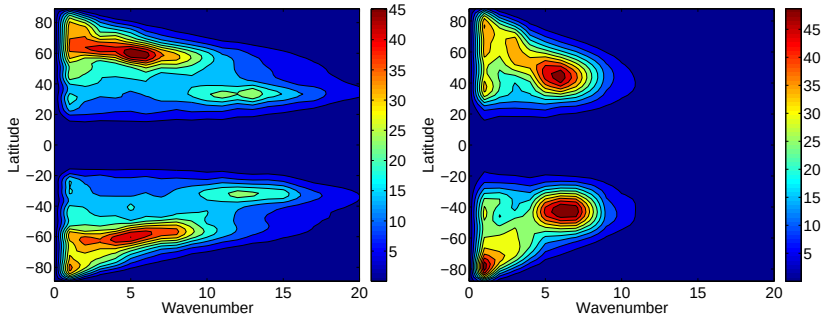

(c) $\Omega = 2$

(d) $\Omega = 1$

Figure 3.12: Fourier amplitude maps of the zonal wavenumber spectra of geopotential height at 500mb from experiments with high rotation rates. Spectra are averaged over one model year. Unit: geopotential metres.

higher latitudes for experiments with lower rotation rates, which is again consistent with the trend that Hadley cells tend to expand, pushing extratropical jets (along with associated eddies) polewards as the rotation rate decreases.

3.4 Cyclostrophic, superrotation regime

Experiments with $\mathcal{R}_o > 1.5$ are characterised by circulations featuring strong prograde winds above the equatorial region, resembling the atmospheres of Venus and Titan. Atmospheres in this regime are usually found on slowly rotating planetary bodies where the Coriolis force is not strong enough to balance the pressure gradient force in the meridional direction. Instead, the principal mechanical balance in the horizontal direction is the cyclostrophic balance between centrifugal force and the pressure gradient force, which is similar to the situation in small-scale vortices (like

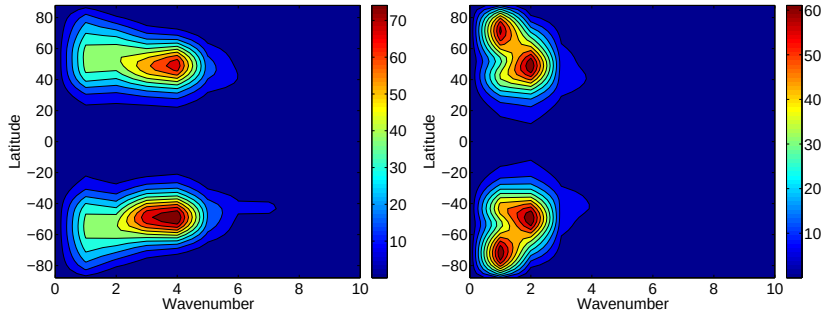

(a) $\Omega = 1/2$ (b) $\Omega = 1/4$

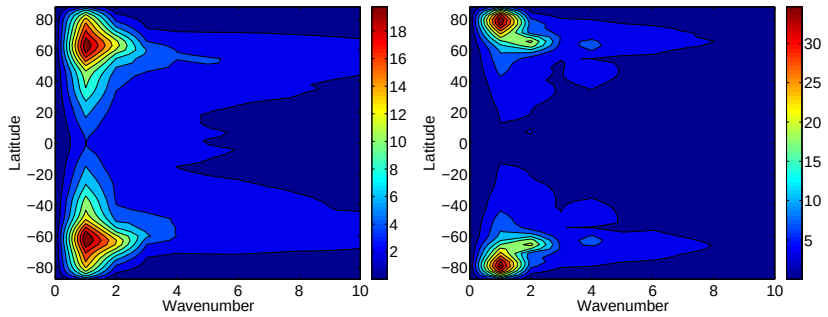

(c) $\Omega = 1/8$ (d) $\Omega = 1/16$

Figure 3.13: Same as Fig. 3.12, but from experiments with low rotation rates.

tornadoes) in the Earth's atmosphere. The most prominent feature of this circulation regime is the equatorial super-rotation, which means the angular momentum of the atmosphere above the equatorial region is significantly larger than the angular momentum it would have if it was in solid body rotation at the same rotation rate with the underlying planet. The axial component of atmospheric specific angular momentum is defined by

$$m = a\cos\phi\big(\Omega a\cos\phi + u\big), \tag{3.19}$$

where a is the planetary radius, ϕ the latitude, Ω the planetary rotation rate, and u the zonal wind velocity. An objective measure of such equatorial super-rotation can be defined as (Read (1986a))

$$s = m/(\Omega a^2) - 1, \tag{3.20}$$

so that $s = 0$ corresponds to solid body rotation on the equator at rotation rate Ω, and $s > 0$ represents the local super-rotation. Similarly a global super-rotation index can be defined as

$$S = \iiint m \mathrm{d}V/M_0 - 1, \tag{3.21}$$

where $\mathrm{d}V$ is the volume element and M_0 the integrated absolute angular momentum of the fluid in solid body rotation at rotation rate Ω.

Super-rotation is not uncommon among planetary atmospheres. Observations show that the Earth's stratosphere exibits weak equatorial super-rotation during the westerly phase of QBO (Quasi-Biennial Oscillation) due to vertical transfer of momentum by vertically propagating gravity waves, Kelvin waves, and mixed Rossby-gravity waves (James (1995)). Significant equatorial (and global) super-rotation has been found on Venus with $S \approx 10$(Read (1986a)). In fact, the prograde wind near the cloud tops above the equator of Venus can reach $\sim 100\mathrm{m\ s}^{-1}$, which is about 60 times faster than the underlying solid planet surface. In addition, equatorial super-rotation has also been found on gas giant planets — Jupiter and Saturn, at least at the the level of the visible cloud-decks, possibly resulting from deep convection (Kaspi et al. (2009)) or equatorial waves (Yamazaki et al. (2004)). Recent modeling studies of tidally-locked exoplanets find that equatorial super-rotation should also be expected for close-in Hot-Jupiters, through the Gill mechanism due to the asymmetric heating between the day-side and the night-side (Showman & Polvani (2011)). We will limit the comparison of our experiments only with the slowly-rotating planetary bodies, Venus and Titan.

3.4.1 Hide's theorem

If the atmospheric circulation is axisymmetric and inviscid, then angular momentum is conserved following the flow since there is no net torque exerted on the flow. There-

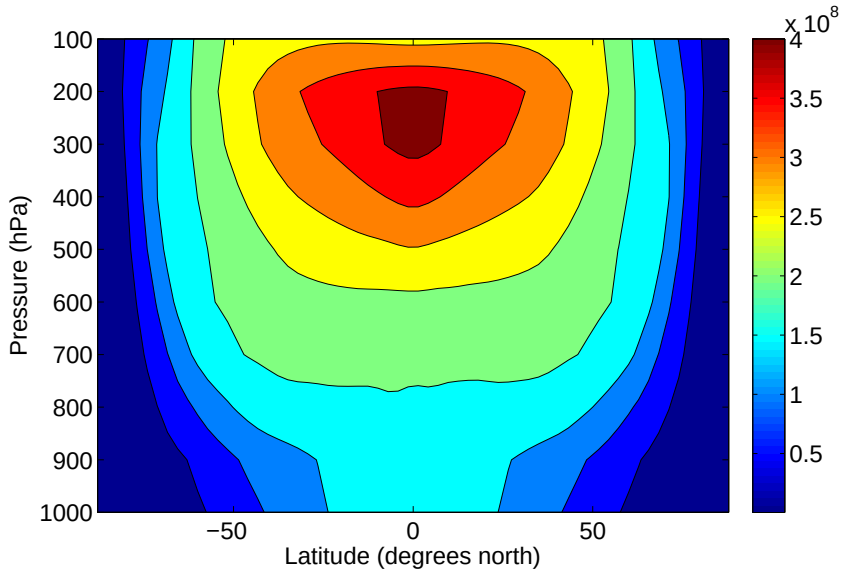

Figure 3.14: Specific angular momentum of the experiment with $\Omega^* = 1/16$ (unit: $m^2 s^{-1}$).

fore, both s and S must not exceed zero for inviscid axisymmetric circulation unless the initial condition is a locally and/or globally super-rotating atmosphere. This constraint is known as Hide's theorem (Hide (1969)). In order for the atmosphere to super-rotate, the effect of non-axisymmetric eddies on the transfer of angular momentum needs to be taken into account. Equatorial super-rotation can only be maintained if there are non-axisymmetric eddies that transfer momentum up the gradient into the angular momentum maximum above the equator (as shown in Fig. 3.14).

3.4.2 GRW mechanism

The mechanism of the formation and maintenance of strong equatorial super-rotation has not yet been fully understood. One of the important paradigms in our current understanding of super-rotation, especially within the context of Venus atmosphere, is the so-called GRW ('Gierasch-Rossow-Williams') mechanism. Gierasch (1975) established a framework of quasi-axisymmetric circulation model by incorporating the effect of eddies into the zonal mean momentum equation in terms of eddy viscosity,

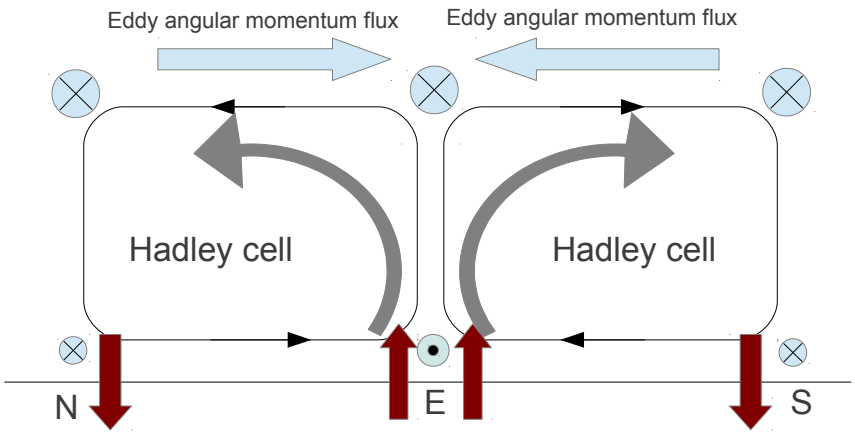

Figure 3.15: Schematic diagram showing the classical GRW mechanism of super-rotation. Dark red arrows denote the angular momentum flux due to surface frictional torque, blue arrows the eddy angular momentum flux, and grey arrows the angular momentum flux by Hadley cells.

and assumed that these eddies tend to mix primarily the vorticity in the horizontal direction. By actively mixing vorticity in the meridional direction these eddies tend to bring the global circulation into a state of solid body rotation, which coupled to a steady overturning circulation will lead to strong equatorial super-rotation (see Mitchell & Vallis (2010)). This is further supported by the studies of Rossow & Williams (1979) in which equatorial super-rotation was observed in a numerical shallow-water model, with the origin of angular momentum-transporting eddies ascribed to extratropical barotropic instability. The classical GRW mechanism is illustrated by the schematic diagram shown in Fig. 3.15.

Apart from the GRW mechanism, recent numerical studies suggest that other processes might also play an important role in the formation and maintenance of equatorial super-rotation. For the case of Venus, thermal tides associated with diurnal cycle have been found to be a major cause of strong equatorial super-rotation (see e.g.Takagi & Matsuda (2007)). Studies by Mitchell & Vallis (2010) and Potter et al. (2014) employ a simple GCM similar to PUMA-S with no diurnal/seasonal cycles and discovers that eddies due to equatorial perturbations (Kelvin waves) are crucial at the early stage of forming equatorial super-rotation, instead of extratropical eddies

as proposed in the GRW mechanism. Another study by Mitchell et al. (2014) using a slightly more complicated model with seasonally-varying Newtonian relaxation scheme suggests that the strength of the seasonal cycle plays an important role in determining whether the atmosphere can evolve into the equatorial super-rotation state. According to Mitchell et al. (2014), strong seasonal cycle tends to prevent the development of equatorial super-rotation.

3.4.3 Experiment results

In the following subsection, we will show a series of diagnostics on the equatorial super-rotation found in our experiments, along with comparisons to the terrestrial circulation regime.

The Eliassen-Palm (EP) flux (see e.g. Eliassen & Palm (1961), Andrews & McIntyre (1978)) is an important diagnostic which reveals the dynamics of the eddy-mean flow interaction. The full ageostrophic form of the EP flux is defined as:

$$\begin{aligned}\mathbf{E} =& \{\mathrm{E}^{(\phi)}, \mathrm{E}^{(p)}\} \\ =& -a\cos\phi\Big\{[u^*v^*] - [u]_p[v^*\theta^*]/[\theta]_p, \\ & [\omega^*u^*] + \big[([u]\cos\phi)_\phi/(a\cos\phi) - f\big][v^*\theta^*]/[\theta]_p\Big\},\end{aligned} \tag{3.22}$$

where a is planetary radius, f the Coriolis parameter. $[\cdot]$ denotes zonal average and $*$ the eddy perturbation. All subscripts represent partial derivatives.

The zonal mean specific angular momentum equation can then be written as (Read (1986a), Vallis (2006)):

$$[m]_t + [\mathbf{u}_*] \cdot \nabla[m] = \nabla \cdot \mathbf{E} + \mathcal{F}/\rho, \tag{3.23}$$

where m is the specific angular momentum, $\mathcal{F}$ the viscous damping, and $[\mathbf{u}_*] = ([v_*], [\omega_*])$ the two components of the residual circulation under the Transformed

Eulerian Mean (TEM) framework:

$$[v_*] = [v] - ([v^*\theta^*]/[\theta]_p)_p, \tag{3.24a}$$

$$[\omega_*] = [\omega] + ([v^*\theta^*]\cos\phi/[\theta]_p)_\phi/(a\cos\phi). \tag{3.24b}$$

Thus the divergence of EP flux reflects the acceleration (eastward torque) exerted by the eddies on the zonal mean flow. The direction of the EP flux vector shows the propagation of the group velocity of planetary Rossby waves.

A latitude-pressure cross section map showing both the vectors of **E** and the corresponding divergence has been advocated as useful diagnostics to give a compact view of the eddy-mean flow interaction. To plot the EP flux and calculate its divergence within the ϕ-p plane, the form of EP flux defined in Eq. (3.22) needs to be modified following Edmon et al. (1980):

$$\{\hat{\mathrm{E}}^{(\phi)}, \hat{\mathrm{E}}^{(p)}\} \equiv 2\pi a^2 g^{-1}\cos\phi\{a^{-1}\mathrm{E}^{(\phi)}, \mathrm{E}^{(p)}\}. \tag{3.25}$$

so that the divergence of EP flux can be conveniently calculated as [3]

$$\Delta = \frac{\partial \mathrm{E}^{(\phi)}}{\partial\phi} + \frac{\partial \mathrm{E}^{(p)}}{\partial p}. \tag{3.26}$$

Fig. 3.16 shows the EP flux and its divergence for the experiment with $\Omega^* = 1$ in the statistically steady state, which largely resembles the situation of Earth's atmosphere in the annual-mean sense. Throughout the extratropical troposphere, there is

[3] Otherwise the divergence should be calculated as

$$\nabla\cdot\mathbf{E} = \frac{1}{a\cos\phi}\frac{\partial}{\partial\phi}(\cos\phi \mathrm{E}^{(\phi)}) + \frac{\partial}{\partial p}(E^{(p)}).$$

It can be shown that in the $\phi - p$ plane,

$$\int \nabla\cdot\mathbf{E}\mathrm{d}m = \int \Delta \mathrm{d}\phi\mathrm{d}p$$

where $\mathrm{d}m = 2\pi a^2 g^{-1}\cos\phi\mathrm{d}\phi\mathrm{d}p$ is the mass element in the form of a latitudinal ring.

a net westward torque exerted by eddies on the zonal flow as reflected by the convergence of EP flux. The direction of EP flux indicates the upward propagation of Rossby waves in the mid-latitudes and its equatorward propagation at the upper levels. Fig. 3.17 shows the EP flux and its divergence for the experiment with $\Omega^* = 1/16$ in the statistically steady state where equatorial super-rotation is found. It shows significant differences compared with the terrestrial regime in Fig. 3.16. The EP flux vector is predominantly horizontal, implying the relative significance of meridional momentum flux ($[v^*u^*]$) compared with the heat flux ($[v^*\theta^*]$). There is net divergence of EP flux over the equatorial and subtropical region, indicating an eastward (prograde) torque exerted by the eddies on the zonal flow. The typical mid-latitude baroclinic turbulence regime with upward pointing EP flux vector disappears in this scenario, since the Rossby deformation radius is larger than the domain size with $\Omega^* = 1/16$. Thus the scenario of equatorial deceleration of zonal flow through the breaking and dissipation of Rossby wave at critical latitudes is absent in the equatorial super-rotation case. There is no significant EP flux convergence/divergence at the upper levels above the equator, which is consistent with the findings of Mitchell & Vallis (2010) and Saravanan (1993) that once the equatorial super-rotation is established, the absence of equatorial torques over the super-rotating levels allows the regime to maintain itself for a long period with very little momentum convergence/divergence.

The EP flux shown in Fig. 3.17 shows significant wave activities at the 600-700mb levels. This is due to the strong meridional eddy momentum flux ($[v^*u^*]$) (see Fig. 3.18). In contrast with the poleward momentum flux as found in terrestrial case (see Fig. 3.19), the eddy momentum flux is equatorward with maximum transport at the 700mb level.

Fig. 3.20 shows the EP flux of the experiment $\Omega^* = 1/16$ during the spin-up phase. The fluxes tend to be weaker than in the statistically steady state. But significant divergence can still be found over the equatorial region, indicating the existence of

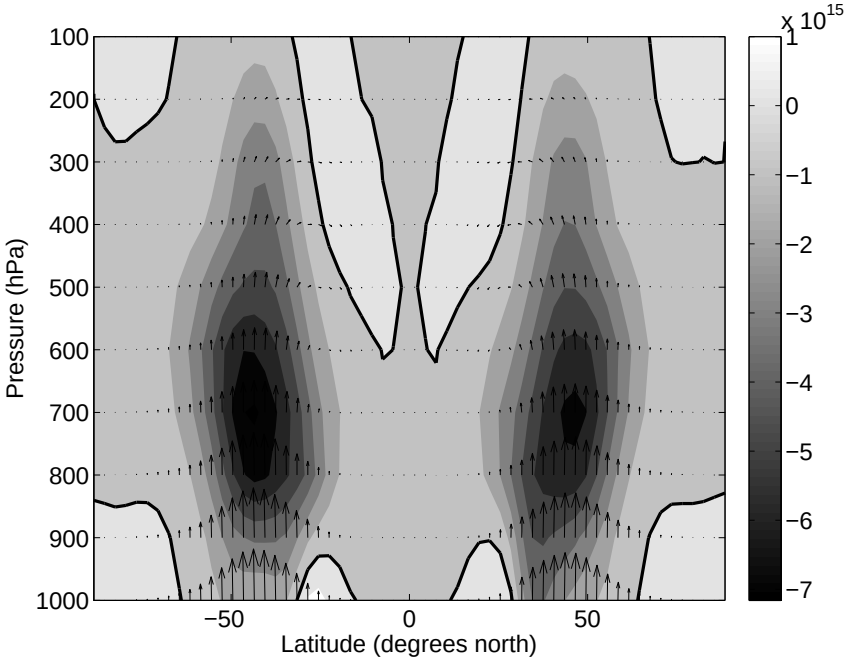

Figure 3.16: Annual mean EP flux (vectors) and its divergence (contour), based on the experiment of $\Omega^* = 1$. Unit of divergence: m^3.

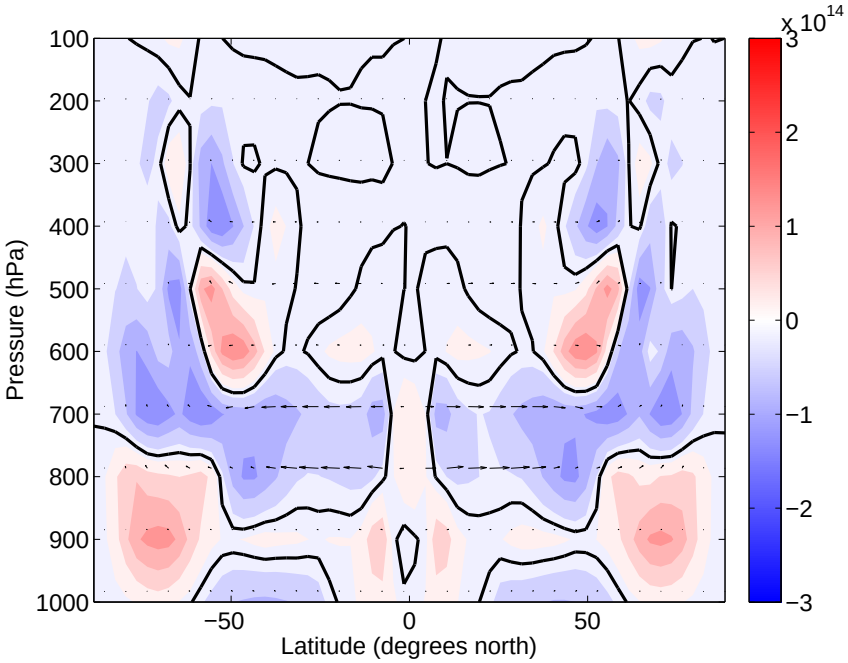

Figure 3.17: Annual mean EP flux (vectors) and its divergence (contour), based on the experiment of $\Omega^* = 1/16$. Unit of divergence: m^3.

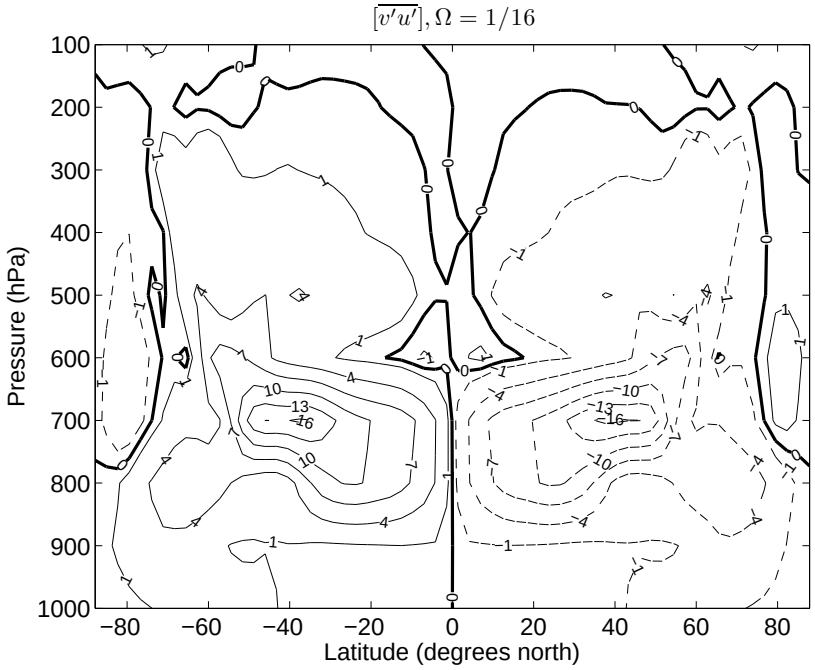

Figure 3.18: Zonal and temporal mean eddy momentum flux, based on the experiment of $\Omega^* = 1/16$. Unit: $\mathrm{m^2 s^{-2}}$.

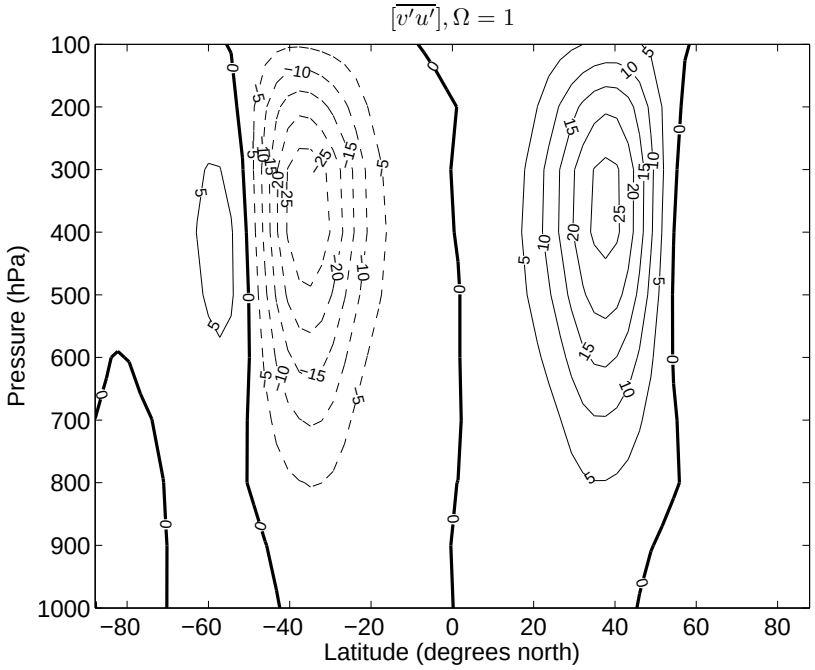

Figure 3.19: Zonal and temporal mean eddy momentum flux, based on the experiment of $\Omega^* = 1$. Unit: $\mathrm{m^2 s^{-2}}$

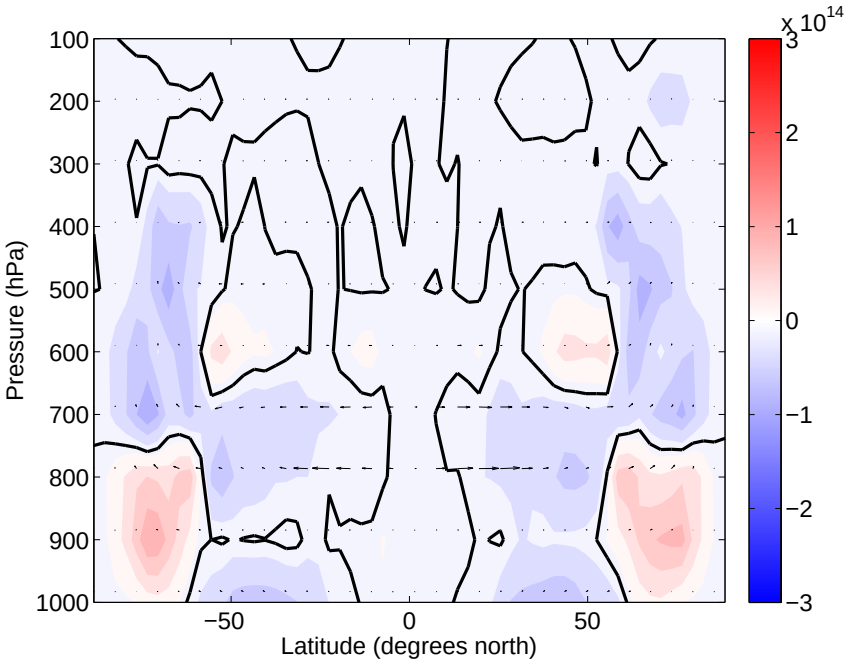

Figure 3.20: EP flux (vectors) and its divergence (contour) during the spin-up phase of $\Omega^* = 1/16$, averaged from day 200 to day 250. Unit of divergence: m^3.

eddy-induced prograde equatorial torques during the spin-up phase.

The nature of the generation of the eddies responsible for the wave activities shown in EP flux analysis can be revealed by analysing the development of the corresponding hydrodynamic instability within the flow. The potential candidates include inertial instability, barotropic instability and baroclinic instability. It is unlikely that the modelled atmosphere shows merely one pure kind of instability. Instead, there may well exist a mixture of instabilities.

Inertial instability refers to the instability that an air parcel moving in the meridional plane might encounter when the imbalance between the pressure gradient force and the Coriolis force tend to bring the perturbed air parcel away from its original position. It is mathematically similar to the static instability which occurs in the vertical direction. The (*sufficent* and *necessary*) condition for inertial instability to occur is that $f[q] < 0$ where $[q]$ could be either zonal mean absolute vorticity or potential vorticity.

Barotropic instability is essentially a kind of horizontal shear instability that occurs within a background zonal flow $u(y)$ on a β-plane. The first *necessary* condition (Rayleigh-Kuo inflection point criterion) for the flow to be barotropically unstable is that the meridional gradient of absolute vorticity (or PV), $\partial[q]/\partial y$, changes sign within the flow domain. The second *necessary* condition (Fjørtoft's criterion) is that $\partial[q]/\partial y(u-u_s)$ where u_s is the value of $u(y)$ at which $\partial[q]/\partial y$ vanishes, must be positive somewhere in the domain (Vallis (2006)). The Fjørtoft condition is satisfied if the extremum of vorticity occurs in the interior of the domain and not at the boundaries.

Baroclinic instability occurs within a stably stratified atmosphere with horizontal temperature gradient, and is usually pictured as 'sloping convection' which acts to convert available potential energy into kinetic energy in spite of the stable vertical stratification. The Charney-Stern-Pedlosky *necessary* condition for baroclinic instability states that one of the following criteria must be satisfied:

1. $\partial[q]/\partial y$ changes sign in the interior;
2. $\partial[q]/\partial y$ takes the opposite sign to $\partial[u]/\partial z$ at the upper boundary;
3. $\partial[q]/\partial y$ takes the same sign as $\partial[u]/\partial z$ at the lower boundary;
4. $\partial[u]/\partial z$ takes the same sign at the upper and lower boundaries.

In the terrestrial atmosphere criterion 3 is usually satisfied with positive $\partial[q]/\partial y$ and $\partial[u]/\partial z$. Note that all these conditions for barotropic and baroclinic instabilities are *necessary* conditions only. Thus the flow may well be stable even if these conditions are satisfied, and satisfying these conditions should only be considered as an indication that the flow may be barotropically/baroclinically unstable.

In order to reveal the instability responsible for the generation of eddies, the zonal mean Ertel PV ($q = -g(f+\zeta)\partial\theta/\partial p$) is shown in Fig. 3.21. According to the Rayleigh-Kuo criterion for barotropic instability, the zonal wind is barotropically

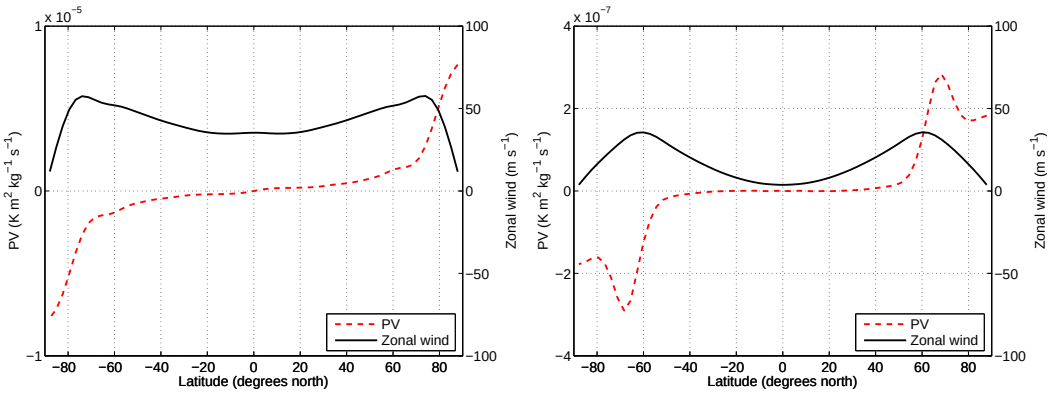

Figure 3.21: Zonal mean zonal wind and PV at the 200mb (left) and 700mb (right) level at statistically steady state, based on the experiment with $\Omega^* = 1/16$.

stable at 200mb, which is the level of most significant equatorial super-rotation, but probably unstable at the 700mb level over high-latitude regions, as indicated by the extremum of PV (Note that the Rayleigh-Kuo criterion is just a *necessary* condition). This is consistent with the significant wave activity seen at the 700mb as reflected by the eddy momentum flux and EP flux shown in Figs. 3.18 and 3.17. It is also consistent with the findings of Mitchell & Vallis (2010) in which their maximum EP flux was found at the $\sigma = 0.7$ level in the steady state of their equatorial super-rotation experiment.

The analysis of zonal mean PV during the spin-up phase can provide further insights into the role of eddies at the 200mb and 700mb levels in generating super-rotation as shown in Figs. 3.22 and 3.23. At the 200mb level, the PV gradient has weak extrema over a few latitude nodes during the early stages of spin-up, which quickly disappear as the super-rotation gradually develops. In contrast, the PV gradient at 700mb has two persistent extrema over the high-latitude region throughout the spin-up phase shown in Fig. 3.23. This implies the importance of eddy generation and the corresponding horizontal eddy momentum transfer at the 700mb level. A heuristic picture that can be summarised from these diagnostics is that eddies generated through barotropic instability associated with jets at high latitudes transfer momentum equatorward in the lower atmosphere. This extra momentum is then transported

upwards over the equator mainly by the meridional overturning circulation, feeding the equatorial super-rotation in the upper atmosphere.

However, it should be noted that this does not mean that the mechanism of the formation of equatorial super-rotation found in our experiments are indeed the GRW mechanism. From the above diagnosis, it is unclear as to what mechanism is responsible for transporting momentum from extratropical regions to the equator. Rossby waves have the property of converging momentum towards the source of perturbation, which in our case is the extratropics. Therefore it is unlikely that the momentum convergence towards the equator in our experiments is done by Rossby waves. The study of Mitchell & Vallis (2010) suggests that equatorial perturbation and the associated Kelvin waves are responsible for equatorward momentum transport, though in our case no clear evidence can be found about instabilities over the tropics. With studies by Mitchell et al. (2014) and Potter et al. (2014) in mind, further analysis on the nature of waves needs to be performed to really understand the exact mechanism in our experiments. Besides, the direct applicability of the above discussions to the real planetary super-rotation (e.g. superrotation of the atmosphere of Venus) can be problematic. The mechanism present in our model is somewhat similar to the classical GRW mechanism in the sense that eddies associated with the barotropically unstable high-latitude jets are mainly responsible for the equatorward momentum transfer. But the strength of the equatorial super-rotation produced in our experiments is far weaker than that observed/modelled for the atmosphere of Venus. Recent studies (e.g. Takagi & Matsuda (2007), Lebonnois et al. (2010), Mendonça et al. (2012)) have shown that the much stronger equatorial super-rotation in the upper atmosphere of Venus is largely maintained by thermal tides induced by the diurnal cycle of solar irradiation. As our experiments adopt a permanent annual mean thermal forcing with no diurnal cycle, the equatorial super-rotation obtained is thus much weaker than that of Venus. For Titan, however, our experiment becomes more relevant in

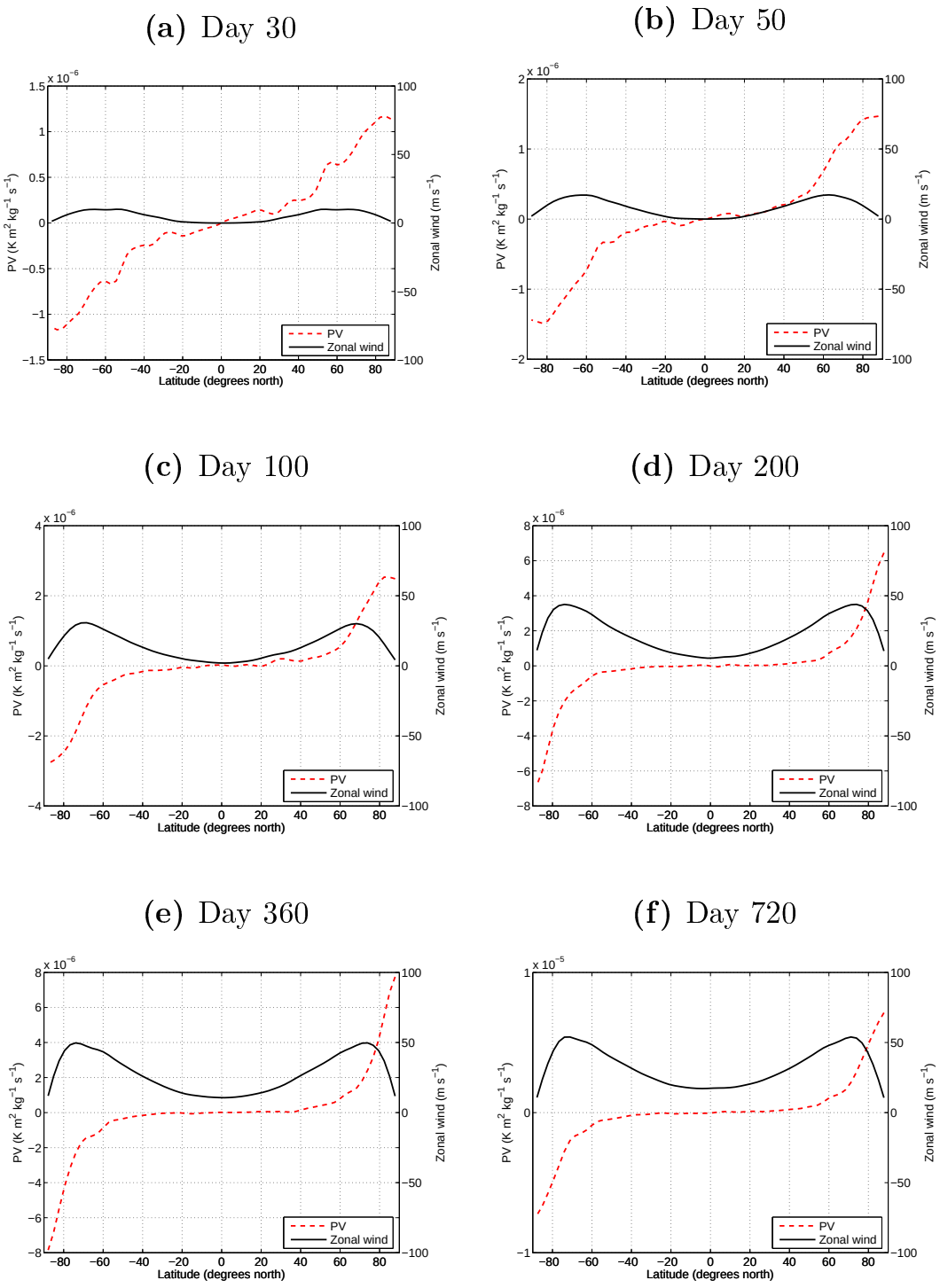

Figure 3.22: Zonal mean PV and zonal wind during spin-up phase at 200mb on day 30, 50, 100, 200, 360 and 720, based on the experiment of $\Omega = 1/16$.

(a) Day 30

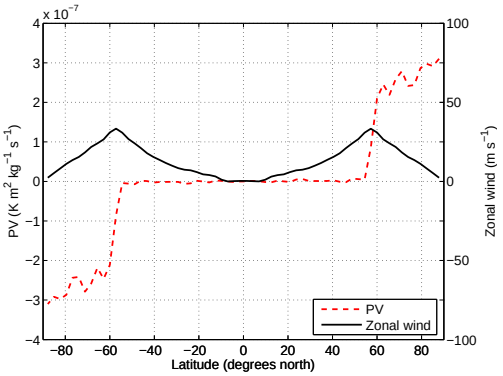

(b) Day 50

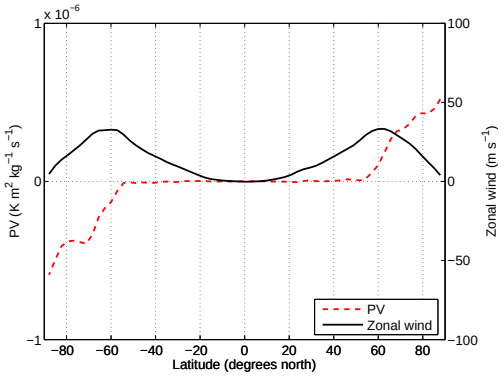

(c) Day 100

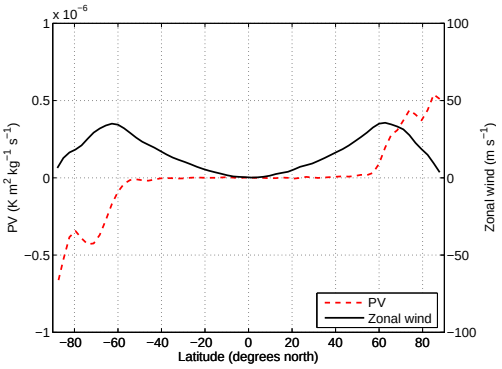

(d) Day 200

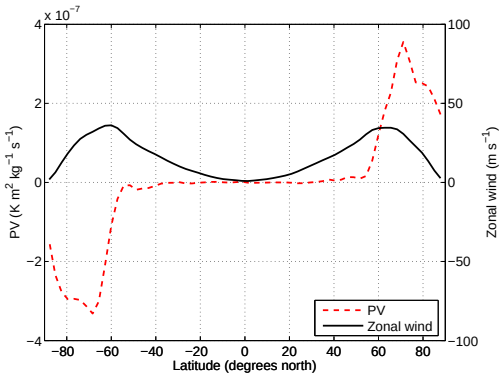

(e) Day 360

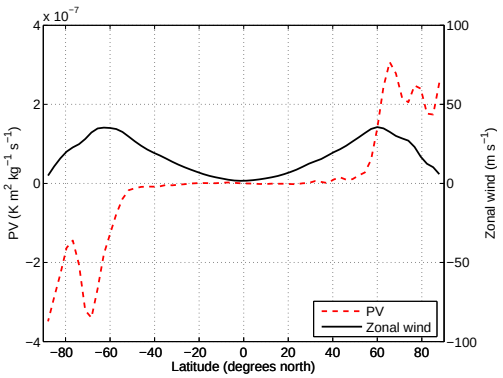

(f) Day 720

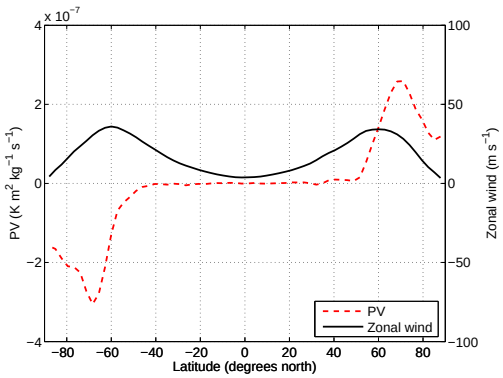

Figure 3.23: Same as Fig. 3.22, but for 700mb.

that the diurnal cycle on Titan is much less significant than its seasonal cycle[4] and GCM simulations have shown that a GRW-like mechanism is mainly responsible for superrotation on Titan (see e.g. Lebonnois et al. (2012)).

3.5 Regular baroclinic waves regime

A regular baroclinic wave regime lies in the range $0.1 < \mathcal{R}_o < 1.5$ within the non-axisymmetric region. Favouring intermediate rotation rates and moderate imposed meridional/radial temperature contrasts, it is also one of the major flow regimes observed in laboratory rotating annulus experiments (see e.g. Hide & Mason (1975)). Featuring baroclinic waves with one or two dominating wavenumbers and their harmonics, this regime is distinguished from irregular/chaotic baroclinic wave regimes by its high regularity/predictability due to the presence of steady or (quasi-)periodic vacillating waves.

Linear theories of baroclinic instability and eddy growth, being the classic pivotal framework in dynamic meteorology studies, have been successful in delineating the initial development of unstable disturbances on the background axisymmetric flow and predicting the location of the transition boundary between axisymmetric and non-axisymmetric flow regimes within the regime diagram (Hide & Mason (1975)). But for the regular baroclinic wave regime, as the eddies/disturbances grow to amplitudes non-negligible compared to the background domain (known as waves of 'finite amplitude'), linear theories begin to fail and nonlinear eddy-eddy and eddy-mean flow interactions need to be taken into account. As an analytical first attempt, weakly nonlinear theories have been proposed since the 1960s (Pedlosky (1970), Pedlosky (1971)) which assumes the flow to be just weakly supercritical to baroclinic instability so that only a small range of wavenumbers is unstable and grows relatively slowly

[4]Titan has a tidally-locked orbit around Saturn and has an obliquity of $\sim 27^\circ$ which is quite similar to that of the Earth

compared to the wave phase speed. Although these idealised models tend to predict the existence of vacillating or steady waves under appropriate conditions of viscous dissipation, there have been frequent debates as to whether these weakly nonlinear models are applicable to the fully developed baroclinic instability (e.g. see Boville (1981), Esler & Willcocks (2012)). The challenge of the nonlinearity hinders the development of a complete analytical understanding of the equilibration process of these regular finite-amplitude baroclinic waves. But insights can somehow be obtained from numerical modelling studies based on the fully nonlinear primitive equations.

The regular baroclinic wave regime found in our study may also be relevant to the planetary scale baroclinic waves that have been observed in the Martian atmosphere. Quasi-periodic surface pressure variations (especially in the northern winter hemisphere) have been observed by in-situ measurement (Viking landers) which can be attributed to large scale baroclinic wave activity (Ryan et al. (1978), Barnes (1981)). A highly regular regime dominated by zonal wavenumber 3-4 could be inferred from these observations, indicating that they are quite akin to what we have observed in our idealised GCM experiments. Compared with Earth's irregular and chaotic atmosphere, the Martian atmosphere can be classified as a member of the regular baroclinic wave regime. Admittedly, there are a number of differences between Mars and Earth that might contribute to the formation and maintenance of such coherent baroclinic waves within the Martian atmosphere. For example, the lack of a thermal contrast between continents and oceans, as well as the lack of strong latent heating by phase changes of water. But the laboratory annulus experiments and our idealised GCM studies suggest that these factors should be of marginal significance (e.g. note that chaotic circulation is found on aqua-planet experiments with higher rotation rates), whereas the larger $\mathcal{R}_o$ (due to smaller planetary size) and the much stronger radiative damping of the Martian atmosphere are likely to be primarily responsible for these regular baroclinic waves.

The larger $\mathcal{R}_o$ of Mars (and of our experiments within the regular baroclinic wave regime) can partly explain the dominance of zonal wavenumber 3, which is significantly smaller compared with the dominant wavenumber 5-6 that is usually observed in Earth's atmosphere. As shown in the previous section, this is related to the scaling of the energy-containing wavenumber with Rossby/Rhines wavenumber which is ultimately proportional to $\mathcal{R}_o$. As for the thermal (radiative) damping, it has been shown by the early work of Pedlosky (1970) and Pedlosky (1971) that weak dissipation leads to wave vacillation whereas strong dissipation enables steady regular waves. Later supported by the Q-G β-plane model study by Barnes (1981) and idealised Mars GCM study of Collins & James (1995), it is shown that the timescale of thermal damping (as well as surface friction, in the case of Collins & James (1995)) is a crucial factor in determining the regularity of baroclinic waves. We have therefore further conducted a series of experiments at $\Omega^* = 1/2$ with various combinations of thermal and frictional damping timescale to reveal their effects on planetary baroclinic waves.

3.5.1 Regime diagram

Fig. 3.24 shows the regime diagram based on the 25 experiments at $\Omega^* = 1/2$ with various τ_r and τ_f. The lower left region of the diagram (corresponding to strong frictional and thermal damping) is dominated by relatively weak waves with maximum Fourier power amplitude of geopotential height at 500mb level smaller than 30 geopotential metres. The right end of the diagram (corresponding to weak thermal damping) is dominated by waves with 2-3 mixed dominating wavenumbers, indicating a weakly irregular transitional state towards the irregular/turbulent regime. The region between the weak wave regime and the mixed wavenumber regime is mainly characterised by relatively coherent regular baroclinic waves with a single dominating wavenumber. Fig. 3.25 shows the geopotential height at 500mb level for two repre-

sentative cases with dominating wavenumber 3 and 4 respectively. In the early study by Collins & James (1995), similar experiments were performed by varying thermal and frictional damping timescales in a simplified GCM. The main difference between our work and Collins & James (1995) is that parameters are varied in a larger range in our experiments, and regimes of $m = 2$ and 4 were found in addition to the $m = 3$ regime in our experiments.

The trend of these regimes with respect to the strength of frictional and thermal damping is intuitive if we consider the growth and life cycle of baroclinic eddies. Baroclinic eddy growth tends to be suppressed under strong damping (for example, strong thermal damping means that Newtonian relaxation is very efficient at restoring the temperature perturbations back into the axisymmetric equilibrium state, making the growth of eddies largely suppressed), which explains the dominance of weak waves at the lower left corner of the regime diagram. In contrast, under weak dampings eddies can grow into larger amplitudes, leading to regimes of waves with significantly larger amplitudes and smaller dominating wavenumbers. With weak enough dampings, more than one wavenumber component can grow to large amplitude and compete for dominance through wave-zonal flow interactions (see e.g. Hart (1981), Appleby (1988)), leading to the mixed wavenumber (or wavenumber vacillation) regime with quasi-periodic switch of dominating wavenumbers among 2-3 wavenumber components.

3.5.2 Spectral analysis

Flows of the regular wave regime with intermediate strength of frictional and thermal damping are characterised by one dominant wavenumber component and its harmonics. This is reflected in Figs. 3.26-3.27, which show the zonal amplitude spectra of geopotential height at the 500mb level along 50°N with respect to zonal wavenumber from two representative runs with dominant wavenumbers 3 and 4 respectively. In the

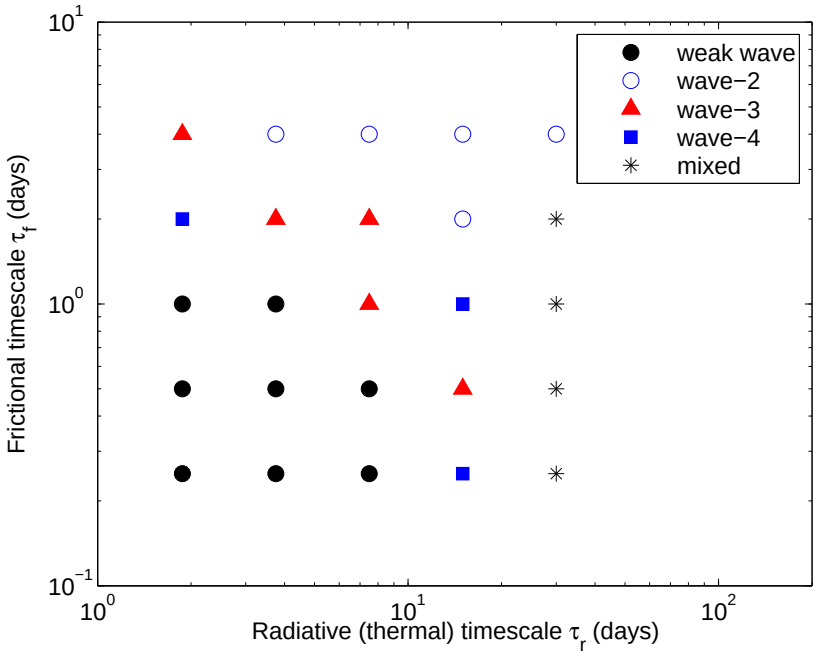

Figure 3.24: Regime diagram constructed by thermal timescale and frictional timescale. We use the thermal timescale in the free atmosphere ($\sigma < 0.8$) as the horizontal axis and the averaged frictional timescale in the boundary layer ($\sigma \geq 0.8$) as the vertical axis.

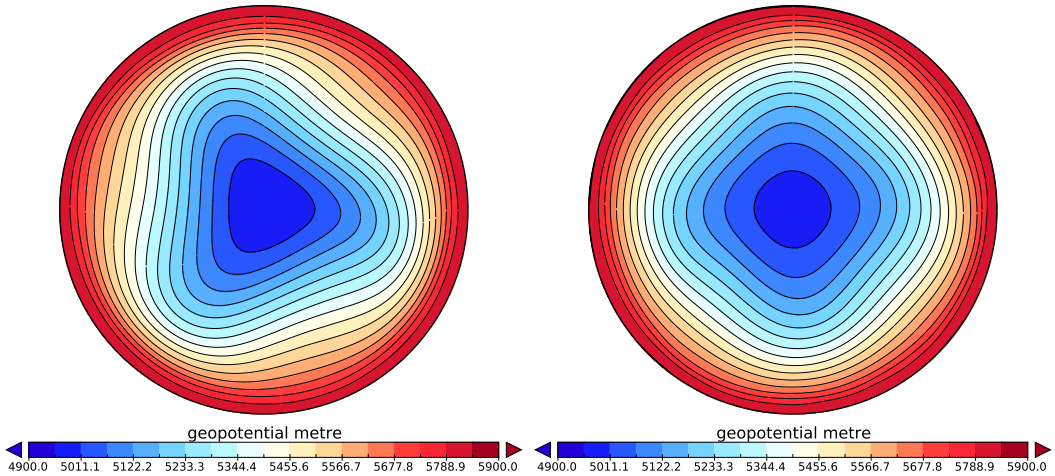

Figure 3.25: Snapshot of the geopotential height at 500mb level viewed from North Pole, showing the wavenumber-3 regime (left) with $\tau_f = 1.0$ day and $\tau_r = 7.5$ days, and wavenumber-4 regime (right) with $\tau_f = 2.0$ days and $\tau_r = 1.625$ days.

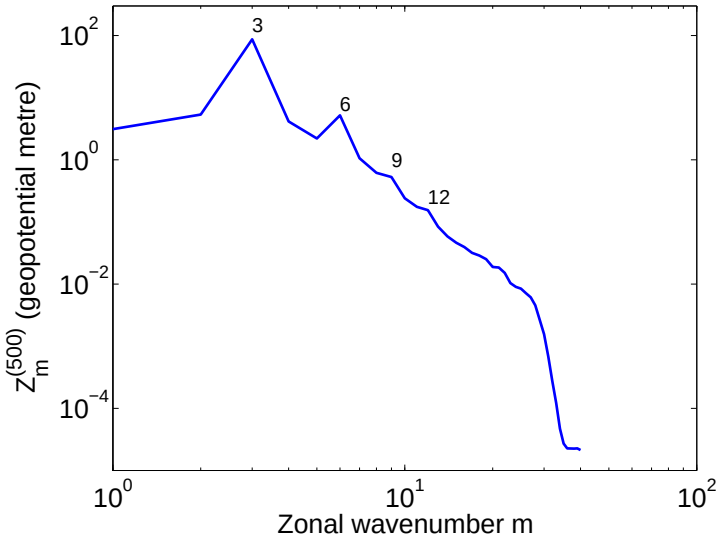

Figure 3.26: Fourier amplitude of geopotential height at 500mb level along 50°N with respect to zonal wavenumber, based on the run with $\tau_f = 1.0$ day and $\tau_r = 7.5$ days, averaged over three model years.

case of Fig. 3.26, well-defined signal peaks can be found at wavenumber 3 as well its harmonic component wavenumber 6, with less obvious peaks at wavenumbers 9 and 12, both of which are also harmonics of wavenumber 3. In the case of Fig. 3.27, the signal peaks at wavenumber 4 with a secondary peak at its first harmonic component wavenumber 8. These circulations, with a single dominant zonal wavenumber and its harmonics, have a latitudinally coherent structure as well, as shown in Fig. 3.28.

The regular waves observed in most of our experiments are not actually steady waves that drift around the globe with a constant amplitude. Instead, their amplitudes undergo temporal evolutions, making the waves more akin to the (modulated) amplitude vacillation regime that has been found in laboratory annulus experiments (Hide & Mason (1975),Read et al. (1992),Young & Read (2008)). Fig. 3.29 shows a Hovmöller diagram from the wavenumber-3 regime along 50°N. The zonal structure of the flow is dominated by the wavenumber-3 component throughout the model time, though there are noticeable variations of the wavenumber-3 perturbation amplitude. A Fourier spectral analysis was performed on the amplitude timeseries to reveal the quasi-periodicity of this modulated amplitude vacillation, as shown in Fig. 3.30, with

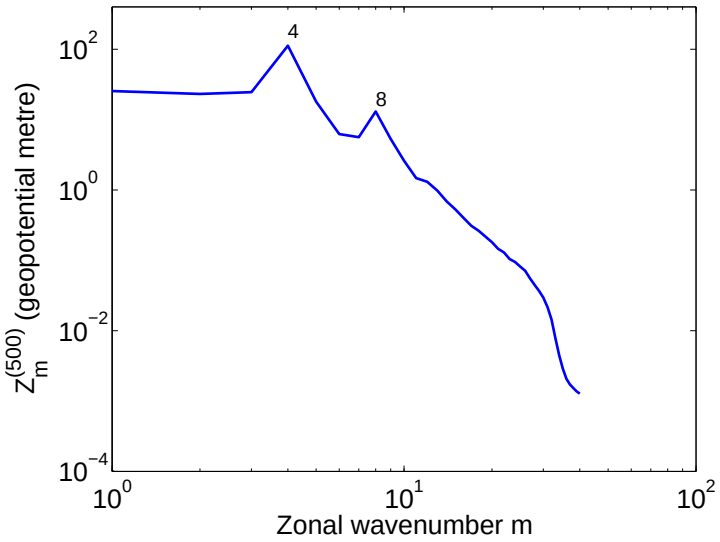

Figure 3.27: Same as Fig. 3.26 but for the run with $\tau_f = 1.0$ day and $\tau_r = 3.25$ days.

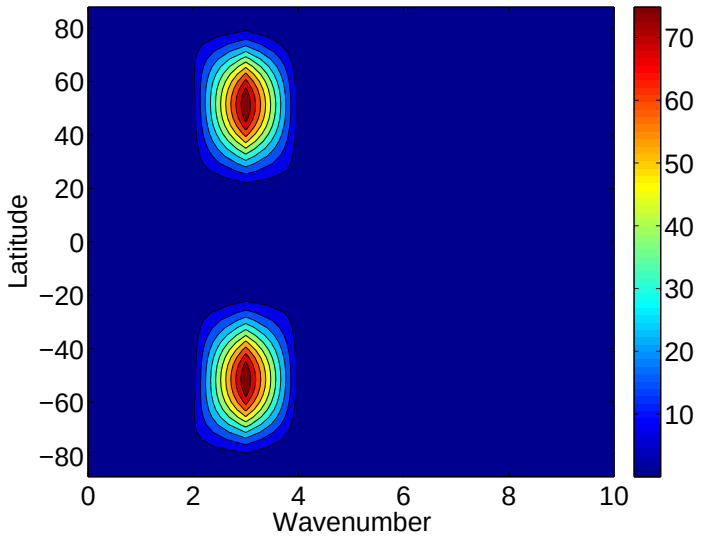

Figure 3.28: Latitudinal Fourier power amplitude of geopotential height at 500mb level with respect to zonal wavenumber, based on the run with $\tau_f = 1.0$ day and $\tau_r = 7.5$ days, averaged over three model years.

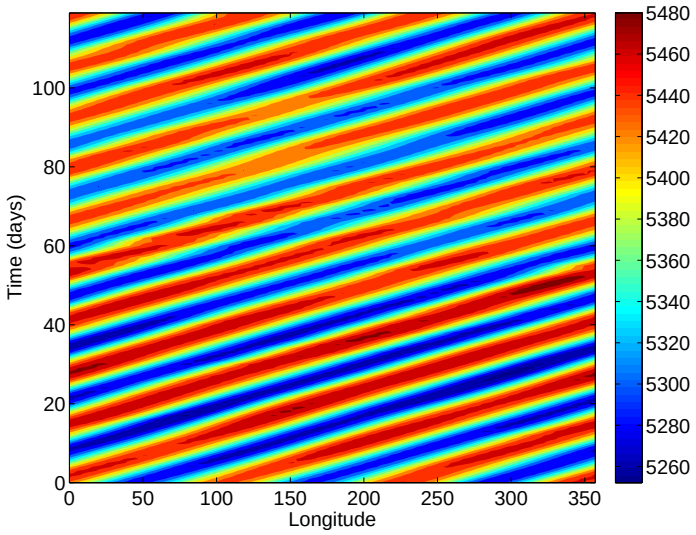

Figure 3.29: Hovmöller diagram of the geopotential height at the 500mb level along 50°N, based on the run with $\tau_f = 1.0$ day and $\tau_r = 7.5$ days. 120 days are shown.

a single very well defined dominant vacillation period of about 108 days.

3.5.3 Comparison with the Martian atmosphere

As stated at the beginning of this section, quasi-regular baroclinic waves are also observed to be present in the Martian atmosphere, especially in Northern winter when the atmosphere is usually characterised by a dominant wavenumber-3 regime. It is therefore interesting to see where Mars lies in our τ_r-τ_f regime diagram and whether the wavenumber-3 regime found in our experiments has any relevance to the Martian baroclinic waves.

It should be noted that, in order to make the comparison dynamically meaningful and consistent, we should use characteristic dimensionless parameters rather than directly comparing the corresponding timescales. Based on the frictional and thermal timescales, the frictional and thermal Taylor numbers can be defined as the

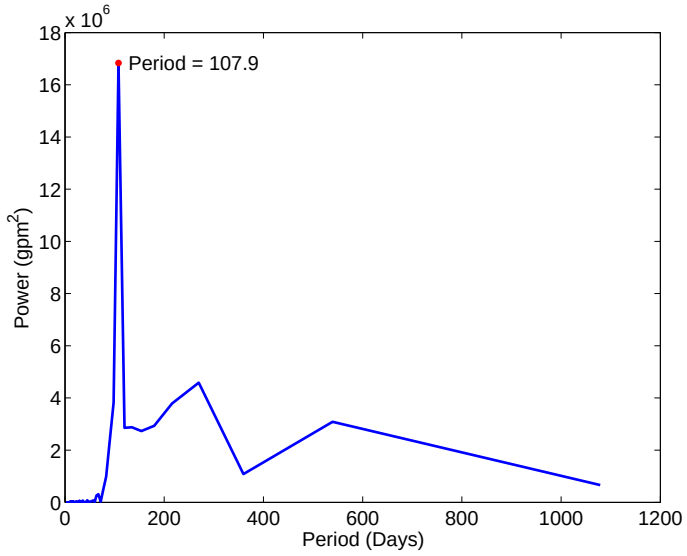

Figure 3.30: Periodogram based on the 3-year time series of Fourier amplitude of geopotential height at 500mb level along 50°N for the run with $\tau_f = 1.0$ day and $\tau_r = 7.5$ days. The red dot shows the dominant period of 107.9 days.

dimensionless parameter characterising frictional and thermal damping:

$$\mathcal{F}_f = 4\Omega^2\tau_f^2, \tag{3.27a}$$

$$\mathcal{F}_r = 4\Omega^2\tau_r^2. \tag{3.27b}$$

Constraints on the globally-averaged thermal and frictional timescales are not directly available from the sparse in-situ measurements of the Martian atmosphere. Our current best estimate of these two timescales can be found in Mars GCMs in which these parameters are tuned to obtain the best-fit global atmospheric circulation and climate compared with observations. In the study by Nayvelt et al. (1997), the average boundary layer frictional timescale τ_f was set to 0.5 Martian days (1 Mars day is to 24h37m, so 1 Mars day can be viewed approximately as 1 Earth day for our comparison), and the free atmosphere thermal timescale τ_r was set to about 3 Martian days (see Fig. 3.31). Given that our experiments run with half the rotation rate of Earth/Mars, these timescales used in the Mars GCM should be doubled before locating them in our τ_f-τ_r regime diagram so that the corresponding point representing

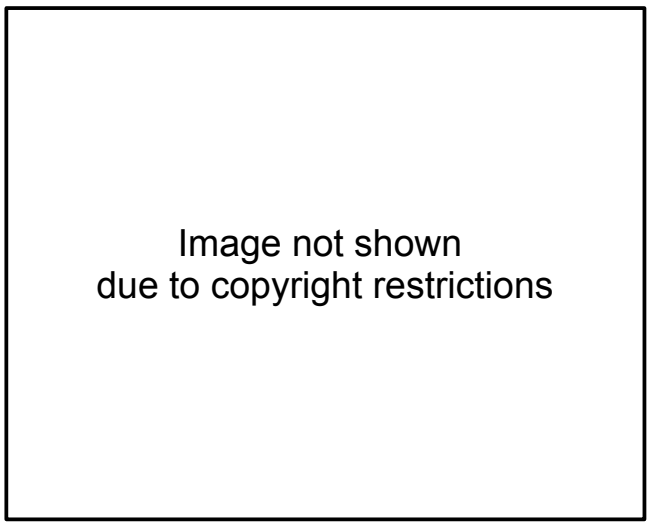

Figure 3.31: Atmospheric thermal damping timescale τ_r with height (σ-coordinate) of a Mars GCM, from Nayvelt et al. (1997)

Mars in the regime diagram is dynamically similar to the real Martian atmosphere in terms of $\mathcal{F}_f$ and $\mathcal{F}_r$. Therefore, the corresponding point representing the Martian atmosphere in the τ_f-τ_r regime diagram is essentially ($\tau_f = 1.0$, $\tau_r = 6.0$), as shown in Fig. 3.32. It is clear that the real Martian atmosphere lies close to the experiment in which a well-defined regular wavenumber-3 regime is discovered. It is therefore concluded that the regular baroclinic waves found in Martian atmosphere may be strongly influenced by the strength of thermal and frictional damping. The smaller size of the planet might lead to the dominance of smaller wavenumbers in Martian atmosphere compared with Earth's atmosphere, given a similar Rossby deformation radius on these two planets. But our experiments demonstrate that the regularity of these baroclinic waves and their wavenumber selection significantly depends on the strength of thermal and frictional dampings.

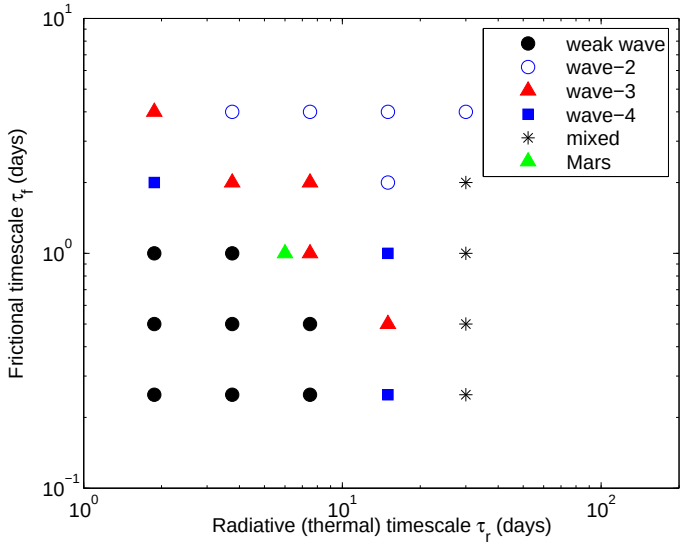

Figure 3.32: Regime diagram as in Fig. 3.24, with the green triangle reprenting the location of Martian atmosphere. Estimation of Martian τ_f and τ_r is from Nayvelt et al. (1997).

Chapter 4

Heat transfer efficiency and atmospheric energetics

This chapter presents studies on the atmospheric heat transport efficiency as well as the atmospheric energetics. Section 4.1 discusses the heat transfer efficiency of the atmospheric dynamic processes based on the PUMA-S experiments described in the previous chapter. Section 4.2 then presents the analysis of Lorenz energy cycle for each case considered in Chapter 3 which reveals the primary eddy generation process.

4.1 Heat transfer efficiency

There is a clear trend in the zonal mean temperature field from $\Omega^* = 8$ to $\Omega^* = 1/16$ in that the horizontal temperature gradient becomes smaller as the rotation rate decreases. This is especially prominent at the middle and high levels of the atmosphere, where the isothermal contours become almost horizontal at low rotation rates, due to the strong and extensive overturning Hadley cell in each hemisphere which is highly efficient in smoothing out the horizontal temperature inhomogeneity. Near the ground level, ΔT_h does not vary significantly with Ω due to the shorter relaxation timescales of the lower atmosphere (a shortcoming that is overcome in

PUMA-G, see Chapter 6 and 7). At higher rotation rates, the meridional temperature variation shows staircase-like features (see Fig. 4.1), indicating the existence of zonally parallel baroclinic zones and belts, resembling the banded structure of the Jovian atmosphere.

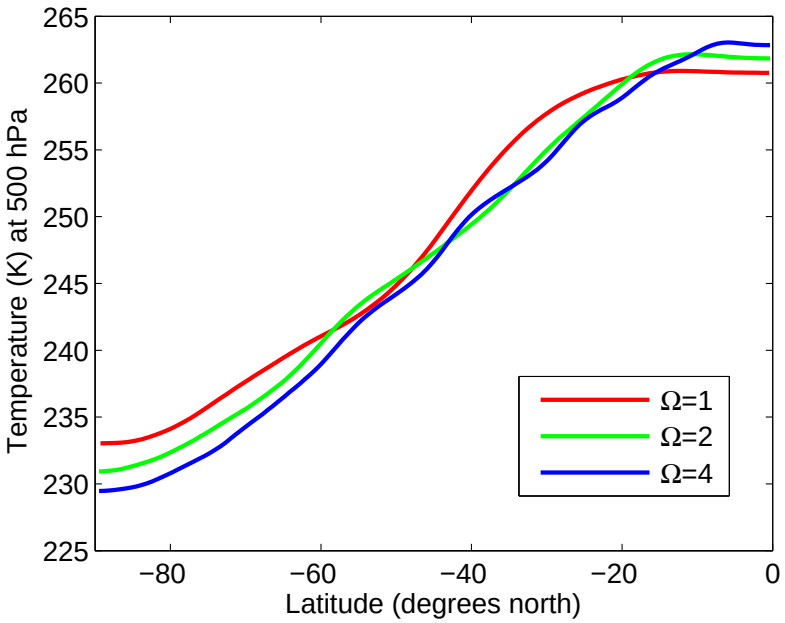

Figure 4.1: Zonal and temporal mean temperature at 500 hPa level for $\Omega^* = 1, 2$, and 4 in the southern hemisphere.

Meridional eddy heat flux, which can be formulated as $[\overline{v'T'}]$, provides an intuitive estimate of the intensity of meridional heat transfer by eddies. Figs. 4.2 and 4.3 show the zonal and temporal average of meridional eddy heat flux $v'T'$ for experiments with different rotation rates as obtained in PUMA-S runs with $\Delta T = 60$K. It can be seen that in all of these experiments, the atmosphere (especially the lower atmosphere) is dominated by poleward eddy heat transport. The strength of eddy heat flux reaches its maximum in the extratropical baroclinic regions, with multiple cores of maximum for experiments with higher rotation rate (e.g. $\Omega^* = 2, 4, 8$), which is consistent with the existence of multiple baroclinic zones in these experiments.

Since the term $v'T'$ is significant only in the extratropical regions (where the atmo-

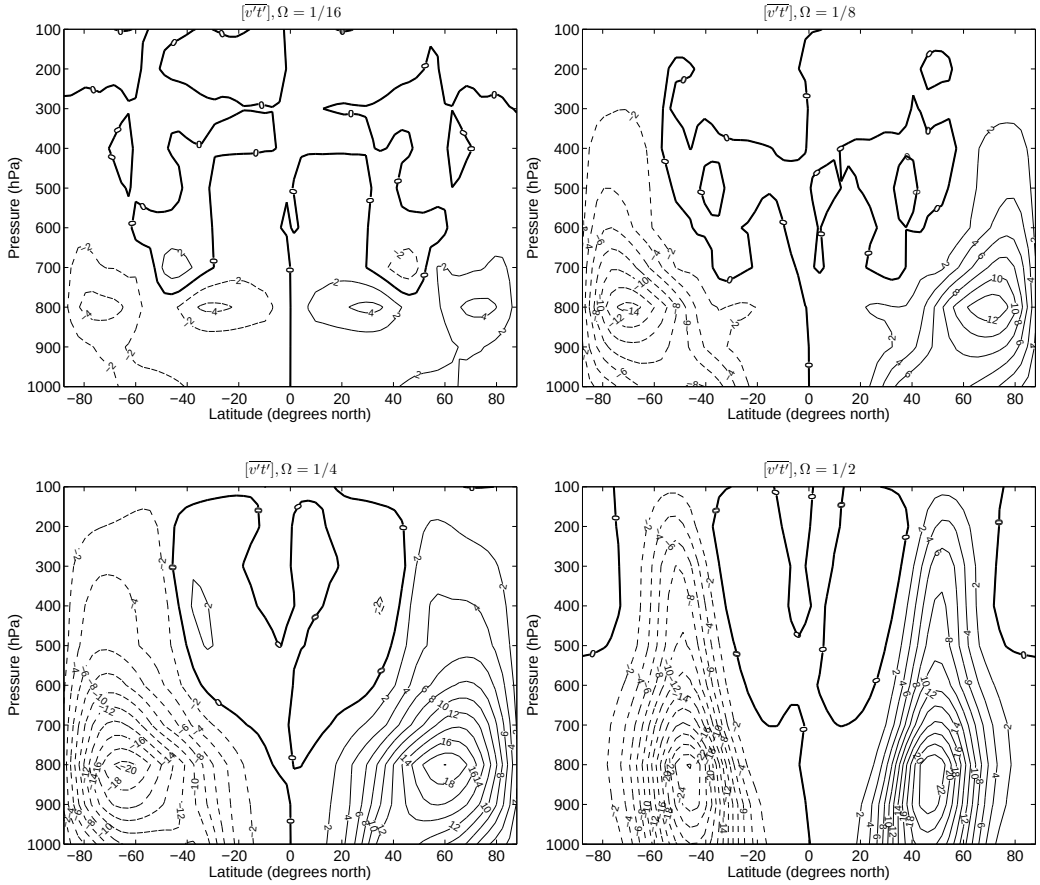

Figure 4.2: Zonal and temporal mean of meridional eddy heat flux $v'T'$ for experiments with $\Omega^* = 1/16, 1/8, 1/4, 1/2$. Unit: K ms^{-1}.

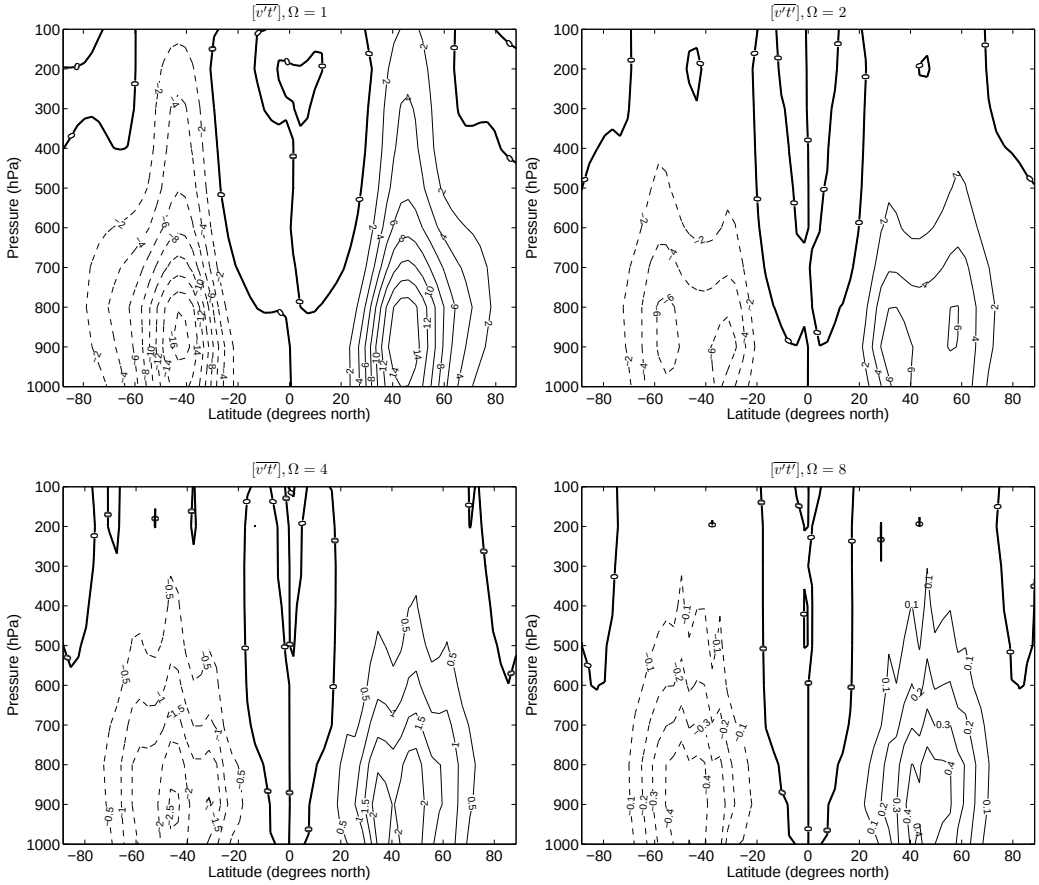

Figure 4.3: Zonal and temporal mean of meridional eddy heat flux $v'T'$ for experiments with $\Omega^* = 1, 2, 4, 8$. Unit: K ms^{-1}.

sphere is characterised by eddies and waves rather than quasi-axisymmetric circulation cells), the areal and mass average of $v'T'$ over the whole globe is not informative. One way to obtain a more insightful estimate of the gross effect of $v'T'$ is to calculate its average weighted by $\partial[u]/\partial y$:

$$\langle v'T' \rangle = \frac{\int [\overline{v'T'}] \frac{\partial[\overline{u}]}{\partial y} \mathrm{d}m}{\int \frac{\partial[\overline{u}]}{\partial y} \mathrm{d}m}, \tag{4.1}$$

where overbar denotes time average, and square brackets denote zonal average.

The sensitivity of this appropriately defined meridional eddy heat flux $\langle v'T' \rangle$ to changes of rotation rates is shown in Fig. 4.4 (blue squres). It can be seen that as rotation rate decreases from $\Omega^* = 8$, the strength of meridional eddy heat flux increases monotonically until it reaches its maximum at $\Omega^* = 1/2$, indicating the prominence of baroclinic eddies at this rotation rate. As the rotation rate decreases further below $\Omega^* = 1/2$, meridional eddy heat flux becomes less intense, indicating that the global circulation is dominated by meridional overturning Hadley cells which extend far into the high-latitudes at slow rotation rates.

A nondimensional measure of the atmospheric heat transport efficiency can be defined as the following:

$$E_h = \frac{\langle \partial_z \theta_e / \partial_y \theta_e \rangle}{\langle \partial_z \theta / \partial_y \theta \rangle}, \tag{4.2}$$

where $\langle \cdot \rangle$ is the global and temporal average, θ the potential temperature observed in the GCM results, θ_e the prescribed (equilibrium) potential temperature used by the Newtonian relaxation scheme, and ∂_z, ∂_y the vertical and meridional derivatives respectively. $\partial_z \theta_e / \partial_y \theta_e$ essentially represents the meridional isentrope slope of the restoration potential temperature field (i.e. the baroclinicity of the atmosphere). When dynamics is allowed to redistribute heat around the globe, the isentrope slope will be modified such that the energy can be converted from the form of (available)

potential energy into atmospheric kinetic energy. The more efficient the dynamic heat transfer, the lower the realised isentrope slope. Therefore, higher values of E_h correspond to more efficient atmospheric heat transfer. This diagnostic provides a nondimensional measure of the efficiency of dynamic heat transport, which redistributes heat not only along the meridional direction as reflected in Fig. 4.1, but also along the vertical direction. It should also be noted that E_h measures the total heat transport including the transport by both the meridional mean circulation (e.g. Hadley cell) and the eddies.

Fig. 4.4 (red circles) shows the comparison of E_h based on experiments with $\Delta T_{ep} = 60K$ at various rotation rates. It can be seen that fast rotation rates tend to inhibit the redistribution of heat by dynamical processes, which include direct meridional overturning circulation (Hadley cells) as well as non-axisymmetric waves and eddies. This trend is consistent with that shown in Fig. 4.1. Note that the downward trend is almost arrested around $\Omega^* = 1/4 - 1$, which indicates that the eddy heat transport tends to prevent the total heat transport from collapsing as rotation rate increases. This is similar to the findings of laboratory and numerical annulus experiments where nonaxisymmetric flows exhibit larger total heat transport than axisymmetric flows as rotation rate increases (Read (2003)).

4.2 Energy cycle and eddy generation mechanisms

4.2.1 Formulation of the Lorenz energy cycle

The generation and growth of eddies within terrestrial planetary atmospheres requires the conversion into eddy kinetic energy from other forms of energy in the background environment, the ultimate source of which is stellar irradiation. This process of energy conversion can be illustrated with the classic Lorenz energy cycle (Lorenz (1955)) which formulates the global mean atmospheric kinetic energy and available potential

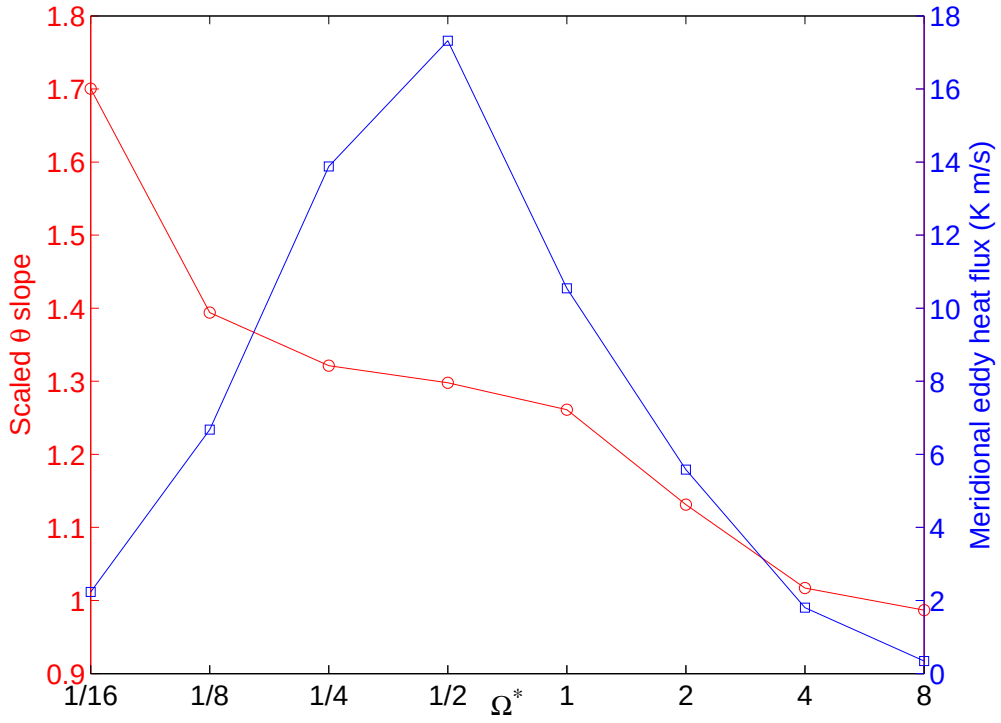

Figure 4.4: Globally mass-weighted average isentropic slope in latitude-height plane for experiments with different Ω, scaled by the corresponding mean isentropic slope of the equilibrium state that the model atmosphere relaxes towards.

energy, as well as the conversion rates between the zonal mean and eddy components of these energy forms. The globally averaged kinetic energy and available potential energy of the zonal mean and eddy parts of the atmosphere are defined as (James (1995)):

$$\mathrm{KZ} = \Big\langle \frac{1}{2}\overline{[u]^2} \Big\rangle, \tag{4.3a}$$

$$\mathrm{KE} = \Big\langle \frac{\overline{[u^{*2} + v^{*2}]}}{2} \Big\rangle, \tag{4.3b}$$

$$\mathrm{AZ} = \Big\langle \frac{h^2}{2s^2}\overline{[\theta_A]^2} \Big\rangle, \tag{4.3c}$$

$$\mathrm{AE} = \Big\langle \frac{h^2}{2s^2}\overline{[\theta^{*2}]} \Big\rangle, \tag{4.3d}$$

where KZ, KE, AZ, and AE refer to zonal mean kinetic energy, eddy kinetic energy, zonal mean available potential energy, and eddy available potential energy respectively. h and s are defined as:

$$h(p) = \frac{R}{p}\Big(\frac{p}{p_R}\Big)^{\kappa}, \; s^2 = -h(p)\frac{\partial \theta_R}{\partial p}.$$

θ_R is the global mean potential temperature so that $\theta(x, y, p, t) = \theta_R(p) + \theta_A(x, y, p, t)$. Overbar and brackets refer to temporal and zonal average. $\big\langle \cdot \big\rangle$ represents global mass and areal average such that

$$\big\langle Q \big\rangle = \frac{1}{4\pi a^2 g} \iiint Q \mathrm{d}m.$$

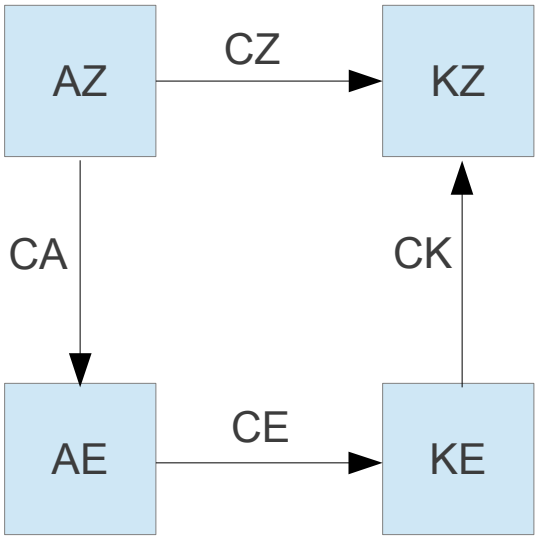

Figure 4.5: Schematic of Lorenz energy cycle. AZ: zonal mean available potential energy; AE: eddy available potential energy; KZ: zonal mean kinetic energy; KE: eddy kinetic energy.

Following Peixóto & Oort (1974), the conversion rates among these components (see Fig. 4.5) in pressure-coordinate can then be written as:

$$\mathrm{CE} = \Big\langle -g\Big(\overline{\frac{u'}{a\cos\phi}\frac{\partial Z'}{\partial\lambda}} + \overline{\frac{v'}{a}\frac{\partial Z'}{\partial\phi}} + \frac{\overline{u}^*}{a\cos\phi}\frac{\partial \overline{Z}^*}{\partial\lambda} + \frac{\overline{v}^*}{a}\frac{\partial \overline{Z}^*}{\partial\phi}\Big)\Big\rangle, \tag{4.4a}$$

$$\mathrm{CA} = \Big\langle -\frac{h^2}{s^2}\frac{\partial\overline{[\theta]}}{a\partial\phi}\overline{[v^*\theta^*]} - \frac{\partial}{\partial p}\Big(\overline{\frac{h^2}{s^2}[\theta]}\Big)\overline{[w^*\theta^*]}\Big\rangle, \tag{4.4b}$$

$$\mathrm{CZ} = \Big\langle \overline{[v]}g\frac{\partial\overline{[Z]}}{a\partial\phi}\Big\rangle, \tag{4.4c}$$

$$\mathrm{CK} = \Big\langle \overline{[u^*v^*]}\frac{\partial\overline{[u]}}{a\partial\phi} + \overline{[v'^2 + \overline{v}^{*2}]}\frac{\partial\overline{[v]}}{a\partial\phi} + \overline{[\omega^*u^*]}\frac{\partial\overline{[u]}}{\partial p} + \overline{[\omega^*v^*]}\frac{\partial\overline{[v]}}{\partial p} - \overline{[v]}\overline{[u'^2 + \overline{u}^{*2}]}\frac{\tan\phi}{a}\Big\rangle. \tag{4.4d}$$

There are at least two principal mechanisms of eddy generation within planetary atmospheres: barotropic instability and baroclinic instability. The physical pictures of these two different eddy-generation mechanisms can be clearly distinguished from the viewpoint of energy conversion. Eddies generated through barotropic instability are fed directly by the zonal mean kinetic energy, implying the conversion route

of KZ→KE to be important. Baroclinic instability, on the other hand, converts available potential energy into eddy kinetic energy through the so-called 'sloping convection', which corresponds to the conversion route of AZ→AE→KE. Therefore, the dominating mechanism of eddy generation can be appreciated by comparing the relative intensity and direction of CK and CE.

4.2.2 Experiment results

Fig. 4.6 shows the globally-averaged Lorenz energy cycles obtained from experiments with different rotation rates. In the rapidly-rotating experiments ($\Omega^* \geq 1/4$), the conversion route of KZ→KE is reversed, indicating that the atmosphere is barotropically stable in general. Eddies are generated predominantly by baroclinic instability, which is consistent with the significant meridional temperature gradient as shown in the previous section. In the slowly-rotating experiments ($\Omega^* < 1/4$), the direction of conversion between KZ and KE becomes KZ→KE, which suggests that barotropic instability begins to take a significant role in the eddy generation process. These slowly-rotating runs show a mixed barotropic-baroclinic form of instability, with barotropic instability gradually overtaking the baroclinic instability in generating eddies as rotation rate decreases (at $\Omega^* = 1/16$, the conversion into KE become dominated by the route KZ→KE), which is consistent with the observed weak meridional temperature gradient (i.e. weak baroclinicity) and strong horizontal wind shear in these experiments. The change of sign of CK at $\Omega^* = 1/4$ is consistent with the fact that thermal Rossby number $\mathcal{R}o$ begins to exceed 1 at this rotation rate (see Fig. 3.2).

The direct conversion between AZ and KZ also changes sign at $\Omega^* = 1/4$, which reveals the strengthening of Hadley cells as rotation rate is decreased. The Hadley cell, also known as the 'thermally direct' cell (driven directly by differential heating), converts the zonal mean available potential energy into kinetic energy of the zonal mean flow. Weak Coriolis force caused by slow rotation rate enables Hadley cells

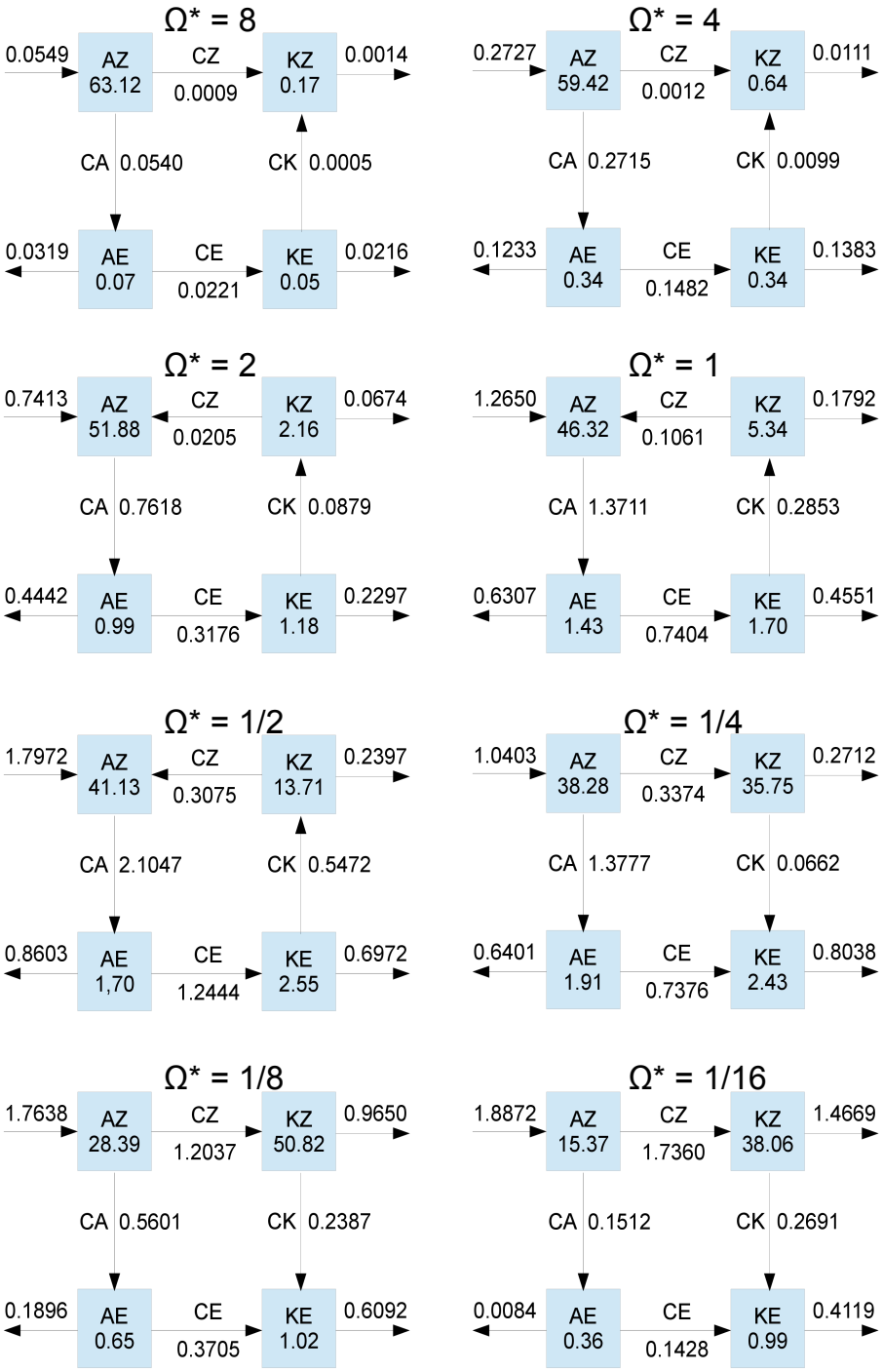

Figure 4.6: Lorenz energy cycles obtained from experiments with different rotation rates. Numbers in boxes represent globally averaged energy (in $10^5 \mathrm{Jm}^{-2}$). Conversion rates are in unit of Wm^{-2}.

to expand to higher latitudes and become dominant over the 'indirect' Ferrel cells, leading to the global mean conversion from AZ to KZ. The strength of baroclinic conversion rate CE reaches its maximum at $\Omega^* = 1/2$, which agrees with results from Del Genio & Suozzo (1987) in which baroclinic eddies peak in energy conversion efficiency at $\Omega^* = 1/2$, and is also consistent with the peak of meridional eddy heat flux at $\Omega^* = 1/2$ as shown in the red curve in Fig. 4.4. Note that the Rhines scale starts to exceed the planetary radius a at $\Omega^* = 1/4$ as rotation rate decreases, as shown in Table 3.1. As the Rhines scale represents the characteristic meridional width of baroclinic zone, atmospheres with rotation rate of $\Omega^* = 1/4$ or slower tend to have less well-developed baroclinic eddies, thus leading to the weaker eddy heat transport.

Chapter 5

Eddy scales, jet formation, and atmospheric macroturbulence

This chapter presents the studies on atmospheric macroturbulence, with a special focus on jet formation and the role of eddies. Section 5.1 describes the characteristic scales of eddies. Section 5.2 discusses the theories on geostrophic turbulence which have been considered as an idealisation of the atmospheric macroturbulence. Section 5.3 then shows the kinetic energy spectra based on PUMA-S experiments. The corresponding spectral transfer fluxes are shown in Section 5.4. Some comments and conclusions are summarised in Section 5.5.

5.1 Characteristic scales of eddies

Planetary atmospheres at the global scale are essentially fluids at very high Reynolds number ($Re = UL/\nu$), which means the corresponding flow is highly turbulent with eddies growing and interacting over a wide range of spatial and temporal scales. The study of how the eddies distribute energy/enstrophy with respect to these scales and what determines such a distribution has been pivotal to the community of turbulence research. Under the framework of the 3-D isotropic turbulence theory proposed by

Kolmogorov in 1941 (Kolmogorov (1941), later known as the K41 theory), eddies tend to break into smaller and smaller ones within an inertial range (the range of scales over which the fluid is assumed to be free from small scale dissipation and large scale anisotropic forcing). Later extended to 2-D turbulence by Kraichnan (1967), it is found that eddies in 2-D turbulence tend to merge with each other and cascade energy inversely to larger scales. Eddies in the Earth's atmosphere, however, turn out to follow neither of these two theories exactly and have a preferred spatial scale which is neither down to the viscous Kolmogorov scale, nor up to the whole globe (Boer & Shepherd (1983)).

The preferred scale can be more rigorously defined as the energy containing wavenumber n_e, based on the global barotropic eddy kinetic energy spectrum of the atmosphere (Schneider & Walker (2006)[1]):

$$n_e(n_e+1) = \frac{\sum\limits_n E_n}{\sum\limits_n \left[n(n+1)\right]^{-1} E_n}, \tag{5.1}$$

in which E_n is the barotropic eddy kinetic energy density at spherical harmonic wavenumber n, computed following Koshyk et al. (1999) for the components with non-zero zonal wavenumber.

Linear theories of baroclinic instability (Eady (1949), Charney (1947)) predict the characteristic eddy length scale to be the wavelength of the fastest growing unstable mode, which can be estimated by the first baroclinic Rossby deformation radius. But if nonlinear eddy-eddy interactions and the consequential inverse energy cascade are taken into account, the characteristic eddy length scale will be the scale at which the inverse energy cascade is inhibited[2]. This is shown to be characterised by the

[1] According to the argument made in Schneider & Walker (2006), using this -1 moment gives a better approximation of the observed energy containing wavenumber than the conventional first moment, since the former is closer to the maximum of the KE spectra of Earth's atmosphere and their series of simulations.

[2] Most previous literatures use the word "halted" , which is argued against by Sukoriansky et al. (2007) as discussed later in this chapter. We follow the argument of Sukoriansky et al. (2007) and

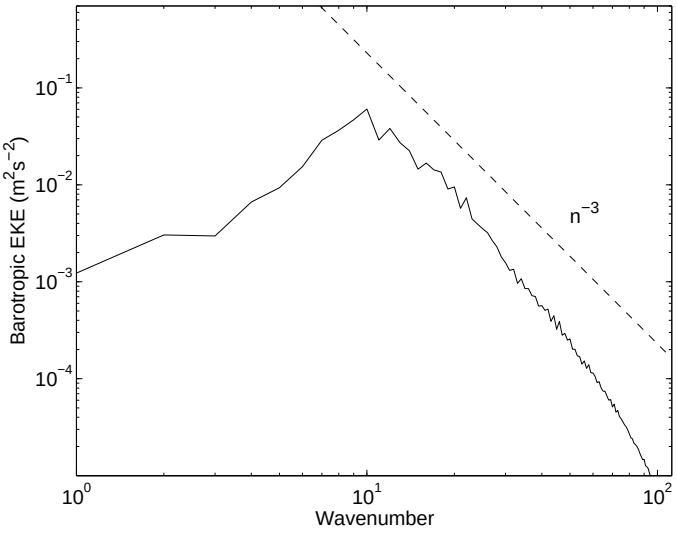

Figure 5.1: Barotropic eddy kinetic energy (EKE) spectrum of experiment with $\Omega^* = 1$. Dashed line represents the slope of -3.

so-called Rhines scale (Rhines (1975)), or the size of the whole domain if the Rhines scale exceeds the bound of the domain. It is therefore interesting to see how Rossby deformation and Rhines scales vary with the rotation rate in our experiments and whether there is a scale separation due to the potential cascade of kinetic energy.

Following Schneider & Walker (2006), the Rossby deformation radius is calculated as:

$$L_D = c_D \frac{NH}{f_0} = c_D \frac{N_p \Delta p}{f_0}, \tag{5.2}$$

where $N_p^2 = -(\overline{\rho}_s \overline{\theta}_s)^{-1} \overline{\partial_p \theta}^s$ is the static stability measure[3], Δp the pressure difference between tropopause and ground level, and ρ_s is the atmospheric density at the surface. Since it is the extratropical (baroclinic) Rossby deformation radius that is interesting to compare with, this deformation radius is averaged within the baroclinic zone whose boundaries are defined as the outermost latitudes at which the meridional heat flux $\overline{v'\theta'} \cos\phi$ at the near surface level (800 mb) exceeds 30% of its maximum value. The empirical constant c_D is chosen to be 1.35 following Schneider & Walker (2006).

use the word "inhibited" to indicate that inverse energy cascade is not completely stopped at the Rhines scale.

[3]Here N_p is estimated using near-surface quantities following the treatment of Schneider & Walker (2006). Using a vertically averaged value of N_p does not change the result significantly.

The Rhines scale is calculated as:

$$L_R = \sqrt{2U/\beta} = \frac{\mathrm{EKE}_{\mathrm{bt}}^{1/4}}{\beta^{1/2}}, \tag{5.3}$$

where U is the rms flow speed, and $\mathrm{EKE}_{\mathrm{bt}}$ is the barotropic eddy kinetic energy density.

The corresponding Rossby wavenumber and Rhines wavenumber can be defined as:

$$n_D(n_D+1) = a^2/L_D^2, \;\; n_R(n_R+1) = a^2/L_R^2.$$

Figs. 5.2-5.3 show the comparison of Rossby wavenumber n_D, Rhines wavenumber n_R and energy-containing wavenumber n_e based on experiments with fast rotation rates ($\Omega^* \geq 1/2$; experiments with slower rotation rates have L_R and L_D exceeding the planetary radius, thus are not shown). It can be seen that these three wavenumbers are almost identical to each other. This agrees with the results of Schneider & Walker (2006) in which they found that the simulated atmospheric macroturbulence tends to self-organise into a state of weak nonlinear eddy-eddy interactions with supercriticality $S_c \sim 1$. Here supercriticality is defined as a nondimensional measure of the slope of isentropes near the ground (see Schneider & Walker (2006)). As the Rhines wavenumber is close to the baroclinic Rossby wavenumber, inverse energy cascade via eddy-eddy interactions is largely inhibited, which is consistent with the fact that no well-defined $-5/3$ slope in barotropic eddy kinetic energy spectrum is observed in our experiments. According to Schneider (2004) and Schneider & Walker (2006), such self-organisation is done through the adjustment of the extratropical thermal stratification by baroclinic eddies, which is not allowed in the traditional quasi-geostrophic theories where the thermal stratification is taken to be fixed. This explains to some extent the historical success of linear or weakly nonlinear theories of dynamical meteorology for extratropical regions. It should be mentioned, however,

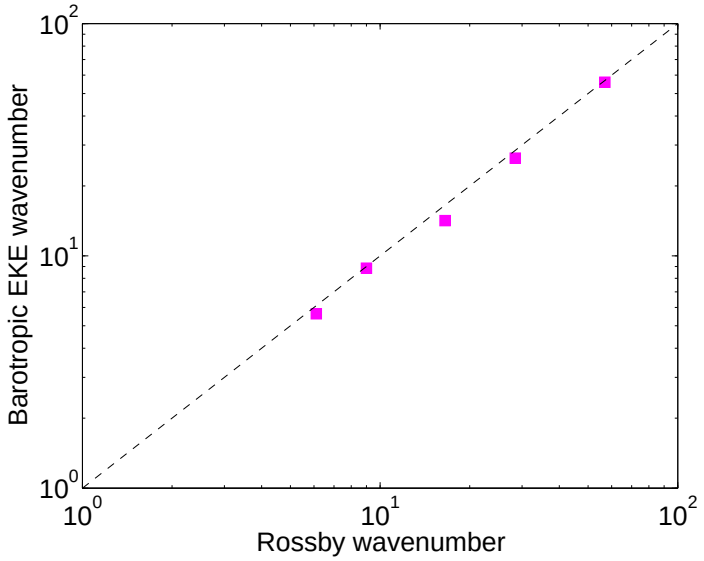

Figure 5.2: Energy-containing wavenumber of barotropic eddy kinetic energy (n_e) vs Rossby wavenumber (n_D) for experiments with $\Omega^* = 1/2, 1, 2, 4, 8$. $n_e = n_D$ along the dashed line.

that some recent studies find that the atmosphere can adjust into states with a supercriticality very different from 1 if the external forcings and planetary parameters are varied sufficiently (e.g. see Zurita-Gotor (2008), Jansen & Ferrari (2012)). Thus the results presented here and in Schneider & Walker (2006) are valid probably only within a subset of the parameter space.

5.2 Jet formation mechanism

As shown in Chapter 3, circulations featuring multiple zonal jets are found in experiments with small thermal Rossby numbers. This multiple-jet regime is very similar to the multiple jets observed in the atmospheres of Jovian planets (e.g. Jupiter and Saturn) as well as in terrestrial oceans. Despite the morphological similarity of the ubiquitous jets in Jovian atmospheres and terrestrial oceans, mechanisms underlying the formation and maintenance of these jets are not necessarily the same. Even for the case of Jupiter alone, at least two classes of conceptual models have been proposed trying to explain the existence of multiple jets at Jupiter's cloud level. These

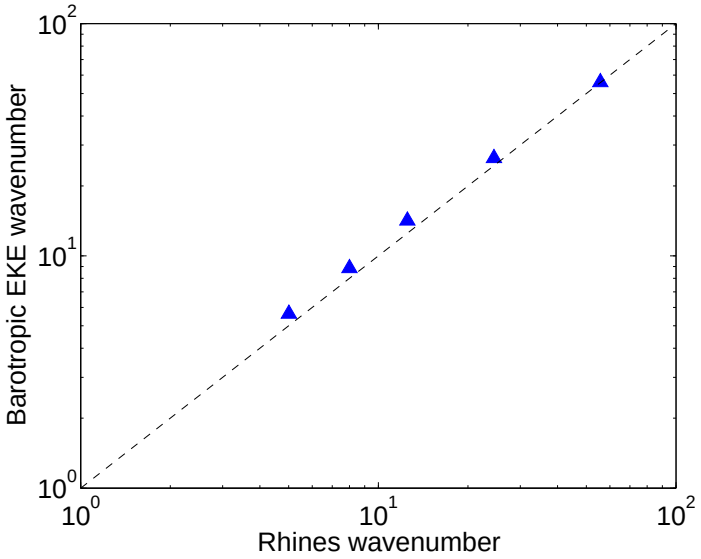

Figure 5.3: Similar to 5.2, but for n_e vs Rhines wavenumber (n_R). $n_e = n_R$ along the dashed line.

are the "shallow models" in which eddies within a shallow 'weather-layer' pump energy upscale into the zonal mean flow leading to the formation of jets confined to this weather-layer (e.g. see OGorman & Schneider (2008), Schneider & Liu (2009)), and "deep models" in which deep thermal convection drives nested Taylor-Proudman cylinders that manifest as jets at the cloud layer (e.g. see Busse (2002), Christensen (2001)). It should be noted that the following discussions will be focussed mainly upon the "shallow model" scenario which is more relevant to our terrestrial GCM experiments.

The concept of geostrophic turbulence, first introduced by Charney (1971), has been an important paradigm for theories of the large-scale planetary atmospheric and oceanic circulations. The flow in geostrophic turbulence tends to be a highly chaotic, quasi-2D (horizontal), quasi-geostrophic flow, featuring an inverse energy cascade if small-scale forcing is present. Planetary rotation, large aspect ratio (between horizontal vertical scales) and statically stable stratification all act to bring planetary atmospheric flows into quasi-horizontal (quasi-2D) motion. Small-scale forcing is usually envisaged as being provided either by baroclinic instability occuring at scales

comparable to the Rossby deformation radius (L_D) or by small-scale convection, as is possibly in the case of Jovian planets (see e.g. Ingersoll et al. (2000), Read et al. (2007)). The energy generated through such processes then becomes a small-scale "agitator" of the inverse energy cascade in the barotropic mode, though the precise mechanism for energising this mode is still not well understood. It is a typical feature of 2-D isotropic (in a 2-D planar sense, or horizontally isotropic) turbulence that energy goes from small scale to large scale through a spectrally-local inverse cascade. The direct consequence of such an inverse energy cascade is the emergence of large circular eddies with no preferred directionality. In the presence of a non-negligible background vorticity gradient (e.g. β-effect), however, it was shown by Rhines (1975) that such large-scale eddies becomes anisotropic, causing an elongation of structures in the zonal direction and ultimately leading to the formation of zonal jets. The characteristic latitudinal length scale of these jets can be estimated by the Rhines scale, as introduced in the previous section.

The Rhines scale is usually interpreted as a transitional scale between the regime of isotropic turbulence (featuring strongly non-linear eddy-eddy interactions) and a regime of quasi-linear Rossby waves. This can be understood via the vorticity equation for a barotropic fluid:

$$\frac{\partial \zeta}{\partial t} + \mathbf{v} \cdot \nabla \zeta + v\beta = 0. \tag{5.4}$$

The advection term, $\mathbf{v} \cdot \nabla \zeta$, is mainly responsible for the non-linear turbulent eddy-eddy interactions, and the β-effect term, $v\beta$, induces the Rossby wave propagation. If $\mathbf{v} \cdot \nabla \zeta \gg v\beta$, then the flow is dominated by 2-D turbulence. If $\mathbf{v} \cdot \nabla \zeta \ll v\beta$, then the flow manifests mainly as Rossby waves. If $\mathbf{v} \cdot \nabla \zeta \sim v\beta$, then a corresponding length scale can be revealed by $U^2/L^2 \sim \beta U$, which yields $L \sim \sqrt{U/\beta}$, the Rhines scale. For scales smaller than the Rhines scale, the nonlinear advection term dominates, leading

to 2-D turbulence. For scales larger than the Rhines scale, the β term dominates and the flow is characterised by Rossby waves. At scales much larger than Rhines scale, the Rossby wave frequency is therefore significantly larger than the turbulence frequency, making the wave/turbulence interactions very inefficient at cascading energy isotropically further towards larger scales. Thus in this sense the Rhines scale can be viewed as the scale at which the isotropic, spectrally-local inverse energy cascade is inhibited, and a pile-up of energy at the Rhines scale might be expected for flows in this 2-D non-divergent barotropic framework.

The anisotropisation of flow structures due to the β-effect is associated with the property of Rossby waves, the dispersion relation of which can be written as:

$$\omega = -\frac{\beta k_x}{k_x^2 + k_y^2} = -\frac{\beta \cos\alpha}{|\mathbf{k}|}, \tag{5.5}$$

where k_x, k_y are the zonal and meridional wavenumber respectively, and $|\mathbf{k}| = \sqrt{k_x^2 + k_y^2}$ the magnitude of wave vector $\mathbf{k} = (k_x, k_y)$. The Rhines wavenumber can be obtained by equating Rossby wave frequency ω to turbulence frequency $U|\mathbf{k}|$, which gives[4]

$$k_R^2 = \frac{\beta}{U}|\cos\alpha|. \tag{5.6}$$

Since the inverse energy cascade tries to pump energy to the smallest k_R, and k_R reaches 0 (minimum value) when $\alpha = \pm 90°$, the inverse cascade tends to favor the route of $\alpha = \pm 90°$. This corresponds to $k_x \ll k_y$, which is essentially a structure highly elongated along the zonal direction (See Vallis & Maltrud (1993)).

Although this classic 2-D non-divergent barotropic framework provides an elegant and insightful explanation of the jet formation via interactions between turbulence and Rossby wave, the real atmospheric jet formation does not follow exactly this

[4]Rhines wavenumber was initially denoted by n_R back in Section 5.1 in the context of spherical geometry. We will use k_R hitherto to represent Rhines wavenumber in general theoretical discussions and reserve n_R for specific discussions where spherical geometry is unambiguously present.

paradigm. In contrast to the picture of successive cascades of energy from small eddies to larger eddies and ultimately into the jets, an additional direct eddy-mean flow (or eddy-jet) interaction is found in practice to be primarily responsible for the upscale energy pumping from eddies into the jets in the context of Earth's atmosphere (see discussions on the weakly non-linear eddy-eddy interaction of terrestrial atmosphere in the previous section, and studies based on reanlysis data by Shepherd (1987) and Burgess et al. (2013)). In addition, a recent numerical study by Srinivasan & Young (2012) have shown that alternating zonal jets can be produced in a quasi-linear system in which nonlinear eddy-eddy interactions are essentially absent. This direct pumping of energy from eddies to the jet is closely related to the fundamental property of Rossby waves to transfer eddy momentum up-gradient (such that $[u^*v^*]\partial[u]/\partial y > 0$, see e.g. Held (2000)) towards the source of eddies (the jet).

The KE spectrum of fully developed turbulence is often observed to exhibit a power law structure over significant ranges of wavenumber, which manifests itself in constant slopes in the logarithmic KE spectrum. This may be an important indicator for distinguishing different turbulence regimes. Figs. 5.4-5.5 show schematic "cartoons" of KE spectra for 3-D and 2-D turbulence. If the classic 3-D isotropic turbulence (as investigated by Kolmogorov (1941)) has an inertial range associated with a forward energy cascade, its spectrum is typically characterised by a $-5/3$ slope. In contrast, 2-D turbulence may have an inertial range associated with an inverse energy cascade with the same $-5/3$ slope, together with another inertial range associated with a forward enstrophy cascade with a -3 slope.

Galperin and Sukoriansky (Sukoriansky et al. (2002), Galperin et al. (2006)) recently proposed the paradigm of *zonostrophic turbulence* as an attempt to characterise universally the regime of eddy-driven multiple zonal jets on a β-plane. Under a strong β-effect, it is proposed that flows can develop into the regime of zonostrophic turbulence which is characterised by a strongly anisotropic KE spectrum with a steep (-5)

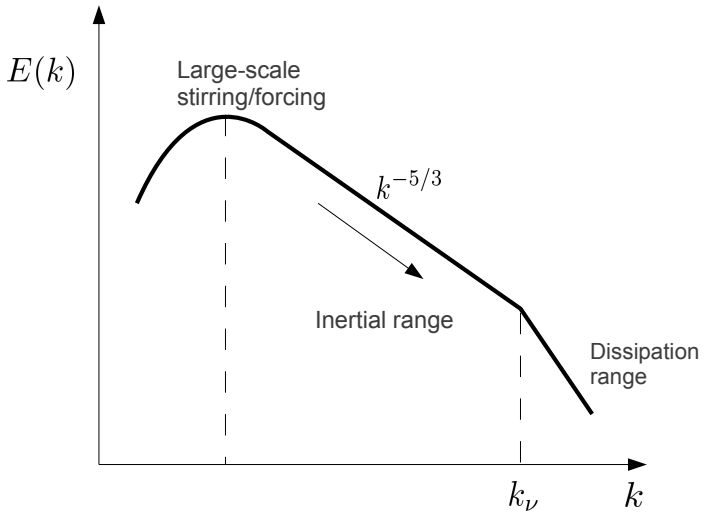

Figure 5.4: Schematic plot of the kinetic energy spectrum of 3-D turbulence. k_ν is the wavenumber representing the so-called Kolmogorov scale where viscous dissipation becomes predominant.

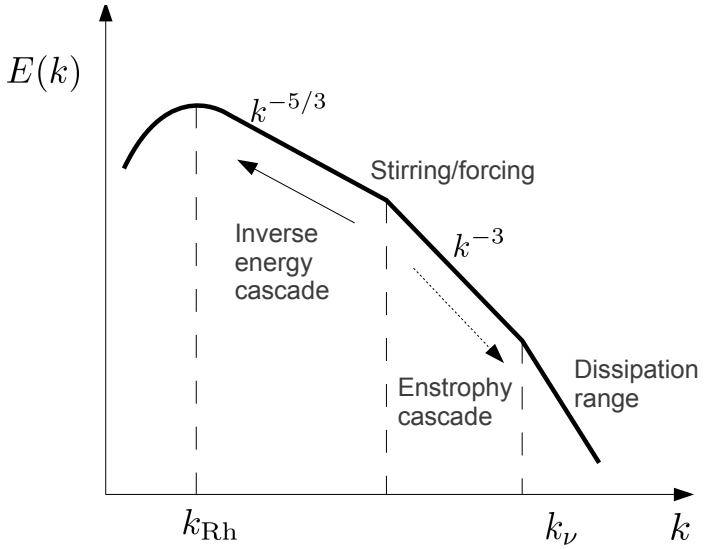

Figure 5.5: Same as Fig. 5.4, but for 2-D turbulence on a β-plane. k_{R} is the Rhines wavenumber at which the β-effect "halts" the inverse energy cascade.

slope for the zonally symmetric flow component and a classic Kolmogorov-Batchelor-Kraichnan (KBK) $-5/3$ slope in the non-axisymmetric eddy/residual modes (as shown in Fig. 5.6). The segments of the spectra in this regime take the universal form (when appropriately non-dimensionalised):

$$E_Z(n) = C_Z \beta^2 n^{-5}, C_Z \sim 0.5, \tag{5.7a}$$

$$E_R(n) = C_K \epsilon^{2/3} n^{-5/3}, C_K \sim 5, \tag{5.7b}$$

where ϵ is the energy pumping rate of the small-scale excitation (which, in the previous 2-D numerical studies of zonostrophic turbulence, is represented as an artificial energy input at a specific wavenumber n_ξ, see e.g. Huang et al. (2001) and Galperin et al. (2004). In a real planetary atmosphere, this can be due to barotropic or baroclinic eddies, or in the case of gas giants, possibly from small-scale moist convection as well.). C_K is the universal Kolmogorov-Kraichna constant, and C_Z can vary between 0.1 to 1.0, based on various 2-D barotropic simulations (e.g. Huang et al. (2001), Chekhlov et al. (1996)).

According to Sukoriansky et al. (2007), the β-effect can not really 'halt' or 'arrest' the inverse energy cascade at the Rhines wavenumber. Instead, it only makes the upscale energy transfer more anisotropic. The energy transferred into the large zonal modes is ultimately removed through the large-scale friction, which terminates the upscale energy transfer at a characteristic wavenumber n_{fr} as shown in Fig. 5.6.

The transitional wavenumber $n_\beta \sim (\beta^3/\epsilon)^{1/5}$, first revealed by Vallis & Maltrud (1993), is later shown (Sukoriansky et al. (2007), Galperin et al. (2006)) to be a better estimation than the Rhines wavenumber of the scale at which the upscale energy transfer becomes significantly anisotropic. Equating the zonal KE $E_Z \sim \beta^2 n^{-5}$ to the eddy/residual KE $E_R \sim \epsilon^{2/3} n^{-5/3}$, n_β can be revealed as the cross-over wavenumber at which the zonal KE spectrum and the eddy KE spectrum intersect. n_β is subtly

different from the Rhines wavenumber n_R in that n_R is deduced in the framework of unforced flow whereas n_β is a parameter defined specifically for flows continuously forced at a certain small scale (with non-zero upscale spectral transfer rate ϵ). If the small-scale forcing intensity is constant over time (as is the case in various 2D barotropic numerical model studies in which a zonostrophic turbulence regime is found), then n_β will be a stationary parameter whereas n_R will be time-dependent until the flow reaches a statistically steady state.

Since the ultimate large-scale energy removal in a statistically steady state in terrestrial-style model atmosphere is via a linear (typically Rayleigh) drag at the bottom, the arrest of the upscale energy transfer eventually occurs at the frictional wavenumber n_{fr} (defined as the scale where the eddy turnover time $\tau_t = n^{-1}/U(n) = [n^3 E(n)]^{-1/2}$ is comparable to the frictional damping time). It can be shown (Galperin et al. (2006)) that $n_{fr} \sim n_R$ at the statistically steady state as n_R can be essentially viewed as the 'moving energy front' in the spectral space in the unsteady flow (e.g. during the spin-up phase), which ultimately equilibrates at n_{fr} at the steady state. A $-8/3$ slope is shown in Fig. 5.6 at large wavenumbers ($n > n_z$) of the zonal KE spectrum, which is due to the isotropisation of the KE spectrum at small-scales.

The scale separation between n_β and n_R (n_{fr}) as shown in Fig. 5.6 defines a region of strongly anisotropic upscale energy transfer, which Galperin and coworkers refer to as the *zonostrophic inertial range* (though the strict definition of inertial range requiring a constant energy cascade rate is probably not satisfied within this spectral region). If friction is very strong such that $n_{fr} \sim n_\beta$, the zonostrophic inertial range then disappears and the flow is classified as being in a *friction-dominated* regime. Galperin & Sukoriansky (2010) introduced the zonostrophy index $R_\beta = n_\beta/n_R$ to distinguish such regimes, and demonstrated that flows with $R_\beta > 2.5$ will develop the characteristic structures associated with zonostrophic turbulence.

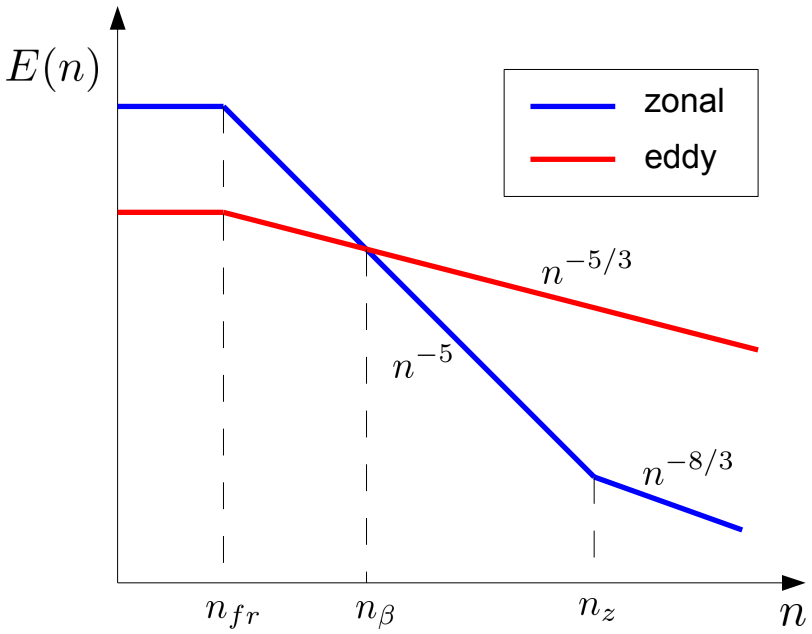

Figure 5.6: Schematic diagram of the KE spectrum of zonostrophic turbulence regime. Blue and red lines represent the zonal and eddy (residual) KE spectra respectively.

5.3 Kinetic energy spectra

In the following subsection, the KE spectrum is employed as the major diagnostic to reveal insights into the jet formation mechanism. Since current theories relevant to atmospheric macroturbulence are predominantly 2-D (as discussed in the previous section), we will focus on the barotropic component of the global KE spectrum. Following Koshyk et al. (1999), the vertically and temporally averaged horizontal KE on a certain pressure level can be calculated by

$$\overline{E_n(p,t)} = \frac{1}{4}\frac{a^2}{n(n+1)}\sum_{m=-n}^{n}\left(\overline{|\zeta_n^m|^2} + \overline{|\delta_n^m|^2}\right), \tag{5.8}$$

where a is the planetary radius, ζ_n^m and δ_n^m the spherical harmonic coeffients of vorticity ζ and divergence δ respectively, n and m the total and zonal wavenumber respectively, and the overbar denotes the time average.

The KE spectrum can be further decomposed into a zonal mean KE spectrum

and an eddy (or residual) KE spectrum as the following:

$$\begin{aligned}\overline{E_n^Z(p,t)} &= \frac{1}{4}\frac{a^2}{n(n+1)}\left(\overline{|\zeta_n^0|^2} + \overline{|\delta_n^0|^2}\right), \\ \overline{E_n^R(p,t)} &= \frac{1}{4}\frac{a^2}{n(n+1)}\sum_{m=-n}^{n}\left(\overline{|\zeta_n^m|^2} + \overline{|\delta_n^m|^2}\right), m \neq 0\end{aligned} \tag{5.9}$$

where E_n^Z and E_n^R represent the zonal and eddy (residual) part of the spectrum respectively.

Fig. 5.7 shows the KE spectrum of the run with $\Omega^* = 1$, the terrestrial scenario. The total KE spectrum (the black curve) demonstrates the classic -3 slope between $n = 10 - 30$, which is consistent with various previous studies based on observational/reanlysis datasets of Earth's atmosphere (see Boer & Shepherd (1983), Koshyk et al. (1999)), indicating the possible existence of a forward enstrophy cascade inertial range. The zonal spectrum is characterised by a much steeper -5 slope, which is still not well-understood despite the prediction of a -5 slope in the early work of Rhines (1975). Rhines shows that near the cross-over scale from Rossby waves to turbulence (i.e. near the Rhines wavenumber k_β), the typical wind speed is $U \sim \beta/k^2$. Since $E = kE(k) = 1/2U^2$, the -5 power law can then be revealed as $E(k) \sim \beta^2 k^{-5}$. But this does not explain the extended -5 slope in the zonal KE spectrum. A study by Huang et al. (2001) indicates that the -5 slope associated with the zonal KE spectrum can be qualitatively explained by the stabilisation effect of β on the zonal jets. According to Huang et al. (2001), the β-effect modifies the necessary condition of barotropic instability from $[u]_{yy} = 0$ to $\beta - [u]_{yy} = 0$ somewhere in the flow domain. This means the stability criterion is eased by the β-effect from $[u]_{yy} \neq 0$ to $\beta - [u]_{yy} \neq 0$, which allows the existence of velocity inflection points ($[u]_{yy}$=0) and enables more energy to reside in the zonal modes without violating the stability criterion. But this does not fully explain why a -5 slope is favoured over any other steep slope as observed here, which leads to the speculation of whether

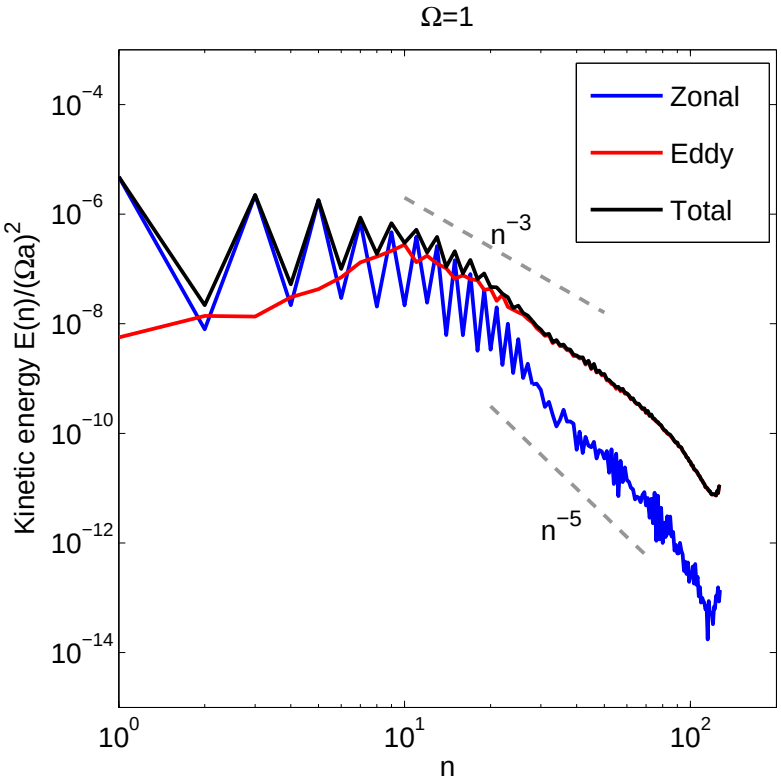

Figure 5.7: KE spectrum with respect to spherical wavenumber n for the experiment of $\Omega^* = 1$ with horizontal resolution T127, scaled by $\Omega^2 a^2$. Black curve represents the total KE spectrum, blue curve the zonal spectrum, and red curve the eddy spectrum. Grey dashed slope lines represent the corresponding power-laws as indicated.

a well-defined power-law scaling relationship even exists for the zonal KE spectrum (Danilov & Gurarie (2004)).

Figs. 5.8-5.9 show the KE spectra of the regime of multiple zonal jets. The strong zigzag feature of the zonal KE spectrum at small spherical wavenumbers is due to the hemispheric symmetry of the predominantly zonal structures across the globe. The classic $-5/3$ slope of an inverse energy cascade can not be found, indicating the picture of 2-D isotropic turbulence may not be applicable to the multilple jet formation of this regime. The -3 slope can still be found in the eddy KE spectrum, similar to the terrestrial scenario (irregular baroclinic regime). As shown in Section 5.1, the energy-containing wavenumber, Rossby deformation wavenumber, and the Rhines wavenumber appear to coalesce into one scale in this regime. Such lack of

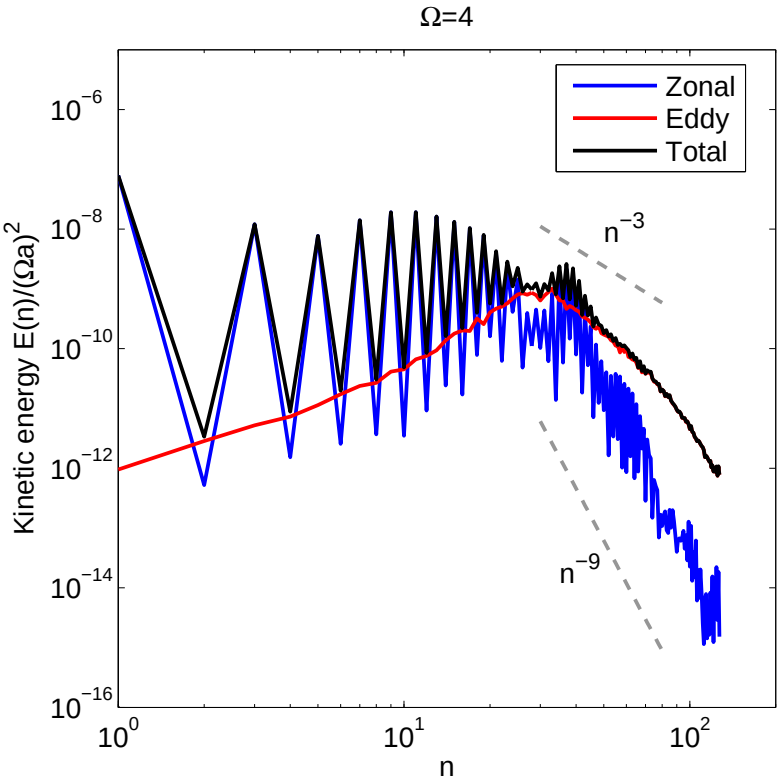

Figure 5.8: Same as Fig. 5.7, but for the experiment of $\Omega^* = 4$.

scale separation suggests the inverse energy cascade through eddy-eddy interactions has been greatly suppressed. The zonal KE spectrum demonstrates a much steeper -9 slope than the -5 slope as observed in the terrestrial scenario. This can be qualitatively understood following the arguments of Huang et al. (2001) that the stronger β-effect of the $\Omega^* = 4$ and 8 experiments allows more energy to stay in the zonal modes compared to the $\Omega^* = 1$ experiment without violating the stability criterion. But a quantitative explanation of the -9 power-law has not been established at this stage.

The lack of the KBK $-5/3$ slope in the KE spectra of the above experiments implies that nonlinear eddy-eddy interactions are greatly suppressed in these experiments, leading to atmospheric circulation states reminiscent of the findings of Schneider & Walker (2006) with n_e, n_D and n_β all at roughly the same scale. But if the surface friction is made weaker, the nonlinear eddy-eddy interactions, as well as

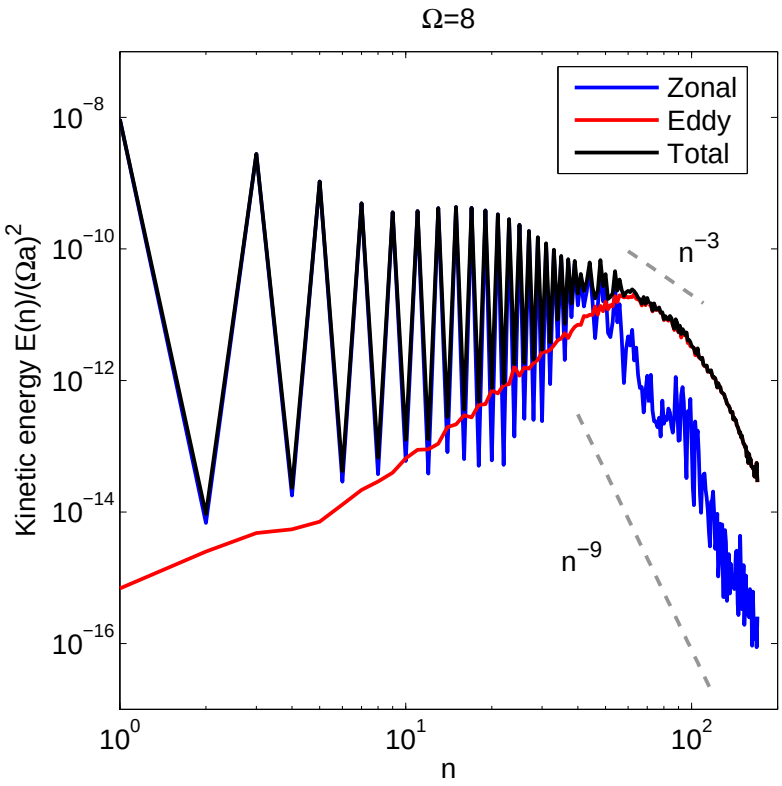

Figure 5.9: Same as Fig. 5.7, but for the experiment of $\Omega^* = 8$ with horizontal resolution of T170.

a $-5/3$ slope in the residual spectrum can indeed be observed. Fig. 5.10 shows the KE spectrum decomposed into zonal and eddy/residual components obtained from an experiment with $\Omega^* = 1$ and permanent January thermal forcing, at a much weaker surface frictional damping. The permanent January forcing breaks the meridional symmetry of the annual mean forcing and thereby eliminates the strong "zigzag" feature in the previous shown zonal KE spectra. The overall configuration of the KE and eddy spectra resembles the zonostrophic regime as shown in the schematic plot of Fig. 5.6, with a well-defined KE inertial range with a $-5/3$ slope between $n = 6$ and $n = 30$ in the eddy spectrum and a steeper (-5 slope) zonal spectrum within the same spectral region. Dashed lines with slopes of -5 and $-5/3$ are plotted following Eqs. (5.7a)-(5.7b) with $C_Z = 0.15$, $C_K = 5.0$. This immediately leads to an estimation of the inertial energy cascade rate of $\epsilon \sim 0.6 \times 10^{-6}\mathrm{m}^2\ \mathrm{s}^{-3}$. The transitional wavenumber n_β can be obtained by equating Eqs. (5.7a) and (5.7b). Adopting these values of C_Z, C_K and ϵ we get $n_\beta \simeq 16.35$, which is close to the crossover wavenumber as shown in Fig. 5.10.

The Rhines wavenumber n_R can be estimated following the approach discussed in Section 5.1, which gives $n_R \simeq 6.28$ in this case. Thus there is now a well-defined scale separation between $n_R \simeq 6.28$ and $n_\beta \simeq 16.35$ which enables the existence of a so-called 'zonostrophic inertial range'. Galperin & Sukoriansky (2010) introduced an approximate chain inequality as a quantitative criterion for the occurrence of a zonostrophic regime:

$$n_\xi \gtrsim 4n_\beta \gtrsim 10n_R \gtrsim 40. \tag{5.10}$$

This is satisfied at least partially, given the values of $n_R = 6.28$ and $n_\beta = 16.35$. The scale of n_ξ, which has a clear definition in numerical 2-D barotropic models energised at a particular scale, however, does not have straightforward explanation in our experiment.

For multiple-jet regimes, zonostrophy-like KE spectra can also be obtained if sur-

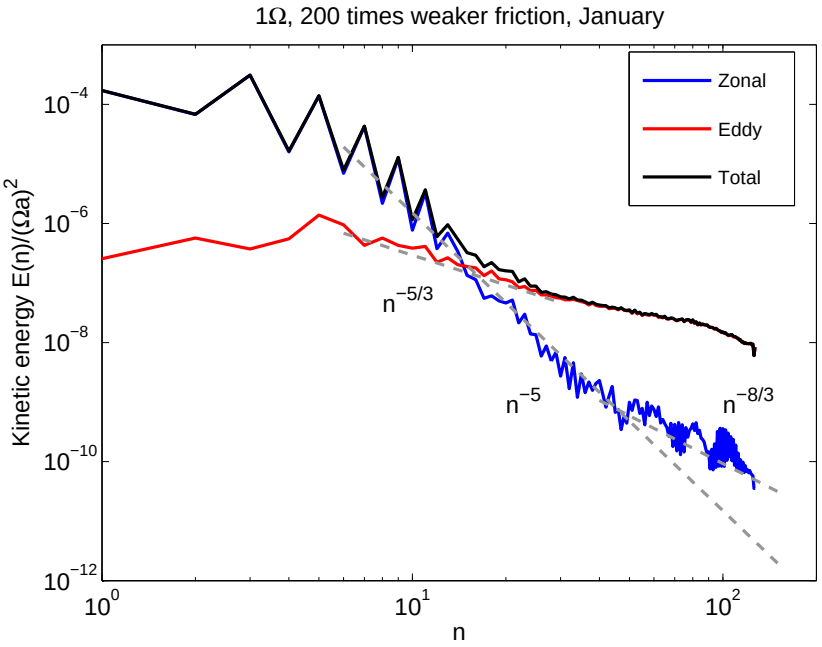

Figure 5.10: Vertical and temporal mean KE spectrum (scaled by $\Omega^2 a^2$) of the experiment with $\Omega^* = 1$ and permanent January forcing. Surface frictional damping timescale τ_f is increased 200 times to a value of 200 Earth days in the planetary boundary layer. Slopes of $-5/3$, -5 and $-8/3$ are plotted as grey lines, in which the -5 slope follows Eq. (5.7a) with $C_Z = 0.15$ and the $-5/3$ slope follows Eq. (5.7b) with $C_K = 5$ and $\epsilon = 7.17 \times 10^{-8}\mathrm{m}^2\ \mathrm{s}^{-3}$

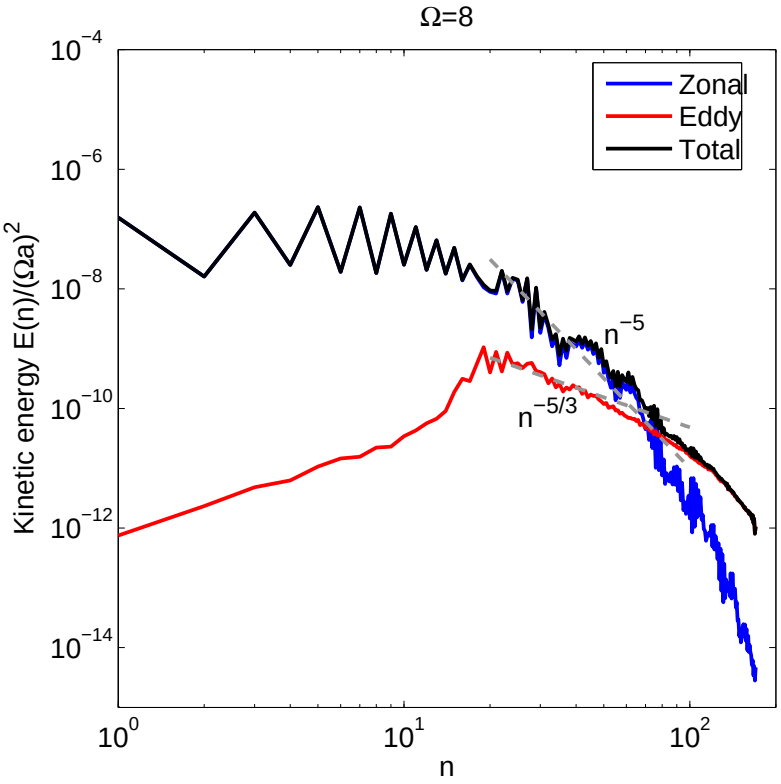

Figure 5.11: Same as Fig. 5.10, but for experiment with $\Omega^* = 8$. $C_Z = 0.1$ and $C_K = 5.0$ is assumed to plot the grey lines of -5 and $-5/3$ slopes.

face friction is made weak enough. Fig. 5.11 shows the KE spectra of the experiment with $\Omega^* = 8$ at the same strength of weak surface friction as the experiment shown in Fig. 5.10. An apparent zonostrophic range can now be found between $n = 20$ and $n = 50 \sim 60$, corresponding to an estimated spectral energy transfer rate $\epsilon \simeq 2.45 \times 10^{-8}\mathrm{m}^2\ \mathrm{s}^{-3}$.

Snapshots of the zonal wind with respect to latitude and longitude can provide intuitive pictures of how the flow field differs between the apparently zonostrophic regime and the weakly nonlinear (friction-dominated) regime. Figs. 5.12-5.13 show a comparison of mid-tropospheric wind field between zonostrophic and friction-dominated flows, with rotation rates of $\Omega^* = 1$ and $\Omega^* = 8$. It is clear that weaker friction enables the atmospheric circulation to become more "zonal", compared to the meandering jet scenario observed in experiments with strong friction. The effect

of surface friction on the flow "zonation" can be related to the hypothesis of the "barotropic governor" (James & Gray (1986), and James (1987)), which describes a mechanism that might be responsible for the effect of surface friction on the baroclinic lifecycle. According to the GCM experiments by James & Gray (1986) and the two-layer analytic study by James (1987), weak surface friction enables larger barotropic (horizontal) shear to develop in a baroclinic atmosphere, which in turn supresses the growth rate of the most unstable baroclinic modes, leaving the final state to be a wave-free atmosphere that is relatively stable to baroclinic perturbations. Such a counter-intuitive paradigm, in which weak (rather than strong) frictional damping suppresses baroclinic eddy activity, is called the "barotropic governor" since it is the enhanced barotropic shear that inhibits the baroclinic eddy growth and governs the evolution and the consequential equilibrated state of the atmosphere. The supression of growth rates of the most unstable baroclinic mode can be understood easily in a qualitative approach. The spatial structure of the most unstable baroclinic mode within an unsheared background flow is an optimal configuration to extract available potential energy from the mean flow and convert that into kinetic energy. Adding shear to the background flow therefore tends to reduce the efficiency of such baroclinic energy conversion. The specific mechansim of this reduction of efficiency through, e.g. meridional confinement of the most unstable baroclinic mode, is illustrated in a two-layer analytic model in James (1987).

It should be noted that the link between our experiment results and this "barotropic governor" mechanism needs to be supported by further diagnostics, e.g. the growth rates of the baroclinically most unstable mode under various strength of surface friction, as well as the corresponding Lorenz energy cycles. It will be very interesting to reveal the potential role of "barotropic governor" in the development and maintenance of zonostrophic turbulence based on such diagnostics.

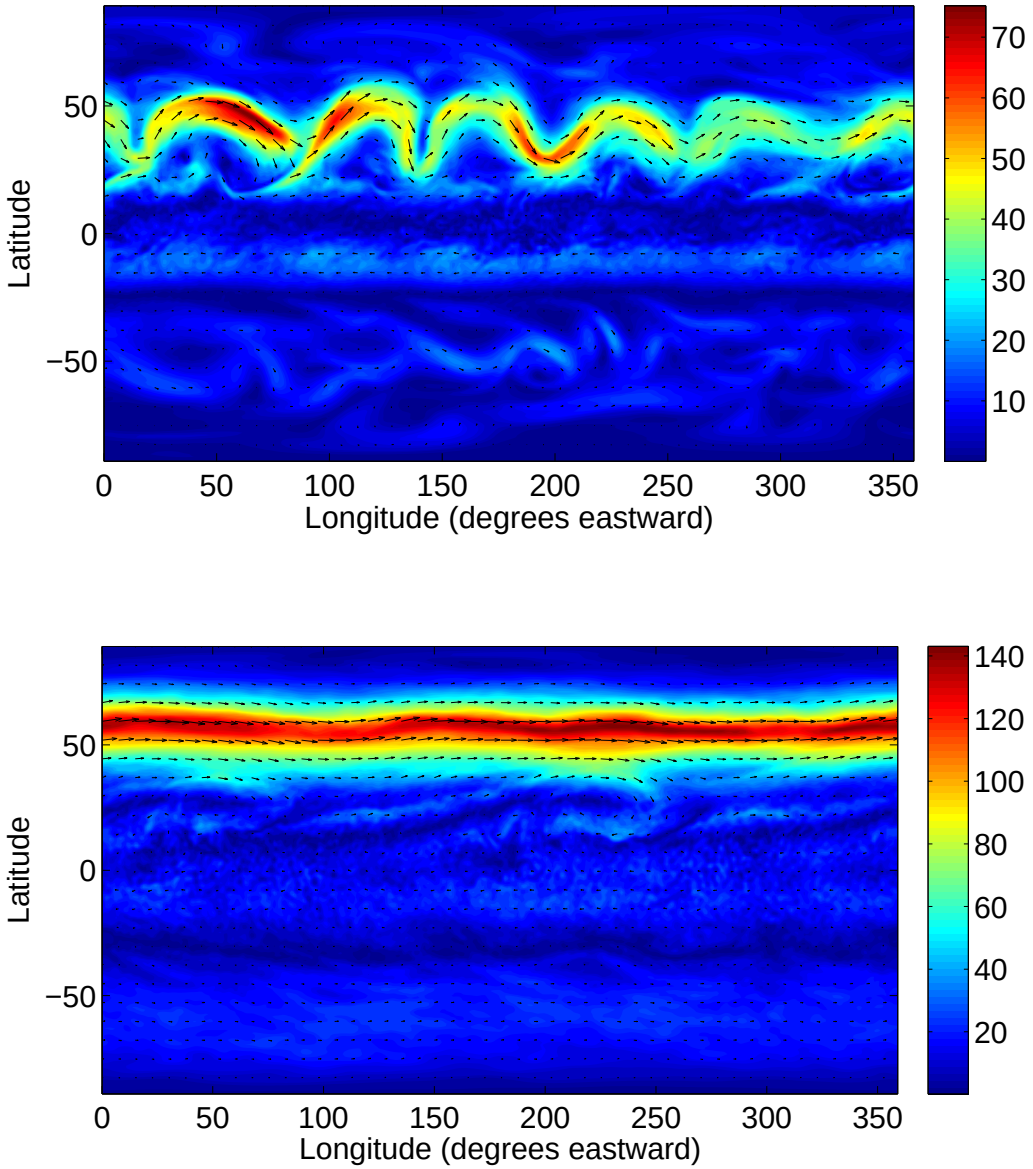

Figure 5.12: Zonal wind vector at 500mb and its magnitude $\sqrt{u^2 + v^2}$ (color) of the experiment with normal friction (above) and 200 times weaker friction (below).

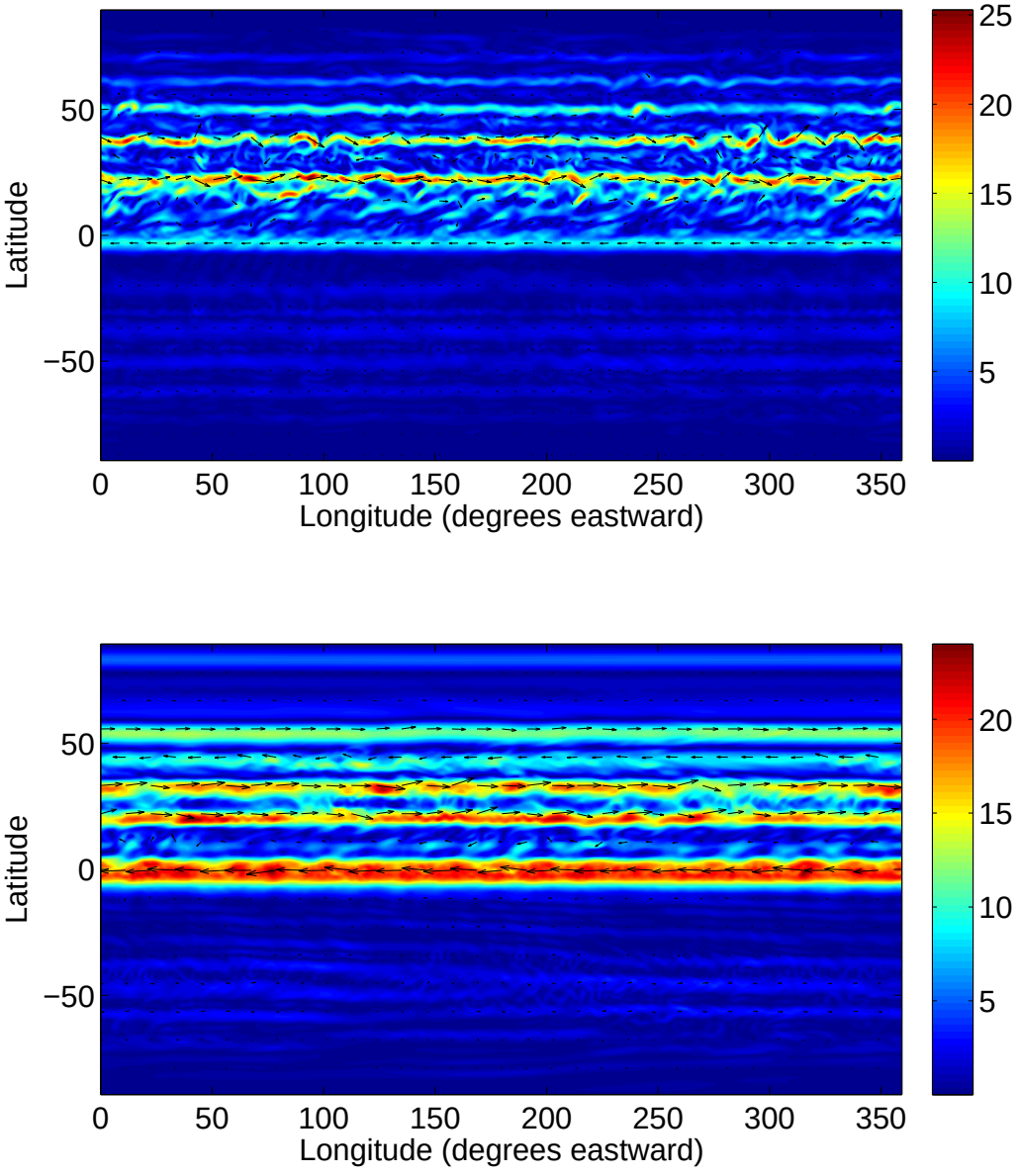

Figure 5.13: Same as Fig. 5.12 but for $\Omega^* = 8$.

5.4 Spectral transfer fluxes of KE and enstrophy

Although power-law slopes observed in the KE spectrum provide encouraging evidence which suggests that the model atmospheric circulations may be demonstrating some features of idealised 2-D turbulence, it should be noted that the existence of a power-law alone cannot provide conclusive insights into the direction of energy/enstrophy cascade. The nonlinear spectral energy/enstrophy transfer flux (Boer & Shepherd (1983), Shepherd (1987), Burgess et al. (2013)) can provide more detailed insights into the energy/enstrophy redistribution among different wavenumbers through nonlinear eddy-eddy interactions. Starting from the vorticity equation

$$\frac{\partial \zeta}{\partial t} = -(\mathbf{v} \cdot \nabla)\zeta - \mathcal{D} \tag{5.11}$$

where $\mathbf{v} = (u, v)$ is the rotational velocity, $\mathcal{D}$ the effects on vorticity evolution due to divergence and other vorticity sources and sinks. Multiply by ζ to obtain the enstrophy equation ($G = \frac{1}{2}\zeta^2$)

$$\frac{\partial G}{\partial t} = -\zeta(\mathbf{v} \cdot \nabla)\zeta - \zeta\mathcal{D}. \tag{5.12}$$

In spectral space this can be rewritten as

$$\frac{\partial G_n}{\partial t} = J_n + \mathcal{D}_n \tag{5.13}$$

where the interaction term J_n is

$$J_n = -\frac{1}{4} \sum_{m=-n}^{n} \left[\zeta_n^{m^*} (\mathbf{v} \cdot \nabla\zeta)_n^m + \zeta_n^m (\mathbf{v} \cdot \nabla\zeta)_n^{m^*}\right] \tag{5.14}$$

The corresponding kinetic energy interaction term I_n can be defined similarly and is related to the enstrophy interaction term J_n by

$$I_n = \frac{a^2}{n(n+1)} J_n \tag{5.15}$$

where a is the planetary radius. Note that interaction terms only redistribute KE and enstrophy among wavenumbers so

$$\sum_{n=0}^{N} I_n = 0 = \sum_{n=0}^{N} J_n.$$

We can then define KE flux and enstrophy flux as

$$\mathcal{F}_{n+1} = -\sum_{l=0}^{n} I_l, \text{ and } \mathcal{H}_{n+1} = -\sum_{l=0}^{n} J_l, \tag{5.16}$$

respectively, where the minus sign is adopted conventionally such that a positive value corresponds to a forward energy/enstrophy cascade while a negative value corresponds to an inverse cascade.

The key to obtaining $\mathcal{F}$ and $\mathcal{H}$ is the calculation of J_n as in Eq. (5.14). Model output of streamfunction was used to calculate the rotational component of velocity. The SPHEREPACK 3.2 code package from CISL (Computational and Information Systems Laboratory)/NCAR was employed for the spherical harmonic transformation and spherical gradient calculations.

The interaction terms and spectral fluxes of KE and enstrophy can be further decomposed into contributions from eddy-eddy interactions and eddy-zonal flow interactions (Burgess et al. (2013)). Nonlinear interaction terms of enstrophy due to purely eddy-eddy interactions can be written as

$$J_n^{(e)} = -\frac{1}{4} \sum_{m=-n}^{n} \left[(\zeta')_n^{m^*} J(\psi', \zeta')_n^m + \mathbf{c.c.} \right] \tag{5.17}$$

where all primed quantities are eddy components with respect to zonal mean flow, $J(\psi', \zeta')$ is the Jacobian of geostrophic streamfunction ψ' and vorticity ζ', and **c.c.** represents the complex conjugate of the first term in square bracket. The contribution to J_n through eddy-zonal mean interactions is then simply $J_n^{(z)} = J_n - J_n^{(e)}$. Similarly, interaction terms of KE can be decomposed in the form of $I_n = I_n^{(z)} + I_n^{(e)}$. In this way, spectral flux of KE and enstrophy can be decomposed as $\mathcal{F}_n = \mathcal{F}_n^{(z)} + \mathcal{F}_n^{(e)}$ and $\mathcal{H}_n = \mathcal{H}_n^{(z)} + \mathcal{H}_n^{e}$.

Fig. 5.14 shows the decomposed spectral KE fluxes ($\mathcal{F}_n$), based on the experiment with weak friction at $\Omega^* = 1$, corresponding to the KE spectra of Fig. 5.10. By examining the total KE flux (black curve) alone, it can be found that the spectral region $n < 60$ is dominated by up-scale KE transfer, as indicated by the negative values of $\mathcal{F}_n$. The majority of this up-scale KE transfer is contributed by the eddy-zonal mean interaction (red curve), which is consistent with the physical picture of the highly zonal structures shown in Fig. 5.12. Contributions from pure eddy-eddy interactions, in contrast, play only a marginal role in this up-scale energy transfer.

Fig. 5.15 shows the decomposed KE spectral flux for the experiment with $\Omega^* = 1$ and normal friction. The up-scale KE transfer region ($2 < n < 16$) is consistent with the findings by Burgess et al. (2013), in which up-scale KE transfer is found in similar spectral ranges based on ECMWF's reanalysis datasets. The total KE transfer flux is mostly contributed by eddy-zonal mean interactions at lower wavenumbers. Figs. 5.16-5.17 show the corresponding KE flux for the experiments of $\Omega^* = 8$ with weak and strong friction. Similar to the cases with $\Omega^* = 1$, KE fluxes are dominated by up-scale transport within the spectral region of $n < 80$.

Figs. 5.18-5.19 show the spectral enstrophy flux ($\mathcal{G}_n$), based on the experiment of $\Omega^* = 1$ with weak and normal (Earth-like) friction. Under weak surface frictional damping, the atmosphere has a rather narrow range of forward enstrophy cascade ($\mathcal{G}_n > 0$) range, compared to the broad forward enstrophy cascade range in Fig. 5.19.

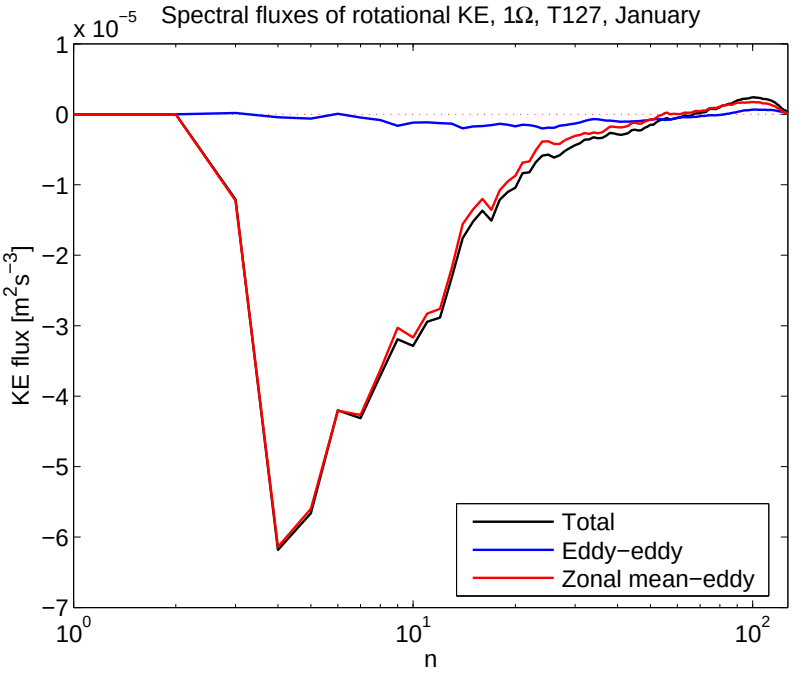

Figure 5.14: Spectral KE flux for the experiment with $\Omega^* = 1$, permanent January thermal forcing and 200 times weaker friction with frictional damping timescale of 200 Earth days in the planetary boundary layer (corresponding to the Spectra in Fig. 5.10).

According to Fjørtoft's theorem (Fjø rtoft (1953)), 2-D turbulence is more efficient at transferring energy up-scale and enstrophy down-scale than transferring energy down-scale and enstrophy up-scale. This narrow range of forward enstrophy cascade is indicative of the development of an up-scale energy cascade range within $n < 30$ which confines the enstrophy cascade range to higher wavenumbers.

5.5 Comments and discussions

The results shown in the previous section examine the jet formation mechanism in terms of KE spectra, with a particular attention to the paradigm of "zonostrophic turbulence" recently proposed by Galperin and coworkers as a potential candidate of universal regime for jet formation in various geophysical fluids including planetary atmospheres. The experiments presented in this chapter demonstrate that under

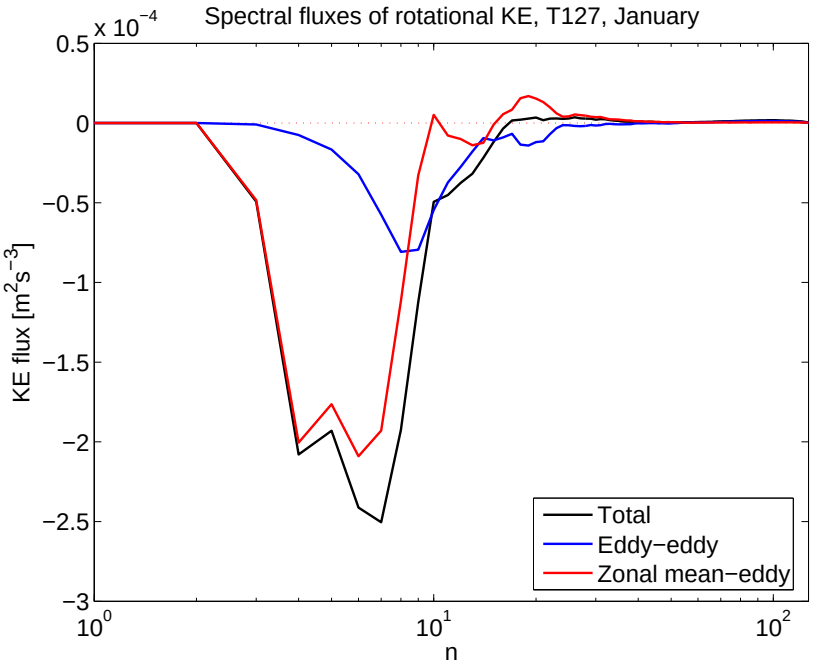

Figure 5.15: Spectral KE flux for the experiment with $\Omega^* = 1$, permanent January thermal forcing and normal (Earth-like) friction.

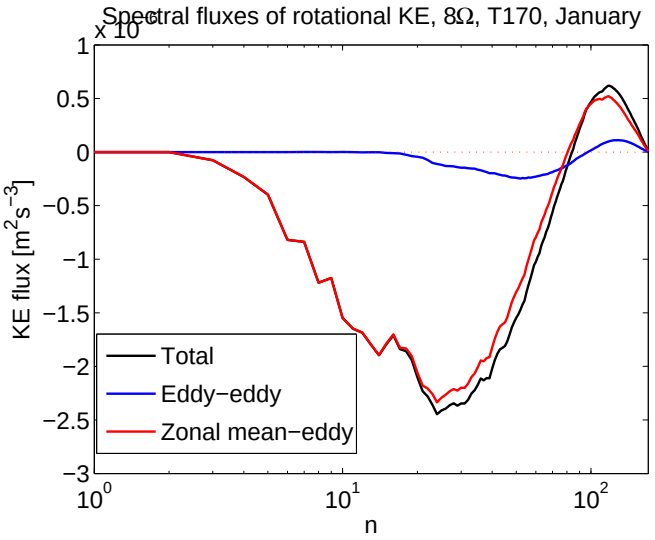

Figure 5.16: Spectral KE flux for the experiment with $\Omega^* = 8$, permanent January thermal forcing and 200 times weaker friction (corresponding to the Spectra in Fig. 5.11).

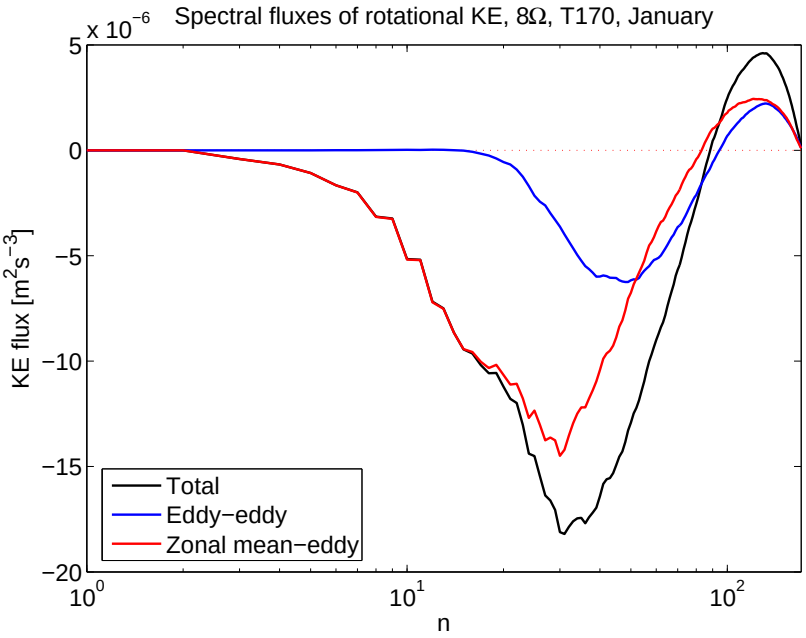

Figure 5.17: Spectral KE flux for the experiment with $\Omega^* = 8$, permanent January thermal forcing and normal friction.

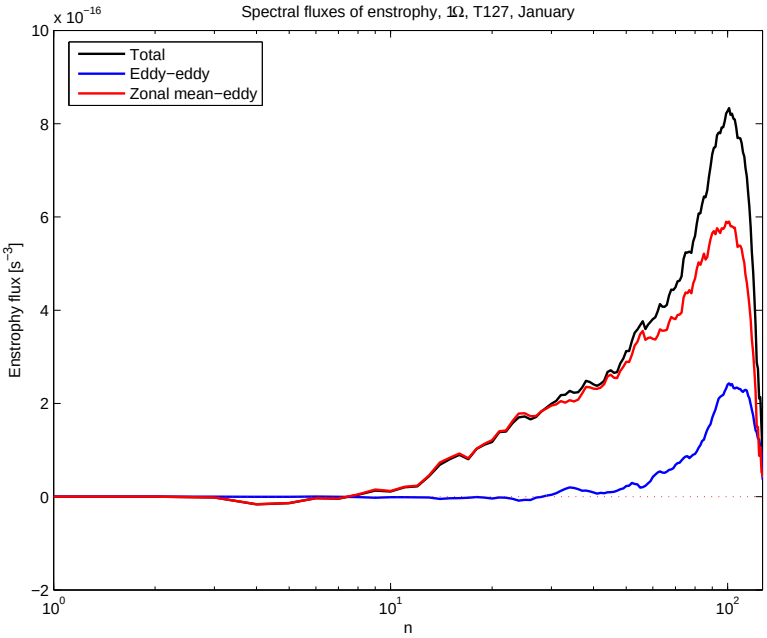

Figure 5.18: Spectral enstrophy flux for the experiment with $\Omega^* = 1$, permanent January thermal forcing and weak friction.

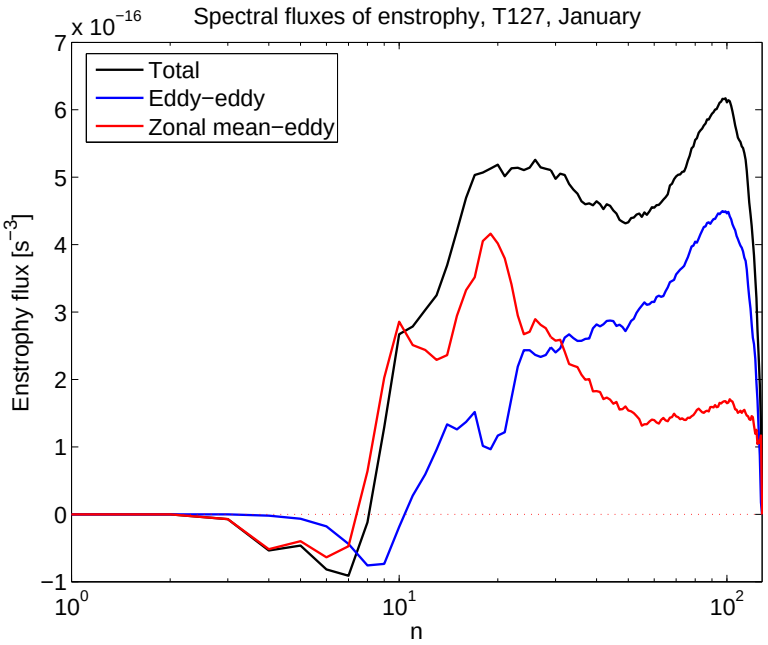

Figure 5.19: Spectral enstrophy flux for the experiment with $\Omega^* = 1$, permanent January thermal forcing and normal friction.

weak surface friction, the atmosphere does develop strongly coherent zonal jets with a highly anisotropic KE spectrum which shares many features in common with the zonostrophic turbulence regime (e.g. -5 and $-5/3$ slopes in the zonal and eddy KE spectra). However, eddy-driven jet streams can still be found with stronger surface friction, though in a weaker and more meandering/wavy form. This is consistent with the "barotropic governor" mechanism which indicates that weak frictional damping leads to stronger barotropic shear in the atmosphere, thereby suppressing the growth of baroclinic instability, and making the circulation equilibrate into a more zonally symmetric state.

It should be noted that the zonostrophic turbulence regime, as Galperin and coworkers have defined, is essentially a kind of anisotropic 2-D barotropic turbulence. Previous studies of this regime have usually employed barotropic numerical models with artificial energy input at a certain high wavenumber, which should be at best viewed as a highly idealised abstraction of a real baroclinic planetary atmosphere.

Linear theories predict that eddies generated via baroclinic instability tend to have their fastest growth rate near the scale of the Rossby deformation radius, though real eddy generation is by no means confined spectrally to such a narrow range as treated in these 2-D barotropic models. Besides, our spectral flux diagnostics imply that the up-scale/down-scale energy/enstrophy transfer is not completely inertial, since the spectral KE/enstrophy fluxes are not constant within the region of up-scale/down-scale transfer.

The lack of scale separation between Rhines wavenumber and Rossby wavenumber, as stated in Section 5.1, indicates that pure eddy-eddy interaction and the associated inertial range of inverse energy cascade is not an appropriate paradigm of the atmospheric macroturbulence. This is consistent with the discussions in Section 5.4 which demonstrates that the KE spectral transfer flux does not have any range of constant value. It is therefore concluded that the eddy-zonal mean flow interaction, characterised by the up-scale and spectrally non-local energy transfer from eddies to zonal jets, plays a major role for the maintenance of jets in the atmosphere.

Chapter 6

A two-band radiative-convective scheme and PUMA-G

As we stated in Chapter 1, the definition of thermal Rossby number $\mathcal{R}_o$ requires knowledge of the meridional temperature difference $\Delta\theta_h$, which is not an externally controllable parameter in GCM experiments. In PUMA-S, $\Delta\theta_h$ usually differs not too much from the imposed temperature difference of the relaxation temperature field. But when it comes to the modelling of planets with obliquities and atmospheric compositions different from those of the Earth, the prescribed specification of a relaxation temperature field and the associated timescales can be rather arbitrary and *ad hoc*. Therefore, in order to explore a parameter space which could include planetary parameters like obliquity and atmospheric opacities, it was desirable to use a more physically-based radiative-transfer scheme for diabatic heating/cooling effects to replace the Newtonian relaxation scheme. In this chapter, we present the description of a two-band semi-grey radiative-convective scheme suitable for this purpose in Section 6.1, whose properties are then illustrated by a 1-D column model. An analytic equilibrium solution (comparable to Guillot (2010)) to the radiative-transfer equation in this semi-grey model is derived in Section 6.2. A comparison of some results of

this model against the observed thermal structure of real planetary atmospheres of Earth, Mars and Venus is discussed in Section 6.3 to assess how well it can represent realistic thermal structures of known atmospheric systems. At the end of this chapter (Section 6.4), we demonstrate how this column model is coupled with the dynamical core of PUMA-S to make a new GCM (PUMA-G), as well as the comparison of its results with those obtained using PUMA-S.

6.1 Model physics

6.1.1 Radiative-transfer

The detailed process of radiative transfer in an atmosphere is highly complex and always poses a significant challenge to numerical modellers. Different gases in the atmosphere have different absorption and scattering signatures, at different wavelengths. In an ideal situation, line-by-line calculations can provide the most accurate representation of the radiative effect of each gaseous component in the atmosphere, but is computationally very demanding. Most GCMs take a more practical approach of grouping the individual absorption lines into several broad spectral bands each with a representative mean absorption coefficient, which saves a lot of computer resource. In our radiative-convective scheme here, we adopt a similar methodology and construct the simplest possible scheme with only two spectral bands, respectively representing a long-wave thermal radiation band (1.7$\sim$250 μm) and a short-wave stellar radiation band (0.1$\sim$5.0 μm). Furthermore, we assume that in each band the extinction coefficient is uniform with respect to the wavelength (i.e. the atmosphere is grey in each band — hence the term "semi-grey" is used). Scattering effects are only partially reflected in the constant extinction coefficient. For simplicity, we assume that there are no condensable constituents in the atmosphere, hence no cloud coverage. Radiatively active gases or aerosol absorbers are assumed to be well-mixed

in the vertical direction.

We use a 1-D model to describe and illustrate the characteristics of this radiative-convective scheme, in which only the atmospheric structure in the vertical direction is represented. Again for simplicity radiative transfer processes are modelled with the assumption of a plane parallel atmosphere, which regards the atmosphere to be a flat slab in which there are effectively only upward and downward beams of radiation. The diffusivity approximation (e.g. see Andrews (2010) and Vardavas & Taylor (2007)) is employed to express the Schwarzschild radiative transfer equations in their classical form:

$$-\frac{dF^{\uparrow}}{d\tau^*} + F^{\uparrow} = \pi B(T), \tag{6.1a}$$

$$\frac{dF^{\downarrow}}{d\tau^*} + F^{\downarrow} = \pi B(T). \tag{6.1b}$$

Here τ^* is a scaled optical depth. In our scheme, it is estimated following Ramanathan et al. (1985) as:

$$\begin{aligned} \tau^* &= \frac{1}{1.5 + 0.5/(1 + 4\tau + 10\tau^2)}\tau \\ &\equiv D\tau, \end{aligned} \tag{6.2}$$

in which

$$D \equiv \frac{1}{1.5 + 0.5/(1 + 4\tau + 10\tau^2)}$$

is known as the *diffusivity factor* representing the effect of integrating over a hemisphere. Some radiative transfer schemes use a constant value of diffusivity factor, like 3/2 (Goody & Young (1995)) or 1.66(Andrews (2010)) for example, to approximate the integration (which seems straightforward at first sight, but could be fairly tricky in practice[1]). Our approach here is more accurate than the single value approximation

[1]The explicit result of the upward flux of surface emitted radiation reaching the top of the

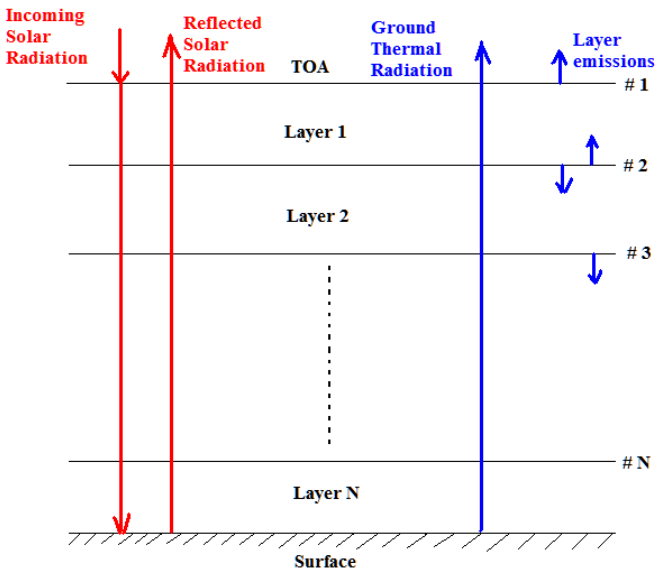

Figure 6.1: Schematic of the radiative transfers in the 1-D model, levels are marked by #.

(see Ramanathan et al. (1985) for more details).

Fig. 6.1 illustrates the framework for the radiative transfer computations represented by our 1-D model. We typically use 40 vertical layers in the standard setting. Each layer has an upper boundary and a lower boundary, which are referred to as levels. Thus 40 layers correspond to 41 levels in the vertical direction, with the first level representing the top of the atmosphere, and the 41st level representing the ground. Stellar radiation enters the top of atmosphere and gets partially attenuated on its way to the ground. When it hits the planetary surface, part of it is absorbed by the ground and the other part reflected back towards the space. The planetary bond albedo is assumed to be 0.3 by comparison with the Earth. On the other hand, the planetary surface as well as the atmosphere itself is emitting long wave thermal radiation. In a typical calculation, the model starts from an isothermal atmosphere. Radiative fluxes (measured in Wm^{-2}) are calculated at each level, and heating rates are then calculated within layers based on the net fluxes between adjacent levels. Temperatures are

atmosphere integrated over all directions (a hemisphere) can be written as $2\pi BE_3(\tau_0)$, where πB is the surface emission and $E_3(\tau_0)$ represent the effect of atmospheric extinction. Special function $E_n(x)$ is formulated as $E_n(x) = \int_1^\infty t^{-n}\mathrm{e}^{-xt}\mathrm{d}t = x^{n-1}\int_x^\infty t^{-n}\mathrm{e}^{-t}\mathrm{d}t$.

then updated by the calculated heating rates at each layer. This temperature profile is then further updated by a convective adjustment scheme. When the temperature tendency at consecutive timesteps becomes lower than a certain prescribed threshold value, the atmosphere is assumed to be in a radiative equilibrium state.

The optical thickness of layer i with zenith angle θ_z is defined by:

$$\tau(i,\mu) = \frac{1}{\mu}\int_b^t k\rho_e dz, \tag{6.3}$$

in which $\mu = \cos\theta_z$, $k = k_a + k_s$ is the total extinction coefficient, taken to be the sum of an absorption coefficient k_a and a scattering coefficient k_s, and ρ_e is the density of the gas attenuating the radiation. Using the hydrostatic relationship, Eq.(6.3) can be rewritten as

$$\tau(i,\mu) = \frac{k}{\mu}\frac{\rho_e}{\rho_a}\frac{\Delta p_i}{g}, \tag{6.4}$$

where ρ_a is the density of the environment atmosphere, Δp the pressure difference between the top and bottom of layer i, and g the constant gravititional acceleration.

If we define $k^* = k\rho_e/\rho_a$ as the scaled extinction coefficient, then $\tau(i,\mu)$ can be expressed in a more compact form:

$$\tau(i,\mu) = \frac{k^*\Delta p_i}{\mu g}. \tag{6.5}$$

This is the final expression used in our algorithm to calculate the optical thickness of layer i.

For the shortwave band stellar radiation, its intensity is attenuated exponentially during its transfer within the model atmosphere. For example, the downward stellar radiation flux at level i is:

$$F_s^{\downarrow}(i,\mu) = F_s^{\downarrow}(i-1,\mu)e^{-\tau(i,\mu)}, \tag{6.6}$$

with the boundary condition at the top of the atmosphere:

$$F_s^{\downarrow}(1,\mu) = S_0\mu \tag{6.7}$$

in which S_0 is the stellar irradiance.

At the ground level, this downward stellar radiation flux is partly absorbed according to the prescribed planetary albedo and the rest gets reflected back upwards, which is then also subject to an exponential extinction in its path to space.

In a similar but slightly more complicated way, the upward and downward long-wave thermal radiation fluxes at level i can be calculated by the following equations:

$$F_L^{\downarrow}(i) = E^{\downarrow}(i) + F_L^{\downarrow}(i-1)e^{-\tau(i)/D}, \tag{6.8}$$

where D is the diffusivity factor (as defined in Eq. 6.2), and $E^{\downarrow}(i)$ is the downward atmospheric thermal emission of layer i, which is estimated (see Lacis & Oinas (1991)) by:

$$E^{\downarrow}(i) = (B(T_b) - B(T_t)e^{-\tau(i)/D})\frac{\tau(i)}{\tau(i) - D\ln\left[B(T_t)/B(T_b)\right]}. \tag{6.9}$$

Here $B(T_b)$ is the blackbody radiation flux at the bottom boundary of layer i where the temperature is T_b, and $B(T_t)$ is the blackbody radiation flux at the top boundary of layer i where the temperature is T_t.

For the upward transfer of long-wave thermal radiation, we have:

$$F_L^{\uparrow}(i) = E^{\uparrow}(i) + F_L^{\uparrow}(i+1)e^{-\tau(i)/D}, \tag{6.10}$$

in which $E^{\uparrow}(i)$ is the upward atmospheric thermal emission of layer i estimated by:

$$E^{\uparrow}(i) = (B(T_t) - B(T_b)e^{-\tau(i)/D})\frac{\tau(i)}{\tau(i) - D\ln\left[B(T_b)/B(T_t)\right]}. \tag{6.11}$$

Using these equations, we can calculate the net radiative flux at each model level, and hence derive the heating rate within layer i as:

$$Q(i) = \frac{g}{c_p} \frac{F_n(i+1) - F_n(i)}{p(i+1) - p(i)}, \tag{6.12}$$

in which g is the constant gravitational acceleration, c_p the specific heat capacity at constant pressure of the atmosphere, and $F_n(i+1)$, $p(i+1)$, $F_n(i)$, $p(i)$ refer to the net radiative fluxes and pressures at level $i+1$ and i respectively.

It should be noted that when calculating the short-wave radiation, the above equation is calculated with a specific value of stellar zenith angle θ_z, which is taken to vary with geographical location and time of year. In order to compute the globally averaged annual mean state, we need to perform the following integration to obtain the shortwave stellar radiation heating rate (Crisp (1989)):

$$\frac{dT}{dt}(i)\Big|_{GA} = \frac{1}{2} \int_0^{\pi/2} \frac{dT}{dt}(\theta_z, i) \sin(\theta_z) d\theta_z, \tag{6.13}$$

in which the subscript GA stands for global average. An 8-point Gaussian quadrature algorithm is used to estimate this integral.

The temperature change at layer i caused by radiative heating/cooling is calculated by:

$$T(i) = T_0(i) + Q(i)\Delta t, \tag{6.14}$$

where $T_0(i)$ is the temperature of layer i at the previous time step, $Q(i)$ the total heating rate (sum of longwave and shortwave heating), and Δt the length of one time step.

For simplicity, the ground is assumed to be a black body that is always in local radiative equilibrium. Thus the following equation stands:

$$F_{ns}(i+1) + F_L^{\downarrow}(i+1) = \sigma T_g^4, \tag{6.15}$$

in which $F_{ns}(i+1)$ refers to the net shortwave stellar radiation flux at level $i+1$ (planetary surface level), $F_L^{\downarrow}(i+1)$ the downward longwave thermal radiation flux at ground level, σ the Stefan-Boltzmann constant, and T_g the ground temperature.

6.1.2 Convective adjustment

The radiative equilibrium temperature profile, given by the pure radiative transfer scheme, has a significant temperature discontinuity near the ground level and is statically unstable to vertical perturbations. Convection could easily be triggered for an atmosphere with such a lapse rate, rapidly transporting heat upwards and modifying the temperature profile. First introduced by climate modellers in the 1960s (Manabe & Strickler (1964),Manabe & Wetherald (1967)), convection schemes nowadays have grown to a formidable complexity, some even with cloud-resolving capability (e.g. see Emanuel (1994), McGuffie & Henderson-Sellers (2005)). In our model, however, we implement the simple dry convective adjustment scheme proposed by Manabe & Strickler (1964). This is not a realistic adjustment scheme that explicitly resolves the vertical overturning motion, but rather a numerical re-evaluation of the temperature profile that is applied when the lapse rate exceeds a critical value to take account of the end state of convective instability.

The convective adjustment subroutine in our model is performed every time the temperature profile has been updated by the radiative heating calculations. It scans from the bottom upwards to check whether the temperature difference between adjacent layers exceeds the temperature difference required by a critical lapse rate, which is set to be the usual dry adiabatic lapse rate ($\Gamma = g/c_p$). If $dT/dz < -\Gamma$, the temperature of these two layers is modified with the constraint of conserving total enthalpy (i.e. equivalent to conserving total potential energy), and the local lapse rate is then restored to the critical value of Γ. For the bottom layer (layer N) adjacent to the ground, the temperatures of the atmosphere and the ground are modified according

to:

$$\frac{c_p}{g}\Delta p_N[T_N^{(1)} - T_N^{(0)}] = \sigma\Delta t\Big\{[T_g^{(0)}]^4 - [T_g^{(1)}]^4\Big\}, \tag{6.16a}$$

$$T_N^{(1)} = T_g^{(1)} - LRC_N, \tag{6.16b}$$

in which Δp_N is the pressure difference between level N and level $N+1$, $T_N^{(1)}$ the temperature of layer N after the adjustment, $T_N^{(0)}$ the temperature of layer N before the adjustment, $T_g^{(0)}$ the temperature of the ground before the adjustment, $T_g^{(1)}$ the temperature of the ground after the adjustment, and LRC_N is the critical temperature difference. The first equation (Eq. (6.16a)) basically states that the enthalpy gain of the bottom layer of the atmosphere is equal to the enthalpy lost by the ground. The second equation (Eq. (6.16b)) represents the constraint that the critical dry adiabatic lapse rate is restored after the adjustment step.

For layers (e.g. i and $i+1$) not in direct contact with the ground which are deemed ustable are modified with the following constraint:

$$\frac{c_p}{g}\Big\{\Delta p_n[T_n^{(1)} - T_n^{(0)}] + \Delta p_{n-1}[T_{n-1}^{(1)} - T_{n-1}^{(0)}]\Big\} = 0, \tag{6.17a}$$

$$T_n^{(1)} - T_{n-1}^{(1)} = LRC_n. \tag{6.17b}$$

After this modification, the temperature profile is scanned again to check whether it is statically stable. If not, the above procedures will be repeated until a stable profile is reached.

6.2 Analytical Solutions

Given certain simplifying assumptions, the two-band semi-grey radiative-transfer problem is in fact analytically solvable (Guillot (2010)). The approach used in current literature (see e.g. Guillot (2010)) employs the three moments of the radiative instensity, and essentially follows the formulation in astrophysics literatures. In this section, we will present a new derivation of the radiative equilibrium temperature profile by solving the two-band radiative-transfer equations that are widely used in meteorology literatures.

We consider a static, *non-scattering*, plane-parallel atmosphere with no internal heat source. Stellar radiation flux has a zenith angle of θ ($\cos\theta = \mu$).

For the long-wave (LW) radiative transfer, the two-stream formulation that is widely used in the meteorology literature is as the following:

$$\frac{dF^{\downarrow}}{d(D\tau)} + F^{\downarrow} = \sigma T^4, \tag{6.18a}$$

$$-\frac{dF^{\uparrow}}{d(D\tau)} + F^{\uparrow} = \sigma T^4. \tag{6.18b}$$

Here D is the diffusivity factor which is employed to represent the gross effect of non-vertical (slantwise) LW radiative transfer. $F^{\downarrow}$ and $F^{\uparrow}$ are the downward and upward LW irradiance respectively, τ the LW optical depth measured along the vertical direction, σ the Stefan-Boltzmann constant, and T the temperature.

The short-wave (SW) stellar radiation follows an exponential decay:

$$Q = S_0 e^{-\gamma\tau/\mu}, \tag{6.19}$$

where $\gamma = \tau_{SW}/\tau$, and S_0 is the stellar irradiance at the top of atmosphere (Wm^{-2}).

The stellar heating rate $\propto -\frac{dQ}{d\tau}$ and the LW heating rate $\propto -\frac{d}{d\tau}(F^{\downarrow} - F^{\uparrow})$. So in equilibrium, we must have

$$\frac{d}{d\tau}(Q + F^{\downarrow} - F^{\uparrow}) = 0. \tag{6.20}$$

At the top of the atmosphere, there is no net irradiance, i.e. $Q + F^{\downarrow} - F^{\uparrow} = 0$ Therefore we have $Q + F^{\downarrow} - F^{\uparrow} = 0$ for all levels within the atmosphere.

According to Eq.(6.20), we have

$$\begin{aligned}
\frac{dQ}{d\tau} &= \frac{dF^{\uparrow}}{d\tau} - \frac{dF^{\downarrow}}{d\tau} \\
&= (DF^{\uparrow} - D\sigma T^4) - (D\sigma T^4 - DF^{\downarrow}) \\
&= DF^{\uparrow} + DF^{\downarrow} - 2D\sigma T^4 \\
&= DQ + 2DF^{\downarrow} - 2D\sigma T^4.
\end{aligned} \tag{6.21}$$

Thus

$$\sigma T^4 = F^{\downarrow} + \frac{Q}{2} - \frac{1}{2D}\frac{dQ}{d\tau}. \tag{6.22}$$

Substituting this equation into Eq.(6.18a), we have

$$\frac{1}{D}\frac{dF^{\downarrow}}{d\tau} + F^{\downarrow} = F^{\downarrow} + \frac{Q}{2} - \frac{1}{2D}\frac{dQ}{d\tau}. \tag{6.23}$$

Thus

$$\begin{aligned}
\frac{dF^{\downarrow}}{d\tau} &= \frac{DQ}{2} - \frac{1}{2}\frac{dQ}{d\tau} \\
&= \frac{1}{2}\left(DS_0 e^{-\gamma\tau/\mu} + S_0\frac{\gamma}{\mu}e^{-\gamma\tau/\mu}\right) \\
&= \frac{1}{2}\left(DS_0 + S_0\frac{\gamma}{\mu}\right)e^{-\gamma\tau/\mu}.
\end{aligned} \tag{6.24}$$

Integrating with respect to τ, we have:

$$\begin{aligned} F^{\downarrow} &= \frac{1}{2}\int_0^{\tau}\Big(DS_0 + S_0\frac{\gamma}{\mu}\Big)e^{-\gamma\tau/\mu}d\tau \\ &= \Big(\frac{DS_0}{2}\frac{\mu}{\gamma} + \frac{S_0}{2}\Big)\Big(1 - e^{-\gamma\tau/\mu}\Big). \end{aligned} \tag{6.25}$$

From Eq.(6.18a) we can write:

$$\begin{aligned} \sigma T^4 &= \frac{dF^{\downarrow}}{d(D\tau)} + F^{\downarrow} \\ &= \frac{1}{D}\Big(\frac{DS_0}{2}\frac{\mu}{\gamma} + \frac{S_0}{2}\Big)\frac{\gamma}{\mu}e^{-\gamma\tau/\mu} + F^{\downarrow} \\ &= \Big(\frac{S_0}{2} + \frac{S_0}{2D}\frac{\gamma}{\mu}\Big)e^{-\gamma\tau/\mu} + \Big(\frac{DS_0}{2}\frac{\mu}{\gamma} + \frac{S_0}{2}\Big)\Big(1 - e^{-\gamma\tau/\mu}\Big) \\ &= \frac{S_0}{2} + \frac{DS_0}{2}\frac{\mu}{\gamma} + \frac{S_0}{2}\Big(\frac{\gamma}{D\mu} - \frac{D\mu}{\gamma}\Big)e^{-\gamma\tau/\mu}. \end{aligned} \tag{6.26}$$

Assuming the stellar irradiance at TOA can be formulated by $S_0 = \mu\sigma T_{irr}^4$, where T_{irr} is the effective irradiation temperature, then we can rewrite the above equation as

$$T^4 = \frac{1}{2}T_{irr}^4\mu\Big[1 + D\frac{\mu}{\gamma} + \Big(\frac{\gamma}{D\mu} - \frac{D\mu}{\gamma}\Big)e^{-\gamma\tau/\mu}\Big]. \tag{6.27}$$

If the diffusivity parameter is taken to be $D = 3/2$ (e.g. Goody & Young (1995)), we have

$$T^4 = \frac{1}{2}T_{irr}^4\mu\Big[1 + \frac{3\mu}{2\gamma} + \Big(\frac{2\gamma}{3\mu} - \frac{3\mu}{2\gamma}\Big)e^{-\gamma\tau/\mu}\Big]. \tag{6.28}$$

This represents the temperature profile under purely radiative equilibrium condition. In the case of a highly transparent short-wave band ($\gamma \to 0$),

$$e^{-\gamma\tau/\mu} \approx 1 - \gamma\tau/\mu.$$

Then Eq. (6.28) becomes

$$T^4 \approx \frac{1}{2}T_{irr}^4\mu\Big(1+\frac{\gamma}{D\mu}-\frac{\gamma^2\tau}{D\mu^2}+D\tau\Big). \tag{6.29}$$

Ignoring terms of order $O(\gamma)$ and higher, we have

$$T^4 \approx \frac{1}{2}T_{irr}^4\mu(1+D\tau), \tag{6.30}$$

which is essentially the equilibrium temperature profile derived under the assumption of a classical grey atmosphere (see Andrews (2010)).

6.3 Comparison with Earth, Mars and Venus

In this section, we will use suitably calibrated versions of the 1-D model in an attempt to emulate the temperature profiles of Earth, Mars and Venus, for comparison with the realistic global mean profiles.

6.3.1 Mars

The Martian atmosphere is largely composed of CO_2 (95.3% by mole fraction), with only trace amounts of water vapor and various other gases. Compared with the Earth and Venus, Mars' atmosphere is particularly well-suited to be computed using our 1-D R-C model, mainly because it has no locally concentrated, short-wave absorbing gas components like the ozone layer on Earth nor does it have any dense cloud layers which significantly reshape the temperature profile as found on Venus. The annual mean globally averaged thermal structure, therefore, should be calculated reasonably accurately by our 1-D model, although note that the transient, yet radiatively significant, dust storms that occur sporadically on this planet (Read & Lewis (2004b)) are not represented in this model.

The optical depth assumed in this two-band scheme is essentially the gross optical depth averaged over a wide range of wavelengths. Based on the available experimental line-by-line spectroscopic data, such an average can be obtained by calculating the Rosseland mean optical depth (Seager (2010)):

$$\tau_m^{-1} = \frac{\int \tau_\nu^{-1} B_\nu(T) d\nu}{\int B_\nu(T) d\nu}, \tag{6.31}$$

where τ_m is the averaged optical depth, τ_ν the optical depth at wavenumber ν, $B_\nu(T)$ the Planck function for temperature T at wavenumber ν. The average value here is calculated by the Rosseland mean because this approach gives more weight to spectral bands in which the atmosphere is less opaque. This captures the physics that most radiation goes through the atmosphere in the most transparent wavelengths. It gives a more accurate representation of the gross spectroscopic features of an optically thick atmosphere (see Seager (2010) for more details) compared with the Planck mean, which gives more weight to optically-thick spectral bands. Using the spectroscopic data from the NASA Ames Mars 1-D Radiation code with 5 infrared bands, we obtained an average total optical depth for the long-wave (infrared) band of ~ 0.3 following Eq. (6.31). Further assuming that the atmosphere is transparent to the short-wave (visible) incoming solar radiation (which corresponds approximately to the dust-free Martian atmosphere), then the radiative-convective equilibrium temperature profile can be obtained using our two-band scheme, as shown in Fig. 6.2. By comparing the model result and observed temperature profile in Fig. 6.2, it can be seen that the model captures the characteristic thermal structures of Martian atmosphere to a relatively accurate extent, with a surface temperature of $\sim$ 225 K. It should be noted that the agreement between our model and the observation in Fig. 6.2 does not mean that our model can always reflect the true state of the vertical thermal structure of Mars at any time. Due to strong seasonal cycle as well as

low temperature, a significant portion of the Martian atmosphere (CO_2) consolidates into dry ice over polar regions near solstices. Besides, the occurence of overwhelming global dust storms every couple of Martian years can strongly alter the radiative property of the Martian atmosphere. Our two-band semi-grey scheme is not meant to be able to capture these details. The temperature profile shown in Fig. 6.2 should only be viewed as an annual mean state in a relatively calm (dust-free) Martian year.

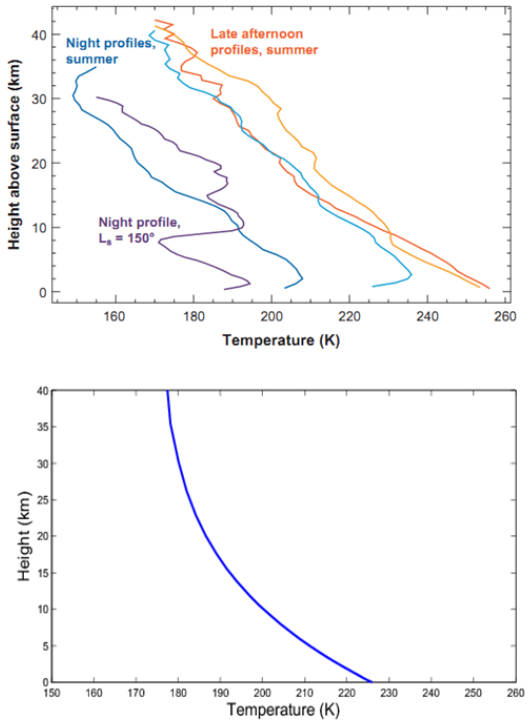

Figure 6.2: Comparison of a set of observed temperature profiles over Martian southern hemisphere mid-lattitudes using MGS radio occultation data (from Smith (2008), purple profile denote a nighttime profile taken near the Tharsis volcanoes at solar longitude $L_s = 150°$.) and modelled temperature profile of the Martian atmosphere.

6.3.2 Venus

Similarly, we can obtain a temperature profile for an optically thick atmosphere similar to that of Venus using the two-band scheme, as shown in Fig. 6.3. The long-wave (infrared) band optical depth is again estimated by the Rosseland average, based on

spectroscopic data from Lee & Richardson (2011). The short-wave (visible) band optical depth is tuned so that the total solar irradiation at the ground level is approximately 20 Wm^{-2}, which fits with the observational data (see Titov et al. (2007) and references therein). Despite having no representation of the ubiquitous clouds on Venus, the simulated equilibrium temperature profile, with a near-isothermal stratosphere at around 200K and a convectively adjusted troposphere extending to a surface temperature of 760K or so, fits surprisingly well with the observed temperature profile (VIRA), given the simplicity of the two-band scheme and the crude assumption of well-mixed absorbers in the vertical direction.

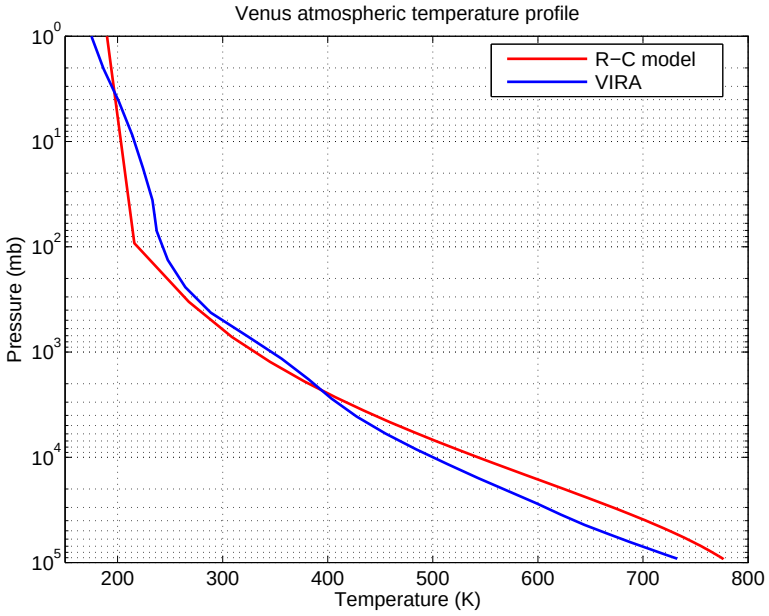

Figure 6.3: Radiative-convective equilibrium temperature profile of the 1-D two-band scheme (red solid line), compared with VIRA (Venus International Reference Atmosphere, see Kliore et al. (1992)) profile (blue solid line). 1-D scheme assumes $\tau_{lw} = 473.56$ and $\tau_{sw} = 1.40$. Bond albedo of the 1-D scheme is set to 0.76 (which is the bond albedo of Venus, see Taylor (2010)).

6.3.3 Earth

The radiative-convective temperature profile predicted by the 1-D semigrey model features an isothermal stratosphere and a statically stable troposphere. This is at first sight quite different from the "zigzag" temperature profile observed in the Earth's atmosphere (see Fig. 6.4). The 1-D model, however, assumes that the short-wave absorbers are uniformly distributed in the vertical direction (i.e. with the same mass concentration everywhere, as stated in Section 6.1). Thus, there is no local concentration of absorbers to create a localised temperature maximum. In the Earth's atmosphere, however, the existence of a concentrated ozone layer at altitudes of $30-40$ km creates a temperature maximum at the top of the stratosphere (roughly the 1 mb level in Fig. 6.4). If the ozone was not locally concentrated within a certain layer but spread uniformly in the vertical direction, then there would be no temperature maximum in the blue curve. If we were to remove ozone from the atmosphere, there would be no significant absorption of solar radiation in the stratosphere, and the vertical temperature structure would then tend to resemble the classical grey atmosphere curve (shown in red in Fig. 6.4), which reproduces reasonably the structure of the troposphere and the tropopause temperatures. Therefore, apart from features that are related to the distribution of absorbers, the fundamental attributes of the atmospheric thermal structure (e.g.surface temperature, lapse rate, upper atmospheric temperature and so on) should be predicted reasonably well by the model.

Based on the above-stated comparisons between the results of our radiative-convective model and the realistic planetary atmospheres, it can be concluded that the two-band semi-grey radiative-convective model, despite its simplicity, essentially captures the characteristic vertical thermal structures of typical terrestrial planetary atmospheres, provided clouds are not too significant. Although features of localised

[1]Data available from NCAS British Atmospheric Data Centre at http://badc.nerc.ac.uk/view/badc.nerc.ac.uk__ATOM__dataent_CIRA

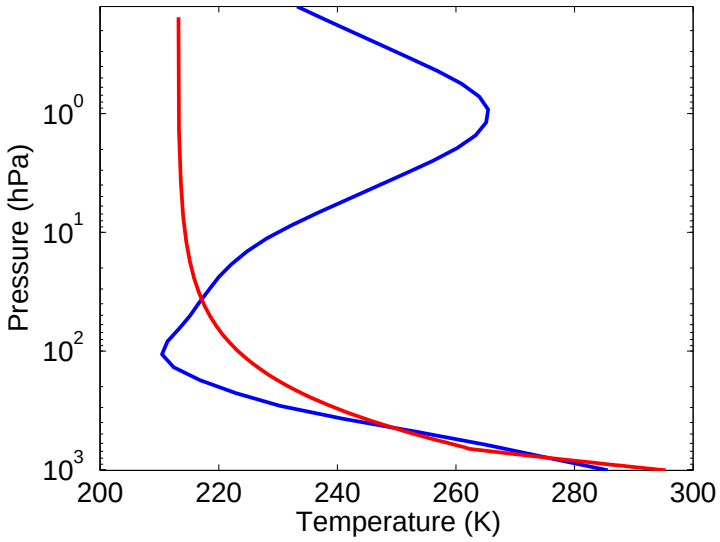

Figure 6.4: Radiative-convective equilibrium temperature profile of the 1D model (red solid line), compared with the climatological profile of Earth's atmosphere (blue solid line, based on the COSPAR International Reference Atmosphere (CIRA-86)[1]). 1D model assumes $\tau_{lw} = 2.0$ and $\tau_{sw} = 0.0$.

temperature inversion associated with layers of short-wave absorbers (e.g. ozone layer of the Earth, and the organic haze layer in Titan's stratosphere) cannot be reproduced using our model, it should be noted that structures of extensive temperature inversion can be captured in our model by setting the short-wave optical depth larger than that of the long-wave (see discussion on anti-greenhouse atmospheres in Chapter 5). Our study is focussed upon the most fundamental processes in determining the atmospheric dynamical and thermodynamical structures with no intention to simulate the peculiar details unique to any planet, so we conclude that the two-band semi-grey radiative-convective scheme is suitable for our purpose, thanks to its capability to reproduce gross thermal structures and its intermediate levels of complexity.

6.4 Coupling with the dynamical core

The two-band radiative-convective scheme outlined in the previous section was presented in the form of a 1-D model which has no horizontal variation or dynamic

transport. In this section, we will describe how we couple this semi-grey scheme with the pseudo-spectral dynamical core of PUMA. This was done by replacing the Newtonian heating/cooling at each grid box[2] with the local heating/cooling calculated by the two-band scheme.

6.4.1 Incoming stellar radiation (ISR) at top of atmosphere for different latitudes

The instantaneous incoming stellar radiation at the top of the atmosphere for a certain location on a planet depends on a variety of factors: the local time, the latitude, the obliquity of the planet, and the stellar irradiance. For a non-synchronously rotating planet in a circular orbit, the daily average stellar insolation at TOA on day j is

$$F(\phi, j) = \frac{S}{\pi}\mu(\phi, j)H(\phi, j), \tag{6.32}$$

in which ϕ is the latitude, S_0 the stellar irradiance reaching the planet's orbit, $\mu(\phi, j)$ the daily average value of $\cos\theta_z$ (θ_z is the stellar zenith angle), and $H(\phi, j)$ the half day length (half of the time span from sunrise to sunset) scaled by 2π.

$\mu(\phi, j)$ and $H(\phi, j)$ can be calculated following Vardavas & Taylor (2007) as:

$$\mu(\phi, j) = \sin\phi\sin\delta(j) + \cos\phi\cos\delta(j)\frac{\sin H(\phi, j)}{H(\phi, j)}, \tag{6.33}$$

and

$$H(\phi, j) = \arccos\left[-\tan\phi\tan\delta(j)\right], \tag{6.34}$$

where

$$\delta(j) = -\varepsilon\cos\frac{2\pi}{N}j \tag{6.35}$$

[2]This involves transformation from spectral space into physical space.

is the stellar declination angle[3] of day j (Cooper (1969)). Here ε is the planetary obliquity in radians, and $N = T_r/T_s$ (T_r is the revolutionary period, T_s is the spin period) represents the number of days in a year of the planet in consideration.

Special attention should be paid to polar regions where polar day/night could occur over a certain period of a year. If $\tan\phi\tan\delta(j) > 1$, then $H(\phi, j) = \pi$; if $\tan\phi\tan\delta(j) < -1$, then $H(\phi, j) = 0$.

The annual mean insolation at a certain latitude ϕ is:

$$\overline{F(\phi)} = \frac{1}{N}\sum_{j=1}^{N} F(\phi, j). \tag{6.36}$$

The annual mean zenith angle for a certain latitude ϕ can be obtained by:

$$\overline{\mu(\phi)} = \frac{\overline{F(\phi)}}{S}. \tag{6.37}$$

It should be particularly noted that the above calculations are based on the assumption that the orbit of the planet is circular rather than elliptical. If the orbit was to be elliptical with a non-negligible eccentricity, there would be various additional complicated modifications to the above equations. Other orbital factors, such as the position of equinox points along the orbit, the eccentricity and so on, would appear in the calculation (see Liou (2002) for more details). It might seem that the position of equinox points does not directly influence the insolation for a given latitude, but combined with eccentricity, it determines the insolation difference between the two hemispheres[4]. In this study, however, we will only consider circular orbits for simplicity.

The daily averaged insolation at each latitude within one year calculated by Eq.

[3]stellar declination angle is defined as the angle between the equatorial plane and the line joining the substellar point and the star. For Earth, it varies between $-23.45°$ and $23.45°$ at present.

[4]For Earth, the change of the position of equinox points in the orbit in geological time scale is known as *apsidal precession* , which is a major component of the Milankovitch cycles. The physical cause of such orbital 'drift' is the gravitational interaction of the Earth with Jupiter and Saturn.

(6.32) for parameters of Earth's orbit is shown in Fig. 6.5. Note that the northern and southern hemispheres are perfectly symmetrical in our calculations of received ISR. But in fact, the Earth's orbit is slightly elliptical, which causes the southern hemisphere to receive more insolation than the northern hemisphere since the Earth is closer to the sun near southern hemisphere summer, thus leading to a small asymmetry between the two hemispheres. The resultant annual mean insolation with respect to latitude calculated by Eq. (6.36) is shown in Fig. 6.6.

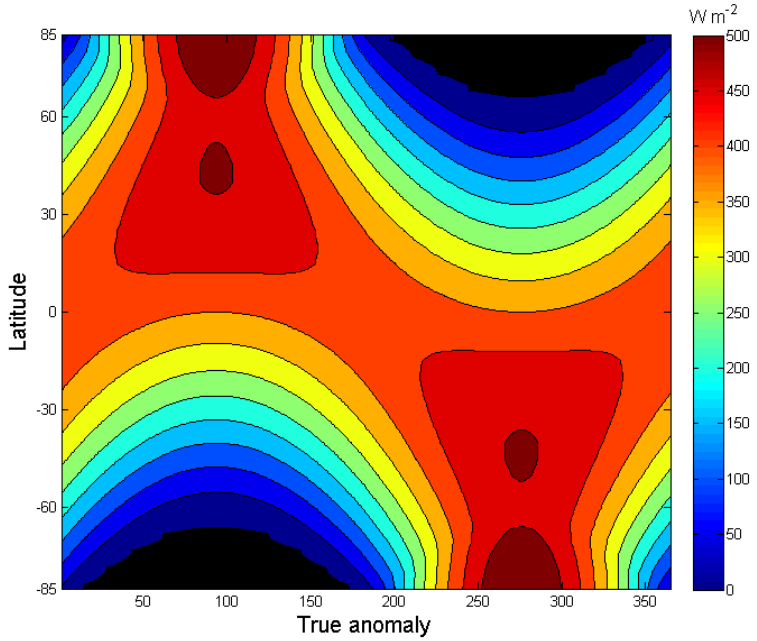

Figure 6.5: Spatial and temporal distribution of daily average ISR at TOA of the Earth. Black regions represent polar night. The abscissa *true anomaly* is the angular difference (in degrees) between the direction of periapsis and the position of the planet, which could be viewed as an indicator of time in one astronomical year.

This scheme for calculating the annual mean incoming stellar radiation at the top of the atmosphere has a range of parameters which can be tuned to represent different orbital configurations. The obliquity is particularly interesting in our study and its effect on the distribution of incoming stellar radiation can be seen in Fig. 6.6, which shows the distribution of incoming stellar radiation at the top of the atmosphere for a planet at three different obliquities. For an obliquity angle of 85°, the planet's polar regions receive far more stellar radiation than the tropics. Note that the critical

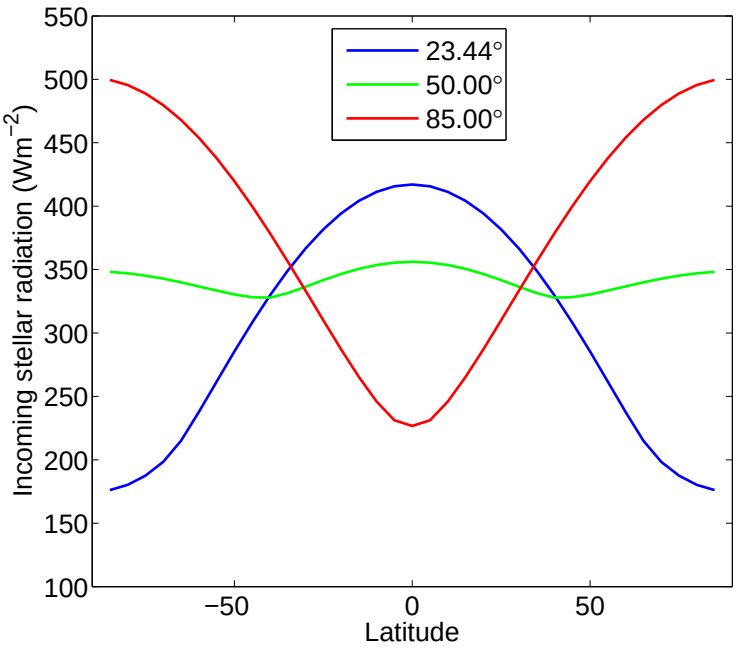

Figure 6.6: Incoming stellar radiation (ISR) at TOA at different latitudes for three different obliquities. The blue curve represents the scenario of present-day Earth, with obliquity of 23.45°. The red curve represents the Earth with a rather large obliquity angle of 85°, somewhat resembling Uranus. The green curve stands for a middle state with obliquity 50°.

obliquity under which the average incoming stellar radiation over the equator is equal to that over the poles is approximately 50°. This is slightly different from the value $\sim 54°$ predicted by the Milankovitch theory (see e.g. Williams (1975)), but this is based on assuming an elliptical orbit rather than the circular orbit assumed here.

6.4.2 Computational procedure and benchmark tests of the coupled two-band semi-grey GCM

The PUMA-G model, which employs the above-stated semi-grey radiative-convective scheme, is based on the simple GCM PUMA-S introduced in Chapter 2. Dynamical and physical processes are computed separately within the PUMA-S model. Linear terms of the primitive equations are integrated in spectral space while the physical

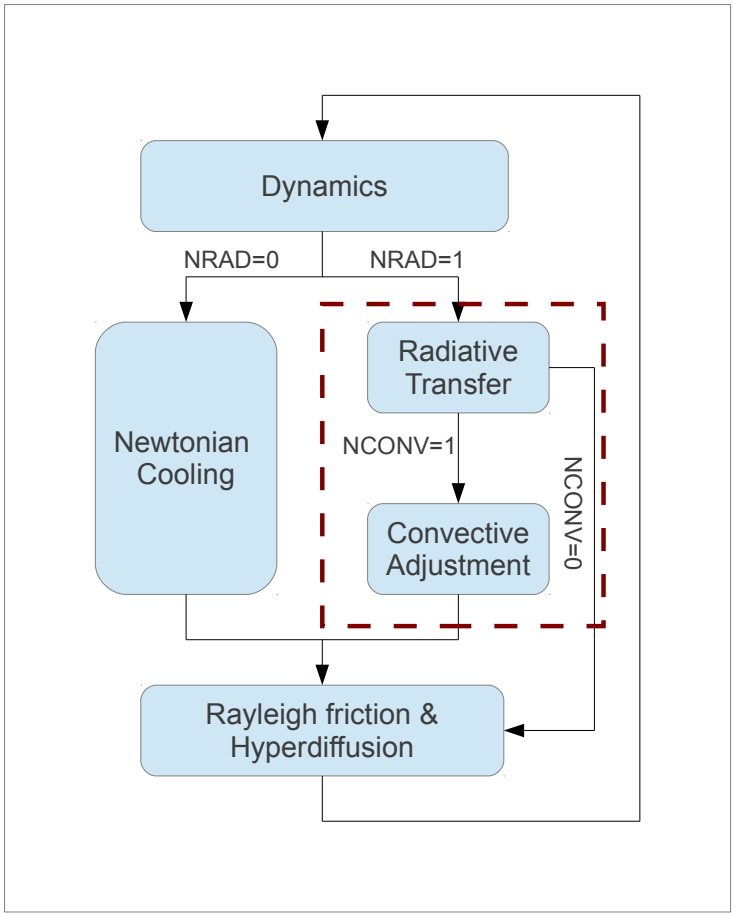

Figure 6.7: Flow chart of the execution loop of PUMA-G model. Processes within the red dash line box, which are executed only every 20 dynamic time steps, are what differs from the PUMA-S.

processes (Newtonian cooling, Rayleigh friction etc.) plus non-linear terms of the primitive equations are computed in physical (grid-point) space. The two-band semi-grey radiative-convective scheme is implemented in the model by introducing two switches NRAD and NCONV, which controls the execution of radiative and convective computations respectively. If NRAD = 1 then the two-band radiative transfer is used instead of Newtonian relaxation at each grid box. If NCONV = 1 then the dry adiabatic convective adjustment is performed to keep the atmosphere in a statically neutral stable state. In order to accelerate the computation, radiative transfer and convective adjustment are calculated every 20 dynamical timesteps. Fig. 6.7 shows a schematic execution flow chart of the PUMA-G model.

A benchmark test was conducted by setting $\tau_{lw} = 1.0$ (which corresponds to a total optical depth of approximately 2.0 under the diffusivity approximation) and $\tau_{sw} = 0.0$. Radiative forcing from the star at the top of the atmosphere was set to the values shown in Fig. 6.6. This configuration gives a thermal forcing which mimics that received by the Earth's atmosphere at a distance of 1 AU from the Sun. A comparison of the annually-averaged zonal mean fields from PUMA-S and PUMA-G results is shown in Fig. 6.8.

It can be seen that the zonal mean fields produced by PUMA-S and PUMA-G share various features in common. A mid-latitude jet stream can be found in each hemisphere for both simulations located around 45° N/S. In each hemisphere, the general circulation exhibits the classical 3-cell regime with a thermally-direct Hadley cell in the tropics and an eddy-driven indirect Ferrel cell in the mid-latitudes. The zonal mean temperature in the troposphere has a maximum near the tropical ground level and gradually decreases towards the upper atmosphere and the poles. A couple of differences exist, however, between the output of these two models. The mid-latitude jet produced by PUMA-G does not have a closed core like its counterpart in PUMA-S. Instead, the zonal wind speed increases all the way up to the top of the atmosphere in PUMA-G. This is essentially caused by the significant meridional temperature difference in the upper atmosphere of PUMA-G, consistent with the thermal-wind relationship. In PUMA-S, the temperature field always relaxes towards a prescribed equilibrium temperature field, which has been prescribed to give an isothermal tropopause/stratosphere. The maintaining of this isothermal cap over the troposphere requires both the presence of an ozone layer in the stratosphere and a latitudinally-varying concentration of water vapor near the ground. In PUMA-G, however, diabatic heating/cooling is realised solely by radiative and convective processes. Since we are assuming that (for conceptual simplicity) the radiatively active absorbers are well-mixed in the atmosphere, there can be neither an ozone

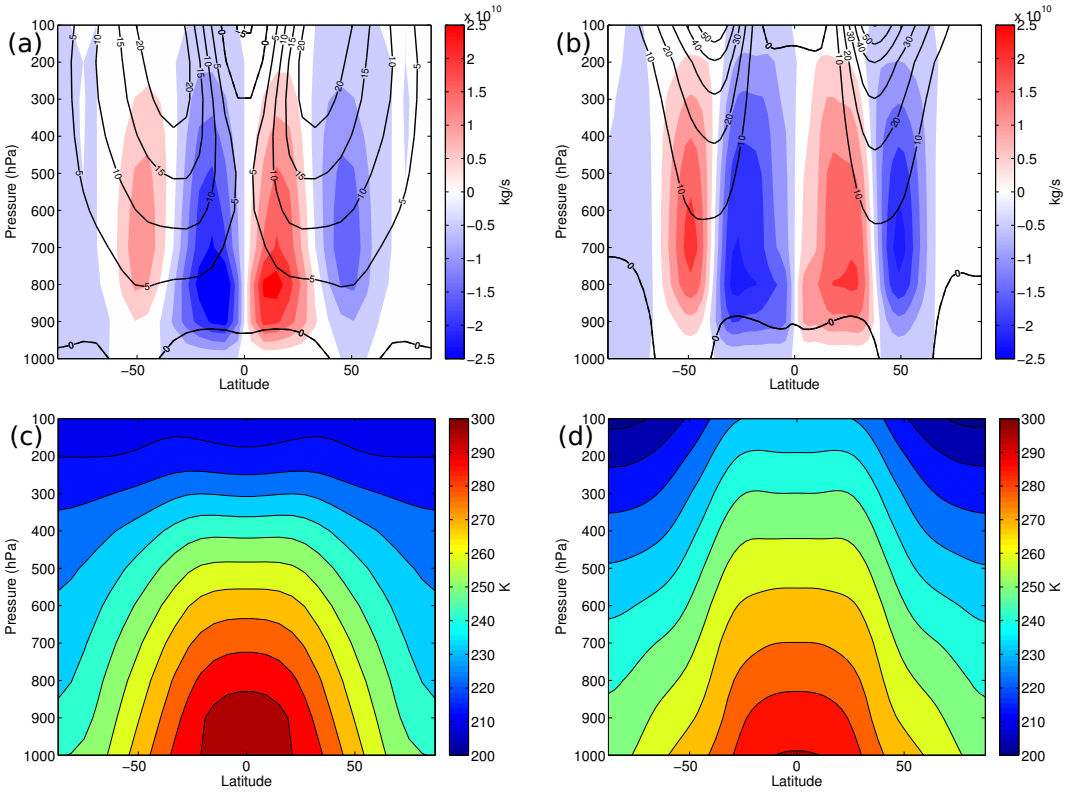

Figure 6.8: Comparison between the temporal and zonal mean fields of PUMA-S and PUMA-G. (a): zonal mean zonal wind (m/s, contour) and the meridional mass stream function (kg/s, colour) of PUMA-S. (c): zonal mean temperature (K) of PUMA-S. (b): same as (a) but for PUMA-G. (d): same as (c) but for PUMA-G.

layer nor a build-up of water vapor in the lower atmosphere to modify the heating distribution. Thus an isothermal tropopause cannot be produced using this version of PUMA-G. But apart from this difference, the simulated climatology by PUMA-G is reasonably good and reflects the physical consistency of the assumptions we have made.

Chapter 7

Circulation regimes of an atmosphere modelled by PUMA-G

This chapter presents studies based on the controlled experiments using PUMA-G. Section 7.1 describes the setup of experiments and the regime diagrams obtained using PUMA-G. This is followed by a survey of the zonal mean diagnostics on a series of representative runs in Section 7.2, with the aim of highlighting the meridional climatological structures of various circulation regimes. Section 7.3 and 7.4 then discuss the regime diagrams obtained under different obliquities. Section 7.3 shows the comparison between PUMA-S regimes and their counterparts obtained using PUMA-G at obliquity of 23.44°. Section 7.4 describes circulation regimes found at higher obliquity of 50° and 85°. This is followed by discussions on the impact of the greenhouse parameter $\mathcal{G}$ in Section 7.5. Section 7.6 investigates the impact of the defining parameters on the atmospheric heat transport efficiency.

7.1 Experiment design and regime diagram

As a GCM with slightly more complicated physics than PUMA-S used in Chapter 3, PUMA-G is employed in this chapter to study the circulation regimes when some

characteristic external parameters are changed. Apart from varying the planetary rotation rate as in Chapter 3, we will also investigate effects of changing the planetary obliquity and the band-averaged atmospheric opacities on planetary global circulation, thanks to the explicit representation of radiative-transfer processes in PUMA-G which enables the modification of these parameters in a self-consistent approach without introducing *ad hoc* relaxation temperature fields and radiative timescales as needed in PUMA-S.

Following the practice of PUMA-S experiments described in Chapter 3, PUMA-G was configured with terrestrial values of planetary radius, gas constant, gravity constant, surface pressure and c_p. The rotation rate was varied to 8, 4, 2, 1, 1/2, 1/4, 1/8, and 1/16 times the current Earth's rotation rate. Planetary obliquity was set to values of $\varepsilon = 23.44°, 50.00°, 85.00°$, in which $23.44°$ represents the current Earth, $50.00°$ the intermediate obliquity which makes the equator and the poles receive approximately same amount of stellar irradiation at the top of the atmosphere averaged over the year, and $85.00°$ an extreme case with Uranus-like obliquity, making the poles receive much more annual mean irradiation than the tropics. The atmospheric optical depth ratio $\mathcal{G} = \tau_{sw}/\tau_{lw}$ was set to $0, 1,$ or 5[1], which correspond respectively to atmospheres with a substantial greenhouse effect (transparent to short-wave radiation, but opaque to long-wave, like the Earth's atmosphere), a neutral-greenhouse effect (equally opaque at all wavelengths), and an anti-greenhouse effect (opaque to short-wave radiation, but transparent to long-wave). Stellar irradiation was represented in the form of an annual mean, which is symmetric with respect to the equator. Experiments were conducted with all possible combinations of these three parameters (Ω^*, ε, and $\mathcal{G}$), leading to 72 experiments in total.

Since there are three independent dimensionless parameters, the resultant parameter space is in 3-D. Instead of plotting the regime diagram directly in a 3-D space, a

[1]The globally averaged long-wave optical depth of the atmosphere is set to 2.0, which is approximately the value of the Earth's atmosphere.

clearer way to show the regime diagram is adopted by plotting 2-D sections at three different values of $\mathcal{G}$.

Fig. 7.1 shows the regime diagram corresponding to the greenhouse atmosphere with $\mathcal{G} = 0$. For experiments with terrestrial obliquity $\varepsilon = 23.44°$, the circulation regimes are similar those shown in Chapter 3, with equatorial super-rotation for experiments at slow rotation rate, regular/irregular baroclinic waves for experiments at intermediate rotation rate, and multiple zonal jets for experiments at fast rotation speed. Two regimes can be found for experiments with intermediate planetary obliquity of $\varepsilon = 50.00°$. Purely axisymmetric flow is found in fast-rotating ($\Omega^* \geq 1$) experiments whereas flows with baroclinic wave activity is found in slowly-rotating ($\Omega^* < 1$) runs. For the Uranus-like high obliquity experiments, the circulation observed is dominated by a strong retrograde ("sub-rotation") wind field with maximum wind speed of $\sim 100\text{m s}^{-1}$ over the low-latitudes.

Figs. 7.2-7.3 show the regime diagrams for experiments of neutral-greenhouse and anti-greenhouse atmospheres. These two regime diagrams are almost the same and they are not too different from the regime diagram of greenhouse atmospheres shown in Fig. 7.1, which implies that planetary rotation and planetary obliquity play a dominant role while the greenhouse parameter only has a marginal effect on the organisation of the general circulation. Nevertheless, it should be noted that although the regime diagram may change very little with respect to different values of $\mathcal{G}$, the thermal structure of the atmosphere changes significantly when $\mathcal{G}$ is assigned a different value, as will be shown in the following section.

7.2 Zonal mean diagnostics

In this section, collages of zonal and temporal mean cross-sections of dynamical and thermal structures of the modelled atmospheres are presented (Figs. 7.4-7.9) based

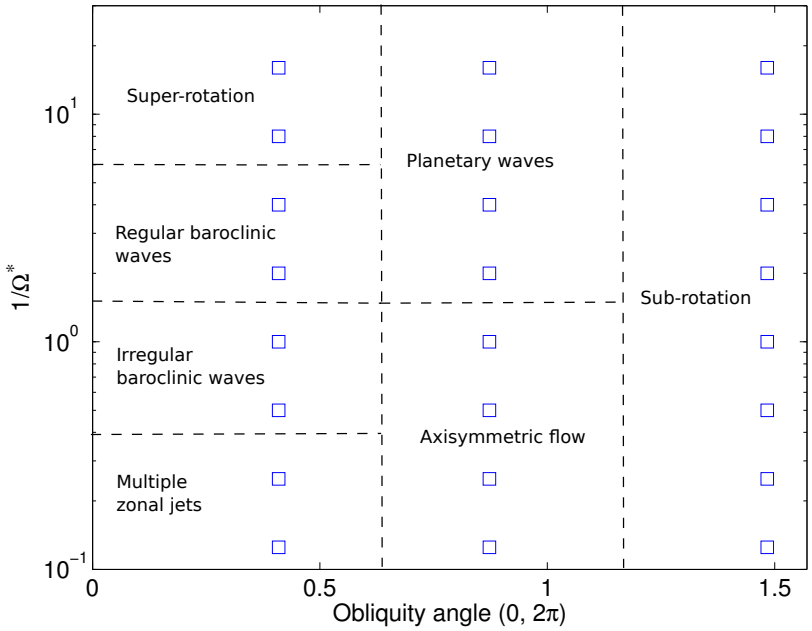

Figure 7.1: Regime diagram based on experiments with $\mathcal{G} = 0$ (Greenhouse atmosphere).

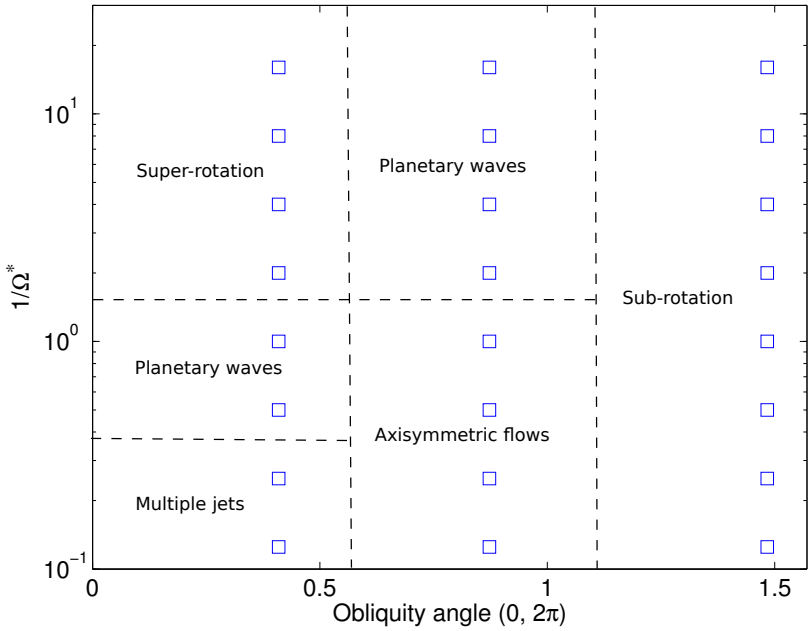

Figure 7.2: Regime diagram based on experiments with $\mathcal{G} = 1$ (Neutral-greenhouse atmosphere).

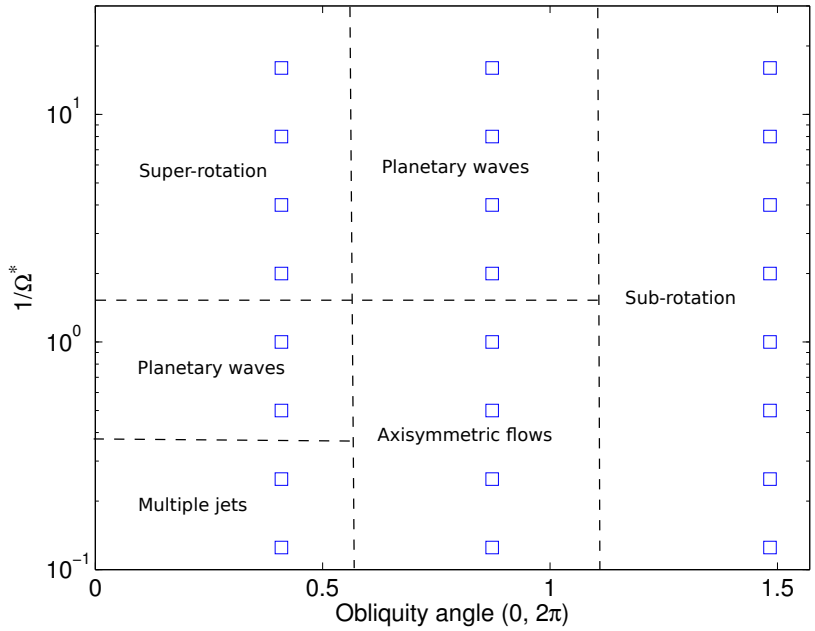

Figure 7.3: Regime diagram based on experiments with $\mathcal{G} = 5$ (Anti-greenhouse atmosphere).

upon 36 representative experiments selected from the 72 runs. For each experiment, zonal wind and meridional mass streamfunction are plotted to reveal the circulation dynamics regime, while atmospheric thermal strutures are shown by latitude-height temperature and potential temperature maps. The representative subset uses only 4 values of Ω (selected from the 8 values of Ω stated in the previous section), and includes all possible combinations of $\Omega^* = \{1/16, 1/4, 1, 4\}$, $\mathcal{G} = \{0, 1, 5\}$, and $\varepsilon = \{23.44°, 50.00°, 85.00°\}$.

Figs. 7.4-7.5 show the results of experiments with $\mathcal{G} = 0$ (corresponding to the regime diagram of greenhouse atmospheres shown in Fig. 7.1). Experiments with $\varepsilon = 23.44°$ ((a) and (c) in Figs. 7.4 and 7.5) are essentially comparable to the PUMA-S runs with the corresponding values of Ω shown in Figs. 3.8-3.11. Significant equatorial super-rotation is found in experiments with $\Omega^* = 1/16$ and $1/4$, and a multiple-jet structure is found in the fast-rotating experiment with $\Omega^* = 4$. A terrestrial-like circulation regime with planetary-scale waves is found with $\Omega^* = 1$. It should be noted that the temperature structures produced by PUMA-G demon-

strate larger variations near the surface when Ω is changed, compared to what we found with PUMA-S experiments (Figs. 3.10-3.11). This is probably due to the more realistic representation of radiative-transfer in PUMA-G, in contrast to the Newtonian relaxation scheme of PUMA-S which has stronger damping near the ground. The meridional surface temperature gradient is much smaller at low rotation rates ($\Omega^* = 1/16, 1/4$), which is consistent with the expansion of the Hadley cells. As stated in Chapter 6, the upper atmosphere of PUMA-G at $G = 0$ and $\varepsilon = 23.44°$ does not have the small meridional temperature gradient like PUMA-S. This is not unduly surprising based on our idealised assumptions about the distribution of radiatively-active absorbers/emitters in PUMA-G (see discussions at the end of Chapter 6).

For experiments with intermediate obliquity ($\varepsilon = 50.00°$, (b) and (d) of Figs. 7.4 and 7.5), the temperature field exhibits a very small meridional gradient (meridional temperature difference < 10K) at all vertical levels, with relatively warmer regions over the equator and the poles and relatively colder regions near 50°N/S. This small horizontal temperature contrast leads to weaker Hadley cells compared with their counterparts in experiments with $\varepsilon = 23.44°$ and thermally-direct weak polar cells are formed polewards of 50°N/S. The thermal wind relationship leads to prograde jets equatorward of 40°N/S and weak retrograde jets poleward of 40°N/S. Wave-free, axisymmetric flows are found for experiments with fast rotation rate, the mechanism of which will be discussed in Section 7.4.1.

For experiments with high obliquity ($\varepsilon = 85.00°$, (c) and (f) of Figs. 7.4 and 7.5), the polar regions receive most of the irradiation and are significantly warmer than the equator. This induces thermally-direct Hadley cells circulating in the opposite direction to their counterparts with a terrestrial-like small obliquity. If the upper branch of the Hadley cell is nearly inviscid, as is usually assumed in Hadley cell studies (e.g. Held & Hou (1980)), then angular momentum conservation will naturally lead to retrograde flows over the lower latitudes.

Figs. 7.6-7.7 show the results of experiments with $\mathcal{G} = 1$ (corresponding to the regime diagram of "neutral greenhouse" atmosphere shown in Fig. 7.2). In this case the atmosphere is non-selective to short-wave stellar radiation and long-wave planetary thermal radiation, and the consequential radiative-equilibrium temperature field features approximately vertical isotherms. This vertical isotherms structure is especially coherent for fast-rotating experiments ($\Omega > 1$) due to the suppression of direct meridional advection by Hadley cells.

Figs. 7.8-7.9 show the results of experiments with $\mathcal{G} = 5$ (corresponding to the regime diagram of anti-greenhouse atmosphere shown in Fig. 7.3). The circulation regimes observed under this scenario are qualitatively similar to those found with $\mathcal{G} = 1$ as stated in the previous section. But the thermal structures are very different from those of $\mathcal{G} = 1$ in that most the stellar irradiation is absorbed by the upper atmosphere, making the atmosphere heated from above like Earth's oceans. This leads to a highly statically stable stratification, which is reflected by the larger potential temperature gradient along the vertical direction, compared to experiments with $\mathcal{G} = 0$.

7.3 Comparison with PUMA-S results at Earth's obliquity

Since PUMA-G shares the dynamical core of PUMA-S, with the only difference being the representation of diabatic heating/cooling and convective adjustment, it will be insightful to compare the circulation regimes obtained using these two models when similar external parameters are adopted. Our results indicate that PUMA-G experiments with $\mathcal{G} = 0$ and $\varepsilon = 23.44°$ exhibit qualitatively similar circulation regimes with those obtained using PUMA-S, given the rotation rates are set to the same values as those in PUMA-S experiments.

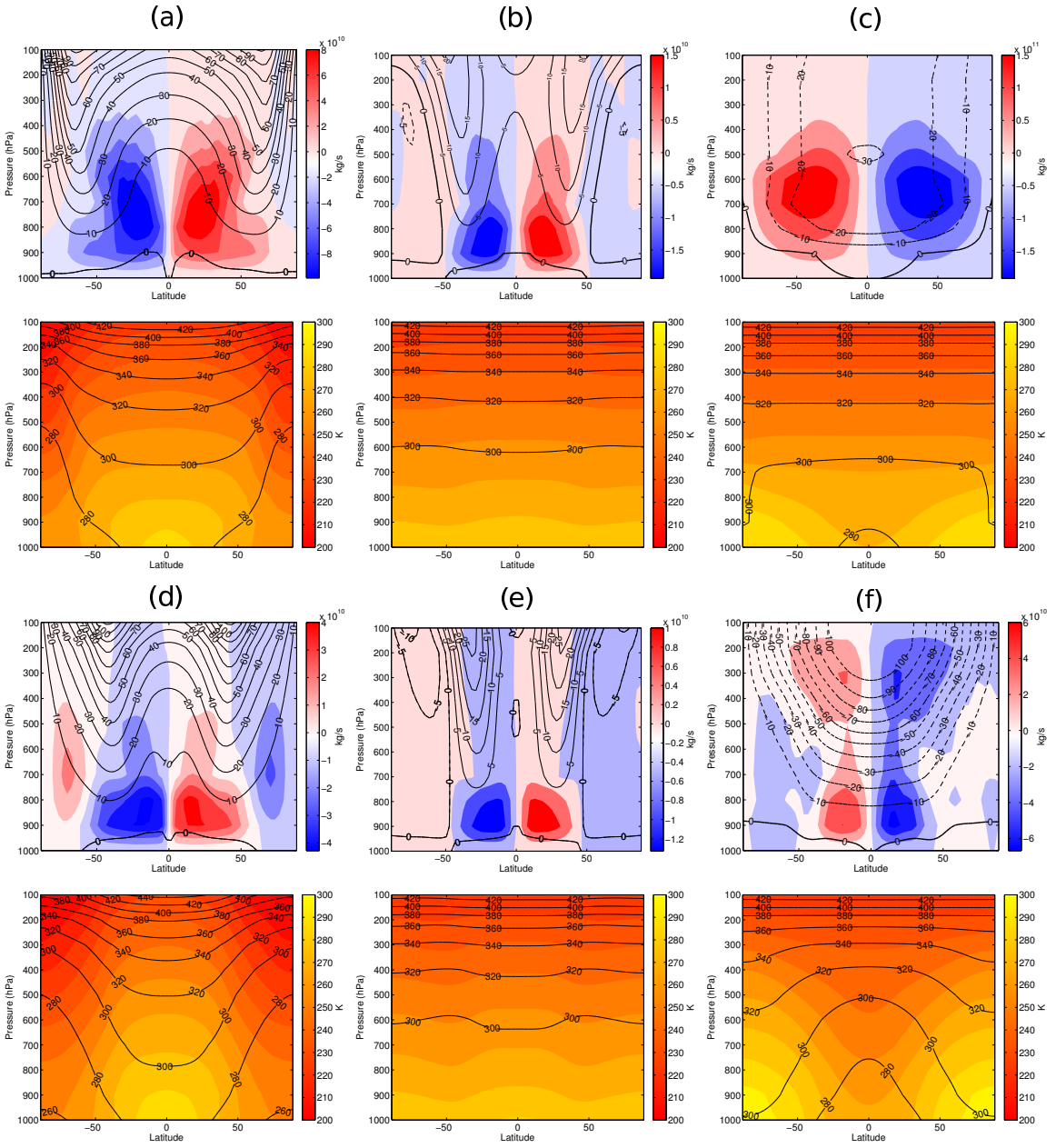

Figure 7.4: Zonal and temporal mean cross sections of zonal wind (contour, upper panel), meridional streamfunction (colour, upper panel), temperature (colour, lower panel) and potential temperature (contour, lower panel). All six experiments are atmospheres with $\mathcal{G} = 0$. $\Omega = 1/16$ for (a), (b) and (c); $\Omega = 1/4$ for (d), (e) and (f). Obliquity angle $\varepsilon = 23.44°$ for (a) and (d), 50.00° for (b) and (e), and 85.00° for (c) and (f).

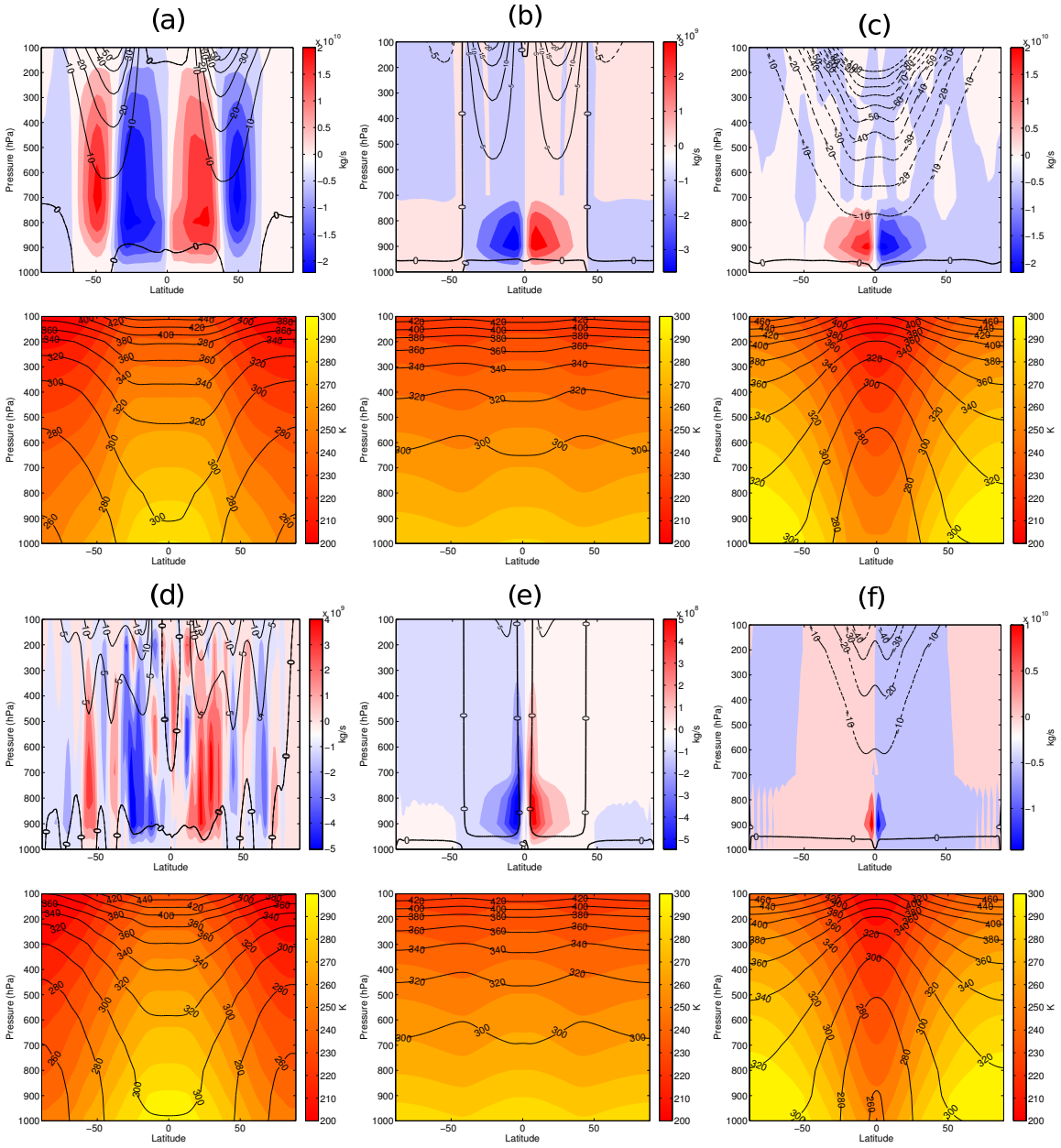

Figure 7.5: Same as Fig. 7.4, but with $\Omega = 1$ for (a), (b) and (c); $\Omega = 4$ for (d), (e) and (f). Obliquity angle $\varepsilon = 23.44°$ for (a) and (d), 50.00° for (b) and (e), and 85.00° for (c) and (f).

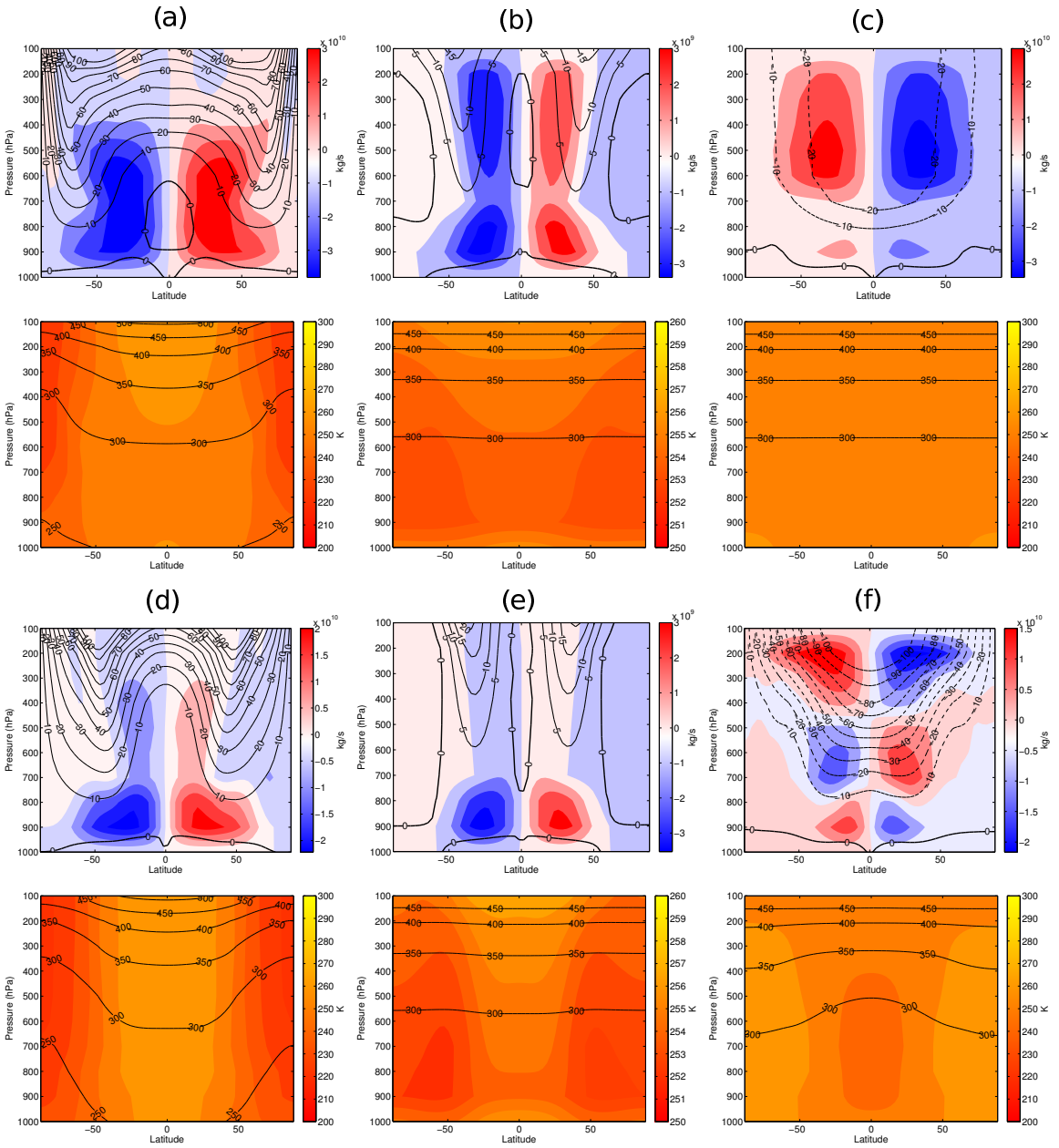

Figure 7.6: Zonal and temporal mean cross sections of zonal wind (contour, upper panel), meridional streamfunction (colour, upper panel), temperature (colour, lower panel) and potential temperature (contour, lower panel). All six experiments are atmospheres with $\mathcal{G} = 1$. $\Omega = 1/16$ for (a), (b) and (c); $\Omega = 1/4$ for (d), (e) and (f). Obliquity angle $\varepsilon = 23.44°$ for (a) and (d), 50.00° for (b) and (e), and 85.00° for (c) and (f).

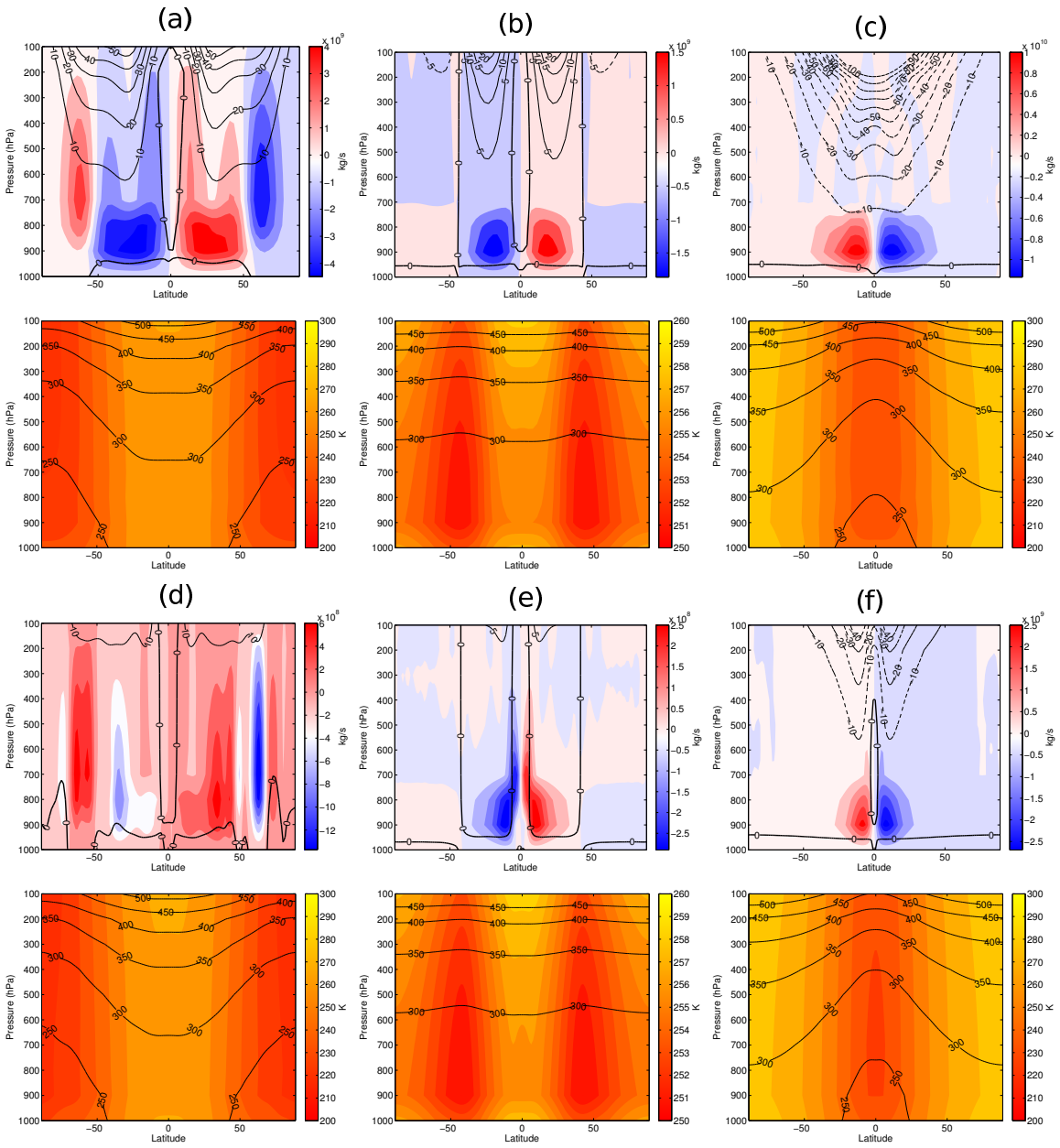

Figure 7.7: Same as Fig. 7.6, but with $\Omega = 1$ for (a), (b) and (c); $\Omega = 4$ for (d), (e) and (f). Obliquity angle $\varepsilon = 23.44°$ for (a) and (d), 50.00° for (b) and (e), and 85.00° for (c) and (f).

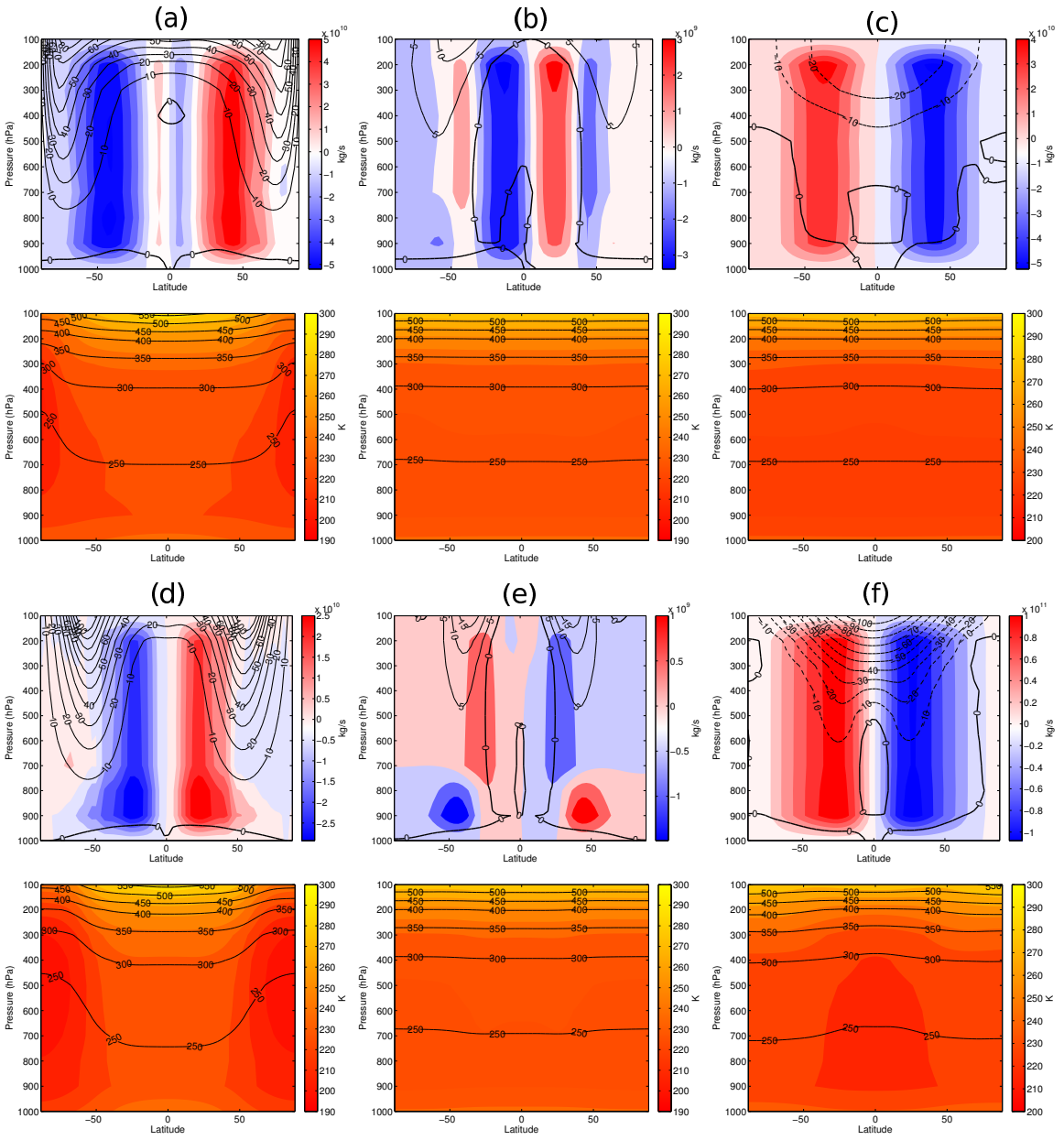

Figure 7.8: Zonal and temporal mean cross sections of zonal wind (contour, upper panel), meridional streamfunction (colour, upper panel), temperature (colour, lower panel) and potential temperature (contour, lower panel). All six experiments are atmospheres with $\mathcal{G} = 5$. $\Omega = 1/16$ for (a), (b) and (c); $\Omega = 1/4$ for (d), (e) and (f). Obliquity angle $\varepsilon = 23.44°$ for (a) and (d), $50.00°$ for (b) and (e), and $85.00°$ for (c) and (f).

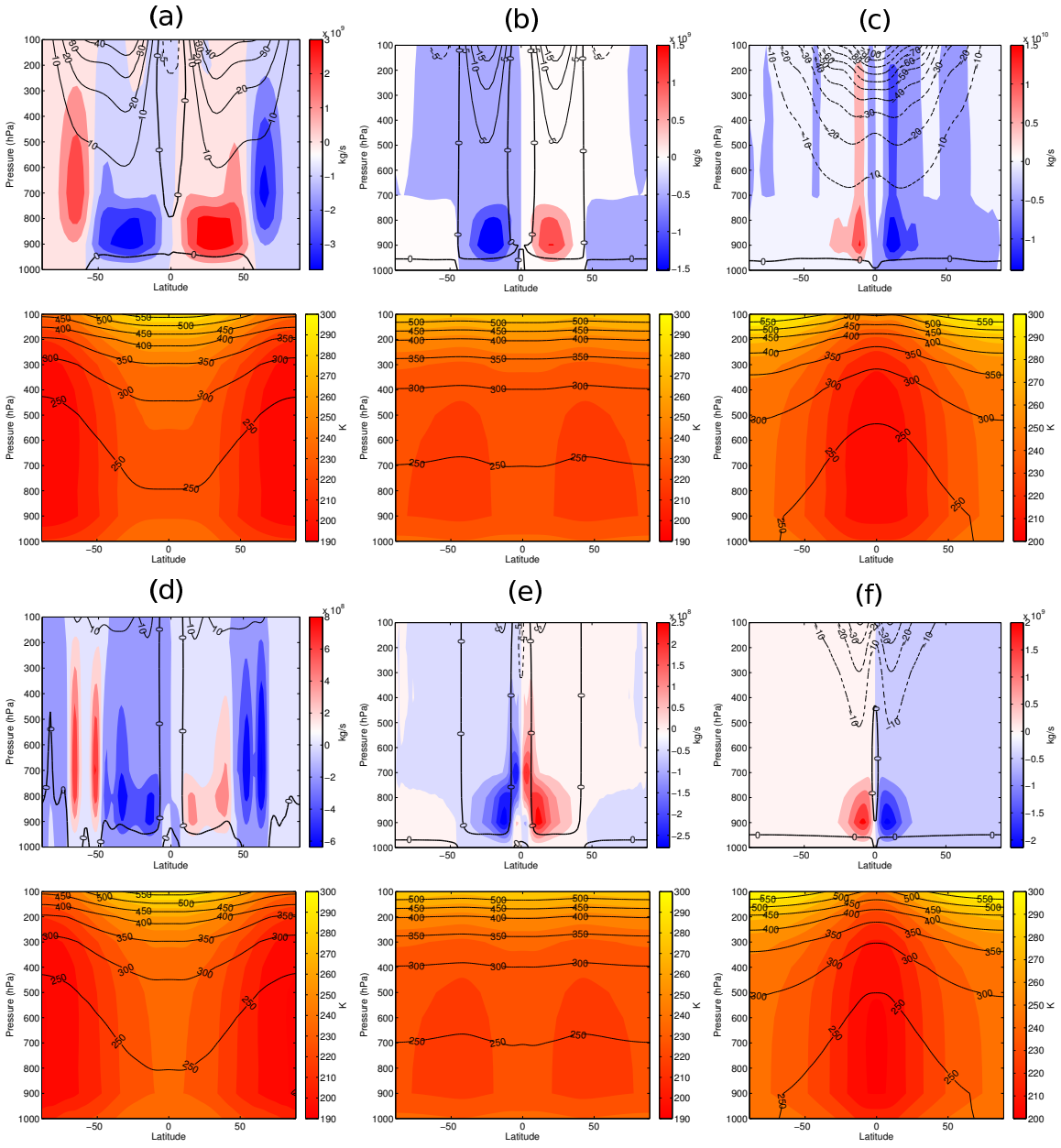

Figure 7.9: Same as Fig. 7.8, but with $\Omega = 1$ for (a), (b) and (c); $\Omega = 4$ for (d), (e) and (f). Obliquity angle $\varepsilon = 23.44°$ for (a) and (d), 50.00° for (b) and (e), and 85.00° for (c) and (f).

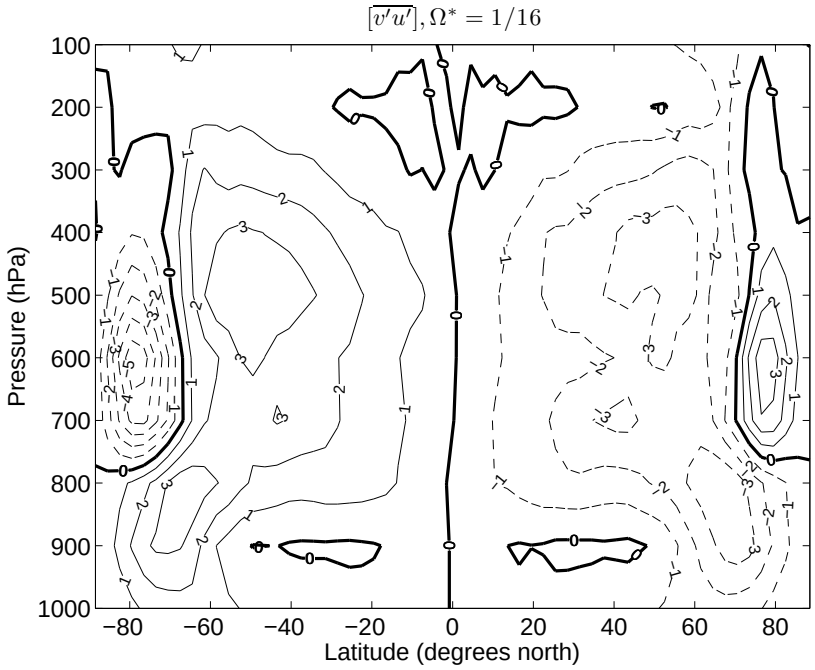

Figure 7.10: Zonal and temporal mean eddy momentum flux at statistically steady state, based on the experiment with $\Omega^* = 1/16$, $\mathcal{G} = 0$, and $\varepsilon = 23.44°$. Unit: $\mathrm{m^2 s^{-2}}$.

7.3.1 Super-rotation regime

The super-rotation regime obtained using PUMA-G at low rotation rates with $\varepsilon = 23.44°$ is similar to that obtained using PUMA-S in Chapter 3, except the lack of the closure of jet due to the different thermal structure of the upper atmosphere. The equator-ward meridional eddy momentum transport and E-P flux averaged over the last 360 Earth days of the simulation are shown in Figs. 7.10-7.11. The meridional eddy momentum transfer is predominantly equatorward, with maximum transfer at mid-troposphere ($\sim$ 500mb) as well as close to the ground. Zonal mean Ertel PV at 500mb and 700mb shown in Fig. 7.12 indicate that the eddies responsible for the super-rotation are generated by barotropic instability, which is similar to the mechanism observed in Chapter 3 using PUMA-S.

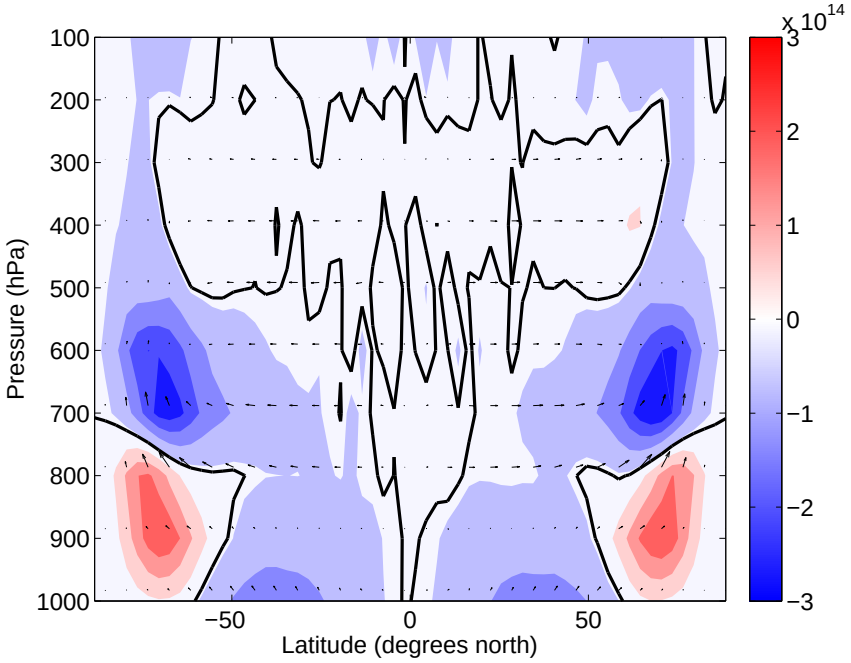

Figure 7.11: Temporal mean EP flux (vectors) and its divergence (contour) at statistically steady state, based on the experiment with $\Omega^* = 1/16$, $\mathcal{G} = 0$, and $\varepsilon = 23.44°$. Unit of divergence: m^3

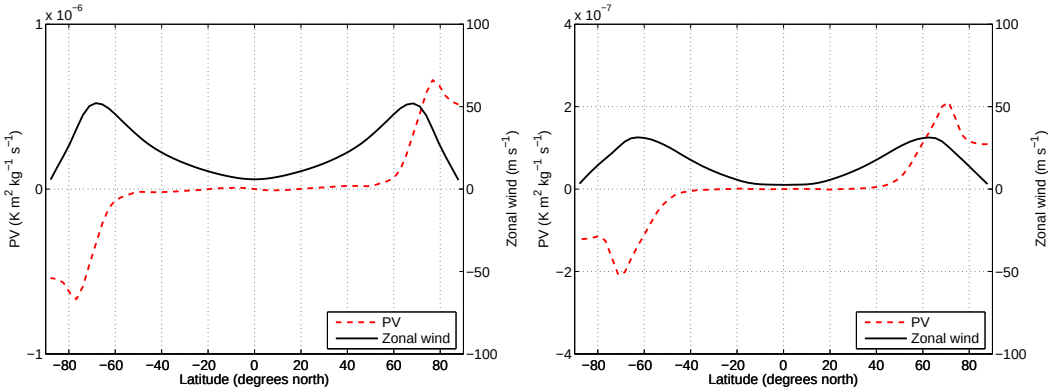

Figure 7.12: Temporal mean zonal wind and Ertel PV at 500mb (left) and 700mb (right), based on the experiment with $\Omega^* = 1/16$, $\mathcal{G} = 0$, and $\varepsilon = 23.44°$.

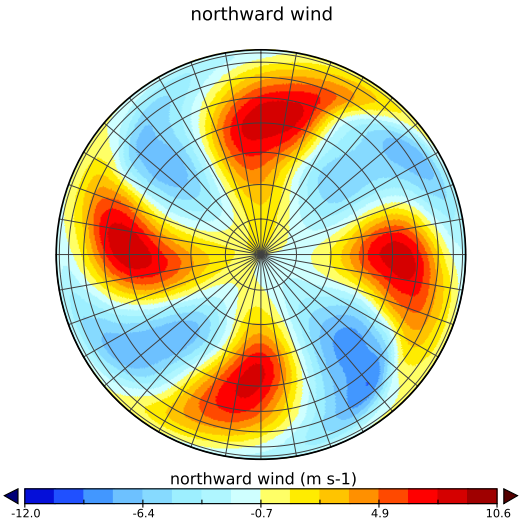

Figure 7.13: North polar view of the meridional wind (v) at the 500mb level, based on the experiment with $\Omega^* = 1/2$, $\mathcal{G} = 0$, and $\varepsilon = 23.44°$.

7.3.2 Regular baroclinic waves regime

Similar to the results shown in Chapter 3, regular baroclinic waves are found in experiments at intermediate rotation rates ($\Omega^* = 0.5$ and 0.25) with $\mathcal{G} = 0$ and $\varepsilon = 23.44°$. Fig. 7.13 shows a snapshot of the meridional wind at the 500mb level for the experiment at rotation rate of $\Omega^* = 0.5$ with $\mathcal{G} = 0$ and $\varepsilon = 23.44°$. A regular baroclinic wave with zonal wavenumber 4 can be seen. This is consistent with the regular wavenumber-4 regime found in the PUMA-S experiment at the rotation rate of $\Omega^* = 0.5$.

7.3.3 Irregular baroclinic waves regime

For experiments with even higher rotation rate, the planetary waves become irregular and chaotic which resembles the Earth's atmosphere. This is again similar to the trend observed in the corresponding PUMA-S experiments. Fig. 7.14 shows the the evolution of the flow field in the Northern Hemisphere over 7 Earth days for the experiment with rotation rate of $\Omega^* = 1$. It can be seen that the shape of the wavy structure changes irregularly with time in terms of both phase and amplitude, which

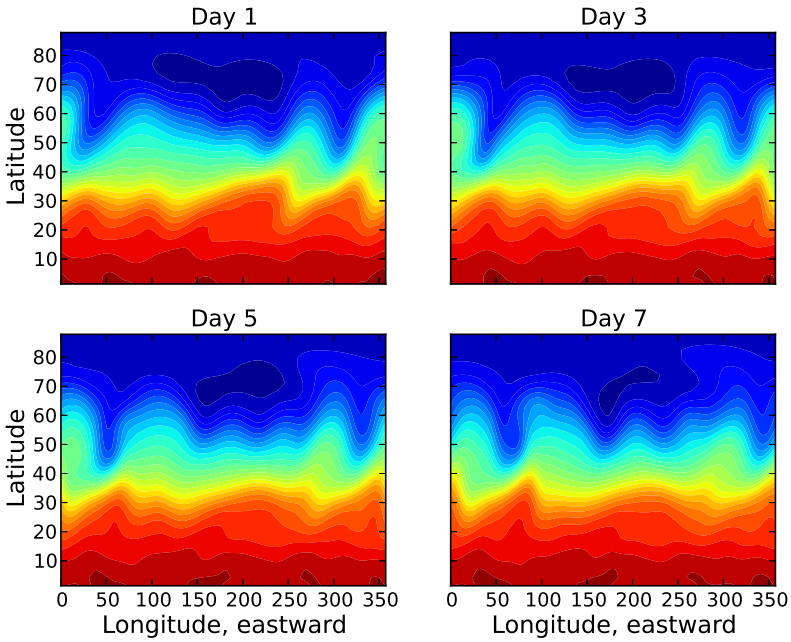

Figure 7.14: Latitude-longitude snapshots of the streamfunction at 500mb level in the Northern Hemisphere for the experiment with rotation rate of $\Omega^* = 1$, $\mathcal{G} = 0$, and $\varepsilon = 23.44°$ showing the evolution of the flow over one week (day 3241, 3243, 3245, and 3247 in the 10-year run).

is consistent with the results shown in Fig. 3.5 obtained using PUMA-S.

7.3.4 Multiple-jet regime

Similar to the results shown in Chapter 3, a multiple jet regime is found in experiments at fast rotation rates ($\Omega^* > 2.0$) with $\mathcal{G} = 0$ and $\varepsilon = 23.44°$. Fig. 7.15 shows a latitude-longitude snapshot of the zonal wind on the 200mb level, based on the experiment with $\Omega^* = 4$, $\mathcal{G} = 0$ and $\varepsilon = 23.44°$. Combined with Fig. 7.5(d), it can be seen that each hemisphere has three jets. The corresponding vertically averaged kinetic energy spectrum shown in Fig. 7.16 has similar logarithmic slopes with that obtained using PUMA-S as shown in Fig. 5.8, with -3 slope for the eddy/residual spectrum and -7 slope for the zonal mean spectrum. Fig. 7.17 shows the corresponding spectral KE flux defined in Chapter 5. The spectral flux is dominated by

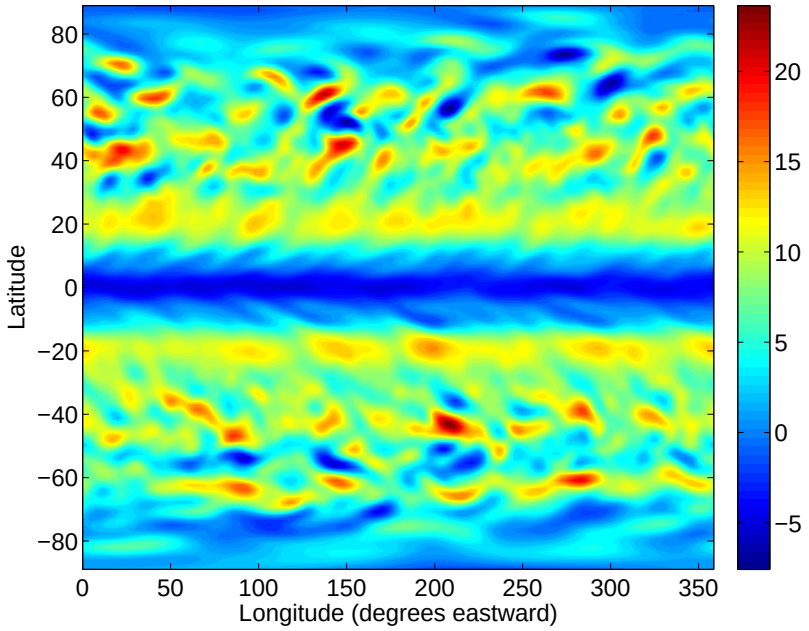

Figure 7.15: Snapshot of zonal wind u on 200mb level of the experiment with $\Omega^* = 4$, $\mathcal{G} = 0$ and $\varepsilon = 23.44°$. Unit: m/s.

negative values (which refers to upscale transfer of KE) over the wavenumber range of $n < 45$, contributed mainly by eddy-eddy interactions over $10 < n < 45$ and by eddy-zonal mean interactions over $n < 10$. Such "handing off" phenomenon has also been found by Burgess et al. (2013). This indicates that the mechansim of jet formation is similar in this case to that found with PUMA-S experiments, for which direct eddy-mean flow interaction tends to be primarily responsible.

7.4 Regimes at obliquity of $50°$ and $85°$

7.4.1 Axisymmetric regime

Experiments with a fast rotation rate and intermediate obliquity angle $\varepsilon = 50°$ tend to equilibrate into a wave-free axisymmetric circulation regime. The radiative equilibrium temperature field for obliquity angle of $\varepsilon = 50°$ has its lowest surface temperature at mid-latitudes, which enables the development of two thermally-direct circulation

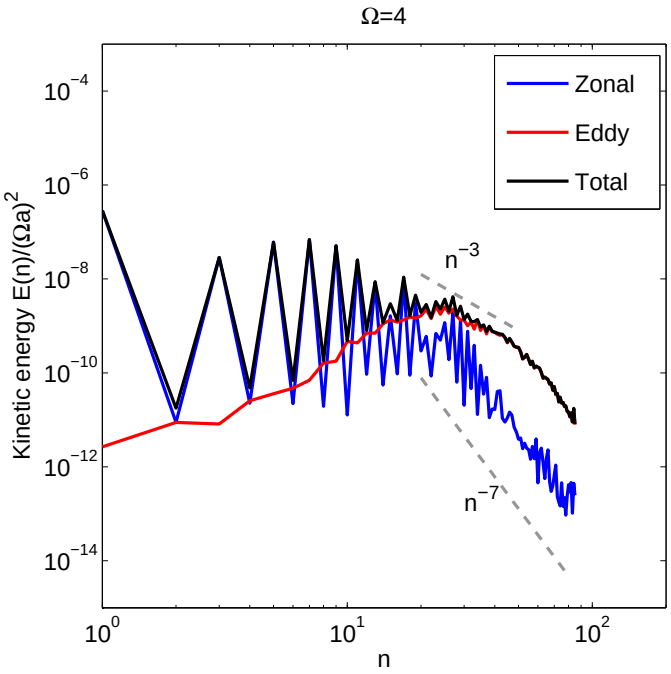

Figure 7.16: KE spectrum with respect to spherical wavenumber n for the experiment of $\Omega^* = 4$, $\mathcal{G} = 0$ and $\varepsilon = 23.44°$ with horizontal resolution T85, scaled by $\Omega^2 a^2$. The black curve represents the total KE spectrum, the blue curve the zonal spectrum, and the red curve the eddy spectrum. Grey dashed slope lines represent the corresponding power-laws as indicated.

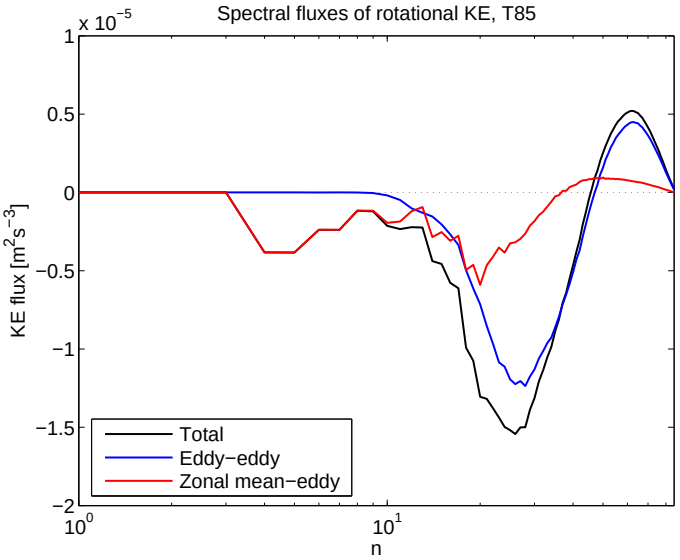

Figure 7.17: Spectral transfer fluxes of KE for the experiment of $\Omega^* = 4$, $\mathcal{G} = 0$ and $\varepsilon = 23.44°$ with horizontal resolution T85. The black curve represents the total transfer rate. The red curve represents the contribution from eddy-zonal mean interactions. The blue curve represents the contribution from pure eddy-eddy interactions.

cells in each hemisphere. The higher latitude region is characterised by a thermally-direct "polar" cell with upwelling over the poles and downwelling over mid-latitudes, leading to a weak retrograde jet near $50 - 60°$N/S. The lower latitude region is dominated by a classic Hadley cell driven by the temperature difference between the warm equator and the cool mid-latitudes. Prograde sub-tropical jets are formed due to the upper branch of the Hadley cell carrying angular momentum polewards. There are two external factors setting the extent of the Hadley cell in the scenarios with obliquity angle of $\varepsilon = 50°$. One is the surface temperature minimum point at the mid-latitudes ($\sim 45°$). The other is the Coriolis parameter f, the effect of which on Hadley cell extent has been thoroughly investigated by previous analytical/numerical studies (e.g. see Held & Hou (1980) and the review by Schneider (2006)). For experiments with a relatively slow rotation rate ($\Omega^* < 1$), the Hadley cell can expand to higher latitudes, rendering a stronger sub-tropical jet which easily becomes barotropically unstable. For experiments with faster rotation rate, the Hadley cell is highly limited by the strong planetary rotation, and the corresponding sub-tropical jet is found at latitudes lower than those in slow rotation rate experiments. This leads to a much weaker sub-tropical jet in these experiments which tends to be barotropically stable.

Fig. 7.18 shows the zonal mean Ertel PV and zonal wind on the 500mb level for experiments with $\Omega^* = 4$, $\varepsilon = 50°$, and $\mathcal{G} = 0$ (a), 1 (b), 5 (c). There is no sign of a PV extremum within the planetary domain (PV on other pressure levels have also been plotted (not shown) and checked, and no PV extremum was found), indicating that the atmosphere is barotropically stable according to the Rayleigh-Kuo criterion.

7.4.2 Baroclinic waves at $\varepsilon = 50°$

Experiments with lower rotation rates ($\Omega^* < 1$) at intermediate obliquity $\varepsilon = 50°$ are characterised by non-axisymmetric circulations with baroclinic waves in the ex-

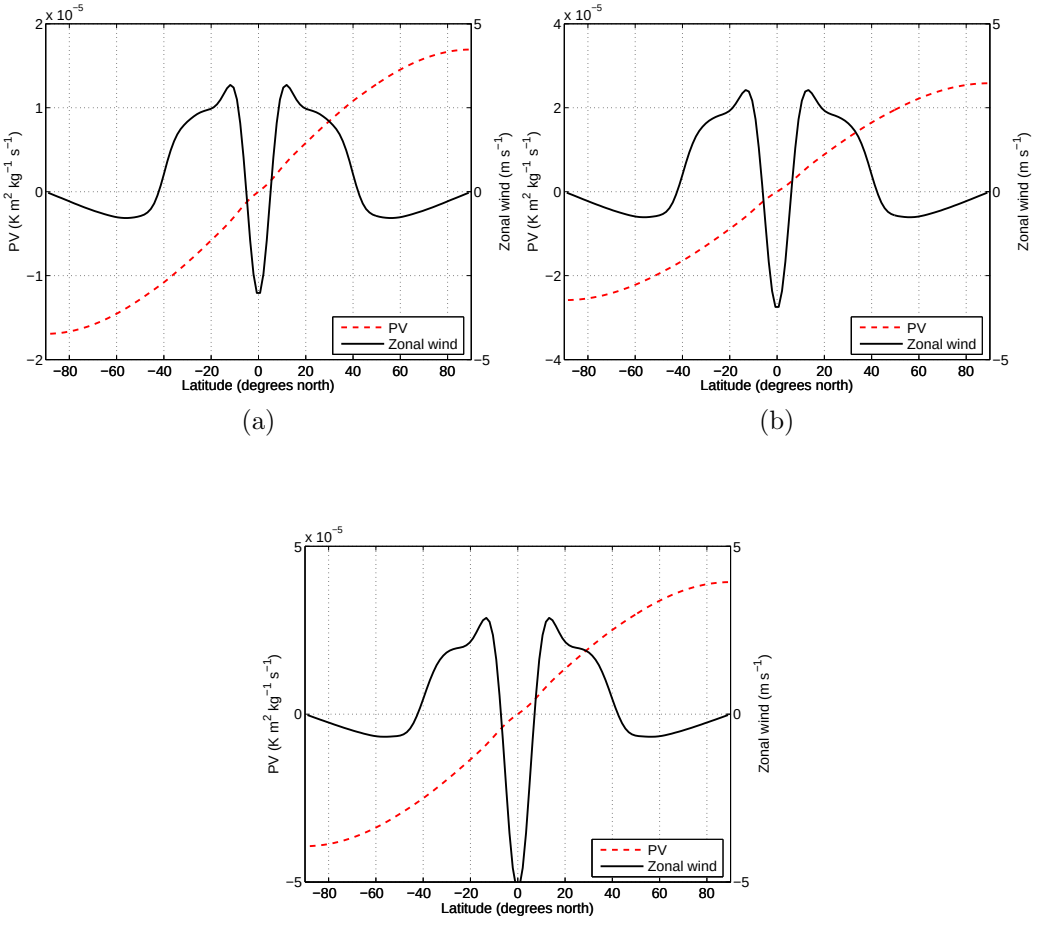

Figure 7.18: Zonal and temporal mean of Ertel PV (red dash line) and zonal wind (black solid line) at 500mb for experiments with $\Omega^* = 4$, $\varepsilon = 50°$, and (a) $\mathcal{G} = 0$; (b) $\mathcal{G} = 1$; (c) $\mathcal{G} = 5$.

tratropics. The surface temperature minimum at mid-latitude leads to $\partial T/\partial y < 0$ in the lower latitudes and $\partial T/\partial y > 0$ in the higher latitudes. Such a temperature configuration enables two separate baroclinic zones in each hemisphere. Fig. 7.19 shows snapshots of latitude-longitude zonal wind maps at the 200mb for experiments with $\mathcal{G} = 0$, $\varepsilon = 50°$. The extratropical region features a westerly baroclinic zone along the lower latitudes and an easterly baroclinic zone along the higher latitudes. Equatorial super-rotation, as found in experiments with similar rotation rates, $\mathcal{G}$ and $\varepsilon = 23.44°$, is absent in these runs with intermediate obliquity. This is due to the weaker extratropical prograde jets, which are less efficient at generating eddies to transport momentum equatorwards. Fig. 7.20 shows the Fourier amplitude of the temperature anomaly with respect to latitude and zonal wavenumber. The dominating wavenumber decreases with rotation rate, from $3 \sim 4$ at $\Omega^* = 1/2$ to $1 \sim 2$ at $\Omega^* = 1/16$, which is consistent with the scaling of Rossby deformation radius and the trend observed in PUMA-S experiments.

7.4.3 Sub-rotation regime at high obliquity

Experiments with obliquity angle $\varepsilon = 85°$ are characterised by significant equatorial and global sub-rotation. The radiative-convective equilibrium temperature field with $\varepsilon = 85°$ has warm poles and cold equator, inducing a thermally-direct "polar" cell that expands into the lower latitudes. The associated jets formed in association with the angular-momentum-conserving upper branch of the cell is located near the equatorward flank of the cell. For experiments with relatively slow rotation rate, such cells can reach the equator, leading to the merging of the two jets at the equator. For experiments with faster rotation rate, the stronger Coriolis effect hinders the equatorward expansion of the "polar" cell as well as the merging of the associated jets. Such trends can be appreciated from Figs. 7.4-7.9 in which the separation of jets is well-defined in runs with $\Omega = 4$.

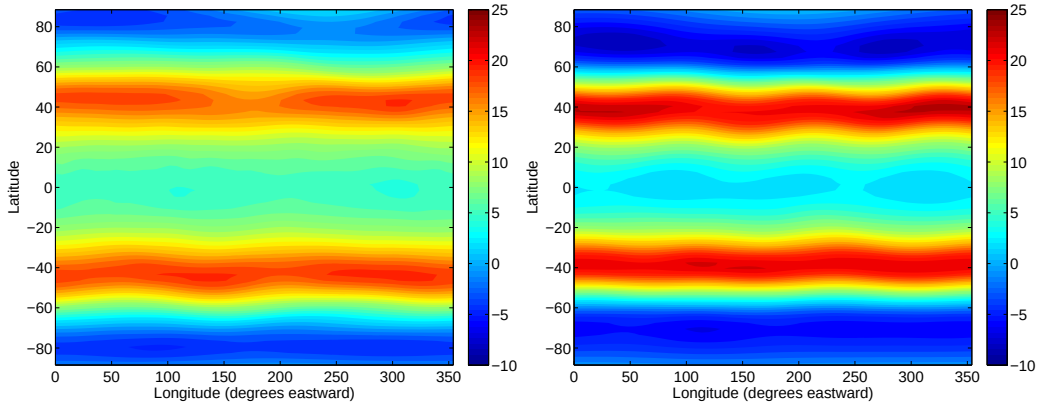

(a) (b)

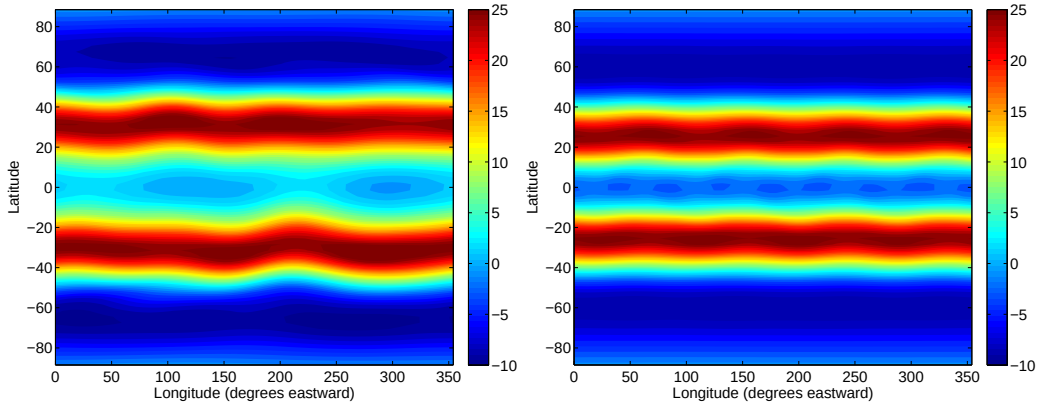

(c) (d)

Figure 7.19: Latitude-longitude snapshot of zonal wind u on 200mb level. Unit:m/s. $\mathcal{G} = 0$, $\varepsilon = 50°$ and (a) $\Omega^* = 1/16$; (b) $\Omega^* = 1/8$; (c) $\Omega^* = 1/4$; (d) $\Omega^* = 1/2$.

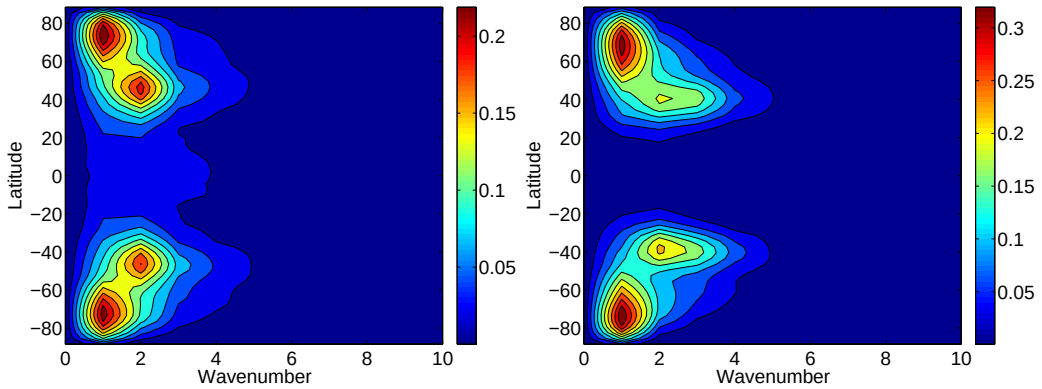

(a) (b)

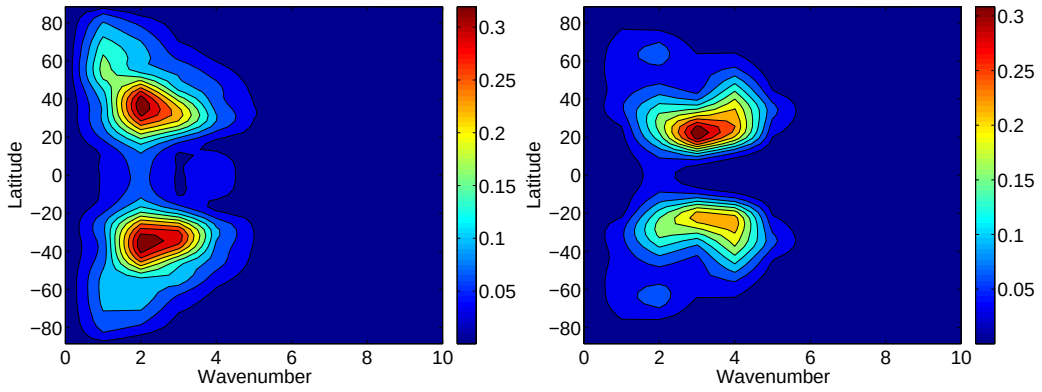

(c) (d)

Figure 7.20: Latitude-zonal wavenumber map of Fourier amplitude of temperature anomaly relative to zonal mean on 200mb level. Unit: K. $\mathcal{G} = 0$, $\varepsilon = 50^\circ$ and (a) $\Omega^* = 1/16$; (b) $\Omega^* = 1/8$; (c) $\Omega^* = 1/4$; (d) $\Omega^* = 1/2$.

The obliquity of $\varepsilon = 85°$ tested in our experiments is not very different from the obliquity angle of Uranus (98°) The observed atmospheric circulation over the cloud level of Uranus is characterised by a retrograde equatorial jet $\sim$ 100 m/s with two prograde mid-latitude jets $\sim$ 200 m/s (Hammel et al. (2005)). This is fundamentally different from the sub-rotation regime found in our experiments which has no prograde extratropical jets, no matter what values of $\mathcal{G}$ and Ω are used. One possible explanation is that the seasonal cycle might play an important role in shaping the global circulation regime when obliquity is very high, which is a process not yet represented in PUMA-G.

The temperature fields from experiments with $\varepsilon = 85°$ show strong dependence on the planetary rotation rate. As shown in Figs. 7.4-7.5, the meridional temperature gradient decreases with rotation rate for experiments with $\varepsilon = 85°$ ((c) and (f) in each figure). The upper atmosphere is almost isothermal along the meridional direction for experiments with $\Omega^* < 1$. This is similar to the trend observed in experiments with $\varepsilon = 23.44°$ ((a) and (d) in each figure).

7.5 Effects of greenhouse parameter $\mathcal{G}$

The effect of greenhouse parameter $\mathcal{G}$ is mainly on the static stability of the atmosphere, which then has a significant influence on the Rossby deformation radius $L_D = NH/f$, where the buoyancy oscillation (Brunt-Väisälä) freqency $N = \sqrt{\frac{g}{\theta}\frac{d\theta}{dz}}$ is ultimately determined by the vertical stratification.

Fig. 7.21 shows the temporally averaged latitude-zonal wavenumber maps of the Fourier amplitude of temperature field at 200mb for experiments with $\Omega = 1$, $\varepsilon = 23.44°$ and $\mathcal{G} = 0, 1, 5$. The dominant zonal wavenumber components for $\mathcal{G} = 0$ is a broad range of $1 \sim 4$, whereas the runs with $\mathcal{G} = 1$ and 5 are dominated by zonal wavenumber 1 planetary wave. This decrease of dominant zonal wavenumber

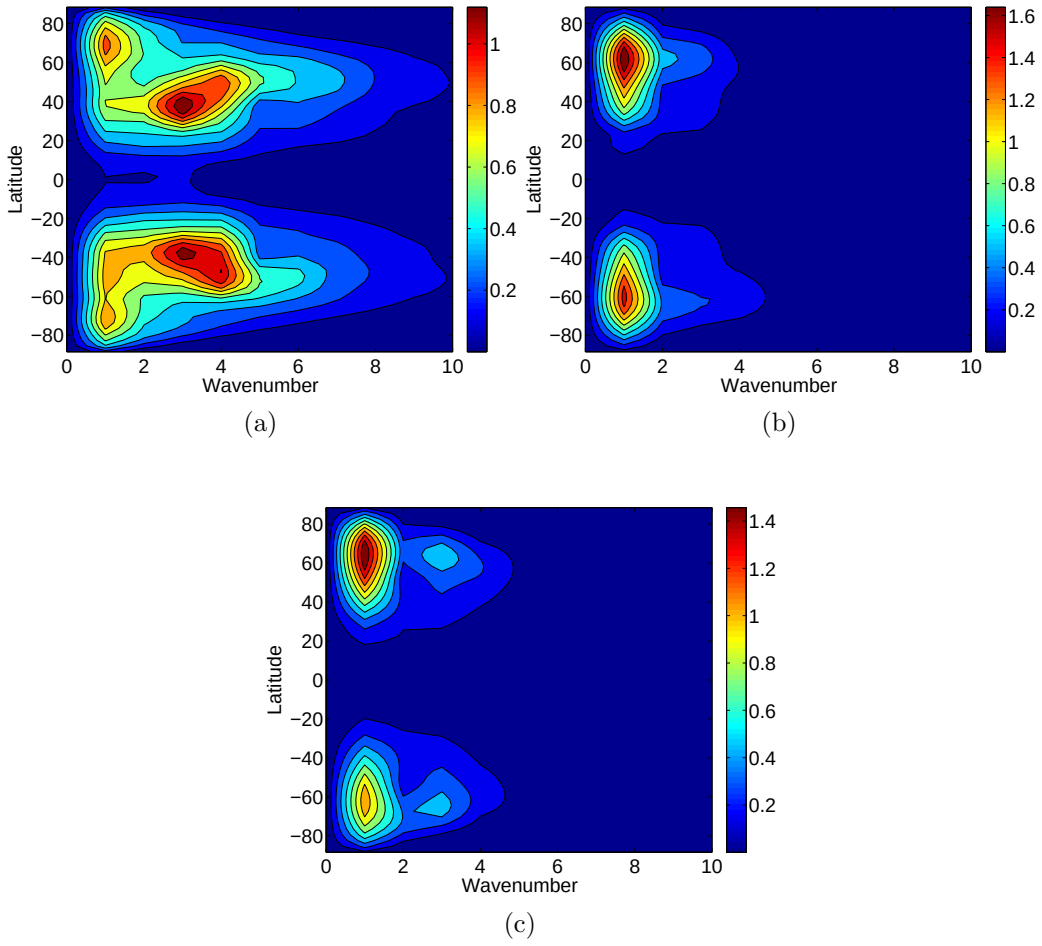

Figure 7.21: Latitude-zonal wavenumber maps of Fourier amplitude of temperature field at 200mb level for experiments with $\Omega = 1$, $\varepsilon = 23.44°$, and (a) $\mathcal{G} = 0$; (b) $\mathcal{G} = 1$; (c) $\mathcal{G} = 5$

with increasing static stability can be explained by the dependence of L_D on N. For experiments with $\mathcal{G} = 1$, the atmosphere can be viewed as approximately isothermal along the vertical direction. For experiments with $\mathcal{G} = 5$, the atmosphere is essentially heated from above. Both scenarios can lead to much more stable vertical stratification than that with $\mathcal{G} = 0$, in which case the atmosphere is heated from below by the surface. The statically more stable stratification of experiments with $\mathcal{G} = 1$ and 5 means the buoyancy oscillation frequency N is larger, which consequentially leads to larger Rossby deformation radius L_D. Therefore the dominating wavenumber tends to be smaller for experiments with $\mathcal{G} = 1$ and 5.

7.6 Atmospheric Energetics

7.6.1 Heat transfer efficiency

Following the discussions in Chapter 3, the meridional heat transport efficiency by dynamical processes is reflected by the scaled isentropic slope, which is defined as the ratio of the globally averaged isentropic slope at radiative-convective equilibrium and the isentropic slope obtained with dynamic transport. This scaled isenstropic slope can be viewed as an index of the heat transport efficiency in that large values of scaled isentropic slope correspond to more efficient dynamic heat transport. Fig. 7.22 shows the comparison of the scaled isentropic slopes obtained from experiments with obliquity of $\varepsilon = 23.44°$ at various rotation rates and different values of the greenhouse parameter $\mathcal{G}$. It can be seen that slowly rotating atmospheres tend to be more efficient at redistributing heat under all three scenarios of different $\mathcal{G}$. Such a coherent trend with respect to rotation rate is consistent with the results discussed in Chapter 3 obtained using PUMA-S. Another trend that can be seen in Fig. 7.22 is that the effect of rotation rate tends to be more prominent for runs with greenhouse atmospheres than those with neutral- or anti-greenhouse atmospheres. This is probably related to the associated stability of stratification. As the value of G increases, the atmosphere becomes less greenhouse-dominated and more statically stable, which tends to suppress the development of waves and eddies to transport heat efficiently.

7.6.2 Lorenz energy cycle

The Lorenz energy cycle has been an important diagnostic of the global atmospheric energetics since first proposed by Lorenz (1955). In Chapter 4, Lorenz energy cycles were calculated for the representative PUMA-S experiments at various rotation rates, which revealed a number of trends regarding the atmospheric energy conversion with implications for the principal eddy-generating mechanism and dominating circulation

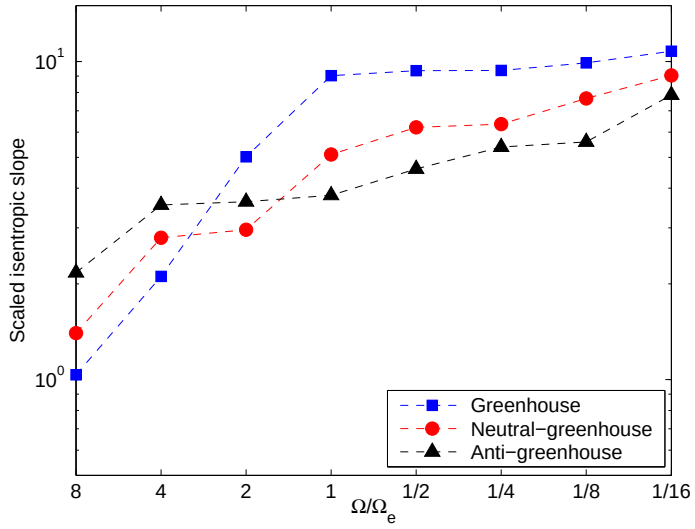

Figure 7.22: The scaled isenstrope slope with respect to the rotation rate Ω^*, reflecting the decreasing trend in heat transport efficiency for experiments with $\varepsilon = 23.44°$. Blue squares represent runs with $\mathcal{G} = 0$. Red circles represent runs with $\mathcal{G} = 1$. Black triangles represent runs with $\mathcal{G} = 5$.

regimes. Since the corresponding ranges of defining dimensionless parameters are also covered by the PUMA-G experiments, it is natural to conduct a similar analysis on such energy conversion processes with the aim of comparing the physical processes of these two models from the energetics perspective.

Following the formulation of full (ageostrophic) energy and conversion terms stated in Chapter 4, the PUMA-G counterpart of the Lorenz energy cycle shown in Fig. 4.6 (i.e. experiments of various rotation rates with $\mathcal{G} = 0$ and $\varepsilon = 23.44°$) is shown in Fig. 7.23. Despite the significant difference in representing diabatic heating/cooling processes in PUMA-S and PUMA-G, their energetics signatures in terms of Lorenz energy cycle are generally consistent. As can be seen in Fig. 7.23, the direction of conversion between KZ and KE changes between $\Omega^* = 1/2$ and $\Omega^* = 1/4$, indicating that barotropic instability begins to become dominant at a global scale for rotation rates slower than or equal to $\Omega^* = 1/4$. The rate of energy conversion following the route of barotropic instability KZ $\rightarrow$ KE exceeds that following the route of baroclinic instability AZ $\rightarrow$ AE $\rightarrow$ KE at the rotation rate of $\Omega^* = 1/16$, which

is consistent with the results of PUMA-S experiments as well (in Fig. 4.6). Along with the change of direction of the CK term (conversion between KZ and KE) at $1/2 < \Omega^* < 1/4$, the conversion between AZ and KZ also changes direction at $1/2 < \Omega^* < 1/4$, which is again consistent with the PUMA-S results in Fig. 4.6. The conversion route of AZ $\rightarrow$ KZ at rotation rates lower than $\Omega^* = 1/4$ indicates that thermally-direct circulation cells (which are mainly contributed by Hadley cells) become more important than the thermally-indirect cells (which are mainly Ferrel cells in baroclinic zones) at such slow rotation rates.

The trend of globally averaged kinetic energy and available potential energy reflected in Fig. 7.23 also demonstrates similarities with that observed in Fig. 4.6. In all of these experiments, it is found that most of the energy is stored in terms of available potential energy, with only a small fraction being converted into kinetic energy. As the planet rotates faster, more energy is stored as available potential energy, indicating that atmospheres of rapidly rotating planets become less efficient at converting available potential energy into kinetic energy.

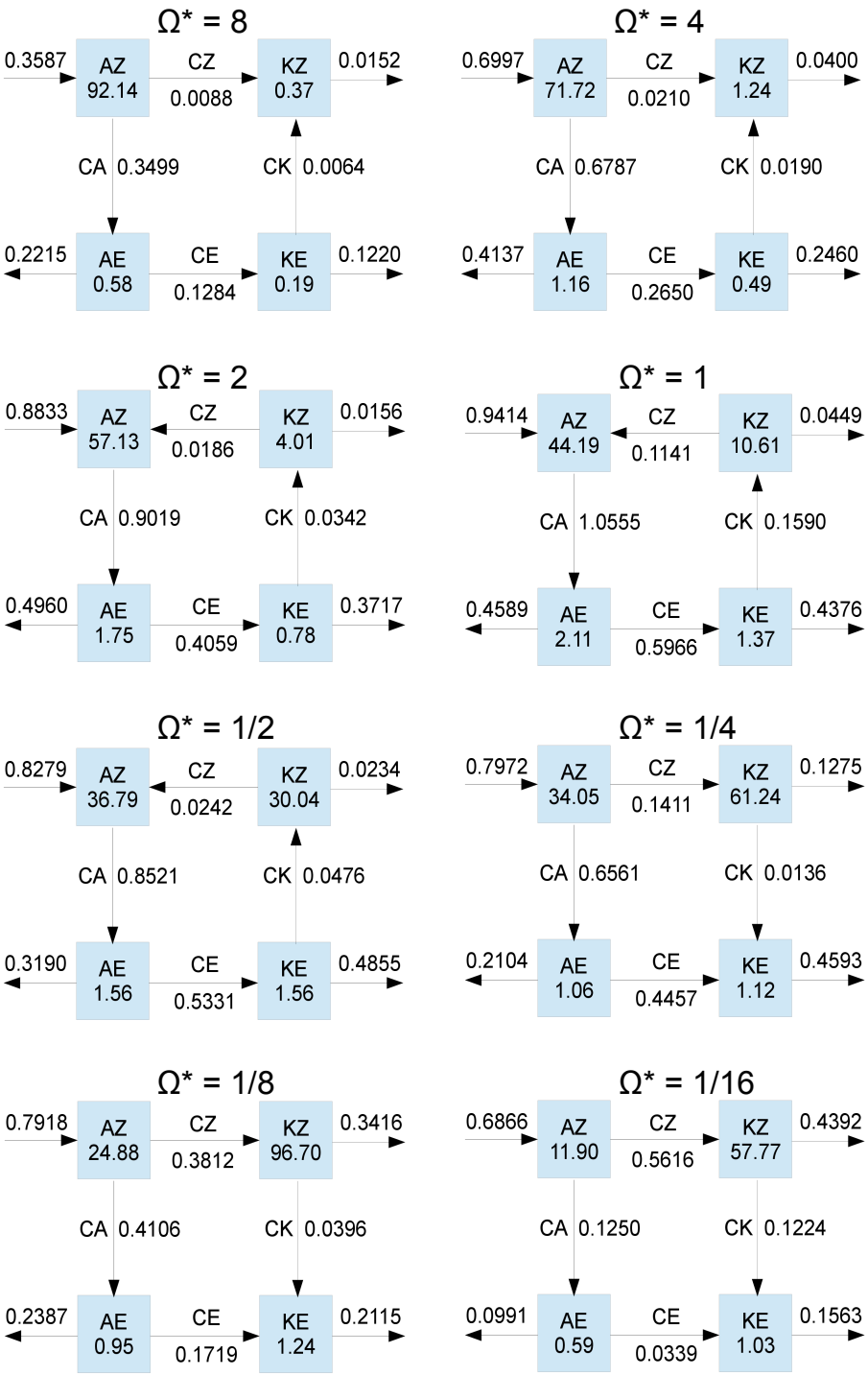

Figure 7.23: Lorenz energy cycles obtained from experiments with different rotation rates. Numbers in boxes represent globally averaged energy (in $10^5 \mathrm{Jm}^{-2}$). Conversion rates are in unit of Wm^{-2}.

Chapter 8

Experiments on tidally-locked planets

Tidal locking occurs when the gravitiational gradient makes one astronomical body rotate synchronously around the other, such that one body always presents the same face to its parent object. A well-known example is the Moon, which is tidally locked to the Earth so that only one side of the Moon is visible to observers on the Earth. For a pure two-body problem, such a tidally locked state is essentially the ultimate equilibrium state. However, the time to reach this state may well exceed the lifetime of the corresponding planetary/stellar system. Thus most of the observed tidal locking scenarios occur for close-in planets or satellites where tidal forces are strong. Given that a significant portion of the exoplanets detected so far are close-in planets (e.g. the so-called "hot Jupiters"), many of them are believed to be in a tidally locked state (e.g. Gliese 581b, Gliese 581c, see Esteves & Jayawardhana (2013)).

The study of circulation and climate on tidally-locked planets was pioneered by Joshi (1997), which investigated the impact of atmospheric mass on the tidally locked planetary climate, with the aim of finding the sensitivity of the range of the habitable zone to the atmospheric mass. A recent study by Merlis & Schneider (2010) then

focussed on the influence of planetary rotation rate and argued that planetary rotation can also shape the climate, especially the dayside-to- nightside heat transport efficiency. Both of these studies adopted GCMs with radiative schemes specifically tuned to model Earth-like atmosphere. For example, the model by Merlis & Schneider (2010) employed the long-wave optical depth representation by Frierson et al. (2006), which implicitly incorporates the optical depth variations associated with variations of water vapor concentration in the lower atmosphere. It is therefore of interest to use PUMA-G, which is designed to avoid such peculiar model assumptions, to study the circulation and climate of tidally-locked terrestrial planets so that results obtained are more generalisable. As Joshi (1997) and Merlis & Schneider (2010) investigated the influence of atmospheric mass and rotation rate respectively, this chapter will also study the relative importance of these two parameters on determining the atmospheric heat transport efficiency.

This chapter is organised as the following. Section 8.1 describes the modified PUMA-G radiative scheme which is capable of modelling insolation of a tidally-locked planet. Section 8.2 then shows the modelled climatological fields in terms of zonal and temporal mean. Section 8.3 compares the heat transport efficiency under various scenarios and concludes with a discussion of the relative importance of rotation rate and atmospheric mass on the heat transport efficiency.

8.1 Model and experiment setup

For fully tidally-locked planets, the planetary obliquity is zero due to the tidal dissipation. Therefore the local stellar zenith angle does not change with time. The incoming stellar irradiation at the top of the atmosphere can be formulated as:

$$S(\phi, \lambda) = S_0 \max(0, \cos(\phi)\cos(\lambda - \lambda_0)), \tag{8.1}$$

where ϕ and λ are latitude and longitude, S_0 the incoming stellar irradiation (in W/m^2) reaching the planet, and λ_0 the longitude of the substellar point[1]. In our experiments, $\lambda_0 = 0$ by definition so the substellar point in a (latitude, longitude) grid is simply $(0, 0)$.

Experiments were designed to test the effect of planetary rotation rate and atmospheric mass (in terms of surface pressure) on the general circulation and climate. Six combinations of $\Omega^* = \{1, 1/10\}$ and $p_s = \{0.1, 1, 10\}$ bar were tested and analysed. When changing surface pressure to values other than 1 bar, the atmospheric optical depth was varied simultaneously as optical depth was formulated to be proportional to pressure in PUMA-G. Therefore a thick atmosphere in terms of surface pressure is also optically thick for our model configuration.

8.2 Zonal mean diagnostics and climatology

Zonal-mean cross-sections of zonal wind, eddy momentum flux, and (potential) temperature of the experiments with different values of rotation rate and surface pressure are shown in Figs.8.1-8.2. By comparing plots (b), (d), and (f) in each figure, it can be found that the meridional temperature gradient is smaller for thicker atmospheres, indicating that a thicker atmosphere tends to be more efficient at dynamical heat transport from the equator to poles. Meridional temperature gradients are also smaller when rotation rate is decreased, as can be seen by comparing the temperature plots in Fig. 8.1 with their counterparts in Fig. 8.2, which can be understood as due to the inhibiting effect of Coriolis forces on meridional transport.

The zonal wind cross-section is dominated by equatorial super-rotation for all experiments. Stronger prograde winds are found in experiments with faster rotation rates and thinner atmospheres. The prograde wind maximum over the equator is mostly accompanied by equatorward eddy momentum fluxes, which maintains the

[1]The latitude of substellar point is always the equator for fully tidally-locked planets.

super-rotation. The mechanism of such equatorial super-rotation has been explained by Showman & Polvani (2011) in a shallow-water framework, based upon the classical Gill model (Gill (1980)). According to Showman & Polvani's study, the fixed inhomogeneous stellar heating on a tidally-locked planet between its day-side and night-side excites a pattern of stationary equatorial Rossby/Kelvin waves along latitude circles in the tropical region. It is a characteristic property of Rossby waves that positive (prograde) momentum can be transferred "up-gradient" into the source region of wave stirring/excitation, which in the case of tidally-locked planets is basically the equatorial region.

Fig. 8.3 shows temporal mean latitude-longitude maps of surface temperature of experiments with a surface pressure of 1 bar at fast ($\Omega^* = 1$) and slow ($\Omega^* = 0.1$) rotation rates. The surface temperature distribution is largely determined by the distribution of insolation, with higher temperatures on the day-side than on the night-side. The highest temperature, instead of being located right at the sub-stellar point, is located to the east of it by $\sim 20^\circ$ in longitude for $\Omega^* = 0.1$ and $\sim 30^\circ$ in longitude for $\Omega^* = 1$. This longitudinal offset of the temperature maximum, also found in various previous studies of tidally-locked exoplanets (see review by Showman et al. (2010) and references therein), is due to dynamical advection by the super-rotating equatorial wind, which is stronger when $\Omega^* = 1$ as shown in Figs. 8.1-8.2. The eastward group velocity of equatorial Kelvin waves may contribute to the displaced temperature maximum as well.

8.3 Heat redistribution by dynamical transport

In a radiative or radiative-convective equilibrium state, the temperature of the night-side planetary atmosphere is essentially 0 K as there is no source of heating from stellar irradiation. The observed surface temperature of the night side in our experiments

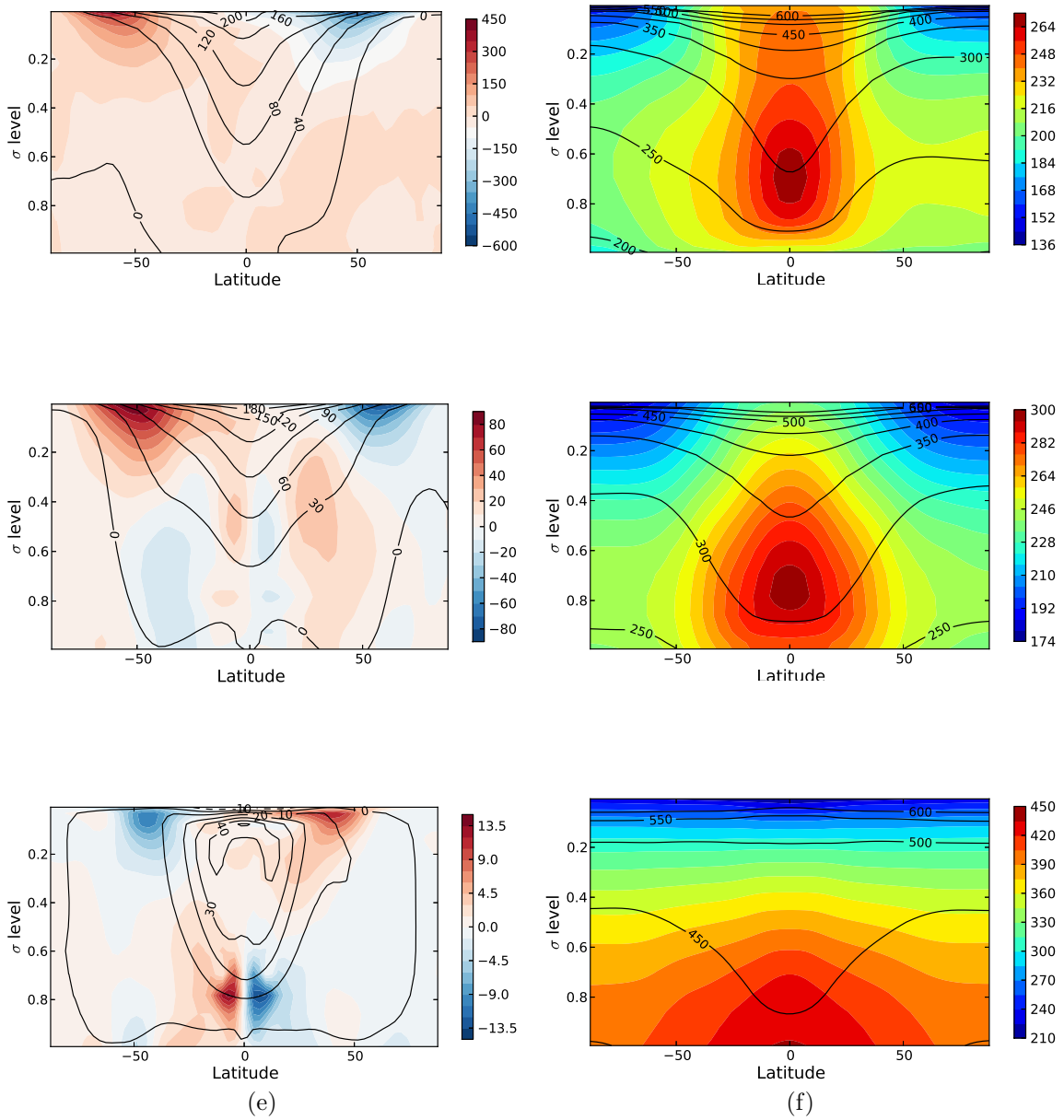

Figure 8.1: Left column: temporal and zonal mean of zonal wind u (contour lines, unit: m/s) and eddy momentum flux u^*v^* (color, unit: $\mathrm{m^2 s^{-2}}$); right column: temporal and zonal mean of temperature (contour lines, unit: K) and potential temperature (color, unit: K). (a)(b): $p_s = 0.1$ bar; (c)(d): $p_s = 1$ bar; (e)(f): $p_s = 10$ bar. $\Omega^* = 1.0$ for all plots.

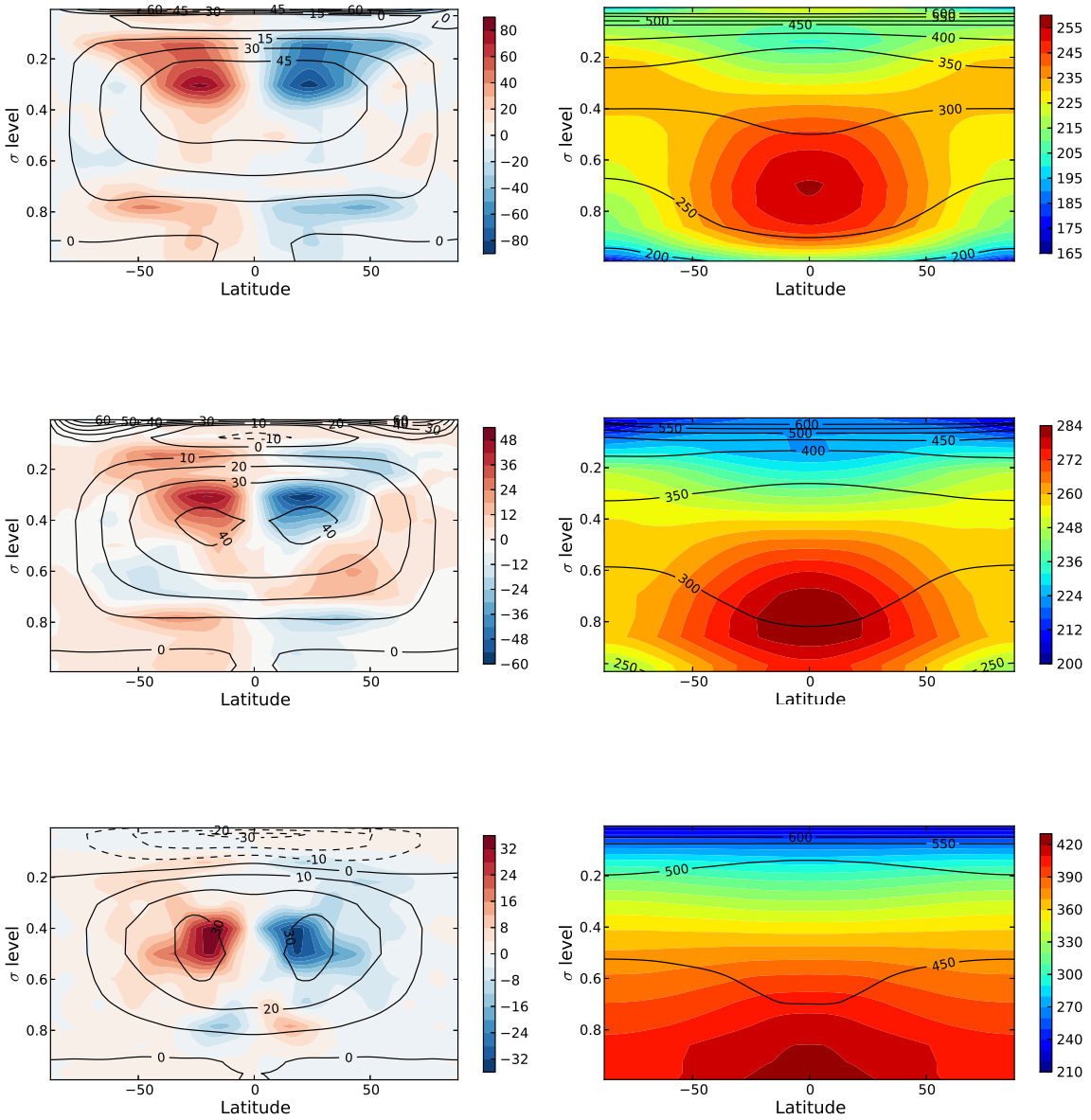

Figure 8.2: Same as Fig.8.1, but for $\Omega^* = 0.1$.

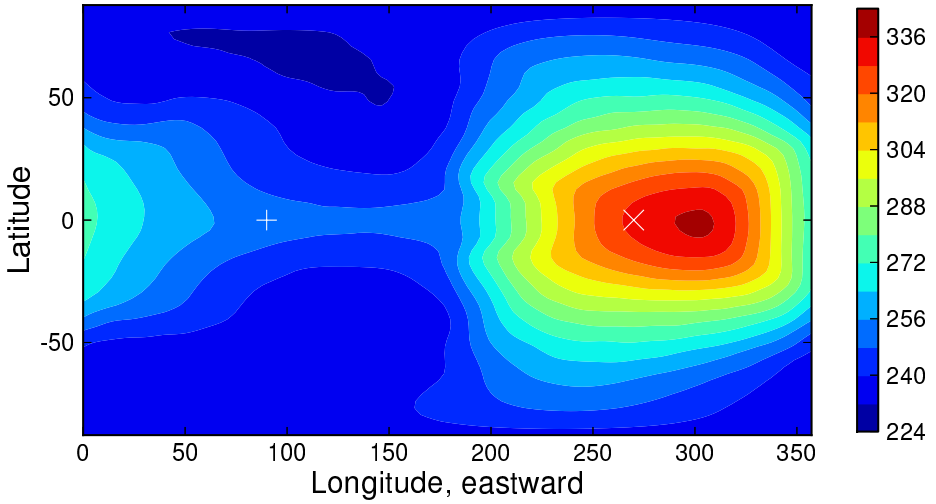

(a)

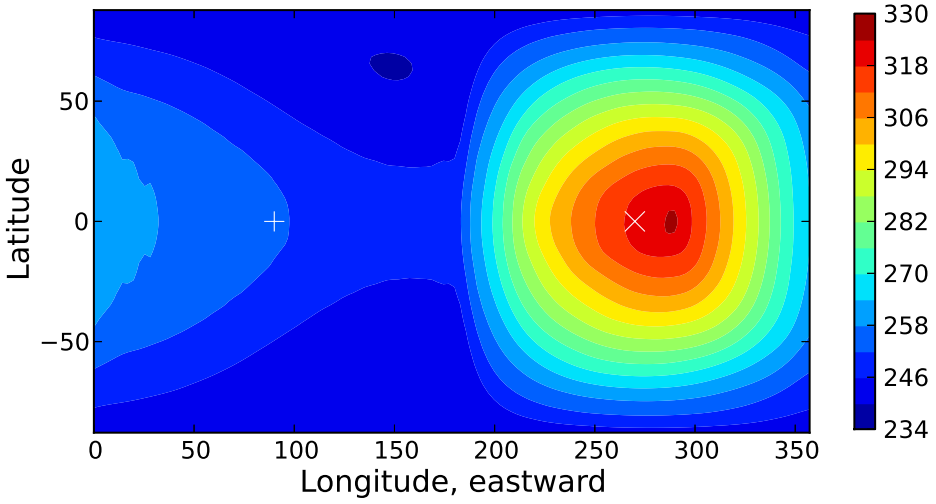

(b)

Figure 8.3: Surface temperature (unit: K) of experiments with surface pressure p_s = 1 bar and (a) $\Omega^* = 1$, (b) $\Omega^* = 0.1$. White X represents the sub-stellar point while white cross represents the anti-stellar point.

as shown in Fig. 8.3 is around 250 K, however, which clearly indicates that heat is redistributed efficiently both in the meridional (from the equator to poles) direction and in the zonal direction (from day side to night side), by dynamical advection. Fig. 8.4 shows the zonal mean cross-sections of temperature and potential temperature on the day side and night side respectively, based on the experiment with $\Omega^* = 1$ and $p_s = 1$ bar. The day-side temperature field features stronger equator-to-pole surface temperature difference than the night side. The night-side temperature field is characterised by a temperature inversion near the top of the boundary layer ($\sigma \sim 0.8$), with warm air over the colder boundary layer. This implies that dynamical transport is most efficient within the free atmosphere where winds are strong. Temperature in the planetary boundary layer of the night side is influenced largely by the strong radiative cooling of the surface.

A measure of the heat redistribution efficiency can be defined as $F_{\rm day}/F_{\rm night}$, where $F_{\rm day}$ represents the day-side outgoing longwave radiation (OLR) and $F_{\rm night}$ represents the night-side OLR. Both $F_{\rm day}$ and $F_{\rm night}$ are averaged over the day/night hemisphere. The dynamical heat redistrubtion is efficient when $F_{\rm day}/F_{\rm night} \sim 1$ and less so when $F_{\rm day}/F_{\rm night} > 1$.

Fig. 8.5 shows the OLR ratio $F_{\rm day}/F_{\rm night}$ based on a series of experiments with different values of rotation rate and surface pressure. It can be seen that for tidally-locked planets, the horizontal heat redistribution efficiency is strongly determined by surface pressure while planetary rotation rate only plays a marginal role. Thicker atmospheres are more efficient than thinner atmospheres at transporting heat from the day side to the night side. This can be understood by comparing the dynamic/advective timescale and the radiative timescale. The advective timescale can be estimated by $\tau_{adv} = a/U$, where a is the planetary radius, and U is a characteristic horizontal wind speed. The observed U as shown in Figs. 8.1-8.2 is mostly determined by rotation rate. Following James (1995) , if the atmosphere can be modelled

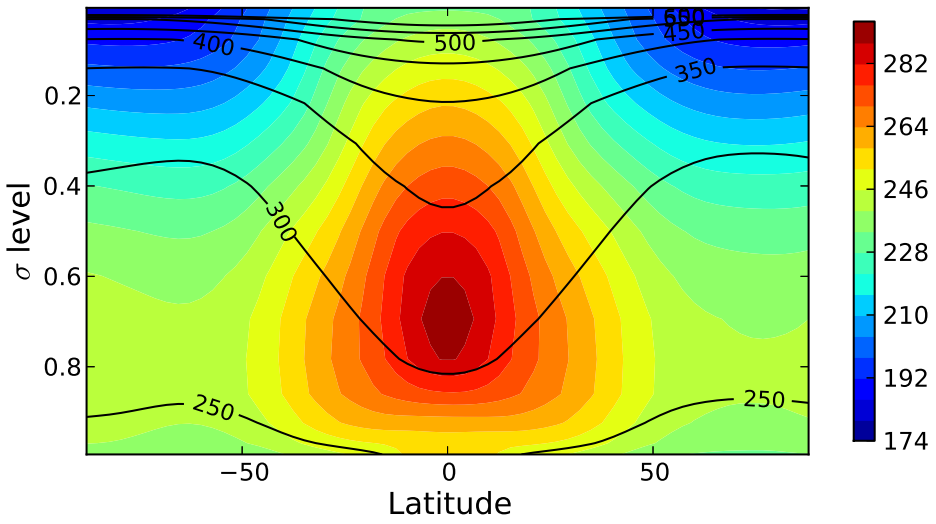

(a)

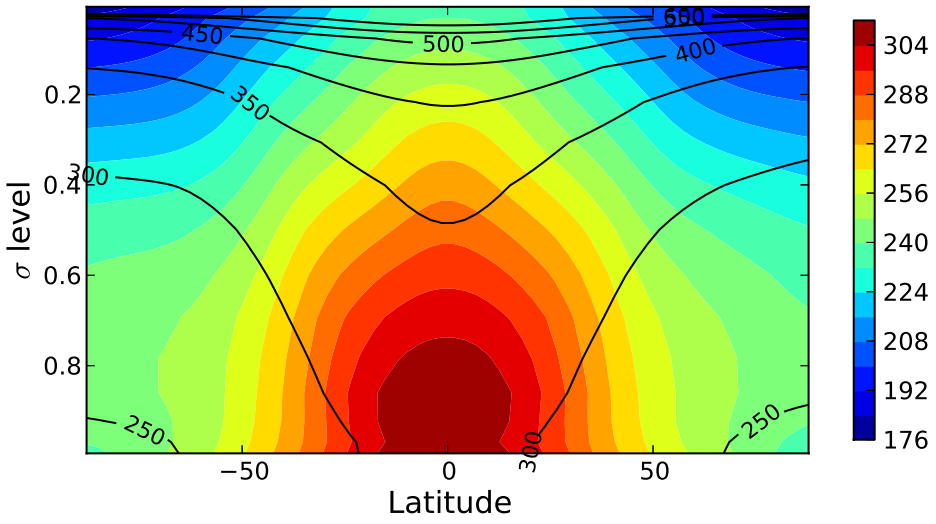

(b)

Figure 8.4: Zonal and temporal mean cross-sections of temperature (color) and potential temperature (contours) of the (a) night side and (b) day side of the planet, based on the experiment with $\Omega^* = 1$ and $p_s = 1$ bar.

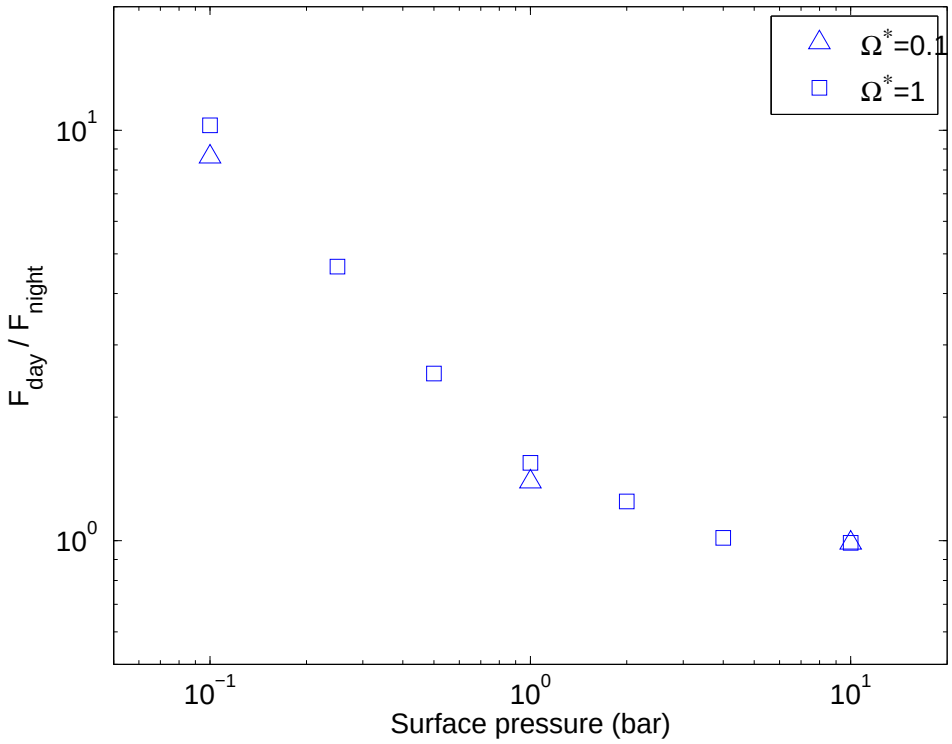

Figure 8.5: Heat redistribution efficiency $F_{\rm day}/F_{\rm night}$ observed in the experiments with different values of surface pressure and rotation rate.

as a single layer with radiative-equilibrium temperature T_{a0} and is transparent to short-wave incoming stellar irradiation, then the radiative timescale can be estimated as

$$\tau_{rad} = \frac{p_s c_p}{4(2-\epsilon_a)\sigma T_{a0}^3 g}, \tag{8.2}$$

where ϵ_a is the ratio of longwave radiation absorbed by the atmosphere (so that the surface longwave emission U has a portion of $\epsilon_a U$ aborbed by the atmosphere). In our experiments, change of surface pressure also results in changes of ϵ_a, thus the radiative timescale for experiments with $p_s = 10$ bar can be roughly 1.7 times that for experiments with $p_s = 1$ bar and ~ 24 times that for experiments with $p_s = 0.1$ bar.

Chapter 9

Conclusions and future work

9.1 Major conclusions and discussions

This thesis presents the work done in my DPhil project on the comparative planetary circulation regimes in simplified GCMs. Two versions of PUMA with different levels of complexity were used to conduct a series of controlled experiments and construct regime diagrams. PUMA-S used the Newtonian cooling scheme to represent the diabatic heating/cooling of the atmosphere. PUMA-G replaced this scheme with a two-band semi-grey radiative-convective scheme, which enabled more realistic simulation on the effect of planetary obliquity and atmospheric optical properties.

The ultimate aim of this project was to build up planetary circulation regime diagrams with respect to several characteristic dimensionless parameters using a hierarchy of numerical models. Effects of varying planetary rotation rate, planetary obliquity and the atmospheric opacity were investigated in terms of their dimensionless combinations—thermal Rossby number, Taylor number, planetary obliquity and the greenhouse parameter. A series of controlled experiments were conducted using both PUMA-S and PUMA-G. Experiments using PUMA-S were coordinated with respect to thermal Rossby number and the frictional/radiative Taylor number, while

PUMA-G experiments were coordinated with respect to relative planetary rotation rate ($\Omega^* = \Omega/\Omega_E$), planetary obliquity and greenhouse parameter. Tidally-locked planetary circulation and the corresponding heat transfer efficiency were studied by modifying the stellar irradiance at the top of the atmosphere in PUMA-G.

9.1.1 Circulation regimes

Circulation regimes revealed by PUMA-S experiments included axisymmetric circulation, super-rotation, regular baroclinic waves, irregular baroclinic waves, and multiple zonal jets.

The axisymmetric regime was found in experiments with relatively small meridional temperature difference and rotation rate, which essentially corresponded to experiments with small thermal Rossby number and Taylor number. This was consistent with the findings of Geisler et al. (1983), where axisymmetric regimes were found in the lower left region of the parameter space constructed by thermal Rossby number and frictional Taylor number. Similar results have also been reported in various laboratory and numerical annulus studies (see e.g. Hide & Mason (1975) and references therein).

The Super-rotation regime was found in experiments at slow rotation rate (small thermal Rossby number), with a GRW-like mechanism maintaining the equatorial super-rotation. Experiments with $\Omega^* = 1/16$ and $1/8$ exhibit significant equatorial super-rotation, which was very similar to the modelled circulation of slowly-rotating planetary bodies like Titan (see e.g. Lebonnois et al. (2012)), where equatorial super-rotation was found together with two jet streams (closed contours in zonal mean cross sections) at the high-latitudes. It should be noted that the equatorial super-rotation found in our experiments is not as prominent as that observed/simulated in the atmosphere of Venus. The equatorial super-rotation on Venus is so overwhelmingly strong that no separate jets (closed contours) can be found off equator. Instead of

the regime of prograde equatorial wind with two separate jets, the atmosphere of Venus tends to exhibit closed contours centered over the equator that extend roughly symmetrically in the meridional direction with respect to the equator (see Fig. 1.4 back in Chapter 1). Recent studies (see e.g. Lebonnois et al. (2010)) indicated that the equatorial super-rotation on Venus was maintained by a synergy of a GRW mechanism and diurnal tides, the latter of which contributed more to the excess angular momentum over the equator. It was therefore anticipated that adding diurnal cycles to the model in the future might enable us to obtain strong Venus-like equatorial super-rotation at small thermal Rossby number.

Another interesting comparison on the equatorial super-rotation regime was between this thesis and the study by Mitchell & Vallis (2010). By using an idealised GCM that was almost same as PUMA-S, they found Venus-like equatorial super-rotation at small thermal Rossby number, by reducing the size of the planet instead of its rotation rate. In order to achieve dynamically similar comparison, a PUMA-S experiment (not shown) was conducted with $\Omega^* = 1/16$ and 16 times the original radiative/frictional timescales, so that the thermal Rossby number and frictional/radiative Taylor numbers were same to those if planetary radius was decreased 16 times. It turned out that even with radiatve/frictional timescales multiplied by 16, the circulation still looked more like that of Titan, rather than that obtained in Mitchell & Vallis (2010). One possible explanation was that another nondimensional parameter was potentially missing, which lead to this degeneracy issue where changing planetary radius and changing rotation rate resulted in two different circulation structure even when their $\mathcal{R}o$, $\mathcal{F}_r$, and $\mathcal{F}_f$ were same with each other.

Experiments with intermediate thermal Rossby number at $\Omega^* = 1/4$ and $1/2$ were characterised by regular (vacillating) baroclinic waves. A survey on the sensitivity of the regular waves to frictional and radiative Taylor number revealed similar wavenumber 3 pattern with the Martian atmosphere (Northern Hemisphere) when frictional

and thermal damping timescales were set to their characteristic values of Mars. This indicated that frictional/thermal damping was crucial in determining the dominating wavenumber for regular baroclinic waves. Compared to the previous study by Collins & James (1995), our experiments covered a wider range of values for both the frictional and radiative timescales, with more regimes like wavenumber 2 and 4 discovered. In addition, comparisons between the dimensionless numbers ($\mathcal{F}_r$, $\mathcal{F}_f$) of our experiments and those used in Mars GCM indicated that the Martian atmosphere was dynamically similar to the highly regular and vacillating wavenumber-3 regime in our experiments.

Irregular baroclinic waves were found in experiments with relatively fast rotation rate (small thermal Rossby number), which resembled the circulation of the Earth's atmosphere. Multiple zonal jets formed when rotation rate is even faster. The experiment at $\Omega^* = 8$ had a similar thermal Rossby number to Jupiter's atmosphere (Read (2011)). The number of jets obtained in this experiment was similar to that of the Jupiter, though the equatorial jet is retrograde, rather than prograde as on Jupiter. The exact mechanism of the generation and maintenance of prograde equatorial jet in Jupiter's atmosphere is still not well understood now. Convective heat fluxes over the equatorial region from internal heat sources has been suggested by various numerical studies as the possible cause of Jupiter's equatorial super-rotation (e.g. see Schneider & Liu (2009), Heimpel et al. (2005)). It is therefore not surprising that our experiments do not produce prograde equatorial jets as there is no internal heat source nor its associated convective heat fluxes in PUMA model.

The above-stated circulation regimes were found in PUMA-G experiments as well, if planetary rotation rate was changed consistently while keeping planetary obliquity 23.44°. If the planetary obliquity was changed to an Uranus-like 85.00°, then the equator received much less stellar irradiation than the poles, and the global circulation was characterised by a strong retrograde jet centred over the equator. For interme-

diate planetary obliquity of 50.00°, the equator and the poles received roughly the same amount of stellar irradiation, leading to a much smaller meridional temperature gradient, with very weak baroclinic regions in the mid-latitudes.

9.1.2 Atmospheric energetics and heat transfer

Atmospheric energetics of different circulation regimes were studied by calculating their Lorenz energy cycles. Energy conversions of experiments at fast rotation rate ($\Omega^* > 1/4$) mainly followed the route of AZ $\rightarrow$ AE $\rightarrow$ KE (Energy converted from zonal mean available potential energy into eddy available potential energy, and then into eddy kinetic energy), which is the classical paradigm of baroclinic conversion. The principal energy conversion route began to transit into barotropic conversion of KZ $\rightarrow$ KE (Energy converted from zonal mean kinetic energy into eddy kinetic energy) around the rotation rate $\Omega^* = 1/4$ as the conversion between KZ and KE changed sign. Our experiments revealed that the conversion between AZ and KZ also changed sign at $\Omega^* = 1/4$, which implies the strengthening of Hadley cell circulation as the rotation rate decreases. The baroclinic conversion rate reached its maximum at $\Omega^* = 1/2$, which was also found in experiments reported in Del Genio & Suozzo (1987). These fundamental changes of energy conversion in Lorenz energy cycles around $\Omega^* = 1/4$ is consistent with the fact that Rhines scale starts to exceed planetary domain at $\Omega^* = 1/4$ as the rotation rate decreases. As the Rhines scale exceeds planetary domain, baroclinic eddies are significantly suppressed, hence the maximum of baroclinic energy conversion rate at $\Omega^* = 1/2$.

This suppression of baroclinic eddies at rotation rates slower than and equal to $\Omega^* = 1/4$ was also demonstrated by the finding that meridional eddy heat flux $v'T'$ reaches its maximum at $\Omega^* = 1/2$. The total heat transport by atmospheric circulation, on the other hand, showed a monotonically decreasing trend with respect to planetary rotation rate. The total heat transport did not change significantly within

the range of $1/4 < \Omega^* < 1$, which was exactly the range where baroclinic eddies were most active. This is consistent with the trend observed in numerical and laboratory annulus studies (e.g. see Read (2003)) where eddy heat transport tend to compensate for the decrease of heat transport by Hadley cells as rotation rate increases.

9.1.3 Jet formation and geostrophic turbulence

The role of eddies in planetary atmospheric circulation and jet formation was studied based on the PUMA-S experiments. Our calculation indicated that the energy-containing wavenumber was approximately equal to the Rhines wavenumber and the Rossby wavenumber. Such lack of scale separation between the Rhines wavenumber and the Rossby wavenumber implies that inverse energy cascade via eddy-eddy interactions, which according to the classical 2-D (geostrophic) turbulence theory should transfer energy from the Rossby wavenumber up to the Rhines wavenumber, is largely inhibited. Calculations of the kinetic energy spectral transfer fluxes demonstrated that the upscale energy tranfer which maintained the zonal jets was primarily contributed by the eddy-zonal mean flow interaction. The nonlinear eddy-eddy interaction, however, only played a marginal role in this upscale energy transfer. Besides, the eddy-eddy component of spectral KE flux did not show any extended range of constant value, which implies that the conventional definition of an inverse energy cascade with an inertial range is not applicable here. The dominance of eddy-zonal mean interaction in the KE spectral transfer flux is consistent with the historical success of the eddy-zonal mean interaction theory in dynamic meteorology.

The decomposition of KE spectrum into zonal mean and eddy components revealed anisotropic structures in geostrophic turbulence. Galperin and coworkers, based mainly on 2-D barotropic model studies, proposed that the atmospheric macroturbulence with strong zonal jets can be characterised by the so-called zonostrophic turbulence with a -5 slope in the zonal mean KE spectrum and $-5/3$ slope in the

eddy KE spectrum. PUMA-S experiments showed that surface friction played an important role in shaping the structure of jets as well as the associated signature in KE spectra. Experiments with weak surface friction exhibited KE spectral slopes similar to those defined in the zonostrophic turbulence regime, whereas experiments with stronger surface friction were more like the friction-dominated regime as defined in Galperin & Sukoriansky (2010). The difference between these two regimes was more intuitively reflected in the wind field, as zonostrophic regime has stronger "zonation" effect with less meandering jets. This can be related to the "barotropic governor" mechanism, which leads to an counter-intuitive paradigm in which weak (rather than strong) frictional damping suppresses baroclinic eddy activities, since it is the enhanced barotropic shear that inhibits the baroclinic eddy growth. Previous studies on zonostrophic turbulence were all based on highly idealised 2-D barotropic models (see e.g. Galperin & Sukoriansky (2010), Huang et al. (2001)). Our study discovered zonostrophic flows in a simplified 3-D GCM, which further supported the concept of zonostrophic turbulence as an important paradigm of planetary atmospheric circulation and jet formation/maintenance.

9.1.4 Tidally locked planets

The stellar irradiation scheme in PUMA-G was modified to enable the simulation of tidally locked planetary atmospheres with $\mathcal{G} = 0$. Consistent with previous studies using different models, strong equatorial super-rotation was found in our experiments. One of the central themes in studying tidally locked planets is the efficiency of dynamic heat transport from the day-side to the night-side. This can be measured by the ratio of the outgoing long-wave radiation (OLR) from the day-side to that from the night-side ($F_{\mathrm{day}}/F_{\mathrm{night}}$). Our experiments indicated that the heat transport efficiency was influenced by both the planetary rotation rate and the atmospheric mass, with the atmospheric mass playing a more significant role. Similar results were obtained by

Leconte et al. (2013) by comparing two specific exoplanets Gl 581c and HD 85512b at various surface pressure using a more complex GCM of a CO_2 atmosphere with a water cycle. Another study by Perna et al. (2012) focussed on the impact of stellar irradiance on the OLR ratios, by comparing a series of specific exoplanets. The effect of varying stellar irradiance can be a part of the future studies on parameter space exploration of exoplanetary atmospheres. The advantage of using simplified GCMs to do parameter space exploration in the context of exoplanet atmospheres is that it offers great generalisability of the results obtained. Future investigations following this line will focus on scenarios with $\mathcal{G} = 1$ and especially $\mathcal{G} = 5$ which corresponds to tidally-locked explanets with anti-greenhouse effect.

9.2 Future work

This thesis presents our efforts to take the first steps to systematically investigate terrestrial planetary circulation regimes in two numerical models with different levels of complexity. The ultimate and complete study of the parametric dependence of circulation regimes requires serious theoretical advancement and computational resources, given our current understanding of the general circulation and the potential number of defining parameters. This thesis is by no means such a definitive study. Instead, it should be viewed as a pilot project which tests the methodology of such a systematic study by focussing only upon a selected subset of planetary parameters. Even so, a great diversity of circulation regimes is revealed and various theoretical insights have been obtained. Progress can be made in the future by further studying the following topics upon reflection.

9.2.1 Seasonal/diurnal cycles and circulation regimes

Seasonal and diurnal cycles are not included in our PUMA-S and PUMA-G experiments for simplicity. The restoration temperature field in PUMA-S and the stellar irradiation at the top of the atmosphere in PUMA-G are set to their annual mean respectively. One of the important directions to go following the study of this thesis is to incorporate seasonal cycle into PUMA-S and PUMA-G experiments.

Previous studies have shown that the impact of seasonal cycle on atmospheric general circulation is nonlinear. For example, Lindzen & Hou (1988) studied the classical Held & Hou model of Hadley circulation and demonstrated that the strength and extent of the axisymmetric Hadley circulation responds nonlinearly to the shift of substellar latitude (specifically, the annual average of meridional mass streamfunction field with seasonal cycle is much more intense than that at the equinox. There is a nonlinear amplification effect.). It is therefore necessary to study how the seasonal cycle influences the structure of the general circulation for various circulation regimes.

Another issue related to seasonal cycle is the effect of orbital eccentricity. The radiative-transfer scheme of PUMA-G assumes that the planetary orbit is perfectly circular for simplicity. Some of the exoplanets detected so far are believed to have significant orbital eccentricity (see e.g. Jones et al. (2006)), which implies that seasonal variation of such planets' mean temperature can be so dramatic that part or all of their atmosphere might condense during certain period in a year (this is essentially the case for Mars, which has a non-negligible eccentricity of 0.1). In order to simulate the circulation on these planets more accurately, a full seasonal cycle must be taken into account, though this will add another dimension to our parameter space.

The diurnal cycle is another factor that needs to be taken into account in future studies using PUMA-G, especially when studying slowly rotating planets where tidal forces might be crucial for producing the reasonable strength of equatorial superrotation, as in the case of Venus. The technical implementation of both seasonal and

diurnal variations is relatively straightforward. By running PUMA-G in parallel on super-computers (which is exactly how the PUMA-G experiments in this thesis were calculated) the added number of simulations to do will be feasible.

9.2.2 Heat transfer parametrisation

Finding out an appropriate parametrisation scheme to represent the effect of heat transfer (especially along the meridional direction) of the atmospheric macroturbulence has been an active area of research in recent decades (see e.g. Held (1999), Schneider (2006), Vallis (2006)). This is not only for pure theoretical interest, but also for improving numerical model developements, especially for ocean models where running eddy-resolving models are computationally too expensive. Current efforts on designing such parametrisation schemes tend to either follow the baroclinic adjustment hypothesis or view the dynamic heat transfer as a diffusive process (see review by Showman et al. (2010)). The diffusive eddy heat transfer can be represented as the following (Held (1999)):

$$c\frac{\partial T}{\partial t} = \nabla \cdot (cD\nabla T) + S(\phi) - I \tag{9.1}$$

where c is the heat capacity of the atmosphere, T is the surface temperature, D is the diffusivity characterising the baroclinic eddy activities. $S(\phi)$ is the absorbed the stellar radiation as a function of latitude ϕ. I is the thermal radiation emitted by the atmosphere.

By simply parameterizing the term I as $I = A + BT$ and $S(\phi)$ as a constant term plus a term proportional to the second Legendre Polynomial $P_2(cos(\phi))$, a steady state solution of the equator–to–pole temperature difference can be obtained (Held (1999)) as

$$\Delta T_{EP} = \frac{\Delta T_{rad}}{1 + 6\frac{cD}{Ba^2}} \tag{9.2}$$

Scheme	D
Stone (1972)	$\frac{H^2 N g}{f^2 \theta_0} \frac{\partial \overline{\theta}}{\partial y}$
Green (1970)	$L_{zone}^2 \frac{g}{N \theta_0} \frac{\partial \overline{\theta}}{\partial y}$
Held & Larichev (1996)	$\frac{g^3}{N^3 \beta^2 \theta_0^3} \left(\frac{\partial \overline{\theta}}{\partial y} \right)^3$
Barry et al. (2002)	$\left(\frac{ea\dot{q}_{net}}{\theta_0} \frac{\partial \overline{\theta}}{\partial y} \right)^{3/5} \left(\frac{2}{\beta} \right)^{4/5}$

Table 9.1: Baroclinic eddy diffusivity parametrisation schemes, after Showman et al. (2010).H is the atmospheric scale height, N the buoyancy oscillation frequency, g the gravitional acceleration, f the Coriolis parameter, θ_0 the reference potential temperature, $\partial\overline{\theta}/\partial y$ the R-C equilibrium meridional θ gradient, L_{zones} the latitudinal range of the baroclinic zone, e a constant of order unity, a the planetary radius, $\dot{q}_{net}$ the net radiative heating/cooling per unit mass that the eddy fluxes are balancing.

where a is the planetary radius and ΔT_{rad} is the pre–determined equator–to–pole temperature difference at radiative equilibrium.

Thus the determination of the temperature difference depends on the value of the eddy diffusivity D. A series of parameterisation schemes of eddy diffusivity D have been proposed based on various assumptions of baroclinic eddy activities (Stone (1972), Green (1970), Held & Larichev (1996), and Barry et al. (2002)) as shown in Table 9.1.

In this project, we have conducted a series of controlled experiments by varying planetary parameters like rotation rate, obliquity angle, atmospheric opacity and so on. It is therefore convenient to use our experiments to test different parametrisation schemes so that a robust and accurate scheme can be found (following the approach of Barry et al. (2002)). It is very likely that the above-mentioned schemes are not accurate when applying to more exotic circulation regimes. And it will be necessary to modify these schemes based on theoretical insights of the atmospheric macroturbulence.

9.2.3 Modification of the model for the Jovian atmosphere

The studies reported in this thesis mainly focus on relatively shallow atmospheres of terrestrial planets[1]. One direction to extend our current study is to modify the PUMA-S/G models to investigate thicker atmospheres, e.g. the Jovian atmosphere.

The two-band semi-grey radiative-convective scheme used by PUMA-G is built upon various idealised assumptions. One crucial assumption is that the radiatively active constituents in the atmosphere are well-mixed in the vertical direction. This is OK for Earth-like atmospheres where one of the dominant greenhouse gases, CO_2, itself is well-mixed in the vertical direction. But if we consider thicker atmospheres, the effect of pressure broadening must be taken into account. And this will lead to some necessary modifications to the assumption of the vertical profile of extinction coeffcient. One straightforward scheme is to use a quadratic form of atmospheric optical depth (Liu & Schneider (2010)):

$$\tau(p) = \tau_0(p/p_0)^2. \tag{9.3}$$

Such a formulation of atmospheric optical depth in the long-wave thermal radiation band has been used in modelling Jovian atmospheres (see e.g. Schneider & Liu (2009), Liu & Schneider (2010)). Fig. 9.1 shows our preliminary effort to put this scheme to work in the context of Jupiter's atmosphere. By coupling this scheme with the GCM dynamical core, it will enable us to better simulate optically thick planetary atmospheres in our future exploration of parameter spaces.

Another important limitation of PUMA-S/G for modelling Jovian atmospheres is that the model assumes the atmosphere is shallow compared to the planetary radius, which is not a valid assumption for gas giants like Jupiter. There are two schools of thoughts on the large scale circulation and the jet formation of Jovian atmosperes —

[1]By "shallow" we mean the vertical scale of the atmosphere is much smaller than the radius of the whole planet

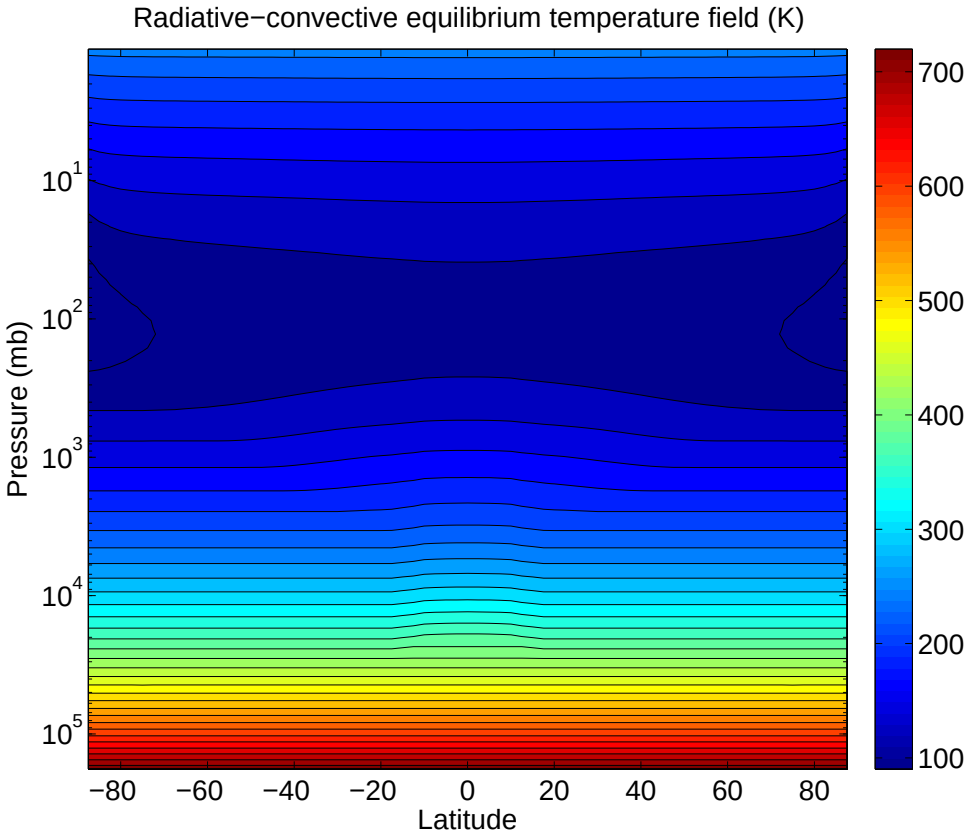

Figure 9.1: Radiative-convective equilibrium temperature field of Jupiter's atmosphere, with atmospheric optical depth represented by Eq. 9.3. Optical depth in the thermal radiation band is set to 80 at 3 bar, and optical depth in the solar radiation band is set to 3.0 at 3 bar, following the treatment of Liu & Schneider (2010).

the "shallow-jet" paradigm and the "deep-jet" paradigm. The "shallow-jet" paradigm argues that the formation of jets and vortices and the observed banded structures in the Jovian atmosphere can be explained by the classical 2-D turbulence framework in a shallow "weather-layer" which only goes down to a few bars level (see e.g. Liu & Schneider (2010)). The other paradigm ("deep-jet") argues that the observed jets and vortices are essentially manifestations of deep Taylor-Proudman cylinders which penetrate deep into the atmosphere. Due to the lack of a solid surface, Jupiter's atmosphere extends deep into the planetary interior (see e.g. Vasavada & Showman (2005)). An important consequence following this fact is that the widely-used primitive equation system in conventional GCMs (including PUMA-S/G) is no longer valid. The full form of the Coriolis force needs to be incorporated into the momentum equations. Besides, anelastic approximation must be adopted to include the effect of varying background density with respect to height (see e.g. Kaspi et al. (2009)).

This raises questions as to the applicability of the zonostrophic turbulence regime observed in our experiments (and also in experiments by previous studies like Galperin & Sukoriansky (2010), Sukoriansky et al. (2002) etc.) to Jovian planetary atmospheres. In essence, zonostrophic turbulence is just a special form of 2-D (geostrophic) turbulence, which follows the assumption that the atmosphere is shallow and the large scale dynamics is quasi 2-D. If the "deep-jet" paradigm is correct, then the zonostrophic turbulence regime might not be applicable to the Jovian atmosphere. Due to lack of observational data, it is currently unclear whether jets and vorticies on jupiter penetrate deep into the planetary interior. With the launch of NASA's spacecraft *Juno* due to arriving at Jupiter's orbit in 2016, more insights into the deep thermal and wind structure of Jupiter are expected to be obtained (see e.g. Helled et al. (2011)) within the next few years.

Bibliography

Andrews, D. G. (2010) *An Introduction to Atmospheric Physics*. Cambridge Univ Press, 2nd ed.

Andrews, D G & M E McIntyre (1978) Generalized Eliassen-Palm and Charney-Drazin theorems for waves on axisymmetric mean flows in compressible atmospheres. *Journal of the Atmospheric Sciences* **35**: 175–185.

Appleby, J. C. (1988) Selection of baroclinic waves. *Quarterly Journal of the Royal Meteorological Society* **114**(482): 1173–1179.

Barnes, JR (1981) Midlatitude disturbances in the Martian atmosphere-A second Mars year. *Journal of Atmospheric sciences* **38**(2): 225–234.

Barry, Leon, George C G.C. Craig, & John Thuburn (2002) Poleward heat transport by the atmospheric heat engine. *Nature* **415**(6873): 774–777.

Boer, G.J. & T.G. Shepherd (1983) Large-scale two-dimensional turbulence in the atmosphere. *Journal of the Atmospheric Sciences* **40**: 164–184.

Boville, BA (1981) Amplitude vacillation on a beta-plane. *Journal of Atmospheric Sciences* **38**(3): 609–618.

Burgess, B. H., Andre R. Erler, & Theodore G. Shepherd (2013) The Troposphere-to-Stratosphere Transition in Kinetic Energy Spectra and Nonlinear Spectral Fluxes as Seen in ECMWF Analyses. *Journal of the Atmospheric Sciences* **70**(2): 669–687.

Busse, F. H. (2002) Convective flows in rapidly rotating spheres and their dynamo action. *Physics of Fluids* **14**(4): 1301.

Charney, J.G. (1947) The dynamics of long waves in a baroclinic westerly current. *Journal of Meteorology* **4**(5): 136–162.

Charney, Jule G. (1971) Geostrophic Turbulence. *Journal of Atmospheric Sciences* **28**(6).

Chekhlov, Alexei, Steven a. Orszag, Semion Sukoriansky, Boris Galperin, & Ilya Staroselsky (1996) The effect of small-scale forcing on large-scale structures in two-dimensional flows. *Physica D: Nonlinear Phenomena* **98**(2-4): 321–334.

Christensen, UR (2001) Zonal flow driven by deep convection in the major planets. *Geophysical research letters* **28**(13).

Collins, M & IN James (1995) Regular baroclinic transient waves in a simplified global circulation model of the Martian atmosphere. *Journal of geophysical research* **100**.

Cooper, PI (1969) The absorption of radiation in solar stills. *Solar energy* **12**(3).

Crisp, David (1989) Radiative forcing of the Venus mesosphere: II. thermal fluxes, cooling rates, and radiative equilibrium temperatures. *Icarus* **413**.

Danilov, Sergey & David Gurarie (2004) Scaling, spectra and zonal jets in beta-plane turbulence. *Physics of Fluids* **16**(7): 2592.

Del Genio, A.D. & R.J. Suozzo (1987) A comparative study of rapidly and slowly rotating dynamical regimes in a terrestrial general circulation model. *Journal of Atmospheric Sciences* **44**: 973–986.

Dowling, TE (1995) Dynamics of Jovian atmospheres. *Annual review of fluid mechanics* : 293–334.

Eady, E. T. (1949) Long Waves and Cyclone Waves. *Tellus* **1**(3): 33–52.

Edmon, H. J. Jr, B. J. Hoskins, & M. E. McIntyre (1980) Eliassen-Palm Cross Sections for the Troposphere. *Journal of Atmospheric Sciences* **37**(12).

Eliassen, Arnt & Enok Palm (1961) On the transfer of energy in stationary mountain waves. *Geofysiske Publikasjoner* **22**.

Emanuel, KA; (1994) *Atmospheric Convection*. Oxford University Press.

Esler, J. G. & B. T. Willcocks (2012) Nonlinear baroclinic equilibration at finite supercriticality. *Geophysical & Astrophysical Fluid Dynamics* **106**(3): 320–350.

Esteves, Lisa J & Ray Jayawardhana (2013) Optical phase curves of kepler exoplanets. *ArXiv* .

Fjø rtoft, Ragnar (1953) On the changes in the spectral distribution of kinetic energy for two-dimensional non-divergent flow. *Tellus* **5**(3).

Frierson, DMW, Isaac M. Held, & Pablo Zurita-Gotor (2006) A gray-radiation aquaplanet moist GCM. Part I: Static stability and eddy scale. *Journal of the Atmospheric Sciences* **63**(10): 2548–2566.

Fultz, Dave, Robert R Long, George V Owens, & Joyce Weil (1959) *Studies of thermal convection in a rotating cylinder with some implications for large-scale atmospheric motions*. American Meteorological Society.

Galperin, B., S. Sukoriansky, N. Dikovskaya, P. L. Read, Y. H. Yamazaki, & R. Wordsworth (2006) Anisotropic turbulence and zonal jets in rotating flows with a β-effect. *Nonlinear Processes in Geophysics* **13**(1).

Galperin, Boris;, Hideyuki; Nakano, Huei-Ping; Huang, & Semion Sukoriansky (2004) The ubiquitous zonal jets in the atmospheres of giant planets and Earth's oceans. *Geophysical Research Letters* **31**(13).

Galperin, Boris & Semion Sukoriansky (2010) Geophysical flows with anisotropic turbulence and dispersive waves: flows with stable stratification. *Ocean Dynamics* **60**(5): 1319–1337.

Geisler, J.E., E.J. Pitcher, & R.C. Malone (1983) Rotating-Fluid experiments with an atmospheric general circulation model. *Journal of Geophysical Research* **88**: 9706–9716.

Gierasch, PJ (1975) Meridional circulation and the maintenance of the Venus atmospheric rotation. *Journal of Atmospheric Sciences* **32**: 1038–1044.

Gill, A. E. (1980) Some simple solutions for heat-induced tropical circulation. *Quarterly Journal of the Royal Meteorological Society* **106**(449): 447–462.

Goody, R; & Y.L; Young (1995) *Atmospheric Radiation: Theoretical Basis*. Oxford University Press, 2nd editio ed.

Green, JSA (1970) Transfer properties of the largescale eddies and the general circulation of the atmosphere. *Quarterly Journal of the Royal Meteorological Society* **96**(408).

Guillot, T. (2010) On the radiative equilibrium of irradiated planetary atmospheres. *Astronomy and Astrophysics* **520**: A27.

Hadley, G (1735) Concerning the Cause of the General Trade-Winds: By Geo. Hadley, Esq; F. R. S. *Royal Society of London Philosophical Transactions Series I* **39**: 58–62.

Hammel, H.B., I. de Pater, S. Gibbard, G.W. Lockwood, & K. Rages (2005) Uranus in 2003: Zonal winds, banded structure, and discrete features. *Icarus* **175**(2): 534–545.

Hart, JE (1981) Wavenumber selection in nonlinear baroclinic instability. *Journal of the Atmospheric Sciences* **38**: 400–408.

Heimpel, Moritz, Jonathan Aurnou, & Johannes Wicht (2005) Simulation of equatorial and high-latitude jets on Jupiter in a deep convection model. *Nature* **438**(7065): 193–6.

Held, IM (1999) The macroturbulence of the troposphere. *Tellus B* **51**(1): 59–70.

Held, I.M. (2000) The general circulation of the atmosphere. In *Woods Hole Oceanographic Institute Geophysical Fluid Dynamics Program*.

Held, IM (2005) The gap between simulation and understanding in climate modeling. *Bulletin of the American Meteorological Society* **86**: 1609–1614.

Held, I.M. & A.Y. Hou (1980) Nonlinear Axially Symmetric Circulations in a Nearly Inviscid Atmosphere. *Journal of Atmospheric Sciences* **37**: 515–533.

Held, IM & VD Larichev (1996) A Scaling Theory for Horizontally Homogeneous, Baroclinkally Unstable Flow on a Beta Plane. *Journal of the atmospheric sciences* **53**(7): 946–952.

Helled, Ravit, John D. Anderson, Gerald Schubert, & David J. Stevenson (2011) Jupiters moment of inertia: A possible determination by Juno. *Icarus* **216**(2): 440–448.

Heng, Kevin (2011) Atmospheric circulation of tidally locked exoplanets: II. Dualband radiative transfer and convective adjustment. *Monthly Notices of the ...* **28**(October): 1–28.

Hide, R (1953) Some experiments on thermal convection in a rotating liquid. *Quarterly Journal of the Royal Meteorological Society* (December): 1952.

Hide, R (1969) Dynamics of the atmospheres of the major planets with an appendix on the viscous boundary layer at the rigid bounding surface of an electrically-conducting. *Journal of the Atmospheric Sciences* **26**.

Hide, R & P.J. Mason (1975) Sloping convection in a rotating fluid. *Advances in Physics* **24**: 47–100.

Holton, JR (1992) *An introduction to dynamic meteorology*. Academic Press, 3rd ed.

Hoskins, B. J. & A. J. Simmons (1975) A multi-layer spectral model and the semi-implicit method. *Quarterly Journal of the Royal Meteorological Society* **101**(429): 637–655.

Huang, Huei-Ping, Boris Galperin, & Semion Sukoriansky (2001) Anisotropic spectra in two-dimensional turbulence on the surface of a rotating sphere. *Physics of Fluids* **13**(1): 225.

Hunt, BG (1979) The Influence of the Earth's Rotation Rate on the General Circulation of the Atmosphere. *Journal of Atmospheric Sciences* **36**: 1392–1408.

Illari, L, J Marshall, P Bannon, S Lee, & R Najjar (2009) WEATHER IN A TANK Exploiting Laboratory Experiments in the Teaching of Meteorology, Oceanography, and Climate. *Bulletin of the American Meteorological Society* .

Ingersoll, AP, PJ Gierasch, D Banfield, & AR Vasavada (2000) Moist convection as an energy source for the large-scale motions in Jupiter's atmosphere. Galileo Imaging Team. *Nature* **403**(6770): 630–2.

James, IN (1987) Supression of baroclinic instability in horizontally sheared flows. *Journal of the Atmospheric Sciences* **44**(24): 3710–3720.

James, IN (1995) *Introduction to circulating atmospheres*. Cambridge Univ Press.

James, IN & LJ Gray (1986) Concerning the effect of surface drag on the circulation of a baroclinic planetary atmosphere. *Quarterly Journal of the Royal Meteorological Society* **112**: 1231–1250.

Jansen, Malte & Raffaele Ferrari (2012) Macroturbulent Equilibration in a Thermally Forced Primitive Equation System. *Journal of the Atmospheric Sciences* **69**(2): 695–713.

Jenkins, Gregory S (1996) A sensitivity study of changes in Earth s rotation rate with an atmospheric general circulation model. *Global and Planetary Change* **11**.

Jones, H. R. A., R. P. Butler, C. G. Tinney, G. W. Marcy, B. D. Carter, A. J. Penny, C. McCarthy, & J. Bailey (2006) High-eccentricity planets from the Anglo-Australian Planet Search. *Monthly Notices of the Royal Astronomical Society* **369**(1): 249–256.

Joshi, MM (1997) Simulations of the atmospheres of synchronously rotating terrestrial planets orbiting M dwarfs: conditions for atmospheric collapse and the implications for habitability. *Icarus* **465**: 450–465.

Kallberg, P, P Berrisford, B Hoskins, A Simmons, S Uppala, S Lamy-Thepaut, & R Hine (2004) ERA-40 atlas, ERA 40 project report series 19. Tech. rep., ECMWF.

Kaspi, Yohai, Glenn R. Flierl, & Adam P. Showman (2009) The deep wind structure of the giant planets: Results from an anelastic general circulation model. *Icarus* **202**(2): 525–542.

Kliore, AJ, GM Keating, & VI Moroz (1992) Venus international reference atmosphere (1985). *Planetary and Space Science* **40**(4): 573.

Kolmogorov, AN (1941) Dissipation of energy in locally isotropic turbulence. *Dokl. Akad. Nauk SSSR* **32**(1).

Koshyk, JN, BA Boville, & Kevin Hamilton (1999) Kinetic energy spectrum of horizontal motions in middle-atmosphere models. *Journal of Geophysical Research* **104**.

Kraichnan, RH (1967) Inertial ranges in twodimensional turbulence. *Physics of fluids* **10**: 1417–1423.

Lacis, AA & V Oinas (1991) A Description of the correlated k distribution method for modeling nongray gaseous absorption, thermal emission, and multiple scattering in vertically inhomogeneous atmospheres. *Journal of Geophysical Research: Atmospheres* **96**: 9027–9063.

Lebonnois, Sébastien, Jérémie Burgalat, Pascal Rannou, & Benjamin Charnay (2012) Titan global climate model: A new 3-dimensional version of the IPSL Titan GCM. *Icarus* **218**(1): 707–722.

Lebonnois, Sébastien, Frédéric Hourdin, Vincent Eymet, Audrey Crespin, Richard Fournier, & François Forget (2010) Superrotation of Venus' atmosphere analyzed with a full general circulation model. *Journal of Geophysical Research* **115**(E6): E06006.

Leconte, J., F. Forget, B. Charnay, R. Wordsworth, F. Selsis, E. Millour, & A. Spiga (2013) 3D climate modeling of close-in land planets: Circulation patterns, climate moist bistability, and habitability. *Astronomy & Astrophysics* **554**: A69.

Lee, C, S.˜R. Lewis, & P.˜L. Read (2005) A numerical model of the atmosphere of Venus. *Advances in Space Research* **36**: 2142–2145.

Lee, Christopher & Mark Ian Richardson (2011) A Discrete Ordinate, Multiple Scattering, Radiative Transfer Model of the Venus Atmosphere from 0.1 to 260 μ m. *Journal of the Atmospheric Sciences* **68**(6): 1323–1339.

Lindzen, RS & AV Hou (1988) Hadley circulations for zonally averaged heating centered off the equator. *Journal of the atmospheric sciences* **45**(17).

Liou, KN (2002) *An introduction to atmospheric radiation*. Academic Press, 2nd ed.

Liu, Junjun & Tapio Schneider (2010) Mechanisms of Jet Formation on the Giant Planets. *Journal of the Atmospheric Sciences* **67**(11): 3652–3672.

Lorenz, Edward N (1967) *The nature and theory of the general circulation of the atmosphere*, vol. 218. World Meteorological Organization Geneva.

Lorenz, EN (1955) Available potential energy and the maintenance of the general circulation. *Tellus* **2**.

Manabe, S & RF Strickler (1964) Thermal equilibrium of the atmosphere with a convective adjustment. *Journal of the Atmospheric Sciences* .

Manabe, S & RT Wetherald (1967) Thermal equilibrium of the atmosphere with a given distribution of relative humidity. *Journal of Atmospheric Sciences* **24**.

Mayor, M & D Queloz (1995) A Jupiter-mass companion to a solar-type star. *Nature* .

McGuffie, K; & A; Henderson-Sellers (2005) *A Climate Modelling Primer*. John Wiley and Sons, 3rd ed.

Mendonça, João M., Peter L. Read, Colin F. Wilson, & Stephen R. Lewis (2012) Zonal winds at high latitudes on Venus: An improved application of cyclostrophic balance to Venus Express observations. *Icarus* **217**(2): 629–639.

Merlis, Timothy M. & Tapio Schneider (2010) Atmospheric dynamics of Earth-like tidally locked aquaplanets. *Journal of Advances in Modeling Earth Systems* **2**: 13.

Mitchell, Jonathan L. & Geoffrey K. Vallis (2010) The transition to superrotation in terrestrial atmospheres. *Journal of Geophysical Research* **115**(E12): 1–17.

Mitchell, Jonathan L., Geoffrey K. Vallis, & Samuel F. Potter (2014) Effects of the Seasonal Cycle on Superrotation in Planetary Atmospheres. *The Astrophysical Journal* **787**(1): 23.

Navarra, A. & G. Boccaletti (2002) Numerical general circulation experiments of sensitivity to Earth rotation rate. *Climate Dynamics* **19**(5-6): 467–483.

Nayvelt, L;, P; Gierasch, & K; Cook (1997) Modeling and observations of Martian stationary waves. *Journal of Atmospheric Sciences* **54**: 986–1013.

OGorman, Paul a. & Tapio Schneider (2008) Weather-Layer Dynamics of Baroclinic Eddies and Multiple Jets in an Idealized General Circulation Model. *Journal of the Atmospheric Sciences* **65**(2): 524–535.

Pedlosky, J (1971) Finite-amplitude baroclinic waves with small dissipation. *Journal of Atmospheric Sciences* **28**(4): 587–597.

Pedlosky, Joseph (1970) Finite-Amplitude Baroclinic Waves. *Journal of the Atmospheric Sciences* **27**(1): 15–30.

Peixóto, JP & AH Oort (1974) The annual distribution of atmospheric energy on a planetary scale. *Journal of Geophysical Research* **79**(15).

Peixoto J.P., Oort A H (1992) *Physics of climate*. Springer.

Perna, Rosalba, Kevin Heng, & Frédéric Pont (2012) the Effects of Irradiation on Hot Jovian Atmospheres: Heat Redistribution and Energy Dissipation. *The Astrophysical Journal* **751**(1): 59.

Potter, Samuel F., Geoffrey K. Vallis, & Jonathan L. Mitchell (2014) Spontaneous Superrotation and the Role of Kelvin Waves in an Idealized Dry GCM. *Journal of the Atmospheric Sciences* **71**(2): 596–614.

Ramanathan, V;, R.J.; Cicerone, H.B.; Singh, & J.T.; Kiehl (1985) Trace gas trends and their potential role in climate change. *Journal of Geophysical Research* **90**: 5547–5566.

Read, Peter L, Matfhew Collins, Wolf-gerrit Froh, Stephen R Lewis, & Alistair F Lovegrove (1998) Wave Interactions and Baroclinic Chaos : A Paradigm for Long Timescale Variability in Planetary Atmospheres. *Chaos, Solitons & Fractals* **9**(1): 231–249.

Read, PL (1986a) Superrotation and diffusion of axial angular momentum: II. A review of quasiaxisymmetric models of planetary atmospheres. *Quarterly Journal of the Royal Meteorological Society* : 253–272.

Read, PL (1986b) Superrotation and diffusion of axial angular momentum: I.'Speed limits' for axisymmetric flow in a rotating cylindrical fluid annulus. *Quarterly Journal of the Royal Meteorological Society* : 231–251.

Read, PL (2001) Transition to geostrophic turbulence in the laboratory, and as a paradigm in atmospheres and oceans. *Surveys in Geophysics* : 265–317.

Read, P.L. (2003) A combined laboratory and numerical study of heat transport by baroclinic eddies and axisymmetric flows. *Journal of Fluid Mechanics* **489**: 301–323.

Read, P.L. (2011) Dynamics and circulation regimes of terrestrial planets. *Planetary and Space Science* **59**(10): 900–914.

Read, PL, MJ Bell, DW Johnson, & RM Small (1992) Quasi-periodic and chaotic flow regimes in a thermally driven, rotating fluid annulus. *Journal of Fluid Mechanics* .

Read, P.L. & S.R. Lewis (2004a) *The Martian Climate Revisited — Atmosphere and Environment of a Desert Planet*. Springer-Praxis.

Read, P.L. & S.R. Lewis (2004b) *The Martian Climate Revisited: Atmosphere and Environment of a Desert Planet*. Springer-Praxis.

Read, P.L., Y.H. Yamazaki, S.R. Lewis, P.D. Williams, R. Wordsworth, K. Miki-Yamazaki, J. Sommeria, & H. Didelle (2007) Dynamics of convectively driven banded jets in the laboratory. *Journal of the Atmospheric Sciences* **64**: 4031–4052.

Rhines, Peter B. (1975) Waves and turbulence on a beta-plane. *Journal of Fluid Mechanics* **69**(03): 417–443.

Rossow, WB & GP Williams (1979) Large-scale motion in the Venus stratosphere. *Journal of the Atmospheric Sciences* **36**(3): 377–389.

Ryan, JA, RM Henry, SL Hess, CB Leovy, JE Tillman, & C Walcek (1978) Mars meteorology: Three seasons at the surface. *Geophysical Research Letters* **5**(8): 715–718.

Saravanan, R (1993) Equatorial superrotation and maintenance of the general circulation in two-level models. *Journal of the atmospheric sciences* **50**: 1211–1227.

Schneider, T & J Liu (2009) Formation of jets and equatorial superrotation on Jupiter. *Journal of Atmospheric Sciences* **66**: 579–601.

Schneider, Tapio (2004) The Tropopause and the Thermal Stratification in the Extratropics of a Dry Atmosphere. *Journal of the Atmospheric Sciences* **61**(12): 1317–1340.

Schneider, Tapio (2006) The General Circulation of the Atmosphere. *Annual Review of Earth and Planetary Sciences* **34**(1): 655–688.

Schneider, Tapio & Christopher C. Walker (2006) Self-Organization of Atmospheric Macroturbulence into Critical States of Weak Nonlinear EddyEddy Interactions. *Journal of the Atmospheric Sciences* **63**(6): 1569–1586.

Seager, S (2010) *Exoplanet atmospheres: physical processes*. Princeton University Press.

Seager, S & JJ Lissauer (2010) Introduction to Exoplanets. In *Exoplanets*, Sara Seager, ed., The University of Arizona Press, 3–13.

Seager, Sara & Drake Deming (2010) Exoplanet Atmospheres. *Annual Review of Astronomy and Astrophysics* **48**(1): 631–672.

Shepherd, TG (1987) A spectral view of nonlinear fluxes and stationary-transient interaction in the atmosphere. *Journal of the atmospheric sciences* **44**(8): 1166–1178.

Showman, AP ;, J; Cho, & K; Menou (2010) *Atmospheric circulation of exoplanets, In: Seager, S. (Ed.), Exoplanets.* University of Arizona Press, Tucson, Arizona.

Showman, AP & LM Polvani (2011) Equatorial superrotation on tidally locked exoplanets. *The Astrophysical Journal* (2002).

Smith, Michael D. (2008) Spacecraft Observations of the Martian Atmosphere. *Annual Review of Earth and Planetary Sciences* **36**(1): 191–219.

Srinivasan, Kaushik & W. R. Young (2012) Zonostrophic Instability. *Journal of the Atmospheric Sciences* **69**(5): 1633–1656.

Stone, PH (1972) A simplified radiative-dynamical model for the static stability of rotating atmospheres. *Journal of the Atmospheric Sciences* **29**(3).

Sukoriansky, Semion, Nadejda Dikovskaya, & Boris Galperin (2007) On the Arrest of Inverse Energy Cascade and the Rhines Scale. *Journal of the Atmospheric Sciences* **64**(9): 3312–3327.

Sukoriansky, Semion, Boris Galperin, & Nadejda Dikovskaya (2002) Universal Spectrum of Two-Dimensional Turbulence on a Rotating Sphere and Some Basic Features of Atmospheric Circulation on Giant Planets. *Physical Review Letters* **89**(12).

Takagi, M & Y Matsuda (2007) Effects of thermal tides on the Venus atmospheric superrotation. *Journal of Geophysical Research: Atmospheres* **112**(D9): 1984–2012.

Taylor, F.W. (2010) *Planetary Atmospheres*. Oxford University Press.

Titov, D.V., M.A. Bullock, D. Crisp, N.O. Renno, F.W. Taylor, & L.V. Zasova (2007) Radiation in the atmosphere of Venus. In *Exploring Venus as a Terrestrial Planet*, L.W. Esposito, E.R. Stofan, & T.E. Cravens, eds., American Geophysical Union.

Vallis, GK (2006) *Atmospheric and oceanic fluid dynamics: fundamentals and large-scale circulation*. Cambridge Univ Press.

Vallis, GK & ME Maltrud (1993) Generation of mean flows and jets on a beta plane and over topography. *Journal of physical oceanography* **23**: 1346–1362.

Vardavas, I.M. & F.W. Taylor (2007) *Radiation and Climate*. Oxford University Press.

Vasavada, Ashwin R & Adam P Showman (2005) Jovian atmospheric dynamics: an update after Galileo and Cassini. *Reports on Progress in Physics* **68**(8): 1935–1996.

Williams, G. E. (1975) Late Precambrian glacial climate and the Earth's obliquity. *Geological Magazine* **112**(05): 441–544.

Williams, GP (1988a) The dynamical range of global circulations - I. *Climate dynamics* **2**: 205–260.

Williams, GP (1988b) The dynamical range of global circulations - II. *Climate dynamics* **3**(2): 45–84.

Williams, GP; & JL Holloway (1982) The range and unity of planetary circulations. *Nature* .

Wolszczan, A & DA Frail (1992) A planetary system around the millisecond pulsar PSR 1257+ 12. *Nature* .

Wordsworth, R. D., P. L. Read, & Y. H. Yamazaki (2008) Turbulence, waves, and jets in a differentially heated rotating annulus experiment. *Physics of Fluids* **20**(12): 126602.

Yamazaki, Y.H., D.R. Skeet, & P.L. Read (2004) A new general circulation model of Jupiter's atmosphere based on the UKMO Unified Model: Three-dimensional evolution of isolated vortices and zonal jets in mid-latitudes. *Planetary and Space Science* **52**(5-6): 423–445.

Young, R.M.B. & P.L. Read (2008) Flow transitions resembling bifurcations of the logistic map in simulations of the baroclinic rotating annulus. *Physica D: Nonlinear Phenomena* **237**(18): 2251–2262.

Zurita-Gotor, Pablo (2008) The Sensitivity of the Isentropic Slope in a Primitive Equation Dry Model. *Journal of the Atmospheric Sciences* **65**(1): 43–65.